4

AFGL-TR-89-0070
ENVIRONMENTAL RESEARCH PAPERS, NO. 1023

Atmospheric Chemiluminescence: COCHISE and FACELIF Experiments

S. M. MILLER
D. R. SINCLAIR
J. I. STEINFELD
C. FELL
C. M. PHILLIPS
I. WINKLER
W. T. RAWLINS
M. E. FRASER
H. C. MURPHY
G. E. CALEDONIA
R. A. ARMSTRONG
R. A. STACHNIK

24 February 1989

Approved for public release; distribution unlimited.

OPTICAL PHYSICS DIVISION
PROJECT 2310
AIR FORCE GEOPHYSICS LABORATORY
HANSCOM AFB, MA 01731

"This technical report has been reviewed and is approved for publication"

George A. Vanasse
(Signature)
GEORGE A. VANASSE
Branch Chief

FOR THE COMMANDER

R Earl Good
(Signature)
R. EARL GOOD
Director

UNCLASSIFIED
SECURITY CLASSIFICATION OF THIS PAGE

REPORT DOCUMENTATION PAGE

Form Approved
OMB No. 0704-0188

1a. REPORT SECURITY CLASSIFICATION
Unclassified

1b. RESTRICTIVE MARKINGS

2a. SECURITY CLASSIFICATION AUTHORITY

2b. DECLASSIFICATION / DOWNGRADING SCHEDULE

3. DISTRIBUTION / AVAILABILITY OF REPORT
Approved for public release;
Distribution unlimited

4. PERFORMING ORGANIZATION REPORT NUMBER(S)
AFGL-TR-89-0070
ERP, No. 1023

5. MONITORING ORGANIZATION REPORT NUMBER(S)

6a. NAME OF PERFORMING ORGANIZATION
Air Force Geophysics Laboratory

6b. OFFICE SYMBOL *(If applicable)*
OPI

7a. NAME OF MONITORING ORGANIZATION

6c. ADDRESS *(City, State, and ZIP Code)*
Hanscom AFB, MA 01731-5000

7b. ADDRESS *(City, State, and ZIP Code)*

8a. NAME OF FUNDING / SPONSORING ORGANIZATION
AFOSR

8b. OFFICE SYMBOL *(If applicable)*

9. PROCUREMENT INSTRUMENT IDENTIFICATION NUMBER

8c. ADDRESS *(City, State, and ZIP Code)*

10. SOURCE OF FUNDING NUMBERS

PROGRAM ELEMENT NO.	PROJECT NO.	TASK NO.	WORK UNIT ACCESSION NO.
61102F	2310	G4	19

11. TITLE *(Include Security Classification)*
(U) Atmospheric Chemiluminescence: COCHISE and FACELIF Experiments

12. PERSONAL AUTHOR(S) Miller, S.M., Sinclair, D.R., Steinfeld[†], J.I., Fell[†], C.M., Phillips[†], C.M., Winkler[†], I., Rawlins[*], W.T., Fraser[*], M.E., Murphy[*], H.C., Caledonia[*], G.E., Armstrong[†], R.A., and Stachnik, R.A.

13a. TYPE OF REPORT
Scientific Interim

13b. TIME COVERED
FROM ________ TO ________

14. DATE OF REPORT *(Year, Month, Day)*
1989 February 24

15. PAGE COUNT
176

16. SUPPLEMENTARY NOTATION
* Physical Sciences, Inc., Research Park, PO Box 3100, Andover, MA 01810
† Massachusetts Institute of Technology, Cambridge, MA 02139

17. COSATI CODES

FIELD	GROUP	SUB-GROUP

18. SUBJECT TERMS *(Continue on reverse if necessary and identify by block number)*
Nitric oxide; Nitrous oxide; Nitrogen; Carbon monoxide; Carbon dioxide branching ratio; Multiphoton ionization; Vibration population distribution; Rotational band heads. (KT)

19. ABSTRACT *(Continue on reverse if necessary and identify by block number)*

During the last four years, many experiments have been performed in the COCHISE facility. Each of these experiments has measured a fundamental chemical quantity such as a radiative branching ratio, a quenching rate coefficient or a product vibrational energy distribution.

These measurements are then provided for incorporation into the various atmospheric radiation codes such as NORSE, ARC, AND AARC, where they provide a solid experimental footing for modeling the complex chemical system of the upper atmosphere. They include:

a. $N(^2D,^2P) + O_2 \rightarrow NO(v, \text{high } J) + O$ high rotational energy bandheads. Keywords;

b. $N_2^* + CO \rightarrow N_2 + CO\ (v, J)$ Carbon monoxide bandheads due to energy exchange mechanism.

c. $N_2(W \rightarrow B)$ Wu Benesch radiative electronic transitions and their vibrational branching ratios.

d. Nascent vibrational population distribution of ground state ozone.

e. N_2O production from co-discharged N_2/O_2.

20. DISTRIBUTION/AVAILABILITY OF ABSTRACT
☒ UNCLASSIFIED/UNLIMITED ☐ SAME AS RPT. ☐ DTIC USERS

21. ABSTRACT SECURITY CLASSIFICATION
Unclassified

22a. NAME OF RESPONSIBLE INDIVIDUAL
Steven Miller

22b. TELEPHONE *(Include Area Code)*
(617) 377-2810

22c. OFFICE SYMBOL
AFGL/OPI

DD FORM 1473, JUN 86 *Previous editions are obsolete.*

SECURITY CLASSIFICATION OF THIS PAGE
UNCLASSIFIED

The Experiments that have been performed using the FACELIF (Flowing Atmospheric Chemistry Experiment by Laser Induced Fluorescence) apparatus include:

a. $N(^4S) + O_2 \rightarrow NO(v) + O$ vibrational dependent rate constant

b. NO Multiphoton Ionization power dependence as a function of NO(A) state vibrational level.

c. $N(^2D,^2P) + O_2$ quenching rate constant determination.

d. $N(^2D,^2P) + O$ quenching rate constant determination.

A pair of lasers was used to measure the:

e. $CO_2(021 \rightarrow 020)/CO_2(021 \rightarrow 000)$ radiative branching ratio.

Contents

1. INTRODUCTION 1

2. ROVIBRATIONAL EXCITATION OF NITRIC OXIDE IN THE REACTION OF O_2 WITH METASTABLE ATOMIC NITROGEN
W.T. Rawlins, M.E. Fraser, and S.M. Miller 5

3. COCHISE IR EMISSION FROM $N_2/O_2/AR$ DISCHARGES
W.T. Rawlins, M.E. Fraser, and S.M. Miller 17

4. ROVIBRATIONAL EXCITATION OF CARBON MONOXIDE BY ENERGY TRANSFER FROM METASTABLE NITROGEN
M.E. Fraser, W.T. Rawlins, and S.M. Miller 25

5. SOLID STATE PHOTOMULTIPLIER RESULTS
S.M. Miller 59

6. INFRARED (2 TO 8 μm) FLUORESCENCE OF THE $W^3\Delta_u \rightarrow B^3\Pi_g$ AND $W^1\Delta_u \rightarrow a^1\Pi_g$ SYSTEMS OF NITROGEN
M.E. Fraser, W.T. Rawlins, and S.M. Miller 75

7. DYNAMICS OF VIBRATIONALLY EXCITED OZONE FORMED BY THREE-BODY RECOMBINATION: I. SPECTROSCOPY
W.T. Rawlins and R.A. Armstrong 83

8. DYNAMICS OF VIBRATIONALLY EXCITED OZONE FORMED BY THREE-BODY RECOMBINATION: II. KINETICS AND MECHANISM
W.T. Rawlins, G.E. Caledonia, and R.A. Armstrong 91

9. QUENCHING OF METASTABLE NITROGEN ATOMS ($^2D,^2P$) BY $O(^3P)$
S.M. Miller and C.P. Fell 105

10. DETERMINATION OF NO (V= 0-7) PRODUCT DISTRIBUTION FROM THE $N(^4S) + O_2$ REACTION USING TWO-PHOTON IONIZATION
I.C. Winkler, R.A. Stachnik, J.I. Steinfeld, and S.M. Miller 115

Contents

11. REMEASUREMENT OF N(^{2}P) + O_2 REACTION RATE USING MULTIPHOTON IONIZATION DETECTION OF NITROGEN ATOMS
    C.M. Phillips, J.I. Steinfeld, and S.M. Miller 127

12. EVALUATION OF 2-PHOTON IONIZATION SPECTROSCOPY AS A PROBE OF NO GROUND STATE POPULATION DISTRIBUTIONS
    I.C. Winkler, R.A. Stachnik, J.I. Steinfeld, and S.M. Miller 131

13. 2.7/4.3 MICRON CO_2 BRANCHING RATIO MEASUREMENT
    S.M. Miller 137

14. NEW HEATER CONTROL FOR COCHISE
    D.R. Sinclair 161

Atmospheric Chemiluminescence: COCHISE and FACELIF Experiments

1. Introduction

During the last four years, many experiments have been performed under the auspices of the COCHISE[1,2] facility. Each of these experiments has measured a fundamental chemical quantity such as a radiative branching ratio, a quenching rate coefficient or a product vibrational energy distribution. These measurements are then provided for incorporation into the various atmospheric radiation codes such as NORSE, ARC, and AARC, where they provide a solid experimental footing for modeling the complex chemical system of the upper atmosphere.

The COCHISE apparatus has been used to measure:

a. $N(^2D, ^2P) + O_2 \rightarrow NO(v, \text{high } J) + O$ high rotational energy bandheads.
b. $N_2^* + CO \rightarrow N_2 + CO\ (v, J)$ Carbon monoxide bandheads due to energy exchange mechanism.
c. $N_2\ (W \rightarrow B)$ Wu-Benesch radiative electronic transitions and their vibrational branching ratios.
d. Nascent vibrational population distribution of ground state ozone.

(Received for publication 24 February 1989)

1. Miller, S.M., Lurie, J.B., Armstrong, R.A., Winkler, I., Steinfeld, J.I., Rawlins, W.T., Gelb, A., Piper, L., Caledonia, G.E., Nebblesein, P., Weyl, G., and Green, B.D. (1985) *Spectroscopic, Kinetic and Dynamic Experiments on Atmospheric Species*, AFGL-TR-85-0077, ADA162691.
2. Armstrong, R.A., Kennealy, J.P., Robert, F.X., Corman, A., Rawlins, W.T., Piper, L.G., Caledonia, G.E., Green, B.D., Murphy, H.C., Steinfeld, J.I., Stachnik, R., and Adler-Golden, S.M. (1982) *Atmospheric Chemiluminescence: COCHISE and Related Experiments*, AFGL-TR-82-0305, ADA130546.

e. N_2O production from co-discharged N_2/O_2.

Since each experiment and its results can stand alone, a separate chapter is devoted to each, with self-contained tables, references, and appendixes.

The experiments that have been performed using the FACELIF (Flowing Atmospheric Chemistry Experiment by Laser Induced Fluorescence) apparatus include:

a. $N(^4S) + O_2 \rightarrow NO(v) + O$ vibrational dependent rate constant.
b. NO Multiphoton Ionization power dependence as a function of NO(A) state vibrational level.
c. $N(^2D,^2P) + O_2$ quenching rate constant determination.
d. $N(^2D,^2P) + O$ quenching rate constant determination.

A pair of lasers was used to measure the:

e. $CO_2(021 \rightarrow 020)/CO_2(021 \rightarrow 000)$ radiative branching ratio measurement.

References

1. Miller, S.M., Lurie, J.B., Armstrong, R.A., Winkler, I., Steinfeld, J.I., Rawlins, W.T., Gelb, A., Piper, L., Caledonia, G.E., Nebblesein, P., Weyl, G., and Green, B.D. (1985) *Spectroscopic, Kinetic and Dynamic Experiments on Atmospheric Species*, AFGL-TR-85-0077, ADA162691.
2. Armstrong, R.A., Kennealy, J.P., Robert, F.X., Corman, A., Rawlins, W.T., Piper, L.G., Caledonia, G.E., Green, B.D., Murphy, H.C., Steinfeld, J.I., Stachnik, R., and Adler-Golden, S.M. (1982) *Atmospheric Chemiluminescence: COCHISE and Related Experiments*, AFGL-TR-82-0305, ADA130546.

2. Rovibrational Excitation of Nitric Oxide in the Reaction of O_2 with Metastable Atomic Nitrogen

by

W.T. Rawlins, M.E. Fraser, and S.M. Miller

J. Phys. Chem. **1989**, *93*, 1097–1107 **1097**

Rovibrational Excitation of Nitric Oxide in the Reaction of O_2 with Metastable Atomic Nitrogen

W. T. Rawlins,* M. E. Fraser,

Physical Sciences Inc., Research Park, P.O. Box 3100, Andover, Massachusetts 01810

and S. M. Miller

Infrared Technology Division, Air Force Geophysics Laboratory, Hanscom AFB, Massachusetts 01731
(Received: December 29, 1987)

The dynamics of the reactions of $N(^2D,^2P)$ with O_2 have been investigated by observing the initial vibrational-state population distributions of $NO(X^2\Pi)$ formed in the interaction of oxygen and discharge-excited nitrogen in a cryogenically pumped, low-pressure reaction volume. Infrared chemiluminescence from vibrationally and rotationally excited $NO(v=1-14)$ was observed in the 5–7-μm spectral region, and spectral data were analyzed to obtain $NO(v,J)$ number densities. The results show multimodal vibrational and rotational distributions, indicative of several concurrent processes. In particular, extensive rotational excitation is evident in several vibrational levels of NO, resulting in sharply peaked R-branch band heads characteristic of $J \geq 80$. Surprisal analysis was applied to the data to infer the contributions of the various reaction pathways. This analysis indicates that all the possible reaction pathways for producing $NO(X^2\Pi)$, some of which lead to formation of metastable atomic oxygen, occur with significant probability. The results are discussed in terms of their implications for the detailed collisional dynamics of the reactions and their relevance to the study of upper atmospheric auroral chemistry.

Introduction

The importance of the reactions

$$N(^2D,^2P) + O_2 \rightarrow NO + O \qquad (1)$$

as the principal source of NO in the earth's mesosphere and thermosphere was suggested by Frederick Kaufman and others in 1967.[1] Following the direct rate coefficient measurements and product yield determinations of Lin and Kaufman,[2] first reported in preliminary form in 1970,[3] atmospheric modeling studies[4] showed that the $N(^2D)$ reaction accounted for the large upper atmospheric production of NO observed in rocket experiments.[5] A number of subsequent laboratory investigations[6–8] have provided refinements of the original[2,9] kinetic measurements, and atmospheric modeling studies[10,11] have continued to examine the roles of these reactions in odd nitrogen chemistry of the quiescent and auroral upper atmosphere.

From both an aeronomic and reaction dynamic point of view, the potential of the above class of reactions to form excited-state products, such as $NO(v)$, $O(^1D,^1S)$, and $NO(a^4\Pi,v)$, is of great interest. In a detailed experimental study, Kennealy et al.[12] showed that reaction 1 is an efficient source of highly vibrationally excited $NO(v)$ (up to 12 quanta with a strongly nonstatistical vibrational-state distribution), with implications that $O(^1D)$ might be formed as well. Rocket-borne infrared spectra of a strong aurora showed extensive auroral excitation of $NO(v)$;[13] these results were successfully modeled[11] in terms of direct formation by the reaction of aurorally produced $N(^2D)$ with O_2 as studied in the laboratory.

The possible reaction pathways for reaction 1 are shown in Table I. Also shown are the reaction exothermicities, the maximum energetically accessible (rotationless) vibrational levels in the product NO molecules, and the C_s symmetry species for adiabatic conversion of reactants to products. The symmetry species were determined[6,14] on the basis of the adiabatic correlation rules for atom–diatom reactions having nonlinear intermediate complexes, as described by Shuler.[15] Note that, despite the correlation of both reactants and products to doublet and quartet A′ and A″ surfaces, the reaction of $N(^2P)$ to form ground-state atomic oxygen (reaction 3a) has no adiabatic route; this results from application of the so-called "noncrossing rule" derived by analogy to avoided crossings in atom–atom collisions.[14] As we will discuss later, this is not sufficient reason to rule out the occurrence of this reaction pathway. Clearly, if significant reaction exothermicity goes into product vibrational excitation, it should be possible to identify the relative contributions of the various $NO(X^2\Pi)$ product channels by examining the infrared fluorescence "signatures" in the fundamental vibration–rotation transitions in the 5–8-μm spectral region.

The objective of the present study is to examine the detailed vibrational and rotational energy partitioning in $NO(X^2\Pi)$ formed from reactions 2 and 3. We have used the technique of nascent-product infrared chemiluminescence spectroscopy under near-single-collision conditions in the COCHISE (cold chemiluminescence infrared stimulation experiment) cryogenic reactor/spectrometer facility at the Air Force Geophysics Laboratory. Previous investigation[12] of these reactions on the COCHISE apparatus showed extensive NO vibrational excitation, principally from $N(^2D)$, and inferred the possibility of $O(^1D)$ formation via reaction 2b from surprisal analysis of the NO vibrational distributions. In addition, evidence of significant rotational excitation

---

(1) (a) Kaufman, F., ref 19 in a paper by T. M. Donahue, Invited Papers from the Fifth International Conference on the Physics of Electronic and Atomic Collisions, Leningrad, 1967, p 32. (b) Norton, R. B. ESSA Tech. Memo. IERTM-ITSA 60, 1967.

(2) Lin, C. L.; Kaufman, F. *J. Chem. Phys.* **1971**, *55*, 3760.

(3) Lin, C. L.; Kaufman, F. Presented at DASA Symposia on the Physics and Chemistry of the Upper Atmosphere, Stanford Research Institute, June 1969, and Philadelphia, June 1970.

(4) (a) Norton, R. B.; Barth, C. A. *J. Geophys. Res.* **1970**, *75*, 3903. (b) Strobel, D. F.; Hunten, D. M.; McElroy, M. B. *J. Geophys. Res.* **1970**, *75*, 4307.

(5) (a) Barth, C. A. *Ann. Geophys.* (*C.N.R.S.*) **1966**, *22*, 198. *Planet Space Sci.* **1966**, *14*, 623. (b) Meira, L. G. *J. Geophys. Res.* **1971**, *76*, 202.

(6) Schofield, K. *J. Chem. Phys.* **1979**, *8*, 723.

(7) Iannuzzi, M. P.; Kaufman, F. *J. Chem. Phys.* **1980**, *73*, 4701.

(8) Piper, L. G.; Donahue, M. E.; Rawlins, W. T. *J. Chem. Phys.* **1977**, *91*, 3883.

(9) Black, G.; Slanger, T. G.; St. John, G. A.; Young, R. A. *J. Chem. Phys.* **1969**, *51*, 116.

(10) Kondo, Y.; Ogawa, T. *J. Geomagn. Geoelectr.* **1976**, *28*, 253; **1977**, *29*, 65.

(11) Caledonia, G. E.; Kennealy, J. P. *Planet. Space Sci.* **1982**, *30*, 1043.

(12) Kennealy, J. P.; Del Greco, F. P.; Caledonia, G. E.; Green, B. D. *J. Chem. Phys.* **1978**, *69*, 1574.

(13) Rawlins, W. T.; Caledonia, G. E.; Gibson, J. J.; Stair, A. T., Jr. *J. Geophys. Res.* **1981**, *86*, 1313.

(14) Donovan, R. J.; Husain, D. *Chem. Rev.* **1970**, *70*, 489.

(15) Shuler, K. E. *J. Chem. Phys.* **1953**, *21*, 624.

0022-3654/89/2093-1097$01.50/0

TABLE I: Pathways for NO Formation from $N(^2D,^2P) + O_2$

reacn no.	reacn	adiabatic surfaces	ΔH°_{298}, kcal mol^{-1}	max. v for NO
2a	$N(^2D_u) + O_2(X^3\Sigma_g^-) \rightarrow NO(X^2\Pi) + O(^3P_g)$	$2^2A' + 2^2A'' + {}^4A' + {}^4A''$	−86.80	18
2b	$\rightarrow NO(X^2\Pi) + O(^1D_g)$	$^2A'$	−41.43	8
3a	$N(^2P_u) + O_2(X^3\Sigma_g^-) \rightarrow NO(X^2\Pi) + O(^3P_g)$	none	−114.28	26
3b	$\rightarrow NO(X^2\Pi) + O(^1D_g)$	$^2A''$	−68.91	14
3c	$\rightarrow NO(X^2\Pi) + O(^1S_g)$	$^2A''$	−17.67	3
3d	$\rightarrow NO(a^4\Pi) + O(^3P_g)$	$^2A' + {}^4A' + 2^4A''$	−3.3	1

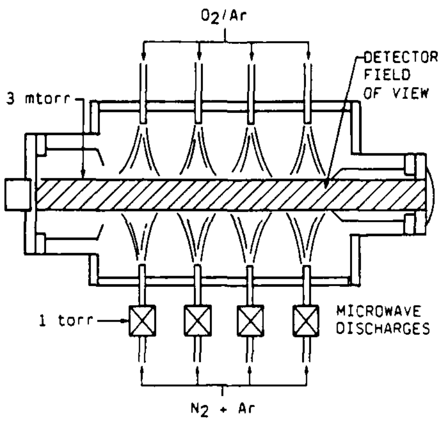

Figure 1. Diagram of the COCHISE reaction chamber. The physical dimensions of the cell are 0.6 m in length and 0.4 m in diameter.

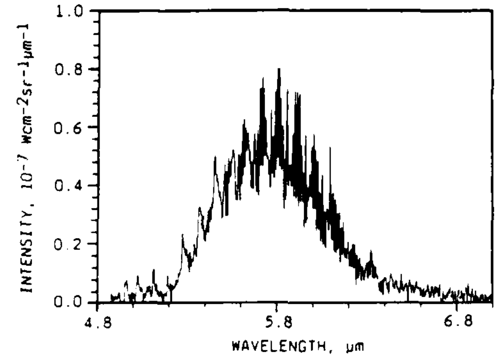

Figure 2. Spectrum of fluorescence observed in the interaction of O_2 with discharged N_2/Ar (12% N_2). Spectral resolution is 0.007-μm fwhm. Gas temperature is 80 K.

was observed at the lowest pressures employed. However, the results were affected by the presence of unidentifiable underlying spectral features at the short- and long-wavelength ends of the spectra, and the contributions due to $N(^2P)$ could not be unambiguously assessed. In the present work, we have taken advantage of increased sensitivity and dynamic range to remove contributions from background radiation and to extend the results to higher vibrational levels. We have identified previously unknown spectral features as R-branch band heads resulting from extensive rotational excitation ($J \sim 100$) in each of at least eight vibrational levels, which we attribute to formation by $N(^2P)$. We have inferred detailed product channels via surprisal analysis of the NO internal energy distributions; the results indicate that the $N(^2D)$ and $N(^2P)$ reactions with O_2 proceed by very different molecular dynamic mechanisms.

Experimental Measurements

The design and operation of the COCHISE facility have been described in detail elsewhere.[16] In brief, the entire radiative environment of the experiment is maintained at a base temperature of approximately 20 K, which effectively eliminates background radiation within the 2–20-μm operating range of the apparatus. The detection system consists of a scanning grating monochromator and a liquid-helium-cooled Si:As detector. Reagent gases are introduced into the reaction cell through temperature-controlled feed lines, as shown in Figure 1. $N(^2D,^2P)$ are produced (together with $N(^4S)$ and excited metastable states of N_2) by passing a flowing N_2/Ar mixture at approximately 1 Torr through four parallel microwave discharges (2450 MHz, 50 W) prior to expanding into a low-pressure (approximately 3 mTorr), cryogenically pumped interaction volume. A counterflow gas (O_2 or Ar) enters the volume from the opposite side to combine with the discharge-excited gas in a stagnation region along the axis of the cell, which coincides with the axis of the cylindrical field of view of the detection system. In the case of an unreactive counterflow, this interaction provides an arrested relaxation condition for studies of infrared fluorescence arising from discharge excitation processes.[17-19] However, in the present experiments, an O_2 counterflow reacts promptly in the field of view with the effluents of the N_2/Ar discharges to give readily identifiable chemiluminescence from vibrationally excited NO under conditions where diffusive loss dominates over radiative or collisional cascade.[12]

For most experiments, reagent gases were introduced at controlled temperatures of 80–90 K; no temperature dependence in the fluorescence intensity or general spectral distribution was observed at temperatures up to 120 K. In each discharge tube, the Ar flow rate was held at 640 μmol s^{-1}, and the N_2 flow rate was systematically varied from 5 to 86 μmol s^{-1} (0.8–12% N_2). Mass-balanced counterflows of either O_2 or Ar were used to produce chemiluminescence or determine background fluorescence levels, respectively. Under these conditions, the gas residence time in the active discharge is approximately 2–5 ms, the transit time from the discharge exit to the field of view is ~0.5 ms, and the residence time in the field of view is ~0.3 ms.

Infrared fluorescence spectra were obtained in the 4–8-μm region with spectral resolutions of 0.007–0.040 μm (2.8–16 cm^{-1} at 5 μm). Some 50 spectral scans were required to survey the parameter space of N_2 mole fraction, O_2 mole fraction, temperature, discharge power, and spectral resolution (including foreground and background scans). The uncertainty in the observed wavelengths (due to a slight periodic fluctuation in the cryogenic monochromator scan rate) is ±0.003 μm; absolute wavelengths were calibrated by using the well-resolved band center of the CO(1→0) vibrational transition excited by energy transfer from discharge-excited nitrogen.[16,20] The spectral data were acquired via phase-sensitive detection, using a computer-interfaced lock-in amplifier and chopping the discharges with a 23-Hz square wave. The observed intensities were corrected to radiometric units by using blackbody calibrations of the absolute spectral responsivity of the detection system.

Results and Discussion

Spectral Data. An example fluorescence spectrum observed in the interaction of discharged N_2/Ar with O_2 is shown in Figure

---

(16) Rawlins, W. T.; Murphy, H. C.; Caledonia, G. E.; Kennealy, J. P.; Robert, F. X.; Corman, A.; Armstrong, R. A. *Appl. Opt.* **1984**, *23*, 3316.

(17) Rawlins, W. T.; Armstrong, R. A. *J. Chem. Phys.* **1987**, *87*, 5202.

(18) Rawlins, W. T.; Caledonia, G. E.; Armstrong, R. A. *J. Chem. Phys.* **1987**, *87*, 5209.

(19) Fraser, M. E.; Rawlins, W. T.; Miller, S. M. *J. Chem. Phys.* **1988**, *88*, 538.

(20) Fraser, M. E.; Rawlins, W. T.; Miller, S. M. *J. Chem. Phys.*, to be submitted.

2 for the highest usable spectral resolution. Spectral scans in which the O_2 in the counterflow was replaced by Ar revealed the presence of weak underlying radiation from various sources throughout the band-pass of interest (4–8 μm). These consist of (1) Ar I Rydberg lines between 4 and 5 μm; (2) $N_2(W^3\Delta_u-B^3\Pi_g)$ bands near 6.5 and 7.5 μm (the (1,0) and (2,1) bands, respectively); and (3) broad but structured emission extending from 5.2 to approximately 7.5 μm. We have previously investigated the first two emission systems in some detail: the Ar I radiation[21] is scattered light from the discharges, and the N_2(W–B) emission[19] arises from discharge-excited species which survive long enough to radiate in the field of view. The third background contribution occurs with signal-to-noise ratios that are too low to permit conclusive identification; however it appears that this feature arises from NO(v) formed in the discharges due to ppm-level oxygen impurity in the discharged gas. The fluorescence spectral distribution is "collapsed" toward shorter wavelengths (lower vibrational levels), indicative of substantial collisional deactivation as expected for the ~1-Torr discharges. The maximum intensity of this feature is about 1 order of magnitude less than that of the chemiluminescence signal, but the contribution to the observed spectrum from the background emission is significant for wavelengths below 5.4 μm and above 6.4 μm ($v \leq 2$ and $v \geq 12$, respectively). Accordingly, the chemiluminescence spectra were corrected for background contributions by subtracting companion background spectra obtained immediately before or after each scan, with all conditions identical except for the substitution of an Ar counterflow instead of O_2. An unfortunate result of this subtraction procedure was to limit the dynamic range at long wavelengths and hence the maximum observable vibrational level. The bulk of the remaining chemiluminescence, between 5.2 and 6.5 μm, can be readily identified through its vibrational and rotational spacings as $NO(X^2\Pi, v'=1-14)$. The maximum spectral intensity occurs for $v' = 5-7$, and the rotational distributions in this portion of the spectrum signify near-thermal equilibrium with the gas temperature. Also present in the background-corrected spectra is a series of eight sharp, red-degraded features between 4.95 and 5.55 μm (cf. Figure 2). These features, which have a constant spacing of 31 ± 2 cm^{-1}, are reproducible in wavelength and relative intensity for all NO chemiluminescence experiments. The features between 4.9 and 5.2 μm were noted in earlier investigations;[12] however, poorer signal-to-noise ratios precluded systematic examination, and the usable spectral resolution in those experiments was too low to reveal the presence of the additional features extending into the main NO band. It is clear that the presence of these features could significantly affect the vibrational analysis of the NO spectrum. Furthermore, the three features between 4.95 and 5.15 μm are coincident with similar spectral features recently observed by a rocket-borne interferometer in an overhead aurora,[22] suggesting that this emission represents a previously unknown aeronomic phenomenon.

The observed spectral features do not correspond to any of the possible transitions that might be excited in the experiments, e.g., vibrationally excited NO^+ or N_2O, or electronic transitions of NO, N_2, and O_2. However, it is straightforward to show that the observed band positions correspond well to those predicted for R-branch band heads of the vibrational transitions of $NO(X^2\Pi)$ itself. The presence of such band heads in a vibrational transition requires an extraordinary degree of rotational excitation. For the $(v',v'') = (1,0)$ transition, for example, the vertex of the Fortrat parabola occurs for $J' \sim 80$, a rotational energy in excess of 1.3 eV. Thus, it appears that the vibrational transitions for at least $v' = 1-8$ have strongly bimodal rotational distributions, with Boltzmann "temperatures" ranging from ~100 to ~10 000 K. The rotational states contributing to the R-branch band heads ($J' \sim 60-100$) should also exhibit P-branch structure extending to 8 or 9 μm; unfortunately, due to the low signal-to-noise ratios at the longer wavelengths, we cannot examine the P-branch distributions to determine the detailed rotational population distributions at large J'. Furthermore, due to extensive overlap by the relatively intense, rotationally "thermal" component beyond 5.6 μm, we cannot determine whether there are weak rotationally excited components for vibrational levels $v' > 8$. By comparison, in experiments where CO/Ar counterflows are used, we observe similar band head formation in several vibrational levels of the CO(Δv=1) system from rotational/vibrational excitation by energy transfer from active nitrogen;[20] these measurements have sufficient intensity to permit resolution of the P-branch structure at large J' and show that a two-temperature bimodal description provides a reasonable approximation to the rotational-state populations. To examine trends in the relative intensities of the "hot" and "cold" rotational components of NO, as well as in the vibrational distributions, several experimental parameters were independently varied. Spectra were obtained over the following ranges: discharge power, 10–50 W; gas temperature, 80–120 K; counterflow O_2 mole fraction, 0.0–1.0 (Ar diluent); and discharge N_2 mole fraction, 0.008–0.12 (Ar diluent). Increasing the discharge power gave increased signal intensity with no discernible effect on the spectral distributions. Increasing the gas temperature did not affect the observed spectral intensities or distributions except for slight increases in the "thermal" rotational temperatures. Reduction of the counterflow O_2 mole fraction gave a corresponding decrease in spectral intensity, with no significant effect on the spectral distributions. Reduction in the discharge N_2 mole fraction by a factor of 15 gave a factor of ~2 decrease in overall signal intensity, with ~30% apparent reduction in the relative high-J' contributions. This latter effect is significant for the present observations and will be discussed further in terms of the derived vibrational-state populations below.

TABLE II: Spectroscopic Constants for $NO(X^2\Pi)$[a,b]

ω_e	1903.937	α_e	0.017554
$\omega_e x_e$	13.970	D_e	5.36×10^{-6}
$\omega_e y_e$	-3.7×10^{-3}	β_e	5.0×10^{-8}
$\omega_e z_e$	5.0×10^{-5}	A_e	123.28
B_e	1.70488	X_e	0.256

[a] Values are from ref 24 except for β_e (see text). [b] Units are appropriate for calculation of transition frequencies in cm^{-1}.

Spectroscopic Analysis. The spectral data were analyzed to determine detailed vibrational-state populations by using a linear least-squares spectral fitting method which we have employed for a number of vibrational excitation studies.[12,13,16-18] The method consists of computing instrument-convolved basis functions for each $\Delta v = 1$ vibration–rotation transition using an accurate spectroscopic formalism and fitting those functions to an observed spectrum to determine the individual integrated intensity of each vibrational transition. These values can then be transformed into upper vibrational state number densities through application of the appropriate band transition probabilities.

The vibration–rotation energies and transition frequencies of $NO(X^2\Pi)$ were computed explicitly,[23] including the effects of spin–orbit coupling, vibrational anharmonicity, vibration–rotation interaction, and centrifugal distortion; effects of electronic rotational interaction (Λ-type doubling) are negligible for these experiments (<0.1 cm^{-1}). The spectroscopic constants used for the computations are shown in Table II. For the most part, these are the same values given by Goldman and Schmidt[24] and used by Rawlins et al.[13] to fit high-resolution auroral spectra. The single exception is the value of β_e, the correction term to the centrifugal constant D_v, which we adjusted in order to better reproduce the positions of the R-branch band heads. The value of β_e given in Table II is about twice that used by Rawlins et al.,[13] who reversed an apparent error of sign in the value given by Goldman and Schmidt.[24] Comparison of the D_v values of Goldman and Schmidt

---

(21) Rawlins, W. T.; Gelb, A.; Armstrong, R. A. *J. Chem. Phys.* **1985**, *82*, 681.

(22) Picard, R. H.; Winick, J. R.; Sharma, R. D.; Zachor, A. S.; Espy, P. J.; Harris, C. R. *Adv. Space Res.*, in press.

(23) Herzberg, G. *Molecular Spectra and Molecular Structure: I. Spectra of Diatomic Molecules*; Van Nostrand: Toronto, 1950.

(24) Goldman, A.; Schmidt, S. C. *J. Quant. Spectrosc. Radiat. Transfer* **1975**, *15*, 127.

to subsequent work by Amiot and Vergès[25] indicates a 2% uncertainty in D_0 at room temperature, which encompasses the change we require for β_e.

For the limited spectral resolution of these experiments, a complete description of the line-by-line rotational intensities is not feasible, nor does adequate information exist for extending these intensities to the high rotational levels observed here. As an approximate treatment, we have used band-averaged Einstein coefficients together with Hönl–London scaling of the relative rotational strengths. The relative intensity of the ith optically thin rotational line emanating from the state (v',J',Ω') is then given by

$$I_i = hc\frac{\nu_i^4}{\nu_B^3}S_i(\mathrm{P,Q,R})A_{v'v''}N_{v'}\frac{\exp(-E(J',\Omega')/kT)}{Q(v')}$$

where ν_i and ν_B are the transition frequencies of the line and the band center, respectively, $S_i(\mathrm{P,Q,R})$ are the appropriate Hönl–London factors as given by Herzberg,[23] $A_{v'v''}$ is the thermally averaged Einstein coefficient for the band, $N_{v'}$ is the population of the emitting vibrational level, and $Q(v')$ is the spin–orbit/rotational partition function for the emitting vibrational level. Note that here we have assumed that the $^2\Pi_{1/2}$ and $^2\Pi_{3/2}$ spin–orbit states are in thermal equilibrium, which in fact seems to be the case, at least for the rotationally thermal component of the spectrum where spin nonequilibrium would be the most apparent.

The individual line-by-line vibrational basis sets are convolved with the instrumental scan function (in this case, an isosceles triangle with full width at half-maximum as the spectral resolution) and are fit to each experimental spectrum by linear least squares to determine the products $N_{v'}A_{v'v''}$. The individual upper state number densities are then determined by application of band-averaged Einstein coefficients for each transition (see below).

In the fitting procedure, the bimodal rotational distributions in each of the lowest eight vibrational levels were approximated by two separate vibrational populations with Boltzmann rotational distributions corresponding to thermal (~100 K) and "hot" (~10000 K) temperatures. These temperatures were independently varied to optimize the fits to the appropriate rotational contours and were found to be typically 120 ± 10 and 10000 ± 4000 K. The quoted uncertainties are based on the variations required to produce recognizable deviations from the observed band shapes near 5.6–6.0 and 4.9–5.2 μm for the "cold" and "hot" components, respectively. Within these ranges of temperature parameters, the vibrational distributions determined from the spectral fits were not significantly affected. We attempted to determine whether the rotational temperature for the "hot" component was dependent on vibrational level. While there was some indication that the R-branch band head structures required somewhat lower rotational temperatures for the higher vibrational levels, the limitations of signal-to-noise ratio, spectral resolution, and band overlap precluded a quantitative determination of this trend.

TABLE III: Band-Integrated Einstein Coefficients for NO($\Delta v = 1$) Emission[a]

v'	$A_{v'v''}$, s^{-1}	v'	$A_{v'v''}$, s^{-1}	v'	$A_{v'v''}$, s^{-1}
1	13.4	8	71.2	15	76.4
2	25.3	9	75.0	16	74.1
3	36.2	10	77.7	17	71.3
4	45.8	11	79.4	18	68.1
5	54.2	12	80.0	19	64.3
6	60.1	13	79.5	20	60.0
7	66.3	14	78.2		

[a] Determined from data of ref 27 and scaled according to predictions of ref 28 (see text).

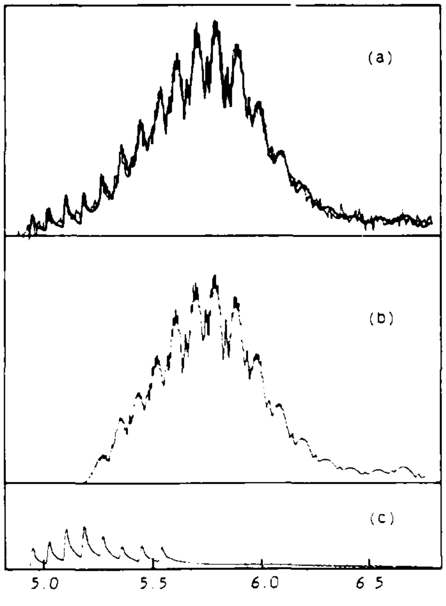

Figure 3. Comparison of computed and observed NO(v) spectra: discharge, 12% N_2 in Ar; counterflow, O_2; gas temperature, 80 K; spectral resolution, 0.013-μm fwhm; corrected for background emission from the discharges. (a) Comparison of calculated (heavy line) and observed (light line) spectra. (b) Contribution to computed spectrum from rotationally "cold" component, $T_{rot} = 120$ K, $v = 1$–14. (c) Contribution to computed spectrum from rotationally "hot" component, $T_{rot} = 10000$ K, $v = 1$–8. The sharp features between 4.9 and 5.6 μm are the R-branch band heads for $v = 1$–8.

The band-averaged Einstein coefficients for each vibrational transition were chosen by logic analogous to that recommended by Rothman et al.[26] The value for the $(v',v'') = (1,0)$ band was taken from the absorptivity measurement of Holland et al.,[27] and the scaling to higher v' followed relative values predicted by Billingsley[28] from ab initio calculations of the dipole moment function. This relative scaling is supported by experimental measurements of the $(\Delta v = 2)/(\Delta v = 1)$ branching ratios for $v' \leq 7$,[29] and the resulting values of $A_{v'v''}$ appear to be reasonably accurate (approximately ±30% or better). Recent COCHISE measurements of $(\Delta v = 2)/(\Delta v = 1)$ ratios extending to higher v' indicate more substantial uncertainty in the theoretical dipole moment function for $v' \geq 9$,[30] but the relative values of $A_{v'v''}$ for the fundamental band are probably not severely affected by this uncertainty. The values of $A_{v'v''}$, determined by the above procedure and used in the analysis of all data discussed in this paper, are listed in Table III. It should be noted that, although the band-averaged Einstein coefficients are nearly independent of rotational temperature up to at least 600 K,[28] there may be effects at high J' due to rotation–vibration coupling and uncoupling of spin and orbital angular momentum (transition to Hund's case b), as noted by Billingsley[28] for $J' \sim 30$. To test for this possibility, we performed more detailed computations accounting for spin uncoupling which indicate that the case a Hönl–London factors provide a good approximation up to $J \sim 100$. More significantly, however, the high-J' states forming the band heads are sufficiently high in the NO manifold to probe the range of internuclear distance where the calculations of Billingsley indicate the onset of downward curvature in the dipole moment function and where our recent $(\Delta v = 2)/(\Delta v = 1)$ data[30] indicate uncertainty in this calculated behavior. Thus, the computed relative rotational in-

---

(25) Amiot, C.; Vergès, J. *J. Mol. Spectrosc.* **1980**, *81*, 424.

(26) Rothman, L. S.; Goldman, A.; Gillis, J. R.; Gamache, R. R.; Pickett, H. M.; Poynter, R. L.; Husson, N.; Chedin, A. *Appl. Opt.* **1983**, *22*, 1616.

(27) Holland, R. F.; Vasquez, M. C.; Beattie, W. H.; McDowell, R. S. *J. Quant. Spectrosc. Radiat. Transfer* **1983**, *29*, 435.

(28) Billingsley, F. P. II *J. Mol. Spectrosc.* **1976**, *61*, 53; *J. Chem. Phys.* **1975**, *62*, 864; **1975**, *63*, 2267; AFCRL-TR-75-0586, Air Force Geophysics Laboratory, Hanscom AFB, MA 01731, 13 Nov 1975.

(29) Green, B. D.; Caledonia, G. E.; Murphy, R. E. *J. Quant. Spectrosc. Radiat. Transfer* **1981**, *26*, 215.

(30) Rawlins, W. T.; Fraser, M. E.; Miller, S. M., manuscript in preparation.

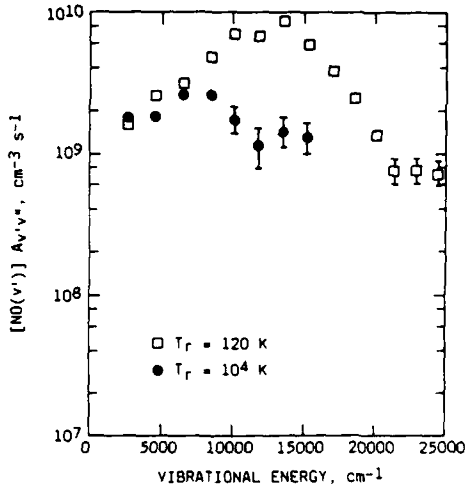

Figure 4. Vibrational band intensities determined from spectral fit in Figure 3.

tensity scaling may not be applicable to the R-branch band heads; the rotationally "hot" vibrational populations determined in this way are then somewhat uncertain. A more detailed determination of the absolute values of $A_{v'v''}(J')$, as well as experimental determination of the transition moment at large internuclear separation, is currently in progress.

Vibrational Population Distributions. A typical comparison of observed and computed least-squares-fit spectra is illustrated in Figure 3, together with the contributions of the rotationally "hot" and "cold" components. The values of $N_{v'}A_{v'v''}$ determined from the fit are plotted in Figure 4. The error bars indicate the statistical standard deviations ($\pm 1\sigma$) in the solutions. Application of the Einstein coefficients of Table III gives the upper state vibrational number densities with the same relative standard deviations. Uncertainties in the Einstein coefficients, which cannot be evaluated statistically and are the same for all the data analyzed, are not shown in our plots of the vibrational populations.

In general, relative vibrational population distributions obtained by omitting the background correction procedure and the "hot" rotational contributions gave excellent agreement with values determined earlier in COCHISE for $v' = 1$–12[12] and with values inferred for reaction 2, $v' = 1$–7 from electron beam excitation of air.[31] Application of background correction reduces the apparent relative population in $v' = 1$ by about 10% and that for $v' = 12$ by more than a factor of 2 from the previous determination; in addition, the present experiments provide information for levels up to $v' = 14$. Inclusion of the rotationally "hot" states gives a further reduction of the "cold" $v' = 1$ population by a factor of ~2, with only minor effects on the higher levels. As described above, the relative distributions were not affected significantly by variations in experimental parameters. Accordingly, the solutions for a series of five spectra, obtained sequentially with spectral resolution of 0.013 μm and carefully optimized signal-to-noise ratio, were averaged together to give a set of absolute vibrational-state populations corresponding to the condition $T = 80$ K, discharge power = 50 W, and discharge N$_2$ mole fraction = 0.12, to be used for subsequent kinetic analysis. This composite averaged distribution is shown in Figure 5 and is well representative of relative distributions determined for all experimental conditions. The remainder of this paper deals with kinetic interpretations of the results in Figure 5 to determine product branching fractions for the reactions in Table I.

Kinetic Interpretations

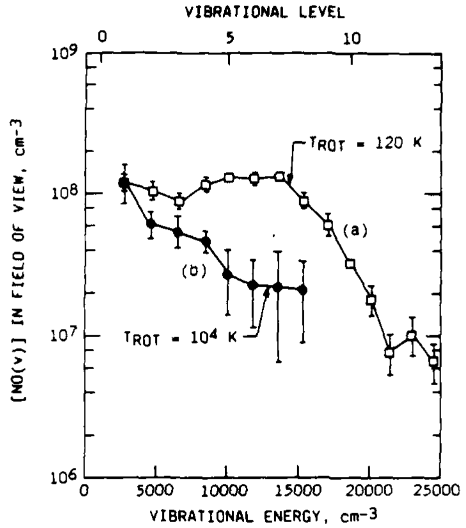

Figure 5. Average vibrational population distributions for (a) rotationally thermal and (b) rotationally "hot" portions of the NO chemiluminescence.

TABLE IV: Estimated Number Densities of Energetic Discharge Effluents[a]

species	number density, molecules cm^{-3}	
	discharge exit	reaction zone
N(^{4}S)	2 × 10^{14}	7 × 10^{11}
N(^{2}D)	(1–4) × 10^{12}	(0.3–1) × 10^{10}
N(^{2}P)	(0.5–1) × 10^{12}	(1–3) × 10^{9}
N$_2$(X$^1\Sigma_g{}^+$,v=1–7)	3 × 10^{15}	1 × 10^{13}
N$_2$(A$^3\Sigma_u{}^+$)	1 × 10^{12}	3 × 10^{9}
N$_2$(W$^3\Delta_u$,v=1–2)	3 × 10^{10}	3 × 10^{8} [b]
N$_2$(a$'^1\Sigma_u{}^-$)	1 × 10^{12}	3 × 10^{9}
N$_2$(w$^1\Delta_u$,v=0–2)	6 × 10^{10}	1 × 10^{8} [b]

[a] Microwave discharge conditions given in the text, approximately 10% N$_2$ in Ar. [b] Based on direct observations reported in ref 19. Higher vibrational levels are affected by radiative losses during transit from discharge exit to reaction zone.

On the basis of the results of previous studies,[12,31] it is reasonable to expect that the rotationally "thermal" vibrational distribution in Figure 5 arises largely from the reaction of N(^{2}D) with O$_2$. However, the rotationally "hot" vibrational distribution may arise from another process involving reaction or energy transfer of other excited species formed in the discharge. The principal energetic species emanating from the Ar/N$_2$ microwave discharges for our fast-flow conditions and surviving into the field of view are N(^{4}S,^{2}D,^{2}P) and N$_2$((X$^1\Sigma_g{}^+$,v),A$^3\Sigma_u{}^+$,W$^3\Delta_u$,a$'^1\Sigma_u{}^-$,w$^1\Delta_u$).[19] The flux of charged species escaping the discharge region is negligibly small; this is verified by the observation of no excitation in CO and N$_2$ counterflows upon interaction with the effluents of 100% Ar discharge. On the basis of a combination of discharge modeling calculations (using methods[18] and electron-impact cross sections[32] described elsewhere), direct observations of discharge effluents in a flow reactor at room temperature,[33] and observations of infrared-radiating states of N$_2$ in COCHISE,[19] we can assemble a set of anticipated discharge effluent number densities for the present experiments at a discharge N$_2$ mole fraction of ~0.1, as shown in Table IV. The molecular metastables arise principally from direct excitation of N$_2$ by electrons (characteristic electron energies are 6–8 eV in dilute N$_2$/Ar mixtures) and metastable argon, and the atomic metastables are produced primarily by electron-impact excitation of N(^{4}S) formed from N$_2$ dissociation. Clearly, N(^{4}S) is the dominant species, but it is too unreactive with O$_2$ at these temperatures to produce significant NO(v).[12,34]

---

(31) Green, B. D.; Caledonia, G. E.; Blumberg, W. A. M.; Cook, F. H. *J. Chem. Phys.* **1984**, *80*, 773.

(32) Caledonia, G. E.; Davis, S. J.; Green, B. D.; Piper, L. G.; Rawlins, W. T.; Simons, G. A.; Weyl, G. AFWAL-TR-86-2078, Air Force Wright Aeronautical Laboratories, Wright Patterson AFB, OH 45433-6503, 1986.

(33) Piper, L. G.; Rawlins, W. T., unpublished work.

Similarly, we do not expect any of the molecular metastables to react with O_2 to form NO(v), as a four-center collision complex would be required. An interesting possible route for NO(v) excitation is via energy transfer from N_2(A) to NO[35] that is formed by N* reactions in the field of view:

$$N_2(A^3\Sigma_u^+) + NO(X^2\Pi,v) \rightarrow N_2(X^1\Sigma_g^+) + NO(A^2\Sigma^+,v)$$

$$NO(A^2\Sigma^+,v) \rightarrow NO(X^2\Pi,v') + h\nu$$

The NO(v') distribution that is formed by the rapid radiative cascade step is governed by the Franck–Condon factors for the transition and is similar to that observed for the rotationally "hot" component in Figure 5. However, due to the low number densities of both N_2(A) and NO in the interaction volume, the NO(v') number densities obtained from this process are about 4 orders of magnitude smaller than those observed in the measurements. Furthermore, although rotational excitation of NO(A) has been observed in this process,[35] there is insufficient exoergicity to account for the much greater rotational excitation observed here. By similar kinetic arguments, it is straightforward to eliminate other electronic-energy-transfer processes, as well as the possibility of rotational excitation by energy transfer to NO from translationally excited atoms emanating from the discharge. While translational excitation of atoms is known to occur by energy transfer from Ar metastables,[36,37] this energy is moderated within microseconds in the 1-Torr discharge tubes, and the number density of "hot" atoms reaching the field of view will be miniscule. Finally, the possibility for collisional quenching from a high vibrational level of NO into a high rotational level of a low vibrational level (V,R transfer), analogous to processes observed for HF,[38] can also be dismissed. To excite the high-J' levels we observe would require quenching of vibrational levels 5–12 or higher. Since we observe very low relative populations for $v \geq 10$ under conditions of 20–30 collisions per observed NO(v) molecule, this would require essentially gas-kinetic quenching of NO(v) by Ar. This is highly unlikely, since direct measurements of the v-dependent quenching of NO(v) by O_2[39] and of CO(v) by CO_2[40] indicate quenching rate coefficients (by whatever mechanism) which are less then 1% gas kinetic even for seven or more vibrational quanta of excitation. Thus, any amount of rotational excitation produced by V,R transfer will be insignificant in our experiments. Similarly, the observed vibrational distributions are not perturbed by collisional deactivation by O, O_2, N_2, N, or Ar, as demonstrated in the earlier work of Kennealy et al.[12] We conclude that the observed vibrational distributions represent composites of the initial product distributions from the reactions of N(^{2}D,^{2}P) listed in Table I. Based on the results of ref 31, the rotationally "cold" distribution appears to arise largely from the N(^{2}D) reactions; by process of elimination, the rotationally "hot" distribution appears to result from N(^{2}P) reactions with O_2.

Due to the composite nature of these product-state distributions, it is difficult to assign the individual reaction channels unambiguously. However, it is instructive to examine the observed composite distributions with the aid of surprisal theory. This approach postulates the existence of an exponential gap law for an individual metathetic reaction:[41]

$$P(v) = P^\circ(v)\ \exp(-\lambda f_v)/\exp(\lambda_0)$$

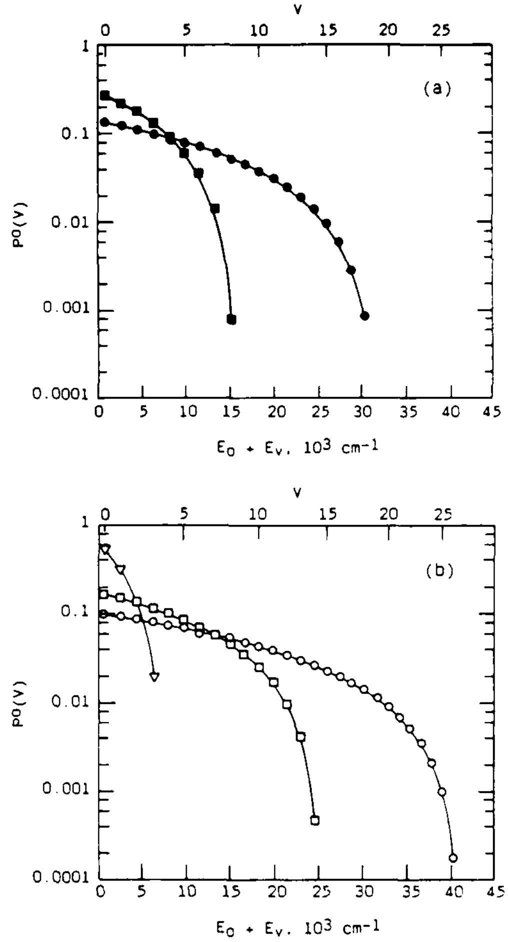

Figure 6. Computed prior distributions for NO(v) formed in N* + O_2 reactions. (a) N(^{2}D) + O_2: ●, O(^{3}P) product; ■, O(^{1}D) product. (b) N(^{2}P) + O_2: ○, O(^{3}P) product; □, O(^{1}D) product; ▽, O(^{1}S) product.

where f_v is the fraction of the reaction exoergicity appearing as vibrational energy in the product, $P(v)$ is the observed relative vibrational population, and $P^\circ(v)$ is the statistical "prior" distribution obtained when all final translational, rotational, and vibrational states are equally probable. Thus, the ratios of the observed and statistical vibrational populations should be exponential in the vibrational energy E_v, with the exponential falloff constant λ quantifying the departure of the observed distribution from a completely statistical product distribution. While this theory does not necessarily hold for all chemical reactions, it does provide useful guidelines for the interpretation of product-state distributions in terms of the molecular reaction dynamics. The prior distributions were determined from the usual relationship for a vibrating rotator:[41]

$$P^\circ(v) = (1 - f_v)^{3/2} \Big/ \sum_{v=0}^{v^*} (1 - f_v)^{3/2}$$

Computed prior distributions are shown in Figure 6 for the reactions in Table I.

Application of surprisal analysis to the vibrational distributions of Figure 5 is by no means straightforward as it is impossible to obtain linear plots of ln ($P(v)$) vs f_v for any single assumed elementary reaction from Table I. Thus, it appears that each distribution, thermal and rotationally excited, is a composite of

---

(34) Winkler, I. C.; Stachnik, R. A.; Steinfeld, J. I.; Miller, S. M. *J. Chem. Phys.* **1986**, *85*, 890.

(35) Piper, L. G.; Cowles, L. M.; Rawlins, W. T. *J. Chem. Phys.* **1986**, *85*, 3369.

(36) Piper, L. G.; Clyne, M. A. A.; Monkhouse, P. B. *J. Chem. Soc., Faraday Trans. 2* **1982**, *78*, 1373.

(37) Rawlins, W. T.; Piper, L. G. *Proc. Soc. Photo-Opt. Instrum. Eng.* **1981**, *279*, 58.

(38) Haugen, H. K.; Pence, W. H.; Leone, S. R. *J. Chem. Phys.* **1984**, *80*, 1839. Yang, X. F.; Pimentel, G. C. *J. Chem. Phys.* **1984**, *81*, 1346.

(39) Green, B. D.; Caledonia, G. E.; Murphy, R. E.; Robert, F. X. *J. Chem. Phys.* **1982**, *76*, 2441.

(40) Caledonia, G. E.; Green, B. D.; Murphy, R. E. *J. Chem. Phys.* **1979**, *71*, 4369.

(41) Bernstein, R. B.; Levine, R. D. In *Advances in Atomic and Molecular Physics II*; Bates, D. R., Bederson, B., Eds.; Academic: New York, 1975; pp 216–297. Bernstein, R. B. *Chemical Dynamics via Molecular Beam and Laser Techniques*; Oxford University Press: New York, 1982.

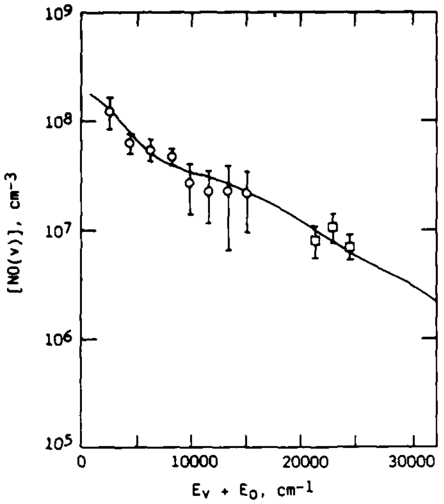

Figure 7. Comparison of rotationally "hot" populations for v = 1–8 and rotationally "thermal" populations for v = 12–14 to composite prior distribution for the N(^{2}P) + O$_2$ reaction (curve).

distributions for more than one reaction channel. Previous work, employing differential quenching of N(^{2}D) and N(^{2}P) by N$_2$ in electron-irradiated N$_2$/O$_2$ mixtures, provides strong evidence that the inverted, rotationally thermal distribution of Figure 5a is due to the N(^{2}D) reaction channels.[31] We therefore believe that the rotationally excited distribution of Figure 5b results from reactions of N(^{2}P) with O$_2$. The rotational excitation required for band head formation, $J \sim$ 80–120, is about 2–3 eV. This plus the number of vibrational levels observed (at least eight) gives a reaction exoergicity of 4–5 eV that is only satisfied by reaction 3a. A combination of reactions 3b and 3c, with roughly equal contributions from each in approximately statistical distributions, can also account for the relatively large populations observed in the v' = 1, 2 states. Furthermore, a statistical combination of all three reaction paths (3a, 3b, and 3c) in equal contributions gives an excellent fit to the data, as shown in Figure 7. It is also interesting to note from Figure 7 that the observed populations of v' = 12–14 from the rotationally "thermal" distribution also fall on the statistical curve for reaction 3. This does not signify a discrepancy in rotational excitation effects, because the spectral contributions from these states are so weak that it is not possible to identify their rotational distributions with any accuracy, and we cannot determine whether their production is associated with the rotationally thermal reaction channel (i.e., N(^{2}D)) or with the rotationally "hot" reaction (N(^{2}P)). As will be shown below, the data for v' = 13–14 seem less consistent with the trends identified for production by N(^{2}D), so it is possible that the observed populations for these states arise primarily from reaction 3. The intermediate states v = 9–11 should also be produced in this reaction, but at levels which are obscured by production of NO(v) from reaction 2. Similarly, population of levels $v > 14$ by reaction 3a may occur but cannot be observed in these experiments because of signal-to-noise limitations. It should be noted that, while the contributions of reactions 3b and 3c are implied by the fit in Figure 7, they can by no means be demonstrated conclusively from these data, as we do not have any positive identification of the energetic O* products of these reactions. Nevertheless, the inclusion of these reactions is consistent with the data and with the picture of a completely statistical product distribution for the N(^{2}P) reaction, as will be discussed below. Alternatively, the entire rotationally hot distribution may be due to reaction 3a alone, with nonlinear surprisal behavior.

We examine the "thermal" component of the observed NO(v) distribution by first noting that correction must be made for partially thermalized contributions from the reaction branch which produces rotationally "hot" NO(v). These contributions are especially evident for levels v = 1–3, where the rotationally thermal populations closely parallel those for the rotationally excited products. To illustrate this effect, we show in Figure 8 the surprisal plots for reactions 2a and 2b where no correction is made for thermalized high-J contributions. This plot shows two interesting effects: (1) the populations for v' = 1, 2 deviate significantly from the trend for v' = 3–7, and (2) reaction 2a appears to make no contribution for $v' < 8$, as evidenced by the break in slope at v' = 7. This general behavior was noted in the surprisal treatment of similar NO(v) distributions in the previous work of Kennealy et al.[12]

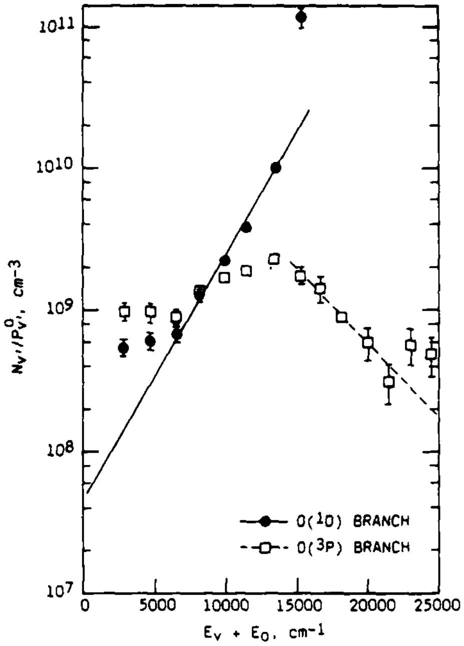

Figure 8. Surprisal plots for NO(v) formed from two branches of the N(^{2}D) + O$_2$ reaction, using the population data from Figure 5a. The lines correspond to surprisal parameters λ of −6.1 and 7.4 for the O(^{1}D) and O(^{3}P) branches, respectively.

Since each initial NO(v,J) molecule is subjected to 20–30 collisions (mostly with Ar and O$_2$) during its residence time in the field of view, it is reasonable to expect substantial rotational thermalization, with deactivation of low to middle rotational levels occurring at nearly every collision and deactivation of the high rotational levels proceeding more slowly. Our data for v' = 1–3 indicate that, at most, half of the rotationally excited NO(v,J) initially formed is thermalized within 30 collisions. This corresponds to an effective rate coefficient on the order of $\sim 10^{-11}$ cm^3 s^{-1}, in agreement with a similar value obtained by Taherian et al.[42] for thermalization of highly rotationally excited NO(v,J) formed from NO$_2$ photofragmentation in He. To correct the "cold" distributions for this contribution from the "hot" reaction channel, we assume as an upper bound that essentially all the v' = 1 population is due to thermalized NO(v,J), scale the "hot" populations accordingly to approximate the contributions from the "hot" channel, and subtract. The maximum correction thus obtained is large for low v' but is minor near the peak of the distribution.

The remaining population distribution, plotted in Figure 9, shows an inversion peaking at v' = 7. Noting that v' = 8 is the thermodynamic limit for reaction 2b, we show in Figure 10 the combined surprisal plots for reaction 2b (v' = 2–7) and reaction 2a (v' = 8–11). The composite population distribution determined from the surprisal fits of Figure 10 is given by the dashed curve in Figure 9. Excellent linearity in the surprisal analysis is now evident, as is the implication that reaction 2b accounts for all the

---

[42] Taherian, M. R.; Cosby, P. C.; Slanger, T. G. *J. Phys. Chem.* **1987**, *91*, 2304.

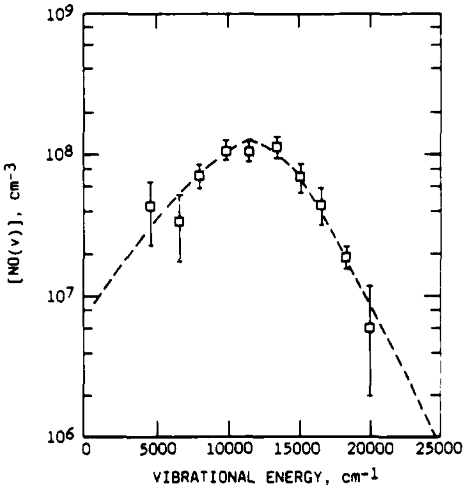

Figure 9. Rotationally thermal populations, corrected for maximum thermalized high-J component. The dashed curve represents populations determined from the surprisal analysis of Figure 10.

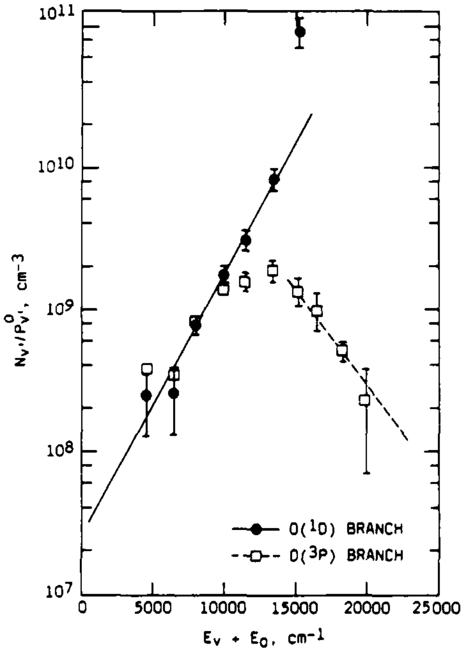

Figure 10. Surprisal plots and weighted least-squares fits for NO(v) formed from two branches of the N(^{2}D) + O_2 reaction: data corrected for maximum thermalized high-J component. Error bars have been omitted from some of the data points for clarity. The least-squares lines correspond to surprisal parameters λ of -6.25 and 9.16 for the O(^{1}D) and O(^{3}P) branches, respectively.

NO(v) production for $v' \leq 7$. In contrast to reaction 3, the reaction of N(^{2}D) with O_2 appears to be strongly channeled into a specific product configuration; this will be discussed further below. The corrected product-state distribution for reaction 2, inferred from Figure 10 and plotted in Figure 9, represents a lower bound for $v' \leq 8$; the upper bound is that of Figure 5a (no "hot" channel correction). The fact that the lower bound gives linear surprisal for $v' = 1$–7 and is consistent with a reasonable "hot" channel correction gives strong support for the choice of this distribution (Figure 9) as the actual nascent vibrational-state distribution for reaction 2.

The observed ratio of rotationally thermal to rotationally excited NO(v>0) is approximately 3. If we correct for rotational thermalization effects and use surprisal extrapolations to higher vibrational levels (see below), the apparent ratio of N(^{2}D) to N(^{2}P) contributions could be as small as ~0.5. However, as noted above, our determination of the number densities of the high-J states may be uncertain owing to effects of curvature in the dipole moment function on the scaling of the rotational line strengths to high J. Thus, the ratio of production rates for reactions 2 and 3 cannot be precisely determined from the present data but may be of order unity or less for temperatures 80–100 K. This is in significant contrast to our expectations based upon room-temperature kinetic data. As shown in Table IV, for room-temperature discharges similar to those used in COCHISE, we typically observe number density ratios of [N(^{2}D)]/[N(^{2}P)] ~ 3 at the discharge exit using atomic resonance absorption and fluorescence techniques.[33] Taken together with the rate coefficient ratio of $k_2/k_3 \sim 2$ at room temperature,[8,33,43] this would indicate a ratio of NO(v) production rates of about 6. There are several possible implications from this discrepancy: (1) our underestimate of the high-J line strengths may be far more severe than expected; (2) there may be a significant unreactive component (i.e., direct energy transfer to O_2 without NO formation) for reaction 2 at low temperature;[44] and (3) the rate coefficients for reactions 2 and 3 may follow opposite temperature dependencies; i.e., k_3 may follow a negative temperature dependence, such that k_2/k_3 becomes considerably smaller at low temperatures. All of these possibilities have significant implications for auroral chemistry, and we are continuing to pursue them in the laboratory.

The final vibrational distribution shown in Figure 9 for reaction 2 is in significant disaccord with the results of Green et al.[31] inferred from electron beam experiments at higher pressures. Specifically, the corrected relative populations from Figure 9 for $v' = 1$–3 are much lower than the initial relative populations for these levels inferred from a time-resolved kinetic analysis of NO(v) distributions created and partially relaxed in a pulsed electron beam experiment irradiating N_2/O_2 mixtures. Green et al.[31] convincingly eliminated N(^{2}P) as a precursor in their experiment by noting that the NO(v) precursor was quenched by N_2 (with a rate coefficient appropriate for N(^{2}D)), whereas N(^{2}P) is not.[6] Under electron beam conditions, much of the N* production is due to dissociative recombination of N_2^+ and NO^+, which would tend to favor N(^{2}D) formation, so that the relatively small N(^{2}P) contribution would be difficult to identify. This is in contrast to microwave discharge conditions, where there is much less ionization and N(^{2}D,^{2}P) are excited by direct electron impact. Thus, Green et al.'s large populations at low v' are probably not due to reaction 3, unless there is some unforeseen excitation or deexcitation mechanism which would cause N(^{2}P) to follow an unexpected kinetic behavior under their experimental conditions. However, their kinetic analysis relied heavily on the assumption of single-quantum collisional deactivation of NO(v). While this appears to be a reasonable approximation for describing the loss rate of a given vibrational level,[39] it may lead to a significant underestimate of the production rate for the lowest levels by multiquantum deactivation of higher levels by atomic oxygen. In classical trajectory studies of O + O_2(v) collisions, we have observed a similar effect, with efficient multiquantum ($\Delta v = 2$–4) deactivation of O_2(v) resulting in rapid population of lower vibrational levels from initially excited higher states.[45] Thus, the discrepancy between the present results for reaction 2 and those of Green et al.[31] for the lower vibrational levels of NO(v) may be due to the effects of multiquantum O + NO(v) deactivation in their experiments. In addition, the rapid quenching of N(^{2}P) by O[46] may compete very effectively with reaction 3 for their

---

[43] Phillips, C. M.; Steinfeld, J. I.; Miller, S. M. *J. Phys. Chem.* 1987, *91*, 5001.

[44] Note that Lin and Kaufman (ref 2) reported unit probability for reactive quenching at room temperature, based on observations of atomic oxygen formation. However, our own measurements using discharge-flow/resonance fluorescence (Piper, L. G.; Rawlins, W. T., unpublished work) indicate that copious atomic oxygen is formed in other processes in the afterglow, so this result may be questionable. See also: Fraser, M. E., Piper, L. G. *J. Phys. Chem.*, in this issue.

[45] Gelb, A.; Rawlins, W. T. *Physical Sciences Inc.* TR-582 under Air Force Contract No. F19628-85-C-0032, Dec 1986.

TABLE V: Surprisal Predictions of Relative Initial Populations of NO(v) in the Reactions of N(^{2}D,^{2}P) with O$_2$

	$N_v/\Sigma N_v$	
v	N(^{2}D) + O$_2$^{a}	N(^{2}P) + O$_2$^{b}
0	1.36×10^{-2}	2.67×10^{-1}
1	2.49×10^{-2}	1.85×10^{-1}
2	4.37×10^{-2}	1.18×10^{-1}
3	7.22×10^{-2}	7.10×10^{-2}
4	1.12×10^{-1}	5.72×10^{-2}
5	1.58×10^{-1}	5.03×10^{-2}
6	1.87×10^{-1}	4.37×10^{-2}
7	1.53×10^{-1}	3.77×10^{-2}
8	1.24×10^{-1}	3.21×10^{-2}
9	5.51×10^{-2}	2.69×10^{-2}
10	2.84×10^{-2}	2.23×10^{-2}
11	1.44×10^{-2}	1.81×10^{-2}
12	7.17×10^{-3}	1.44×10^{-2}
13	3.47×10^{-3}	1.13×10^{-2}
14	1.62×10^{-3}	8.82×10^{-3}
15	7.11×10^{-4}	7.50×10^{-3}
16	2.83×10^{-4}	6.43×10^{-3}
17	9.01×10^{-5}	5.43×10^{-3}
18	1.51×10^{-5}	4.50×10^{-3}
19		3.67×10^{-3}
20		2.88×10^{-3}
21		2.23×10^{-3}
22		1.67×10^{-3}
23		1.13×10^{-3}
24		9.00×10^{-4}
25		3.20×10^{-4}
26		6.00×10^{-5}

^{a} $k_{2a}/k_{2b} = 0.285$. ^{b} $k_{3a}/k_{3b} = k_{3c}/k_{3b} = 1$.

electron bombardment conditions. Alternatively, our upper bound correction for rotational thermalization may be too large (i.e., rotational thermalization is slower than one might expect from the data of ref 42), and the product distribution of reaction 2b simply does not follow linear surprisal behavior.

In an attempt to discriminate between N(^{2}D) and N(^{2}P) effects on the observed NO(v) distributions, we obtained data from five spectral scans over a range of a factor of ~15 in initial N$_2$ mole fraction in the discharge gas mixture, as described above. For this range of conditions, the relative production rates for N(^{2}D) and N(^{2}P) in the discharges remain constant to within 10%, but the N$_2$ quenching contribution to the loss rate of N(^{2}D) in the side arm will provide some variation in the N(^{2}D)/N(^{2}P) ratio entering the reaction zone. Unfortunately, due to the short residence time in the discharge sidearms, this amount of variation in [N$_2$] will provide only about a 30% variation in this ratio, with the ratio decreasing with increasing N$_2$ flow rate. In the experiments, we observe the ratio of rotationally thermal to rotationally "hot" [NO(v)] (summed over all observed v levels) to decrease systematically by a factor of 1.3 with increasing N$_2$ flow rate, as expected for the production of thermal NO(v) by reaction 2 and of rotationally "hot" NO(v) by reaction 3. This result is then consistent with the conclusions from the analysis of the population distributions. However, there is sufficient scatter in the data that an average ratio for all the scans gives a $\pm 2\sigma$ uncertainty of 26%, so the observed trend lies only slightly outside the scatter of the data.

Discussion

The surprisal parameters determined from the above data analysis provide a basis for extrapolation of the results to other vibrational levels for which direct observations cannot be obtained. For the N(^{2}D) reaction, we find that the branch for O(^{1}D) production (reaction 2b) can account for all the production of NO(v' = 1–7), with a surprisal parameter $\lambda = -6.25 \pm 0.14$ (99% confidence level), while the remaining production of NO($v \geq 8$) is due to the O(^{3}P) branch (reaction 2a), with $\lambda = 9.16 \pm 1.19$. The relative initial populations of NO(v) determined from these surprisal fits are shown in Table V. Summing the initial populations for each branch over all v gives the branching ratio $k_{2b}/k_2 = 0.76$ at ~100 K. Similarly, for the N(^{2}P) reaction we infer (at most) equal branching ratios for formation of O(^{1}S), O(^{1}D), and O(^{3}P), with essentially statistical product-state distributions (see Table V).

The aeronomic implications of the present conclusions for the auroral upper atmosphere are quite significant. The production of O(^{1}D,^{1}S) from these reactions has an impact on interpretations and modeling of ultraviolet and visible airglow and auroral emissions from these states and from other species, such as N$_2$($A^3\Sigma_u^+$) and metastable states of O$_2$, which are believed to be linked to their production.[47] Our interpretation that v = 1–2 are inefficiently populated in reaction 2 is a significant revision of previous conclusions[12,31] and will have an important bearing on the interpretation of observed auroral NO(v) distributions, which often show hitherto unexplained "inversions" in the population of v = 2 (v = 1 is known to be strongly populated by nonchemiluminescent processes).[11,13] These results also impact the current views on the roles of O-atom deactivation of higher vibrational levels and of reaction 3 as sources of the observed populations in lower vibrational levels under certain conditions, suggesting that these processes are more important than previously thought. Furthermore, the high degree of rotational excitation provided by the N(^{2}P) reaction will have a dramatic effect on the high-altitude infrared spectrum of auroral NO(v) emission, as evidenced by the R-branch band heads for v = 1–3 observed in a recent rocket-borne interferometer flight.[22] The presence of these R-branch band heads to the blue of the main band means that the corresponding P-branch distributions must appear to the red. Our calculations indicate that the unrelaxed P-branch contributions from the observed eight rotationally excited vibrational states can provide more intensity in the 6–8-μm range than the emission from high vibrational levels (for any rotational distribution) produced from reactions 2a or 3a. Our observations further indicate that the very high J levels responsible for these contributions are deactivated relatively slowly in Ar/O$_2$/N$_2$ mixtures. The extent of collisional coupling in the COCHISE experiments is similar to that expected for NO(v) at altitudes of 110–120 km (assuming the primary loss for NO(v) is by radiative cascade). Thus sensitive, high-resolution measurements of the NO(v,J) spectrum above ~100 km in a strong aurora could ultimately provide a means of estimating the N(^{2}D)/N(^{2}P) ratio and hence the energetics of the auroral event.

Our approach to describing the rotationally "hot" distributions deserves some comment. Due to limitations of spectral resolution and sensitivity, we are unable to directly observe any part of the rotational distributions other than the distinctive R-branch band heads. Thus, there is no clear indication that the low to intermediate J levels are populated, either in the initial reaction or on the time scale of the measurements. It is conceivable that the initial rotational populations are statistical or that the initial population of high J is rapidly randomized by collisions to give an apparently statistical distribution. Such a distribution would have the behavior

$$P_v^{\circ}(J) \propto (2J + 1)\{(E - E_v) - E_r\}^{1/2}$$

where E_r, E_v, and E are the rotational, vibrational, and total reaction energies, respectively. Thus, the rotational "temperature" would depend on the vibrational energy of the emitting state, with higher vibrational levels exhibiting "colder" rotational distributions. We cannot clearly discern this effect in the NO(v,J) spectra, except for the disappearance of obvious band heads above v' = 8. However, in similar studies of CO(v,J) excitation by energy transfer from active nitrogen,[20] we are able to fit the observed rotational distributions better with the statistical formula than with a Boltzmann (v-independent) description. Planned improvements in the measurement sensitivity for NO(v,J) may permit

---

(46) Young, R. A.; Dunn, O. J. *J. Chem. Phys.* **1975**, *63*, 1150.

(47) Vallance Jones, A.; Meier, R. R.; Shefov, N. N. *J. Atmos. Terr. Phys.* **1985**, *47*, 623, and references therein.

us to address this issue more accurately in the future.

The observed product-state distributions imply strongly contrasting behavior in the reaction dynamics of the N(^{2}D) and N(^{2}P) reactions with O_2. For reaction 2b, the high degree of selectivity for the highest accessible vibrational levels is characteristic of a direct, abstraction reaction with a repulsive approach configuration and a very short lived collision complex. It would appear that successful reactive encounters require maximum vibrational motion along the product N–O coordinate, perhaps as a result of a barrier in the N–O_2 entrance channel. The behavior for reaction 2a is somewhat surprising, since the reaction appears to occur only when reaction 2b is thermochemically forbidden. This behavior suggests that all reactive N–O_2 encounters proceed initially along the $^2A'$ surface leading to O(^{1}D) formation, but some, with too much N–O_2 motion in the product channel (insufficient motion along the NO–O coordinate) to form O(^{1}D), undergo enough motion in the collision complex to dissociate to highly vibrationally excited NO + O(^{3}P) via transition to one of the other $^2A'$ or $^2A''$ surfaces that are available (cf. Table I). Thus, there may be no direct path, or perhaps a large energy barrier, to O(^{3}P) formation in reaction 2. If the occurrence of this reaction branch indeed depends upon the lifetime of the collision complex, then its contribution may diminish substantially at elevated collision energies (or higher temperatures). The direct reaction, reaction 2b, ought to follow at least a $T^{1/2}$ temperature dependence, or possibly one somewhat stronger due to the presence of an energy barrier in the entrance channel. For comparison, Slanger et al.[48] observed essentially no activation energy for quenching of N(^{2}D) by O_2 between 240 and 370 K; however, the temperature dependence for NO formation has never been determined. Clearly, the effects of temperature dependence on this reaction need to be studied in more detail, as the present data base lends somewhat ambiguous support to the possibility of an unreactive energy-transfer channel at lower temperatures. This possibility has been suggested in interpretations of aeronomic data on emission from excited states of O_2,[49] albeit on controversial grounds.[50]

In contrast to N(^{2}D), N(^{2}P) appears to react with O_2 through a long-lived collision complex, resulting in complete randomization of the reaction energy. The appearance of high rotational excitation is characteristic of a highly attractive approach configuration. The collisions must satisfy the principles of conservation of angular momentum and energy

$$(2\mu E_i)^{1/2} b_i = (2\mu E_f)^{1/2} b_f + Jh/2\pi$$

$$E_i + \Delta E = E_f + E_v + BJ^2$$

where μ is the reduced mass of N–O_2, E_i and E_f are the initial and final center-of-mass collision energies, b_i and b_f are the initial and final impact parameters, ΔE is the exoergicity of the reaction, E_v is the product vibrational energy, and BJ^2 approximates the product rotational energy after the collision. It is straightforward to show[51] that large values of J can be achieved through highly attractive collisions in which large initial impact parameters are converted to small final impact parameters, with the concurrent result that the final center-of-mass kinetic energy is small. By analogy to the well-studied reaction dynamics for O(^{1}D) with H_2[52] and HCl,[53] this type of collision can occur through a C_{2v} insertion approach, leading to a highly attractive ONO collision complex. Such a complex would probably undergo enough vibrational periods to completely randomize the internal energy, giving rise to statistical product-state distributions. With so much Lissajous motion in the complex, the adiabatic correlation rules given by Shuler[15] would have little relevance,[14,15] so there is no basis for the previously suggested[6,14] prohibition of reaction 3a. The reaction rate coefficient may increase substantially with decreasing temperature, owing to both the dynamics of the initial insertion approach (favored for less O_2 rotational motion) and the increased lifetime of the collision complex at lower temperatures. This trend, together with those suggested above for reaction 2, is consistent with our observation of an unexpectedly large k_3/k_2 ratio at ~100 K.

It is interesting to compare our results for reaction 3 with those of Taherian et al.[42] for NO(v,J) observed in the photolysis of NO_2. Their experiments, conducted at 157.6 nm, are nearly isoenergetic with the N(^{2}P) + O_2 reaction and may probe portions of the same ONO surface. They observed excitation of high rotational states comparable to those reported here, together with a partial vibrational distribution which is not inconsistent with our statistical picture. Most interestingly, they have identified the excitation of $v = 21$, confirming that O(^{3}P) is a primary product of the photodissociation process. However, the authors report upper bounds for O(^{1}D,^{1}S) formation which indicate these to be minor product channels at best. Such a result for reaction 3 would not give a good surprisal fit to our data but certainly cannot be ruled out on that basis alone. Alternatively, this disparity between our results and theirs may arise from the much larger phase space sampled in reactive collisions. It is clear that more definitive product-state identifications are required to confirm our preliminary assignment of the product branching ratios of reaction 3.

Conclusions

We have used the technique of low-pressure infrared chemiluminescence to investigate the vibrational and rotational excitation of NO($X^2\Pi$) formed in the reactions of N(^{2}D,^{2}P) with O_2 near 100 K. The initial vibrational distributions obtained from the experiments are composites from several reaction channels. The results of surprisal analysis indicate that N(^{2}D) reacts with O_2 via a direct abstraction mechanism, probably on a repulsive potential surface, to give a product vibrational distribution which is sharply peaked to high vibrational levels. This interpretation also implies that reaction to form O(^{1}D) comprises 76% of the total NO(v) production at these temperatures. In contrast, the results indicate that N(^{2}P) reacts with O_2 through a long-lived complex, perhaps via an insertion mechanism on an attractive potential surface, to give essentially statistical product-state distributions with extensive rotational excitation of the molecular products. The observed NO(v) distributions are consistent with approximately equal contributions from the reaction channels forming O(^{1}S), O(^{1}D), and O(^{3}P) as products.

The results of this work amplify and extend the information obtained from previous studies of these reactions and provide additional insights into the kinetics and spectroscopy of vibrationally excited NO in the auroral upper atmosphere. However, the results of the present investigations raise a number of issues requiring further study, including the temperature dependencies of the various reaction pathways, the possibility for quenching collisions which do not produce NO($X^2\Pi$), confirmation of O(^{1}D,^{1}S) production, and quantitative determination of the rotational line intensities at high J. We are continuing to address these issues through experiments on the COCHISE facility as well as with discharge-flow reactors using resonance fluorescence and laser-based diagnostics. In addition, these reaction systems lend themselves well to theoretical investigations of quantum mechanical potential energy surfaces and semiclassical collision dynamics.

Acknowledgment. The authors benefited from numerous discussions and suggestions by many scientific colleagues, especially B. D. Green (PSI), G. E. Caledonia (PSI), K. W. Holtzclaw (PSI), and W. A. M. Blumberg (AFGL). The contributions of L. G. Piper (PSI) were essential for interpreting the formation and kinetics of discharge-excited species. The identity of the

---

(48) Slanger, T. G.; Wood, B. J.; Black, G. *J. Geophys. Res.* **1971**, *76*, 8430.

(49) Torr, M. R.; Welsh, B. Y.; Torr, D. G. *J. Geophys. Res.* **1986**, *91*, 4561.

(50) Slanger, T. G.; Llewellyn, E. J., McDade, I. C.; Witt, G. *J. Geophys. Res.* **1987**, *92*, 7753. Torr, M. R.; Owens, J. K.; Torr, D. G. *J. Geophys. Res.* **1987**, *92*, 7756.

(51) Poppe, D. *Chem. Phys.* **1987**, *111*, 17, 21.

(52) For example: Whitlock, P. A.; Muckerman, J. T.; Fisher, E. R. *J. Chem. Phys.* **1982**, *76*, 4468. Aker, P. M.; Sloan, J. J. *J. Chem. Phys.* **1986**, *85*, 1412, and references therein.

(53) Luntz, A. C. *J. Chem. Phys.* **1980**, *73*, 5393. Schinke, R. *J. Chem. Phys.* **1984**, *80*, 5510, and references therein.

R-branch heads was first suggested to W.T.R. by Michael Mumma (NASA/Goddard) in the context of the rocket-borne observations. We are also grateful for the assistance of Henry Murphy (PSI) with the experimental work and of Lauren Cowles, Margrethe DeFaccio, and Melanie Clawson (all of PSI) in the analysis of the data. This work was performed under Contract F19628-85-C-0032 with the Air Force Geophysics Laboratory and was sponsored by the U.S. Air Force Office of Scientific Research under Task 2310G4 and by the Defense Nuclear Agency under Project SA, Task SA, Work Unit 115.

Registry No. O_3, 7782-44-7; N, 17778-88-0; NO, 10102-43-9.

3. COCHISE IR Emission from $N_2/O_2/Ar$ Discharges

by

W.T. Rawlins, M.E. Fraser, and S.M. Miller

Preliminary scoping experiments performed on COCHISE examined IR emission (2 to 8 μm) observed in the reaction chamber following discharge excitation of $N_2/O_2/Ar$ mixtures. The measurements were made for a constant Ar flow of ~3.7 std l/min, both in excess N_2 and in fixed O_2. In excess N_2, the N_2 flow rate was set to ~0.2 std l/min and the O_2 flow rate was varied from 10 to 200 std cm^3/min. In fixed O_2, the O_2 flow rate was set to ~0.1 std l/min and the N_2 flow rate was varied from 10 to 400 std cm^3/min. Discharge tube pressures ranged from 1.0 to 1.7 torr. The temperature of the side arms was maintained at ~80 K for almost all the measurements. No counterflow was employed. The purpose of these measurements was to: (1) identify the various bands comprising the spectral signature of discharged N_2/O_2 mixtures; (2) examine the variation of intensities and spectral distributions as functions of separately varied N_2 and O_2 flow rates to check for quenching or metastable effects; and (3) define an optimum range of experimental conditions for carrying out more detailed investigations. Particular emphasis was placed on characterizing the $N_2O(v_3)$ band near 4.5 μm. We present here a summary of the data in its raw, uncalibrated form as obtained in COCHISE.

SWIR spectral signatures were observed between 2 and 4 μm. Typical spectra showed sharp bands and/or lines atop a weaker, broad continuum peaked near 3 μm. Some of this continuum may result from NO(Δv = 2) radiation, but the continuum persists outside the NO bandpass. The NO-O air afterglow is a possible source of continuum emission in this spectral region. The molecular bands arise predominantly at the shorter wavelengths, that is, nearer 2 µm, with the Wu-Benesch ($\Delta v = 2$) features, normally so prominent between 3 and 4 µm for N_2/Ar discharges, strongly suppressed by the presence of O_2. The features between 2 and 3 µm until the relative contributions of the 3 to 4 µm bands await identification and comparison to our earlier data for N_2/Ar, but may arise in part from the First Positive system of N_2. As the O_2 level is increased to excess O_2 conditions, more of the intensity shifts into the 2 to 3 µm bands until the relative contributions of the 3 to 4 µm bands and the continuum are barely discernable. Thus, in general, the SWIR spectral distribution is markedly different than in N_2/Ar, favoring shorter-wavelength features near 2 to 2.5 µm. These features show a pronounced increase in intensity with increasing O_2. By comparison, previous experiments with Ar/O_2 showed only Ar lines in this spectral region, with intensities decreasing with increasing O_2. Since the Ar lines are even more strongly "quenched" in N_2, it is not likely that there are any prominent Ar lines in the N_2/O_2/Ar spectra. We plan to analyze these data together with the N_2/Ar data to identify these transitions.

MWIR spectra were taken between 4 and 8 µm for excess N_2 and excess O_2 conditions. A representative excess-N_2 spectrum (low resolution, 0.04 µm) is shown in Figure 1 for the lowest O_2 flow rate (10 std cm^3/min). The prominent negative-going feature near 4.5 µm appears to be N_2O emission which is 180° out of phase with the rest of the radiating species; we will examine this point further below. The NO fundamental band arises near 5.3 µm and extends to longer wavelengths. Indeed, the "tail" of this band appears to persist all the way to nearly 8 µm in this particular spectrum. NO(v) is undoubtedly formed in the discharge by reaction of N(^{2}D) with O_2 and is relaxed to a steady-state distribution by a variety of collisional processes. The spectral distribution shown here is strongly peaked to low v, but exhibits bimodal behavior at middle v (~6 µm), and the extended "tail" is indicative of population of higher vibrational levels than are commonly observed in more conventional COCHISE experiments. Of course, contributions from underlying radiators cannot yet be ruled out, but other excitations sources for NO(v) are suggested by these data.

The band near 4 µm appears to be due in part to the (4-2) band of the Wu-Benesch W-B system of N_2; however, the origin of the emission between 4 and 4.5 µm is not yet known. Some of the emission near 4.7 to 5 µm could be due to the O_3 (v_1 v_3) combination band and its hot bands. The sharp bands near 5 µm are the same as those previously observed in the interaction of discharged N_2/Ar with O_2, but we do not yet know their identity conclusively.

In excess fixed N_2 (0.2 std l/min), as the O_2 flow rate increases from 10 to 200 std cm^3/min, the intensities of all the bands decrease except for that of the out-of-phase N_2O feature, which passes through a maximum near the 1 percent O_2 level. This latter behavior is similar to that of $O_3(v > 2)$ as observed in the O_2/Ar discharge experiments. If this trend is supported in future experiments, it could implicate $O_3(v > 2)$ as a precursor of the observed $N_2O(v)$. The decrease in intensity of the other features with increasing O_2 could be due to collisional deactivation by O_2, O, and/or O_3, as well as to colder electron energy distributions in the discharge.

For a fixed O_2 flow rate of ~0.1 std l/min, N_2 flow rates were varied from 10 to 400 std cm^3/min at nominal temperatures of 80 K. In the fixed-O_2 case, the intensities of all spectral features decrease uniformly with decreasing N_2 flow rate. The general spectral distribution is similar to that of the fixed-N_2 spectra, except for some slight variations observed at the lowest N_2 flow rate as shown in Figure 2. Here the N_2O feature is no longer observable, and the NO band exhibits a secondary

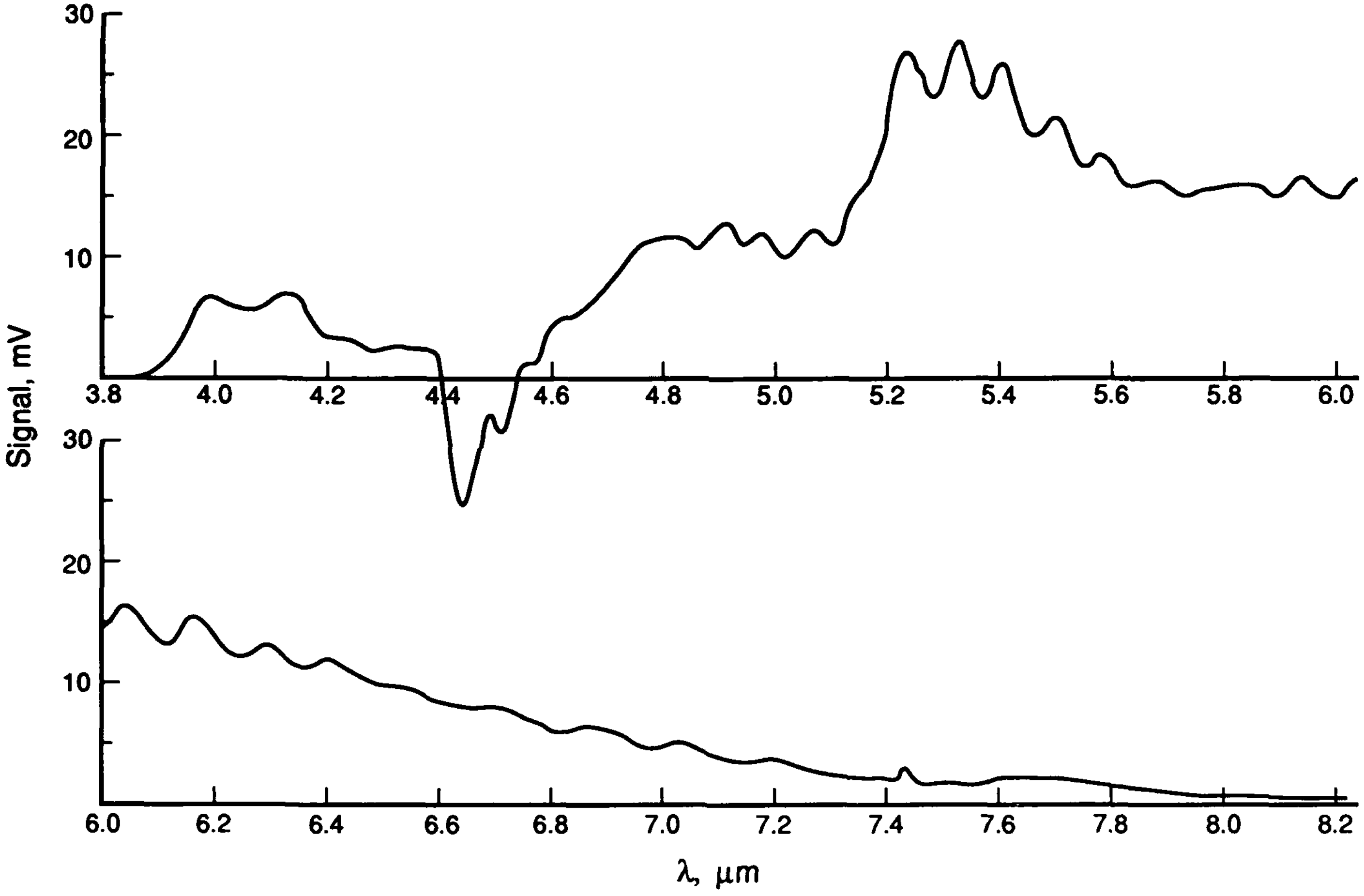

Figure 1. MWIR Signature for Discharged N_2/O_2 Ar Mixture, Excess N_2. Experimental conditions are: $N_2/O_2/Ar$ = 0.2/0.010/3.7 std *l* /min, T = 80 K, P = 1.3 torr, resolution = 0.04 μm (Expt. 312405)

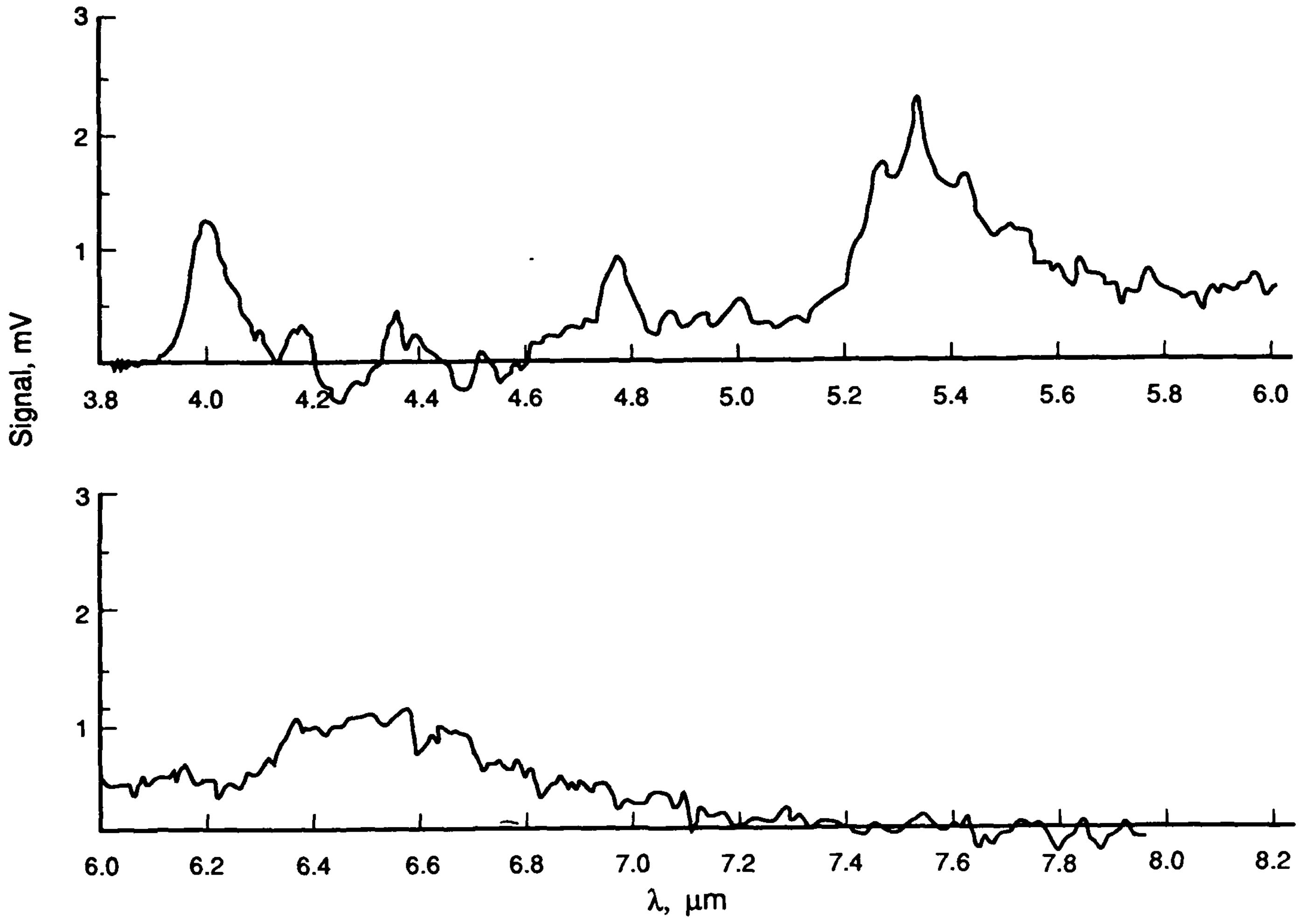

Figure 2. MWIR Signature for Discharged $N_2/O_2/Ar$ Mixture, Excess O_2. Experimental conditions are: $N_2/O_2/Ar = 0.010/0.1/3.7$ std l/min, T = 80 K, P = 1.5 torr, resolution = 0.04 μm (Expt. 312422)

maximum near 6.5 μm. It remains to be determined whether this feature arises from another NO(v) excitation reaction (perhaps $N(^2P) + O_2$?) or from vibrationally excited NO_2 formed in the discharge.

At the highest N_2 flow rates, the S/N was high enough to permit high resolution scans of the N_2O band. Such a scan is shown in Figure 3 for 0.5 mm slits (0.007 μm resolution). The system consists of four distinct bands, each of which appears to be a vibation-rotation band of the $N_2O(v_3)$ mode. Preliminary inspection of the raw data gives $\omega_3^0 = 2226 \pm 3$ cm^{-1}, $x_{33} = 15 \pm 1$ cm^{-1}, in excellent agreement with the values for N_2O used in the AFGL line parameters compilation (2223.76 cm^{-1}, 15.06 cm^{-1}). The narrowness of the bands suggests a very low rotational temperature; however, since the rotational constant for N_2O is only ~0.42 cm^{-1}, this conclusion cannot be stated with certainty until we perform a spectral fitting analysis.

When the sidearm temperature was elevated to 120 K, part of the N_2O emission became in phase with the NO emission. This is demonstrated in Figure 4 by comparison of spectra obtained for the same flow conditions at 80 K and 120 K. Emission from the lowest vibrational level is in phase with NO at 120 K, but emission from the highest levels is not, resulting in a peculiar composite positive- and negative-going spectrum for N_2O. If the excited N_2O were being formed by reactions occurring in the active discharge, we would expect to see the N_2O fluorescence roughly in phase with the NO and N_2 emissions. When the N_2O emission is out of phase, this means that most of the fluorescence seen by the detector occurs after the discharges are off, that is, in the absence of discharge-excited species. In other words, the out-of-phase N_2O emission arises from a slug of undissociated gas. It is difficult to account for this phenomenon. However, the 120 K results suggest that, in the lower temperature experiments, transport of N_2O out of the discharge tubes may be impeded by condensation of discharge-produced N_2O on the walls. (The vapor pressure of N_2O is 10^{-6} torr at 80 K and 0.1 torr at 118 K). Thus, in the 80 K experiments, discharge-produced N_2O would condense and accumulate in the sidearms, exerting its equilibrium vapor pressure. The small amount of N_2O vapor may be destroyed in the active discharge, such that gas phase N_2O only escapes into the viewing region during the period when the discharges are off. It is fascinating to consider that the N_2O appears to retain considerable vibrational excitation in this process. Clearly, these experiments should be repeated at elevated temperatures (120 to 150 K), and a systematic study of temperature dependence is required. In any case, it is clear that N_2O is indeed formed in discharge-excited mixtures of N_2, O_2, and Ar. Identification of the processes responsible for this will be pursued in further investigations.

In summary, we have performed a series of scoping experiments to examine the IR signatures of discharged $N_2/O_2/Ar$ mixtures under a variety of conditions. Band systems of N_2 and NO are observed, but with significantly different spectral distributions than observed in previous experiments employing N_2/Ar discharges and O_2 counterflows. In addition, emission from the v_3 and, in some cases, v_1 bands of N_2O are also observed; however, these data are clouded because the sidearm temperature was too low. It appears that systematic variation of N_2 and O_2 flow rates can be employed to probe the kinetics of the N_2O formation processes. Further experiments should be performed at temperatures above 120 K and with the highest possible resolution, over the same ranges of flow rates employed here. In the meantime, the present data base should be subjected to spectral fitting analysis for quantitative comparisons to previous N_2/Ar discharge work.

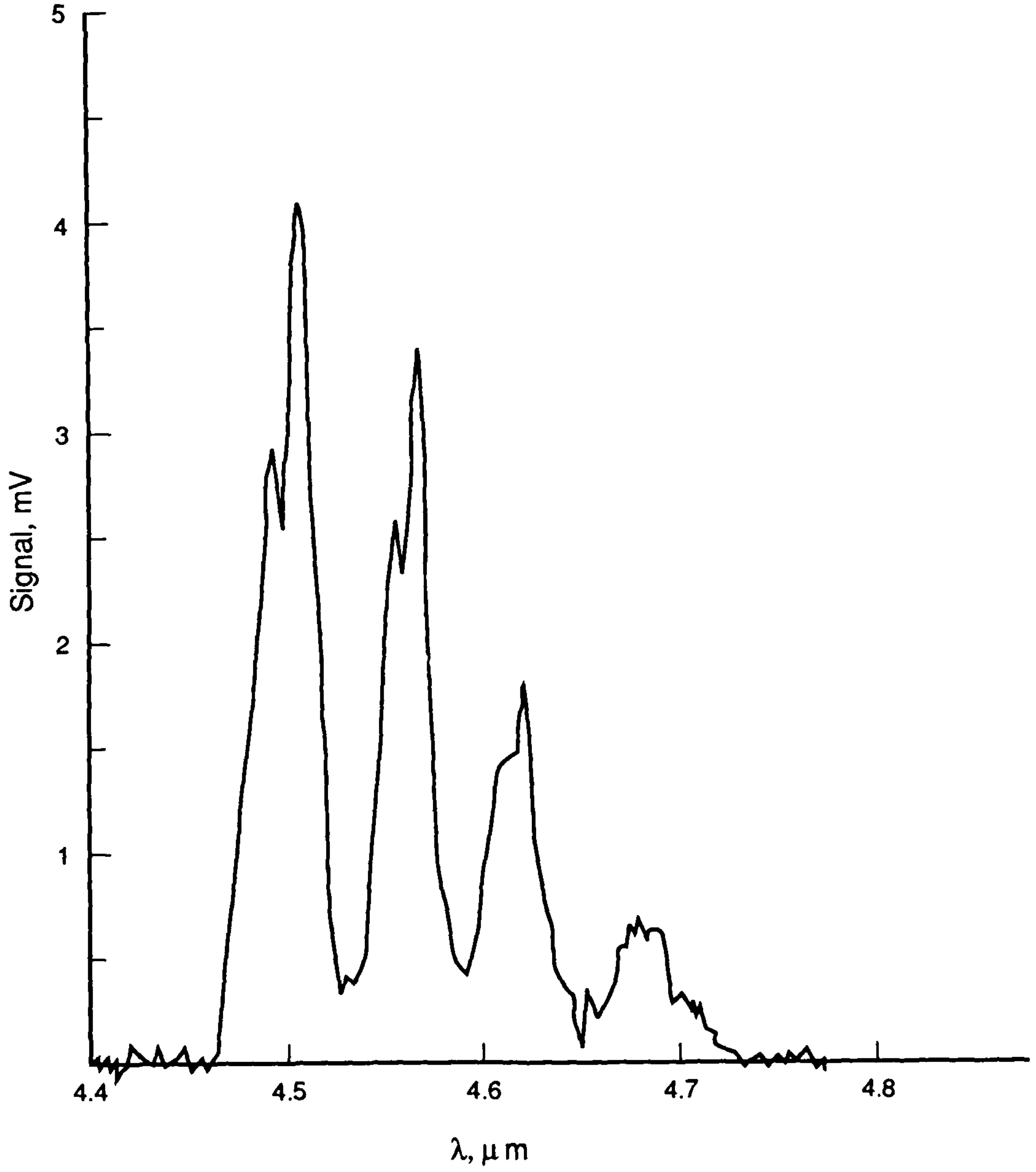

Figure 3. High Resolution Scan of Out-of-Phase Emission from $N_2O(v_3)$.
$N_2/O_2/Ar = 0.4/0.1/3.7$ std l/min, T = 30 K, P = 1.5 torr, resolution = 0.0067 μm or 3.3 cm^{-1}
(Expt. 312424)

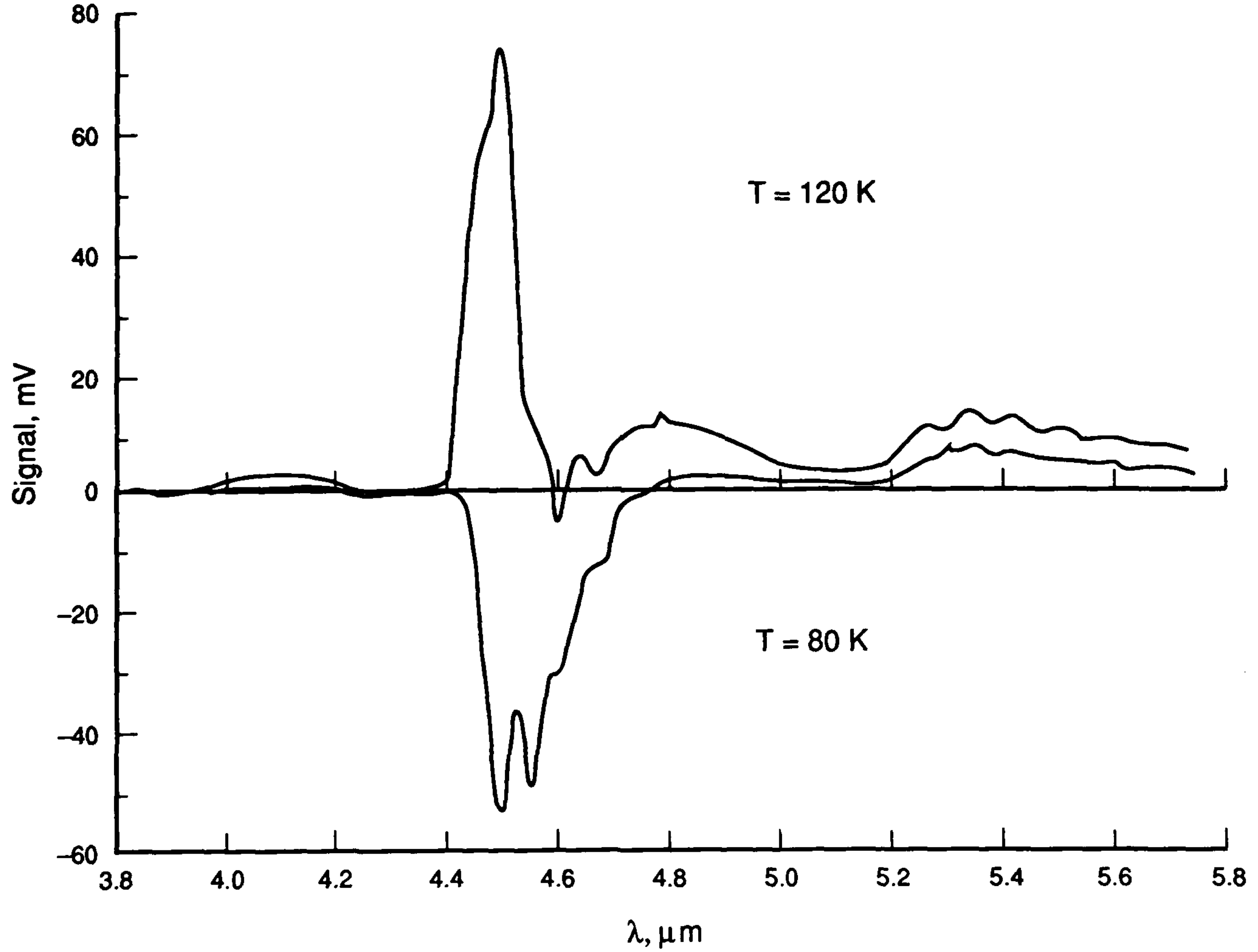

Figure 4. Reversal of $N_2O(v_3)$ Phasing with Temperature. $N_2/O_2/Ar = 0.4/0.1/3.7$ std *l* /min, P = 1.7 torr, resolution = 0.04 µm (Expts. 312426, 312423)

Contents

Abstract 25
1. Introduction 26
2. Experiments 28
3. Results 30
4. Spectral Analysis 32
5. Kinetic Interpretations 38
6. Excitation Mechanism 42
7. Discussion 47
8. Conclusions 53
Acknowledgements 54
References 55

4. Rovibrational Excitation of Carbon Monoxide by Energy Transfer from Metastable Nitrogen

by

M.E. Fraser, W.T. Rawlins, and S.M. Miller

Abstract

CO fundamental vibration-rotation band emission resulting from the interaction of discharged nitrogen with carbon monoxide has been supplied at low pressure (~3 mt) in a cryogenic apparatus. The spectra exhibit bimodal rotational distributions; we have identified fourteen vibrational levels of a thermalized component and eight vibrational levels from a rotationally excited component. The rotationally excited emission is adequately reproduced by a statistical distribution, E = 3.7 eV, which provides sufficient population in the region of the Fortrat reversal (J ~ 90) to account for the observed R-branch band head formation. The excitation reactions are:

$$N_2(v) + CO \rightarrow N_2(v-1) + O(v=1) \tag{a}$$

$$\rightarrow N_2(v-2) + CO(v=2) \tag{b}$$

$$N_2(a'^1\Sigma_u^-) + CO \rightarrow N_2(X,v) + CO(A\,^1\Pi) \rightarrow CO(v \leq 9) + h\nu \tag{c}$$

$$\rightarrow N_2(X,v) + CO(v \leq 14, J) \tag{d}$$

Single and two-quantum transfer from N2(v), reactions (a) and (b), contributes to the thermalized CO(v=1,2) populations. Radiative cascade from CO(A) produced by quenching of $N_2(a')$, reaction (c), also contributes to the thermalized populations. Based on kinetic and energetic arguments we have determined another branch of $N_2(a')$ quenching to be responsible for the rotationally excited components.

Surprisal analysis of the rotational excited component vibrational distribution indicates two dynamic mechanisms. We have modeled this distribution with equal contributions from a direct ($v \leq 4$) and a statistical (all v) process. The vibrational distributions of the rotationally thermal component are reproduced by $CO(A^1\Pi)$ radiative cascade and a contribution from reaction (d).

1. INTRODUCTION

The dynamics of energy disposal in quenching/reaction of excited state species may be determined from the nascent electronic-vibrational-rotational-translational distributions of the product molecules. The observed product state distributions reflect the details of the interaction mechanisms and provide insight into the nature of the potential energy surfaces. We have previously reported observations of infrared chemiluminescence from vibrationally and rotationally excited NO generated from the reaction of metastable atomic nitrogen with molecular oxygen.[1] Surprisal analysis of the data supports two mechanisms: a direct abstraction reaction $(N^2D) + O_2$ producing rotationally thermal but vibrationally excited NO and an insertion reaction $N(^2P) + O_2$ giving essentially statistical vibrational and rotational product state distributions.

This paper reports observations of highly rovibrationally excited CO formed by energy transfer between carbon monoxide and nitrogen metastables. The observed CO fundamental spectra contain rotationally thermalized emission for $v \leq 14$ and rotationally excited bands for $v \leq 8$. The rotationally excited component appears as R-branch band heads that require significant populations in high rotational levels near the vertex of the Fortrat parabola ($J_{vertex} \sim 90$). The energetics of both the thermal and rotationally excited components are attributable to an energy transfer process that deposits up to ~3.7 eV into CO rovibrational states.

Modest energy depositions (typically <1 eV) in CO internal states have been observed in photochemical and abstraction reactions. In general, large fractions of the energy above threshold are manifested in product internal states. For example, photolysis of OCS at 157 nm[2], of acetone[3] at

---

1. Rawlins, W.T., Fraser, S.M., and Miller, S.M. (1989) Rovibrational Excitation of Nitric Oxide in the Reaction of O_2 with Metastable Atomic Nitrogen, *J. Phys. Chem.* **93**:1097.
2. Houston, P.L. (1987) Vector Correlations in Photodissociation Dynamics, *J. Phys. Chem.* **91**:5388.
3. Woodbridge, E.L., Fletcher, T.R., and Leone, S.R. (1988) Photofragmentation of Acetone at 193 nm: Rotational- and Vibrational-State Distributions of the CO Fragment by Time-Resolved FTIR Emission Spectroscopy, *J. Phys. Chem.* **92**:5387.

193 nm, and H_2CO[4,5] produces vibrationally excited CO with rotational excitations up to 0.9 eV. Studies of energy partitioning in CO from the reaction of hot H atoms with CO_2 indicates nearly 1.0 eV in CO internal states[6] with the rotational distribution in the v=0 level following a statistical model.

Greater energy depositions are observed for energy transfer reactions since these interactions have little or no threshold energy. Quenching by $O(2^1D)$[7], $Na(3^2P)$[8,9], $I\ (5^2P_{1/2})$[10], and $Br(4^2P_{1/2})$[10], and $Hg(6^3P_1$ and $6^3P_0)$[11] have been observed to produce vibrationally excited CO. Rotational excitations of ≤0.8 eV have been reported for the Na(32p) + CO quenching reaction[9] which accounts for a large fraction of the total 2.1 eV exoergicity.

The excitation process observed here is energy transfer from a metastable state of nitrogen. Energy transfer to CO from discharged nitrogen has been examined closely, particularly with respect to the N2-CO laser.[12,13] High CO vibrational excitation is produced from near-resonant $N_2(v)$ energy transfer and subsequent CO(v) collisional up-pumping[14,15], reactions (1a and 1b).

$$N_2(v) + CO(v') \rightarrow N_2(v-1) + CO(v'+1) \qquad (1a)$$

$$CO(v) + CO(v') \rightarrow CO(v'-1) + CO(v'+1) \qquad (1b)$$

---

4. Bamford, D.J., Filseth, S.V., Foltz, M.F., Hepburn, J.W., and Moore, C.B. (1985) Photofragmentation Dynamics of Formaldehyde: CO(v,J) Distributions as a Function of Initial Rovibronic State and Isotopic Substitution, *J. Chem. Phys.* **82**:3032.
5. Debarre, D., Lefebvre, M., Péalat, M., and Taran, J.-P.E. (1985) "Photofragmentation Dynamics of Formaldehyde: $H_2(v,J)$ Distributions, *J. Chem. Phys.* **83**:4476.
6. Harding, D.R., Weston, R.E., and Flynn, G.W., *J. Phys. Chem.*, in press.
7. Shortridge, R.G. and Lin, M.C. (1976) The Dynamics of the $O(^1D_2) + CO(X^1\Sigma^+, v=0)$ Reaction, *J. Chem. Phys. Lett.* **42**:4076.
8. Hsu, D.S.Y. and Lin, M.C. (1976) Electronic-to-Vibrational Energy Transfer Reactions: $Na(3^2P) + CO(X^1\Sigma^+, v=0)$, *Chem. Phys. Lett.* **42**:78.
9. Reiland, W., Tittes, H.U., Hertel, I.V., Bonacic-Koutecky, V., and Persico, M. (1982) Stereochemical Effects in the Quenching of Na*(32P) by CO: Crossed Beam Experiment and Ab Initio C1 Potential Energy Surfaces, *J. Chem. Phys.* **77**:1908.
10. Lin, M.C. and Shortridge R.G. (1974) Electronic-to-Vibrational Energy Transfer Reactions: X* + CO(x=0, I and Br), *Chem. Phys. Lett.* **29**:42.
11. Horiguchi, H. and Tsuchiya, S. (1979) Vibrational Distribution of CO and NO Excited by Electronic-to-Vibrational Energy Transfer Collisions with $Hg(6^3P_1$ and $6^3P_0)$, *J. Chem. Phys.* **70**:762.
12. De Benedictis, S. and Cramarossa, F. (1987) Vibrational Analysis of $N_2(B^3\Pi_g$ and $C^3\Pi_u)$ and CO(X) Excited in N_2 Discharge and Post Discharge, *Chem. Phys.* **112**:363.
13. De Benedictis, S., Capitelli, M., Cramarossa, F., D'Agostino, R., and Gorse, C. (1984) Vibrational Distributions of CO in N_2 Cooled Radio frequency Post Discharges, *Chem. Phys. Lett.* **112**:54.
14. Treanor, C.E., Rich, J.W., and Rehm, R.G. (1967) Vibrational Relaxation of Anharmonic Oscillators with Exchange-Dominated Collisions, *J. Chem. Phys.* **48**:1798.
15. Caledonia, G.E. and Center, R.E. (1971) Vibrational Distribution Functions in Anharmonic Oscillators, *J. Chem. Phys.* **55**:552.

Although high CO vibrational levels are produced in this manner, no rotational excitation is observed, which is consistent with the small energy defect for the near-resonant process. The energy defect from $N_2(a^1\Pi)$ quenching[16], reaction (2) has been determined

$$N_2(a^1\Pi) + CO \rightarrow N_2(X,v) + CO(A^1\Pi, v', J') \tag{2}$$

to be largely manifested in rotation but the total energy defect is small (<1000 cm^{-1}), much less than the rotational excitations observed here. The quenching of $N_2(A^3\Sigma_u^+)$ by CO[17] produces $CO(a^3\Pi)$ with no reported observations of a CO(v,J) product channel.

The energy transfer process reported here represents a previously unobserved quenching reaction of CO with metastable nitrogen. We will show that consideration of kinetic and energetic constraints positively identifies $N_2(a'^1\Sigma_u^-)$ as the responsible agent. We will also present and discuss the results of surprisal analysis of the observed vibrational distributions that indicates the rotationally excited component to be formed by two distinct mechanisms.

2. EXPERIMENTS

These experiments were performed in the COCHISE (COld CHemiexcitation Infrared Stimulation Experiment) cryogenic discharge afterglow apparatus which is described in detail elsewhere.[18] A flowing N_2/Ar mixture is excited by four parallel microwave discharges (2450 MHz, 50 W) a flowing N_2/Ar mixture is at ~1 torr total pressure. A diagram of the reaction chamber is shown in Figure 1. After exiting the discharge tubes the gas expands into a low pressure (~3 mt), cryogenically pumped chamber (~20 K) where the molecules enter the collimated field of view of a scanning monochromator/ infrared detector assembly. Residence times in the discharge tubes are on the order of 3 to 5 ms; an average time of flight of 0.5 ±0.1 ms is required for the gases to exit the discharge tubes and enter the field of view. Opposing flows of argon/carbon monoxide are used to create a quasi-static interaction region along the centerline of the field of view, resulting in partial rethermalization of the expansion-cooled rotational distributions. The gas residence time in the field of view is ~0.3 ms. Gaseous helium refrigerant maintains all internal temperatures at 20 K, excepting the gas lines and optics which are held at 80 and 40 K, respectively.

The infrared emissions are observed by a cryogenic 0.5 m Czerny-Turner monochromator equipped with a liquid-helium-cooled arsenic-doped silicon detector and a grating blazed at 3 µm. A chopper located in front of the monochrometer entrance slit modulates the signal at 23 Hz. Data collection is performed with a computer-interfaced lock-in amplifier. The absolute uncertainty in the

---

16. Piper, L.G., Cowles, L.M., and Rawlins, W.T. (1986) State-to-State Excitation of $NO(A^2\Sigma^+, v'=0,1,2)$ by $N_2(A^3\Sigma_u^+, v=0,1,2)$, *J. Chem. Phys.* **85**:3369

17. Dreyer, J.W., Perner, D., and Roy, C.R. (1974) Rate Contestants for the Quenching of $N_2(A^3\Sigma_u^+$ $v_A = 0\text{-}8)$ by CO, CO_2, NH_3, NO, and O_2, *J. Chem. Phys.* **61**:3164.

18. Rawlins, W.T., Murphy, H.C., Caledonia, G.E., Kennealy, J.P., Robert, F.X., Corman, A., and Armstrong, R.A. (1984) COCHISE:Laboratory Studies of Atmospheric IR Chemiluminescence in a Cryogenic Environment, *Applied Optics* **23**:3316.

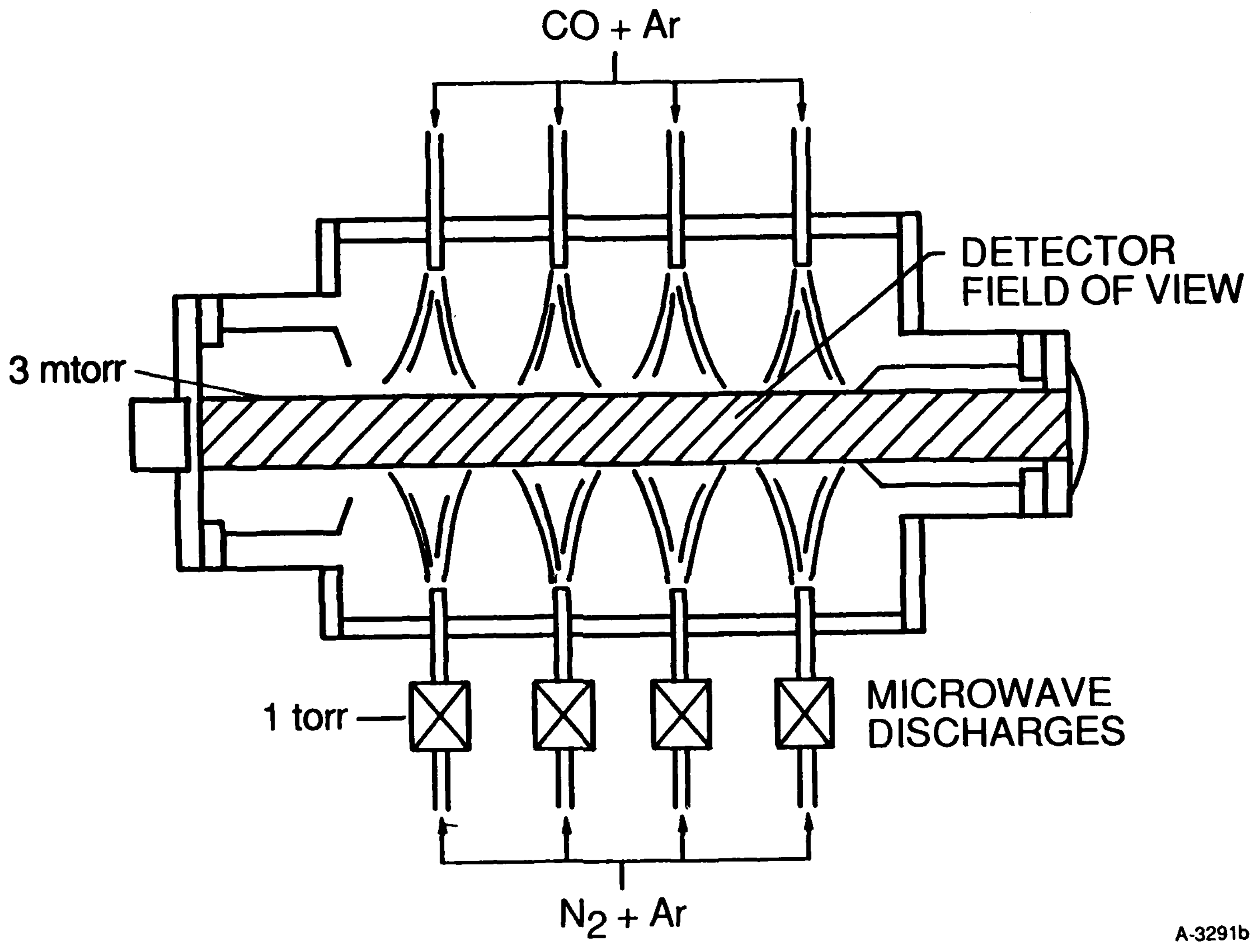

Figure 1. Diagram of the COCHISE Reaction Chamber. The physical dimensions of the cell are 0.6 m in length and 0.4 m in diameter.

wavelengths (due to monochrometer drive error) of the data is ±0.003 μm. The data were corrected for instrument responsivity using blackbody calibration spectra taken in the 300 to 370 K range. The uncertainty in the accuracy of the blackbody temperature is ±3 K, which results in a relative error of ±14 percent for 4.0/6.0 μm intensity ratios. Spectra were taken for N_2/Ar mixtures with N_2 mole fractions of 0.005 to 0.12, with a mass-balanced counterflow of CO/Ar with CO mole fractions of 0.018 to 0.35. The data were typically at the spectral resolution of 0.013 μm (FWHM).

3. RESULTS

In all, 24 emission spectra of the CO fundamental region were obtained at various N_2 and CO mole fraction conditions. The conditions are similar to those in which nitric oxide fundamental emission was examined.[1] The general features of the emissions are relatively invariant with CO mole fraction but the intensity of the CO(1-0) emission exhibits a strong mole fraction dependence as shown in Figure 2.

The envelope degrading to the red of the CO(1-0) band center at 4.666 μm is due to the $\Delta v=1$ progression from $v \leq 14$. The five sharp red-degraded features to the blue of the CO(1-0) band center, which have a spacing of 29.2 ± 1.4 cm^{-1}, cannot be attributed to CO thermalized vibrational emission. These bands have not been previously observed in published spectra of CO fundamental emission taken at higher pressures (>1 torr).[19,20,21] At low pressure with the COCHISE apparatus, these features are observed under all conditions that produce the CO fundamental emission. They have been observed to remain unstructured even at the highest resolution employed (0.0067 μm). Under low nitrogen mole fraction conditions, in which the CO(1-0) emission intensity is greatly reduced, eight bands are observed with three progressing into the thermalized CO($\Delta v=1$) envelope. Considering the overlap of the CO thermalized emission, identification of eight such features represents a lower limit.

These emissions are not observed in the absence of nitrogen in the discharge mixture. Thus, argon metastables and residual ions do not contribute. We have determined these features are not due to CN(v), electronic N_2 transitions, or NCO. The spectral shape of these features, sharply peaked and degraded to the red, is similar to the nitric oxide R-branch band heads identified in spectra of chemiluminescence produced from the reaction of discharged nitrogen with oxygen. CO forms band heads similarly; at sufficiently high rotational excitation band heads will form in the R-branches and the P-branches will extend to the red and do not form band heads. We have used a spectral generation technique to predict the band shapes and positions of the CO R-branch band heads. The methodology and result will be presented in detail in the following section. Using this technique the sharp red-degraded features have been positively identified as CO R-branch band heads. These features are

---

19. Legay-Sommaire, N. and Legay, F. (1970) Vibrational Distribution of Populations and Kinetics of the CO-N_2 System in the Fundamental and Harmonic Regions, *Can. J. Phys.* **48**:1966.

20. Washida, N., Bandow, H., and Inoue, G. (1983) Chemiluminescences in the Carbon Monoxide-Active Nitrogen System, *Bull. Chem. Soc. Japan* **56**:3748.

21. Farrenq, R., Rossetti, C., Guelachvili, G., and Urban, W. (1985) Experimental Rovibrational Populations of CO up to v=40 from Doppler-Limited Fourier Spectra of the Sequences $\Delta V=1,2$ and 3 Emitted by a Laser Type Source, *Chem. Phys.* **92**:389.

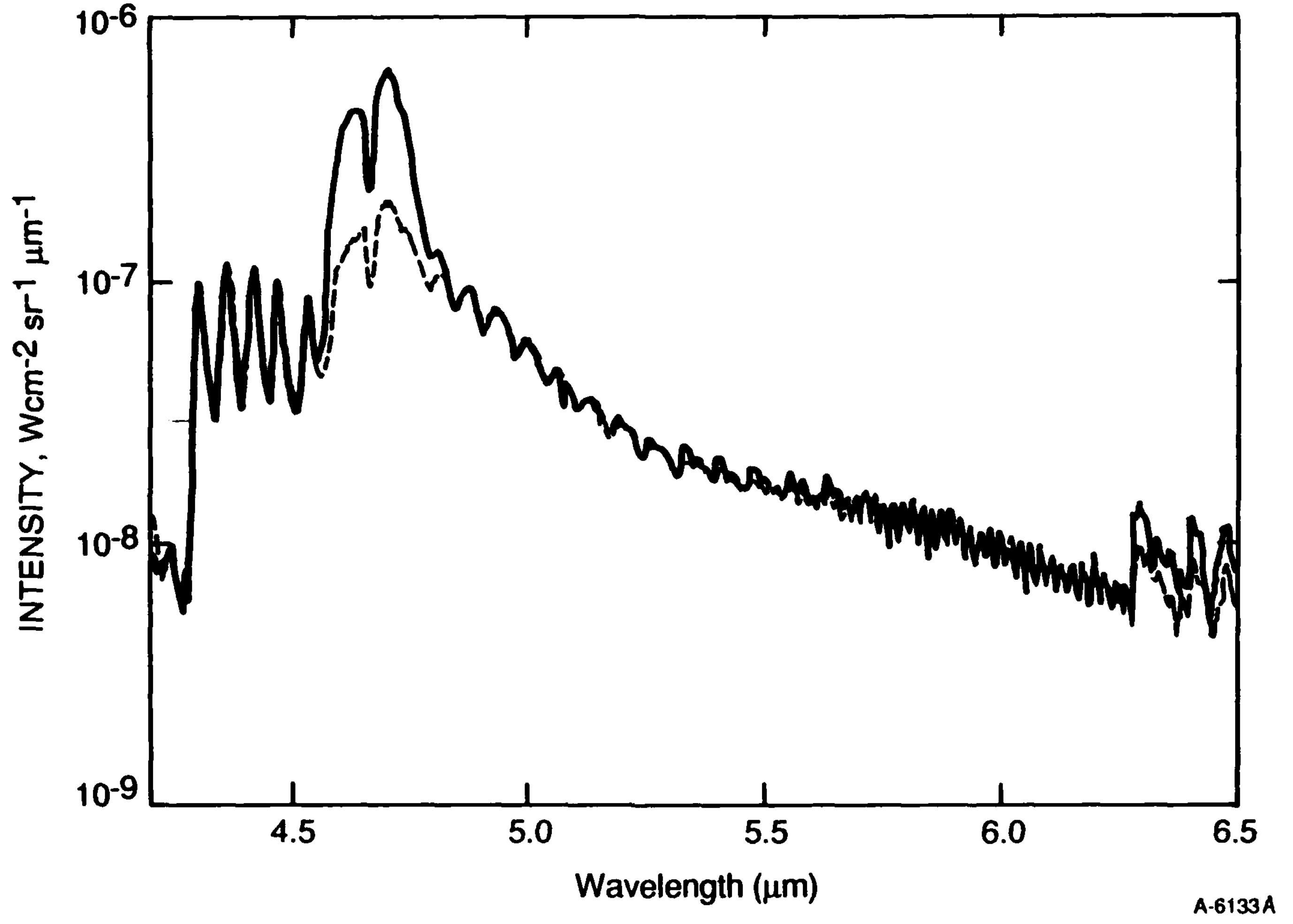

Figure 2. Data Comparison. The dark line shows a typical spectrum obtained under conditions of 12 percent discharged N_2/Ar reacting with a counterflow of 33 percent CO/Ar. The light line shows data taken at 3.17 percent N_2/Ar with identical counterflow conditions.

sufficiently intense that we have been able to determine an optimum rotational distribution. Additionally, the P-branches of the rotationally excited component associated with the R-branch band heads are identifiable, which verifies both the spectral assignment and confirms the appropriate choice of rotational distribution.

4. SPECTRAL ANALYSIS

The data have been analyzed using a spectral generation linear least squares fitting technique.[22] A computed infinite resolution spectrum is convolved with the instrument scan function (in this case, a symmetric triangle with full width at half maximum as the spectral resolution) to create a basis set for each vibrational transition. The basis sets are then fit to each experimental spectrum using a linear least squares method yielding a determination of the product of the upper state density and the spontaneous emission coefficient of the transition, $N_{v'}$, $A_{v', v''}$.

The spectroscopic data used in this study are from Huber and Herzberg.[23] The data were sufficient to adequately reproduce the line positions of both the rotationally thermalized emission features and the R-branch band heads.

The rotational temperatures used to reproduce the CO vibrational progression to the red of 4.6 μm was determined empirically by reproduction of the observed branch structure. The optimum temperature was determined to be 80 K indicating this emission system is rotationally thermalized. The rotational distribution was treated by a simple Boltzman expression, so that band-integrated vibrational number densities and transition probabilities were used. The transition probabilities were calculated using using the dipole moment function of Chackerian et al.[24] Fourteen vibrational levels of thermalized CO emission have been positively identified from the data. This corresponds to vibrational excitation of 3.425 eV.

The band-averaged transition probabilities used for the rotationally excited component are the same as those for the thermalized CO emission. We believe these values to be accurate since the CO ground state is $^1\Sigma$ and therefore not subject to spin-uncoupling at the high J' as discussed for NO. In addition, the dipole moment function of Chackerian et al.[24] extends to v'=40, well above the internuclear separation of the highest V' and J' levels encountered in this study. Thus, Hönl-London scaling of the band-averaged transition probabilities is sufficient to accurately determine the populations of the rotationally excited component.

The 5 cm^{-1} resolution (at 5.0 μm) of the spectral data is insufficient for rotational resolution of the R-branch band heads so the chosen rotational distributions are those which best reproduce the band shapes and peak positions. To adequately fit the R-branch band head features by a Boltzmann

---

22. Fraser, M.E., Rawlins, W.T., and Miller, S.M. (1988) *J. Chem. Phys.* **88**:538.
23. Huber, K.P. and Herzberg, G. (1979) *Molecular Spectra and Molecular Structure IV. Constants of Diatomic Molecules*, Van Nostrand Reinhold, New York.
24. Chackerian, C., Farrenq, R., Guelachvili, G., Rossetti, C., and Urban, W. (1984) Experimental Determination of the $^1\Sigma^+$ State Electric Dipole Moment Function of Carbon Monoxide up to a Large Internuclear Separation, *Can. J. Phys.* **62**:1579.

distribution requires temperature of approximately 20,000 K. Although the fits to the lower vibrational levels are adequate, higher vibrational levels are poorly fit and are better described by lower Boltzmann rotational temperatures. This is evidence for an anti-correlation between rotational and vibrational excitation; that is, the lowest vibrational levels contain the most rotational excitation. Such anticorrelations have been observed in photolysis experiments, abstraction reactions and energy transfer processes.[2-7,9] In these instances, the observed rotational distributions are sometimes best described by a statistical model.[6] Such a model distributes the population statistically over the accessible states. The model that incorporates the observed anticorrelation between vibrational and rotational excitation is given by,

$$P^{0}_{v}(J) \propto (2J + 1)\{(E_T - E_V) - E_J\}^{1/2} \qquad (3)$$

where E_T is the total energy available for the product states, E_V is the vibrational energy, and E_J is the energy of the particular rotational level. Figure 3 contrasts the relative population distributions predicted by Boltzmann and statistical models. The statistical model contains greater relative population in the higher rotational levels at the expense of the lower. Thus, rotational band head formation, which requires significant population of rotational levels in the region of the Fortrat parabola vertex ($J_{vertex} = 92$ for v=1), is readily facilitated by a statistical distribution.

We have examined several values of E_T to determine which produces the best fit to data, that is, reproduction of the positions and spectral shapes of the observed eight band heads. Values of E_T below 3.0 eV reproduce the lower vibrational levels well but the predicted band heads at higher vibrational levels are broadened and red-shifted. The responsible mechanism may be seen from Figure 3. At higher E_V, and lower E_r, the relative population of the rotational levels near the region of the reversal decreases, which causes the observed effects. Values of E_T greater than 4.0 eV predict band head formation for vibrational levels 10 or greater. We prefer a value of E_T between these two bounds. Comparing fits using several values within this range, we have determined E_T = 3.7 eV to be optimum. Values within ±0.2 eV of the optimum value produce adequate fits with only small differences.

Table 1 shows the energetics of CO band head formation for E_T of 3.7 eV. Shown are the values for E_r, the rotational level corresponding to the vertex of the Fortrat parabola, the rotational energy corresponding to this value of J, and the maximum rotational level allowable from E_r.

Figure 4 shows a typical fit to the data using 14 vibrational levels of rotationally thermalized emission and eight vibrational levels with a statistical rotational distribution corresponding to E_T = 3.7 eV. All of the principal spectral features are accurately reproduced. The only features not entirely reproduced fall within the 5.7 to 6.5 μm region. Figure 5 shows an enlarged view of this region from Figure 4. The fit is shown by the heavy line. The spacing of the bands shown in Figure 4 is ~6 cm^{-1}. These features have been observed in all spectra containing sufficient intensity in this wavelength region. The fit shows excellent reproduction of the spectral shapes but does not match the absolute intensity. Figure 4 shows that the thermalized emission does not contribute to this spectral region; the discrete features are reproduced by the P-branches of the rotationally excited component. Inclusion of v>8 of the rotationally excited component improves the fits in this wavelength region. Due to overlap with the thermalized CO envelope, however, unique determination of the populations is not possible, so we have generally excluded these bands from the fits. We describe in the Discussion Section that unique fits may be obtained by fitting the rotational excited component as a single

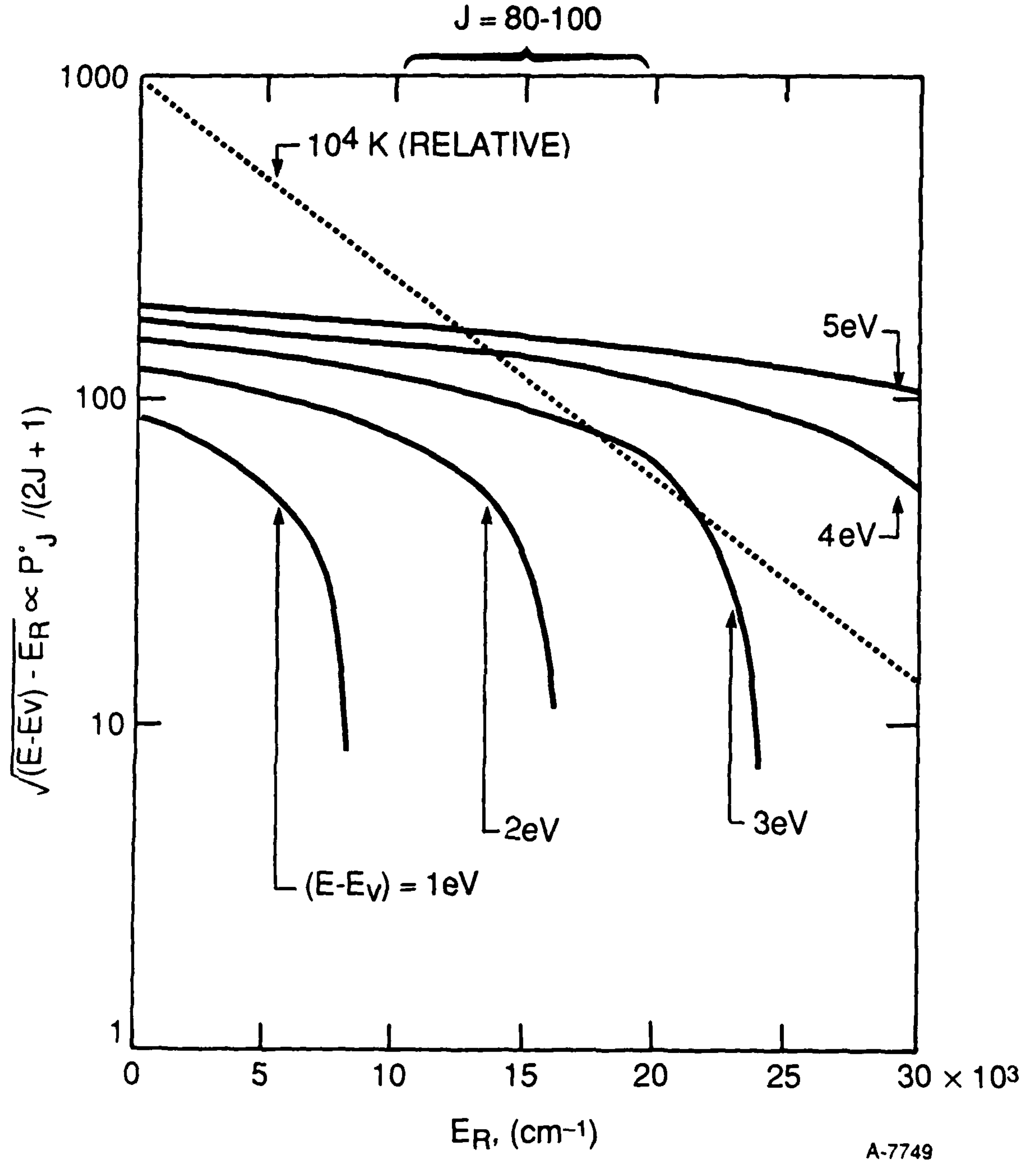

Figure 3. Comparison of Rotational Distributions. Shown are the relative rotational distributions for a 10^4 K Boltzmann and several statistical distributions.

Table 1. Energetics of CO Band Head Formation $E_T = 3.70$ eV

Vibrational Level	E_V(eV)[a]	$E_T - E_V$	J_{vertex}	$E_{J_{vertex}}$(eV)	J_{max}[b]
1	0.266	3.434	92	1.966	123
2	0.528	3.172	91	1.907	118
3	0.788	2.912	90	1.848	114
4	1.044	2.656	90	1.831	109
5	1.296	2.404	89	1.774	104
6	1.546	2.154	88	1.719	98
7	1.792	1.908	87	1.665	93
8	2.035	1.665	87	1.648	87
9	2.274	1.426	86	1.600	81
10	2.511	1.189	85	1.544	74
11	2.744	0.956	84	1.444	66
12	2.974	0.726	84	1.478	58
13	3.201	0.499	83	1.430	48
14	3.425	0.275	82	1.382	35

a. $E_{CO(v=0)} = 0$

b. Calculated from the value for $E_T - E_V$

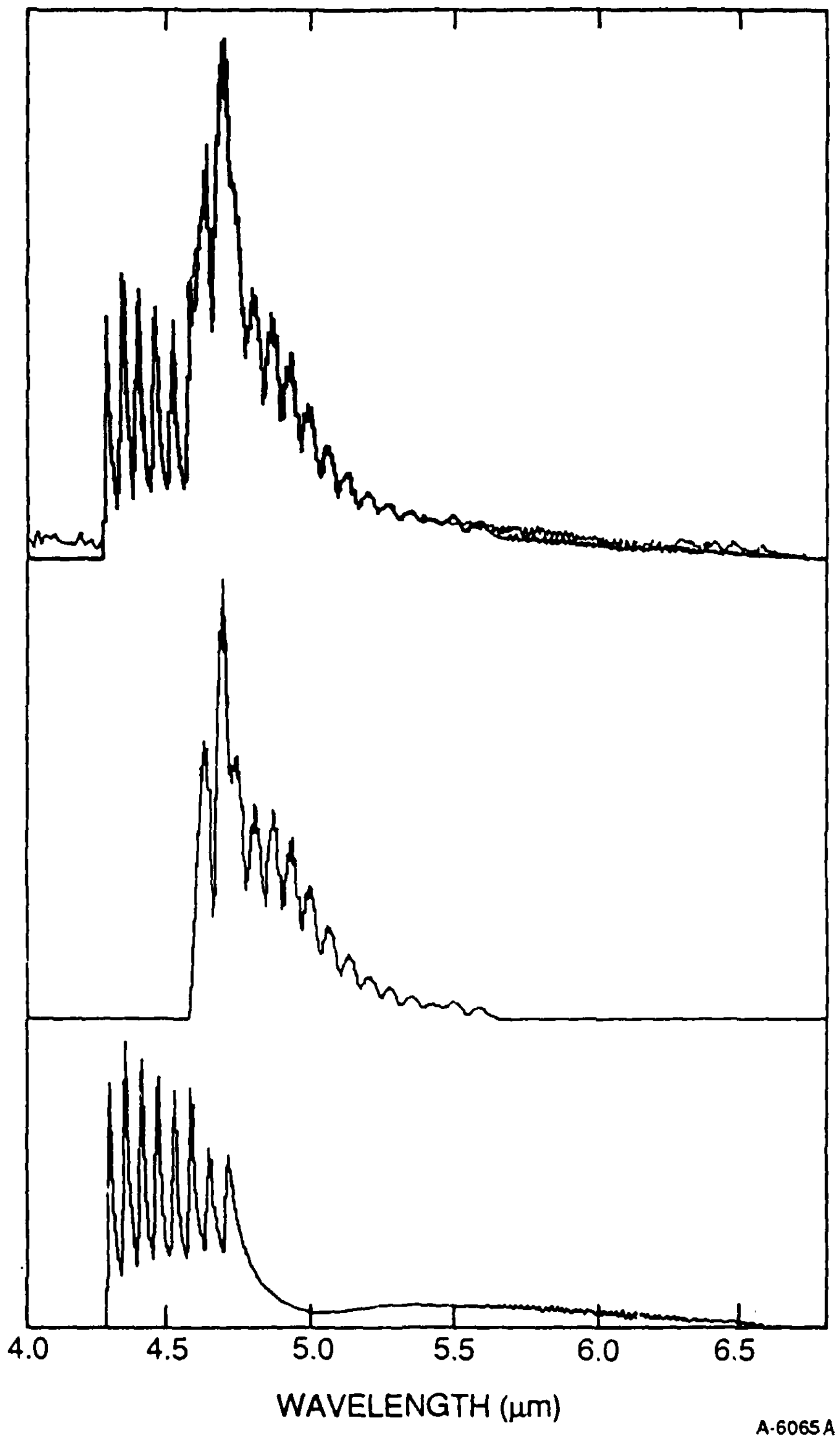

Figure 4. Data (Light Line) and Best Fit (Dark Line). (a) to thermalized (80 K) CO fundamental emission (v′ = 1-14) and CO rotationally excited bands using a statistical distribution with $E_T = 3.7$ eV. The data is the same used for the light line in Figure 2. The spectral resolution is 0.013 μm. The thermalized CO and rotationally excited basis sets which comprise the best fit in (a) are shown in (b) and (c), respectively.

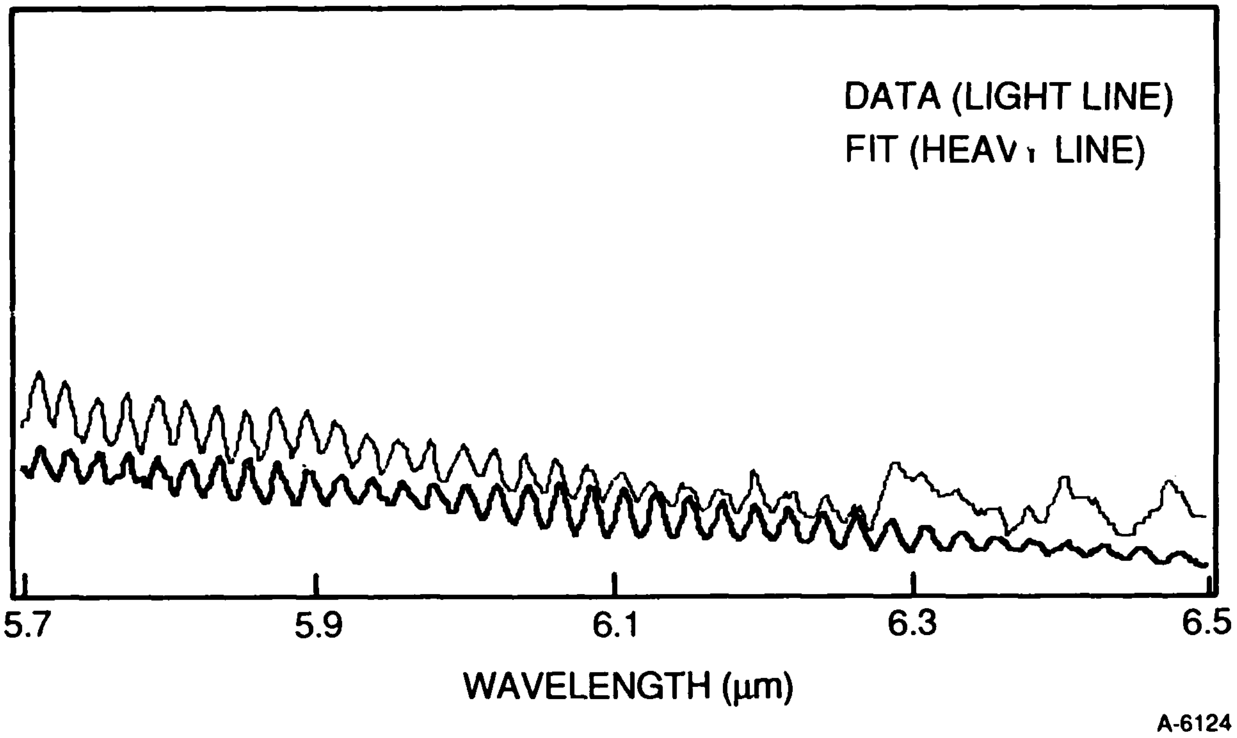

Figure 5. Enlarged View of the 5.7 to 6.5 µs Region of Figure 4. The data is shown by light line, the fit by a dark line.

variable with the relative vibrational levels fixed in ratios from a modeled distribution. By comparing fits with different vibrational contributions to the rotationally excited component, we have determined that the majority of the intensity in the 5.7 to 6.5 μm region arises from the higher vibrational levels (v'=6-8). The relative line spacings may be calculated (omitting D_v correction) from

$$\Delta v = P(J) - P(J=1) = (B_{v'} + B_{v''}) - (B_{v'} - B_{v''})(2J+1). \qquad (4)$$

For v'= 6-8 this wavelength region contains P-branch line spacings of ~6 cm^{-1} for rotational levels 50-80. The $N_2(W^3\Delta_u, v'=1 \rightarrow B^3\Pi_g, v''=0)$ emission in the 6.3 to 6.6 μm region, which we have previously examined and reported[22], and signal to noise considerations, impede determination of the full extent of the P-branch structure. The reproduction of these features, however, by fits to the rotationally excited component confirms the identification of the CO R-branch band heads.

All 24 spectra have been fit using 14 thermalized CO emission bands and eight vibrational levels of the rotationally excited component, as shown in Figure 4. All the fits show similar reproduction of the principal features although many do not accurately reproduce the absolute emission intensity of the P-branch envelope. The discrepancy shown in Figure 4 is typical. Fits to this spectral region are improved by inclusion of higher vibrational levels of the rotationally excited component. Accurate determination of any contribution from the higher levels cannot be determined due to the overlap of these band systems with the thermalized envelope. Bounds for their relative populations will be discussed in the next section.

The statistical rotational distributions employed in these fits provide a better reproduction of the data, both in the R-branch spectral band shapes and the absolute intensity of the P-branches, than do Boltzmann rotational distributions. We consider the statistical model employed here to be a more accurate representation of the true rotational distributions but it cannot be considered to be an unique determination. Signal to noise considerations and band overlap do not permit unambiguous identification of the vibrational-level dependent rotational distributions. The true distributions may deviate from a purely statistical model, containing gaussian character as has been observed in other systems. However, the model employed here has successfully demonstrated an anticorrelation between vibrational and rotational excitation and permitted a bound of ~3.7 eV to be determined for the rotational excited component. Determination of this bound and its similarity to the vibrational excitation of the thermalized component, 3.425 eV, suggests that these two components arise from the same excitation process.

5. KINETIC INTERPRETATIONS

The kinetics of processes occurring in the COCHISE reaction chamber have been previously been described.[1] The low number densities in the reaction zone, the short residence time in the field of view (0.3 ms), and the long radiative lifetimes for the infrared chemiluminescent processes that we observe, allow us to neglect reactions and quenching (excluding rotational) of the excited species created in the reaction zone. Thus, vibrational quenching and CO(v) up-pumping, reaction (1b) can be ignored. The kinetics of [CO(v,J)] are therefore in steady-state according to the production rate and the lifetime of the excited species in the field of view,

$$d[CO(v,J)]/dt = k[M^*][CO] - \tau^{-1}[CO(v,J)] = 0 \qquad (5)$$

where M* denotes the responsible excited species created in the microwave discharges, k is the excitation rate constant, and τ is the residence time in the field of view, 0.3 ms.

Figure 6 shows the absolute populations for the fit in Figure 4. The bimodal nature of the rotational distributions is apparent. The populations for the rotationally excited component exceed those of the thermal component of all vibrational levels except v=1,2. As noted in Figure 2, the lowest thermalized CO vibrational levels exhibit an N_2 mole fraction dependence. We have determined previously that only N_2(v) exhibits a strong variation in its discharge production rate with N_2 mole fraction over the range used here. Thus, relative increases in low CO vibrational population at higher nitrogen mole fraction must be due to the near-resonant energy transfer from N_2(v), reaction (1a).

As illustrated by Figure 2 the lowest CO vibrational populations exhibit a marked dependence with N_2 mole fraction. Examination of the determination populations for all the spectra indicates that only CO(v=1,2) are affected by nitrogen mole fraction. Since CO(v) up-pumping cannot occur under our experimental conditions, the excitation process must be single and two quantum transfer,

$$N_2(v) + CO \rightarrow N_2(v-1) + CO(v=1) \qquad (6a)$$

$$N_2(v) + CO \rightarrow N_2(v-2) + CO(v=2) \qquad (6b)$$

To determine the relative contribution of the N_2(v) energy transfer process to the CO(v=1,2) populations we have plotted the ratios of these populations to [CO(v=3)] as a function of nitrogen mole fraction. Figure 7 shows one of these plots. Extrapolation of these curves to zero determines the relative CO(v=1,2) populations which arise from sources other than N_2(v=1,2) populations which arise from sources other than N_2(v); that is, from quenching of nitrogen metastables. For the data in Figure 7, the multiplicative factors are 3.0 and 1.5 for CO(v=1,2), respectively. The multiplicative factors for all CO mole fractions examined have been determined to be approximately the same.

Using these factors, the contributions to the thermalized CO(V=1,2) populations from N_2(v) transfer and E-V transfer may be separated. Figure 5 shows the CO(v=1,2) number densities corrected for N_2(v) transfer. The relative distributions in both the thermalized and rotationally excited components are now remarkably similar. The vibrational populations of the rotationally excited component typically exceed those of the thermalized component by ~30 percent. This is approximately the ratio determined for all the analyzed spectra. Ratios of the vibrational populations for each component exhibit no dependence on nitrogen or carbon monoxide mole fraction.

As shown in Figure 6 the fraction of the CO(v=2) population attributable to two quantum transfer, reaction (6b), is small. An average ratio [CO(v=2)]/[CO(v=1)] of 0.06 ±0.01 from N_2(v) transfer has been determined for all the observed spectra. This ratio is related to the rate coefficients for reactions (6a, b) by:

$$\frac{[CO(v=2)]}{[CO(v=1)]} = \frac{\sum_v k_v(\Delta v=2)[N_2(v)]}{\sum_v k_v(\Delta v=1)[N_2(v)]} \qquad (7)$$

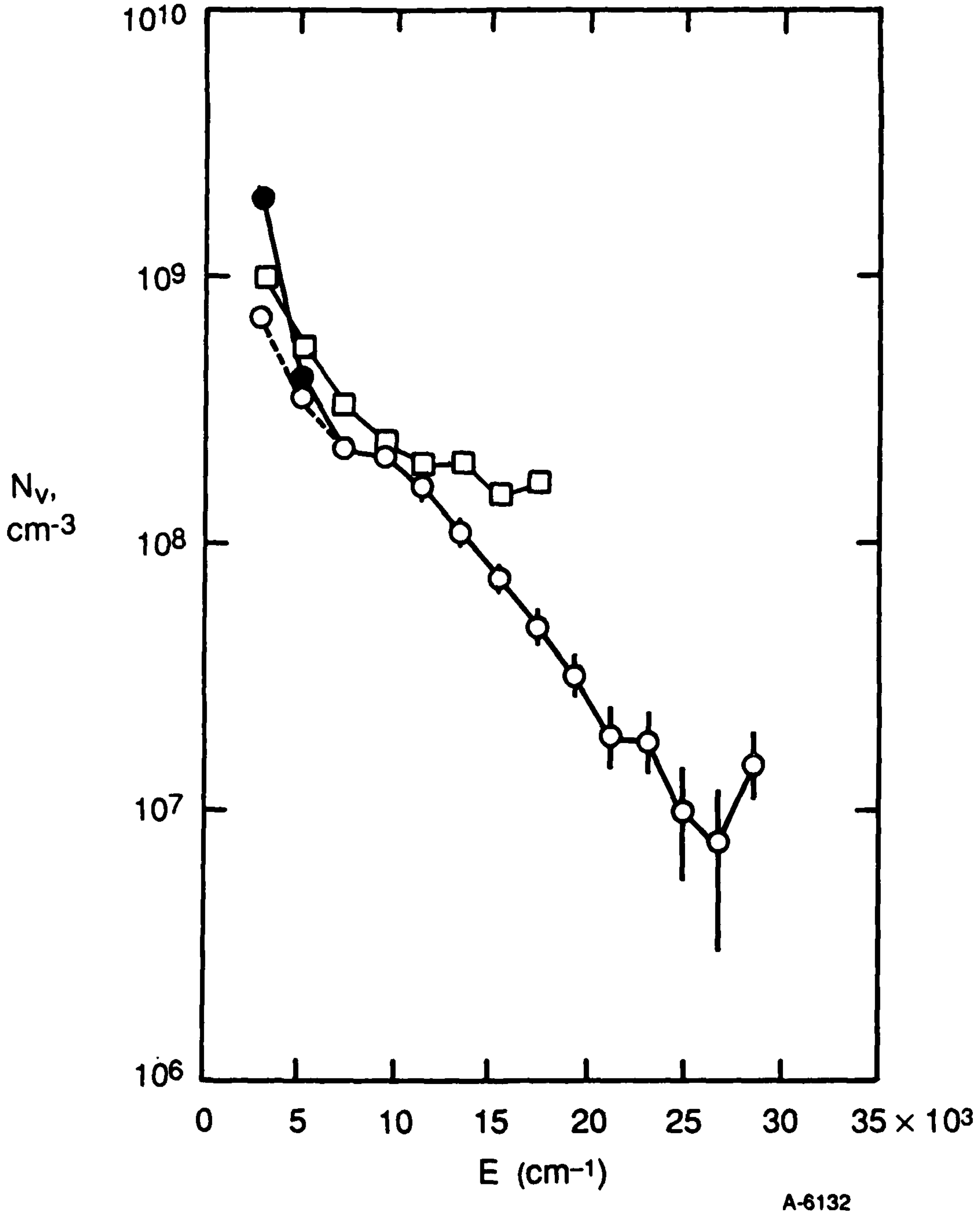

Figure 6. Determined Population Distribution versus E_V, for the Fit Shown in Figure 4. The thermalized component is shown as (O), with contribution to thermalized CO(v = 1,2) as (●), and the rotationally excited component is represented as(☐).

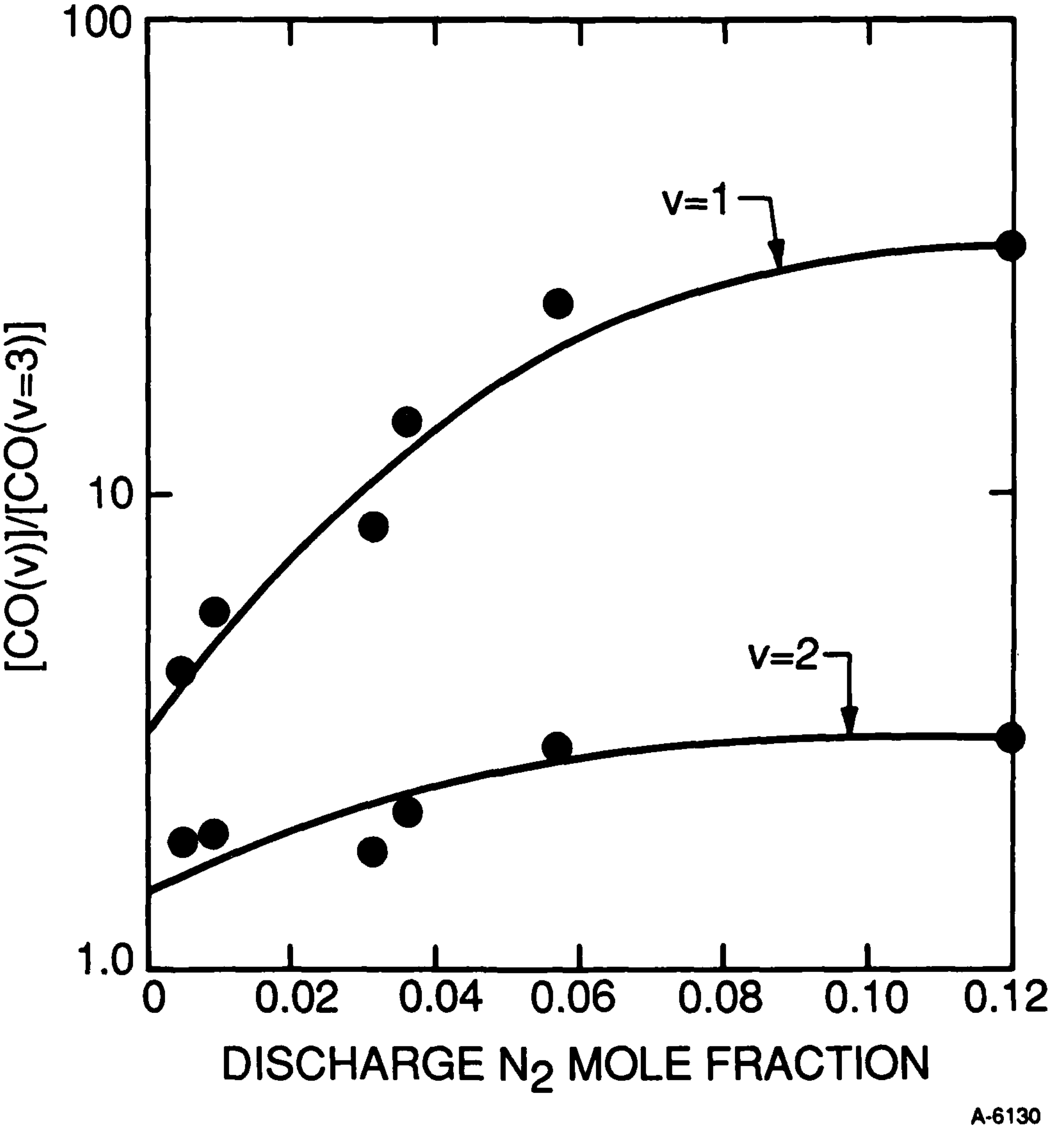

Figure 7. Plot of the Ratio of the [CO(v = 1,2)] to [CO(v = 3)] Populations as a Function of Nitrogen Mole Fraction. The CO mole fraction for these data was 0.33.

Eq. (7) may be resolved for the ratio $\sum_v k_v (\Delta v=2)/\sum_v k_v (\Delta v=1)$ if the $N_2(v)$ distribution can be determined. Discharge-flow measurements using Penning ionization spectroscopy indicate the effluent of our microwave discharges may be represented by a ~6000 K "modified Treanor" distribution in $N_2(v)$.[25] A Treanor distribution contains enhanced populations at higher vibrational levels, relative to a Boltzmann distribution, which are created by collisional up-pumping.[15] Using the modified Treanor distribution, we have determined $\sum_v k_v (\Delta v=2)/\sum_v k_v (\Delta v=1) = 0.1 \pm 0.04$. Owing to the known increase in k_v as a function of v[12,13], the ratio determined here is likely representative of higher v (probably 7 to 8).

Figure 8 shows the average population distributions for the thermalized and rotationally excited components, normalized separately and shown with one-standard-deviation error bars. The population distributions from only 11 spectra were chosen for this average. The spectra containing large contributions to thermalized CO(v=1,2) have been excluded since this emission envelope overlaps the v=5-8 levels of the rotationally excited component, interfering with reliable population determinations of these levels.

The distributions shown in Figure 8 are similar but the distribution of the rotationally excited component appears to be relatively flat above v=4. We have examined the data carefully and determined this trend to be accurate. Fits to the data using a fixed relative vibrational distribution of the rotationally excited component following the distribution of the thermal component seriously underfits the data in the region of v'=5-8 of the R-branch band heads and in the region of the P-branches.

6. EXCITATION MECHANISM

Several processes that may account for all or a portion of the observed emissions require consideration. One possible mechanism for rotational excitation of CO is energy transfer from translationally excited atoms emanating from the discharge. Translationally excited atoms may be produced in the discharges by energy transfer from Ar metastables. Translationally hot H atoms have been reported to excite V,R states of CO.[26] We may discount such processes in our apparatus due to rapid energy accommodation of any "hot" atoms in the 1 torr discharge tubes. The number density of such species reaching the field of view will be minuscule. Collisional quenching of high CO vibrational levels into high rotational levels of lower vibrational levels (V,R transfer), analogous to processes observed for HF[27,28], may also be dismissed. To excite the high J' levels we observed would require nearly gas kinetic multiquantum ($\Delta v \leq 8$) quenching of CO(v). This is unlikely since direct

---

[25] Piper, L.G. and Marinelli, W.J. (1988) Determination of Non-Boltzmann Vibrational Distributions of $N_2(X,v'')$ in He/N_2 Microwave-Discharge Afterglows, *J. Chem. Phys.* **89**:2918.

[26] Chawla, G.K., McBane, G.D., Houston, P.L., and Schatz, G.C. (1988) State-Selective Studies of T→R, V Energy Transfer: The H+CO System, *J. Chem. Phys.* **88**:5481.

[27] Haugen, H.K., Pence, W.H., and Leone, S.R. (1984) Infrared Double Resonance Spectroscopy of V-T, R Relaxation of HF(v=1): Direct Measurement of the High-J Populations, *J. Chem. Phys.* **80**:1839.

[28] Yang, X.F. and Pimentel, G.C. (1984) HF Multiquantum V→R Relaxation Rates with N2 and CO, *J. Chem. Phys.* **81**:1346.

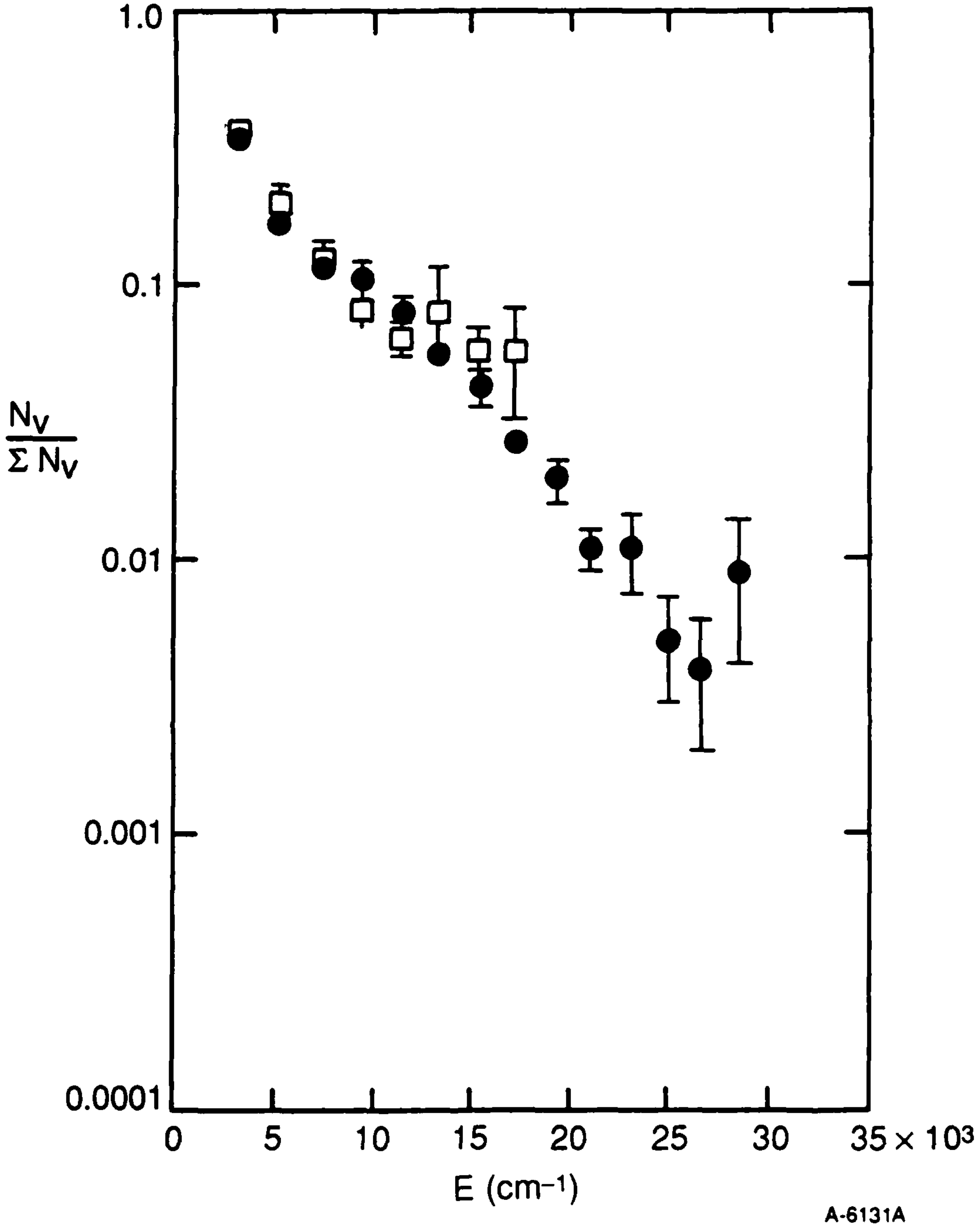

Figure 8. Averaged Relative Population Distributions for 11 Spectra. Both thermalized (●) CO and the rotationally excited component (☐) are shown but have been normalized independently. The error bars represent one standard deviation.

measurements of the v-dependent quenching of CO(v) by CO_2[29] indicate the total quenching rate coefficients to be less than 1 percent gas kinetic. Under quasi-resonance conditions, collisional quenching diatomics in low v, high J levels into high v, low J levels (R,V transfer) may have rate coefficients of 10^{-11} cm^3 s^{-1}.[30] The resonance conditions are given by

$$\frac{\omega_v}{\omega_J} = \frac{\omega_e}{4B_eJ} \tag{8}$$

For CO, resonance is satisfied at J' ~120 which is populated only at the lowest vibrational level for the statistical model. Therefore, R,V transfer should not contribute significantly to the higher vibrational levels of the observed thermalized emissions.

With other possibilities excluded, the mechanism for CO(v,J) excitation must be energy transfer from one or more of the metastable nitrogen species created in the discharge. We have previously determined that to account for the CO(v,J) excitation observed here, the energy transfer reaction must be at least ~3.7 eV exoergic. This constraint, combined with kinetic considerations from Eq. (8), may be used to determine the identity of the responsible species.

Summing the populations of the thermalized and rotationally excited components, a Product k[m*] ~0.5 s^{-1} is required to account for the observed emissions. The measured quenching kinetics for many of the metastable nitrogen species is shown in Table 2. This table contrasts the number densities of the metastable species required in the interaction zone to account for the observed emissions with the number densities determined from modeling studies. The number density calculations have employed the room temperature rate coefficients in the absence of data at 80 K.

Quenching of the metastable nitrogen atoms are shown in reactions (9) and (10). $N(^2D)$ may deposit 2.38 eV into CO

$$N(^2D) + CO \rightarrow N(^4S) + CO(v \leq 9) \qquad \Delta E = 2.38\ eV \tag{9}$$

$$N(^2P) + CO \rightarrow N(^2D) + CO(v \leq 4) \qquad \Delta E = 1.196\ eV \tag{10a}$$

$$\rightarrow N(^4S) + CO(v \leq 15) \qquad \Delta E = 3.576\ eV \tag{10b}$$

rovibrational states, which is well below the ~3.7 eV needed to account for the observed emissions. Additionally, the kinetics of this reaction indicate that contributions to the spectra from this source would be negligibly small. The energetics of $N(^2P)$ quenching to form $N(^4S)$ matches the required ~3.7 eV well. However, the recently determined rate coefficient for quenching of $N(^2P)$ by CO is several orders of magnitude too small for reactions (10a, b) to be the CO(v,J) excitation mechanism.

Excitation of CO(v≤14) by energy transfer from N_2(X, high v) requires multi-quantum transfer from v≤14. The determined contributions to the thermalized CO(v=1,2) populations from N2(v) energy transfer are consistent with a preferred channel for single-quantum exchange and a less favored channel for two-quantum exchange. We have found no evidence for multi-quantum exchange.

---

29. Caledonia, G.E. and Green, B.D. (1979) A Study of Vibrational Level Dependent Quenching of CO(v=1-16) by CO_2, *J. Chem. Phys.* **71**:4369.

30. Stewart, B., Magill, P.D., Scott, T.P., Derouard, J., and Pritchard, D.E. (1988) Quasiresonant Vibration ↔ Rotation Transfer in Atom-Diatom Collisions, *Phys. Rev. Lett.* **60**:282.

Table 2. Measured CO Quenching Kinetics of N_2*, N*

Species	K_Q (300K) $cm^{-3}s^{-1}$	Number Density in COCHISE, cm^{-3} Required for CO(v,J) Excitation	 Estimated for Interaction Zone
N(^{2}P)	≤1.5 (−14)[31]	$> 3^{13}$	1 to 3^9
N(^{2}D)	1.7 (−12)[32]	$> 3^{11}$	3 to 10^9
$N_2(A^3\Sigma_u^+)$,			
v=0	1.5 (−12)[b33]	$> 3^{11}$	1 to 3^9
v=4	1.9(−11)[b33]	3^{10}	1 to 3^9
$N_2(a^1\Pi g)$	2.8 (−10)[a34]	2^9	2^6
$N_2(a'^1\Sigma_u^-)$	1.1 (−10)[a35]	4^9	3^9

a. Includes excitation of CO($A^1\Pi$)
b. Includes excitation of CO($a^3\Pi$)

$N_2(A^3\Sigma_u^-)$ quenches with CO to form CO($a^3\Pi$).[33] Although the

$$N_2(A^3\Sigma_u^-) + CO \rightarrow N_2(X) + CO(a^3\Pi) \tag{11}$$

$$CO(a^3\Pi) + CO \rightarrow 2CO(X, 5 \leq v \leq 13) \tag{12}$$

rate coefficient for the quenching process is known,[33] the absolute yield for reaction (11) has not been measured. Reaction of CO(a) with another CO molecule produces vibrationally excited Co[36,37] with a rate coefficient for the process near gas-kinetic ($k_{12} \sim 1 \times 10^{-10}$ cm^3 s^{-1} at room temperature).[38,39] Quenching of N_2(A) may produce rovibrationally excited CO directly from a branch in reaction (11).

---

31. Rawlins, W.T., Piper, L.G., Fraser, M.E., and Murphy, H.C. (Feb. 1989) *CANOES II: Dynamics of Atmospheric Infrared Thermochemical Excitation*, PSI 9032/TR-901, Final Report, Contract F19628-85-C-0032.
32. Piper, L.G., Donahue, M.E., and Rawlins, W.T. (1987) Rate Coefficients for N(^{2}D) Reactions, *J. Chem. Phys.* **91**:3883.
33. Thomas, J.M., Kaufman, F., and Golde, M.F. (1987) Rate Constants for Electronic Quenching of $N_2(A^3\Sigma_u^+$, v=0-6) by O_2, NO, CO, N_2O and C_2H_4. *J. Chem. Phys.* **86**:6885.
34. Marinelli, W.J., Kessler, W.J., Green, B.D., and Blumberg, W.A.M., The Radiative Lifetime of $N_2(a^1\Pi_g$, v=0-2), *J. Chem. Phys.*, in press.
35. Piper, L.G. (1987) Quenching Rate Coefficients for $N_2(a'^1\Sigma_u^-)$, *J. Chem. Phys.* **87**:1625.
36. Slanger, T.G. and Black, G. (1975) Electronic-to-Vibrational Energy Transfer Between Molecules, *J. Photochem.* **4**:329.
37. Ionikh, Y.Z., Kuranov, A.L., Lobanov, A.N., and Starenkova, L.S. (1986) Vibrational Excitation of CO Molecules in the Reaction $CO^*(a^3\Pi) + CO \rightarrow CO^v + CO^v$, *Opt. Spectrosc.* (USSR) **60**:444.
38. Taylor, G.W. and Setser, D.W. (1973) Quenching Rate Constants for CO($a^3\Pi$: v'=0,1,2), *J. Chem. Phys.* **58**:4840.
39. Clark, W.G. and Setser, D.W. (1975) Comparison of Quenching Rate Constants of CO($a^3\Pi$) at 300 and 77 K, *Chem. Phys. Lett.* **33**:71.

Since $N_2(A)$ lies 6.17 eV above $N_2(X,v=0)$, such a process would be sufficiently energetic. The determined $N_2(A)$ quenching rate coefficient, however, is too small for this process or any derived reactions, such as reaction (12), to be responsible. Additionally, the activation barrier determined for this process by Slanger[40] indicates the rate constant to be $<10^{-13}$ cm^3 s^{-1} at 80K.

The $N_2(W^3\Delta_u, w^1\Delta_u)$ states are sufficiently energetic to produce the observed CO(v,J) emissions; 7.36 and 7.35 eV above the ground state, respectively. The quenching reactions of these two species have not been reported in the literature. We have determined $N_2(W^3\Delta_u, v=1\text{-}5)$ and $N_2(w^1\Delta_u, v=0\text{-}2)$ number densities in COCHISE directly from their IR radiance over the 2 to 4 μm region. Their concentrations in the interaction region are 3×10^8 cm^3 and 1×10^8 cm^3, respectively. Even if these species quench CO with rate coefficients near gas kinetic, they cannot account for the observed CO(v,J) emissions.

Quenching of $N_2(a^1\Pi)$ is rapid, forming $CO(A^1\Pi)$.[34] Since the

$$N_2(a\,^1\Pi) + CO \rightarrow N_2(X,v) + (A\,^1\Pi) \tag{13}$$

yield of CO(A) formation from this reaction has not been determined, a channel forming CO(v,J) is possible. $N_2(a)$ may deposit any fraction of the available 8.4 eV into CO rovibrational states from such a process. However, the radiative lifetime of $N_2(a)$ is short, 56±4 μs[41], which makes the number density of this species in the interaction zone to be too small to account for the observed emissions. The upper limit for $N_2(a)$ number density shown in Table 2 has been determined for the noise level of discharged Ar/N_2 spectra at the wavelength $N_2(a\text{-}a')$ features would occur.[22]

The possible quenching reactions of the $N_2(a'^1\Sigma_u^-)$ with CO are

$$N_2(a'^1\Sigma_u^-) + CO \rightarrow N_2(X,v) + CO(A^1\Pi) \tag{14a}$$

$$\rightarrow N_2(X,v) + CO(X,v,J) \tag{14b}$$

$$\rightarrow N_2(X,v) + CO(I\,^1\Sigma^-, D\,^1\Delta) \tag{14c}$$

$N_2(a')$ may deposit up to 8.5 eV into CO electronic, vibrational and rotational states. The branching ratio forming CO(A) has been measured as $20\,^{+10}_{-8}$ percent.[35] This value, however, was based on an $80\,^{+40}_{-20}$ μs lifetime for the $N_2(a)$ state which has recently been revised to be 56±4 μs. The corrected CO(A) branching ratio is 30 ±8 percent. The remaining fraction must be divided between the other energetically accessible spin-allowed channels. These channels are rovibrationally excited CO(X), reaction (14b), and the $I^1\Sigma^-$ and $D^1\Delta$ states, reaction (14c). At room temperature the total quenching rate constant for reaction (14) is 1.1×10^{-10} cm^3 s^{-1}. Table 2 shows that the kinetics of this reaction are sufficient to account for the observed emissions.

Since $N_2(a')$ is the only species present in the interaction zone that satisfies both the kinetic and energetic constraints, we postulate that reaction (14b) is responsible for the observed CO(v,J)

---

[40] Slanger, T.G., Wood, B.J., and Black, G. (1973) Temperature-Dependent $N_2(A^3\Sigma_u^+)$ Quenching Rate Coefficients , *J. Photochem.* **2**:63.

[41] Marinelli, W.J., Kessler, W.J., Green, B.D., and Blumberg, W.A.M. (1989) Quenching of $N_2(a^1\Pi_g, v'=0)$ by N_2, O_2, CO, CO_2, CH_4, H_2, and Ar, submitted to *J. Chem. Phys.*

excitation. For this hypothesis to be correct, the branching fraction for reaction (14b) must be relatively large, constraining that for reaction (14c) to be small and, owing to the short radiative lifetime of CO(A), the thermalized populations must reflect a contribution from CO(A) radiative cascade.

7. DISCUSSION

Further interpretation of the data may be assisted by surprisal theory.[42,43] This approach postulates the existence of an exponential gap law for an individual metathetic reaction:

$$P_v = P^0(v)\,\exp(-\lambda f_v)/\exp(\lambda_0) \tag{15}$$

f_v is the fraction of the reaction exoergicity appearing as vibrational energy in the product, P(v) is the observed relative vibrational population, and $P^0(v)$ is the statistical "prior" distribution obtained when all final translational, rotational, and vibrational states are equally probable. Thus, the ratios of the observed and statistical vibrational populations should be exponential in the vibrational energy E_v, with the exponential fall-off constant λ quantifying the departure of the observed distribution from a completely statistical product distribution. While this theory does not necessarily hold for all chemical reactions, it has proved useful in the analysis of rovibrational product distributional from several photochemical and reactive interactions.

Both the vibrational extent of the thermalized CO emission ($v \le 14$), E ~ 3.4 eV) and the rovibrational excitation of the rotationally excited component (ET ~ 3.7 eV) can be attributed to an energy transfer process of 3.5 to 3.7 eV. Using a prior distribution for 3.7 eV determined from the usual relationship for a vibrating rotator,

$$P^0(v) = (1-f_v)^{3/2} / \sum_{v=0}^{V^*} (1-f_v)^{3/2} \tag{16}$$

the vibrational surprisal plot for the vibrational populations of the rotationally excited component has been plotted in Figure 9. The change in slope indicates two dynamic mechanisms are responsible for the rotationally excited component: one accounting principally for v=1-4 and another for the higher vibrational levels. The relative populations of the rotationally excited component may be reproduced by a model composed of two such mechanisms as shown in Figure 10. The model is comprised by roughly equal contributions from a low v excitation process and a "statistical" process which contributes to all vibrational levels. The distribution used for the statistical process is the prior calculated for 3.7 eV. This model predicts populations for v>8 of the rotationally excited

---

[42] Bernstein, R.B. and Levine, R.D. (1975) Role of Energy in Reaction Molecular Scattering: An Information-Theoretical Approach, in *Advances in Atomic and Molecular Physics II*, edited by D.R. Bates and B. Bederson, Academic, New York, 216.

[43] Levine, R.D. and Bernstein, R.B. (1975) Thermodynamic Approach to Collision Processes, in *Modern Theoretical Chemistry, Vol. II: Dynamics of Molecular Collisions Part B*, edited by W.H. Miller, Plenum, New York, Chapter 7.

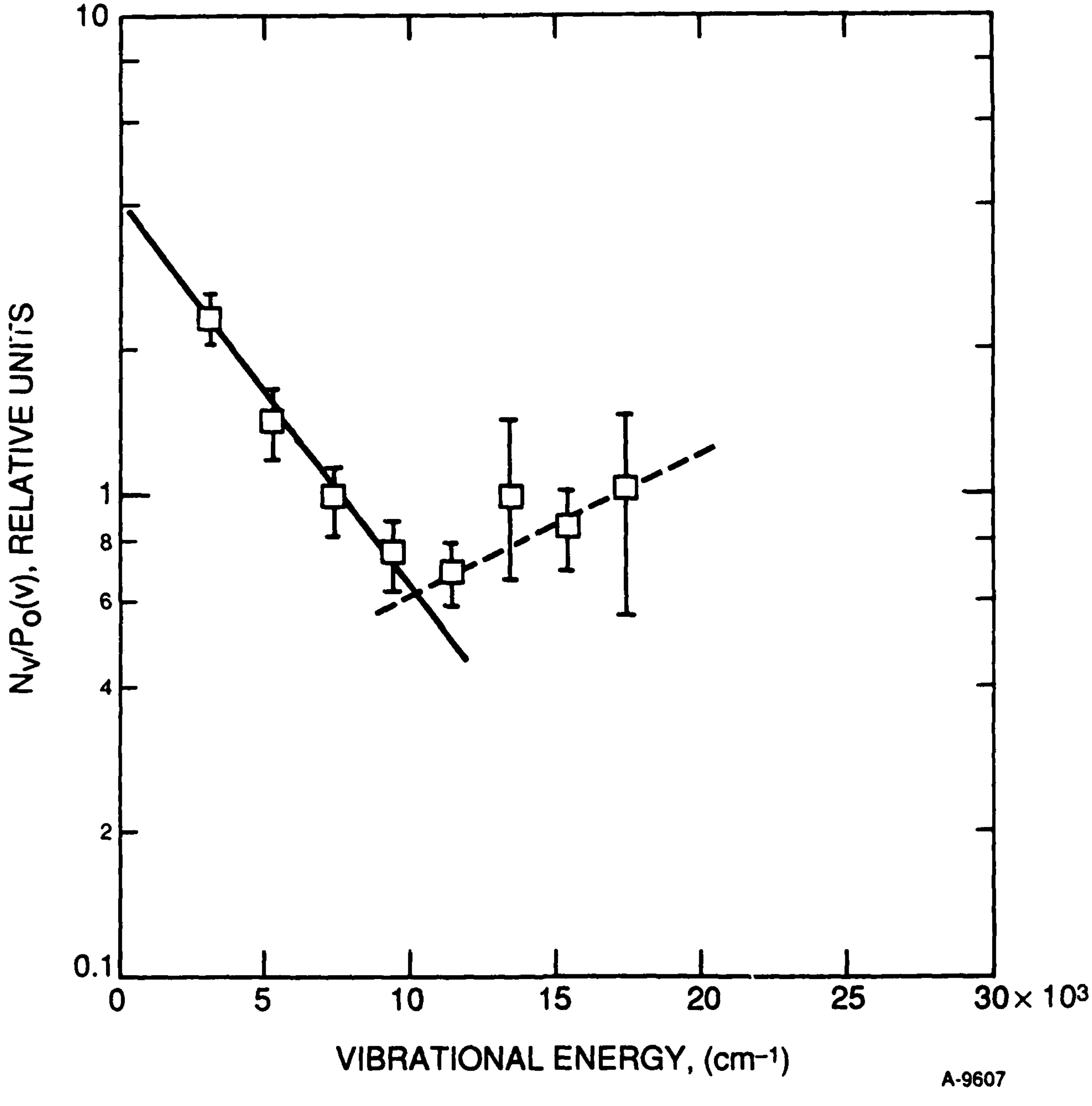

Figure 9. Vibrational Surprisal Plot for the Rotationally Excited Vibrational Populations. The populations are those from Figure 8.

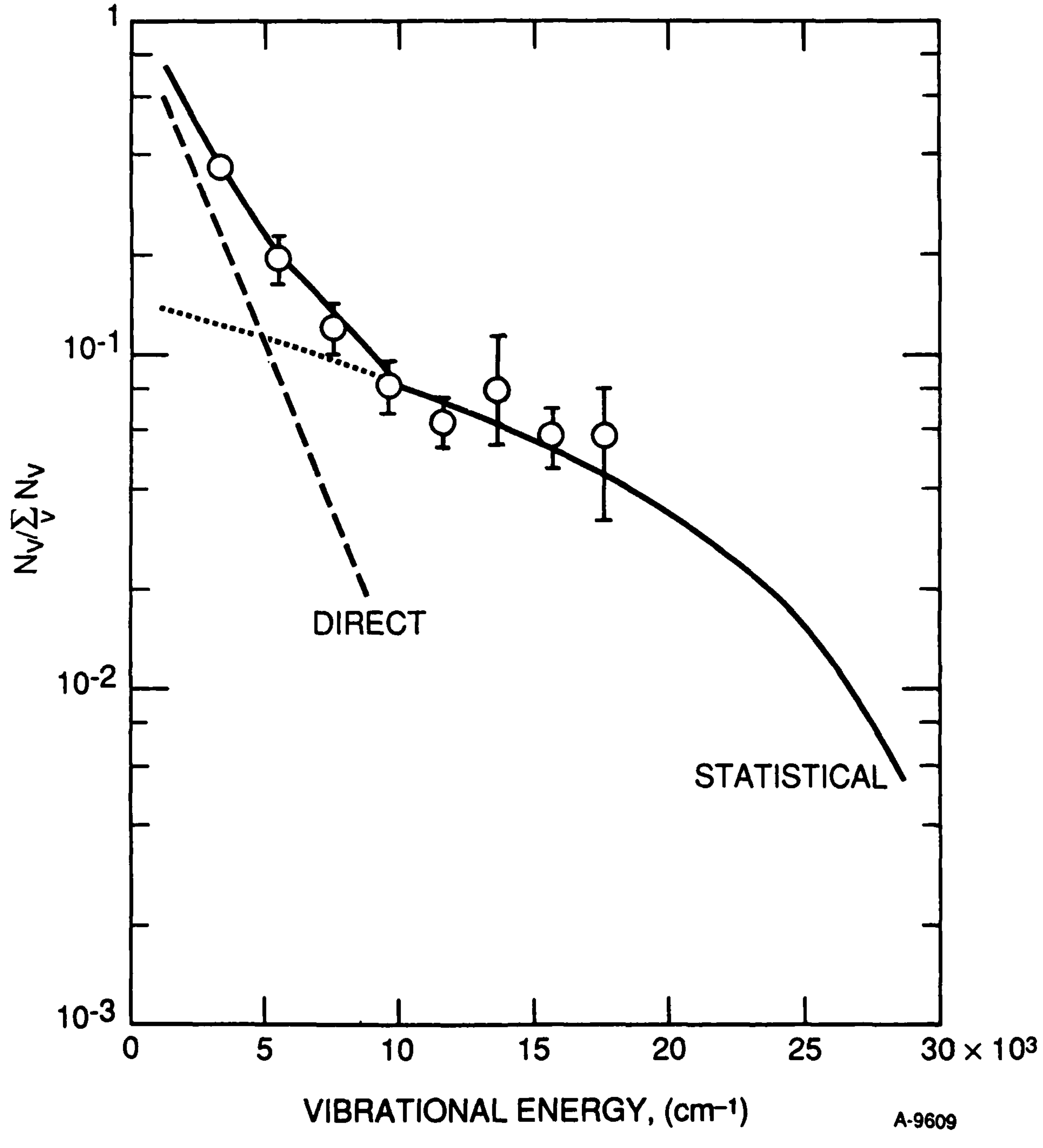

Figure 10. Model Fit to the Rotationally Excited Vibrational Populations. The Model, shown by solid line, has been produced by equal contributions from the direct ($v \geq 4$), (---), mechanism and the statistical mechanism (all v), (· · ·).

component. Absolute populations of these levels cannot be determined from the spectra because these bands overlap the thermalized CO emission features. However, we have performed fits to the data using v=1-14 of the rotationally excited component following the modeled distribution shown in Figure 10. The resulting fits do not exhibit any marked differences from fits excluding v>8 of the rotationally excited component and the match to the absolute intensity in the P-branch region is generally improved. Under these conditions the determined populations of the thermalized component for v>4 are decreased by an average of ~40 percent. Thus, the populations for v>8 of the thermalized component shown in Figure 8 are the upper limits.

Due to implications of the model and the improvement in the P-branch fits, we believe that v>8 for the rotationally excited component are present in the data. However, higher resolution studies will be required to confirm their presence and determine the true population distribution.

Similar analysis of the rotationally thermalized component must include the contribution of reaction (14a) to these populations from CO(A) radiative cascade. Quenching of $N_2(a' \Sigma_u^-, v=0)$ via reaction (14a) yields $CO(A^1\Pi, v \leq 2)$.[35] Owing to the short radiative lifetime of the CO(A) state, ~10 ns, all of the CO(A) created by this process will radiatively cascade to form $CO(v \leq 9)$ with a vibrational distribution reflecting the known branching ratios. Since the maximum energy defect for this process is ~3000 cm^{-1}, $N_2(a',v=0) + CO \rightarrow N_2(X,v=0) + CO(A,v=0)$, we do not expect substantial rotational excitation in the initially formed CO(A) state or, therefore, in the CO(X) populations created by radiative cascade.

Thermalization of the rotationally excited component may also contribute to the observed thermalized component populations. The fraction that may be thermalized will depend on the particular rotational distributions and the quenching rates at 80 K. There are no published quenching studies of high rotationally levels of CO at low temperatures. However, studies of CO(v=0, J) created by formaldehyde photodecomposition at room temperature have determined the rotational relaxation rate constant for transfer of population out of J=12 to be nearly gas kinetic, 3×10^{-10} cm^3 s^{-1}, and that for J=36 to be 5×10^{-11} cm^3 s^{-1}.[44,45] Rotational levels in the region J=80 have rotational spacings of >300 cm^{-1}, greatly exceeding the room temperature value of kT. Thus, quenching of these levels is expected to be significantly slower. At 80 K, kT exceeds the CO rotational spacings for only $J \leq 15$. Assuming this to be the maximum number of rotational levels that may be thermalized within the 20 to 30 collisions in the field of view limits the fraction contributions from the rotationally excited component to be 30 percent for high v and 6 percent for low v.

We may determine the maximum fraction of the CO thermal populations arising from the thermalizations of the rotationally excited component by fitting the observed thermal component population distribution to a model composed of thermalized and CO(A) radiative cascade contributions. The results of this analysis are shown in Figure 11. Reproduction of the observed distribution requires roughly 30 percent of the initially formed CO(v,high J) to be thermalized and a branching fraction for CO(A) excitation of 14 percent.

---

44. Ho, P. and Smith, A.V. (1982) Rotationally Excited CO from Formaldehyde Photodissociation, *Chem. Phys. Lett.* **90**:407.

45. Brechignac, Ph. (1978) Transfer of Rotational Population in CO by IR Laser Double Resonance *Opt. Commun.* **25**:53.

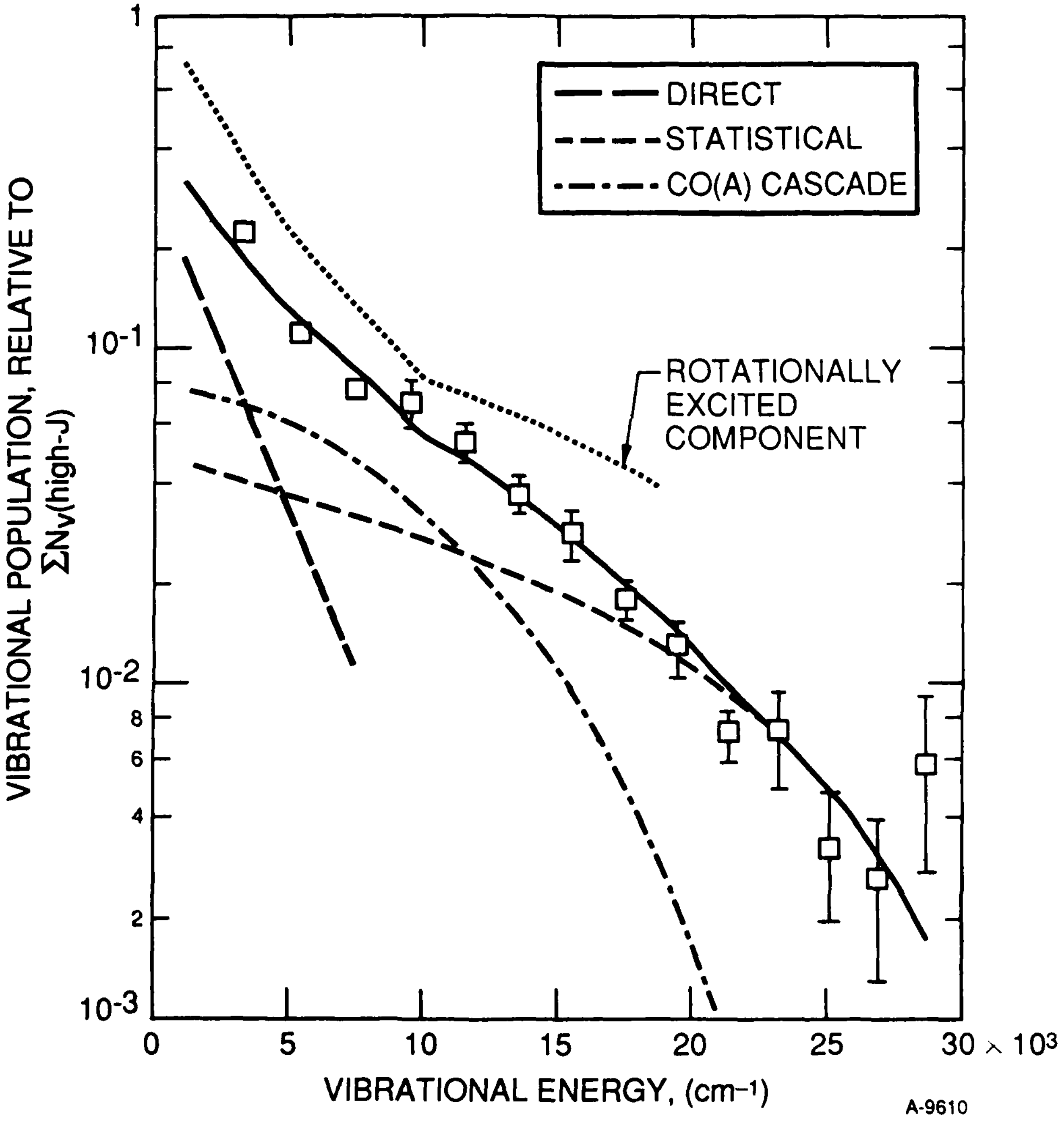

Figure 11. Model Fit to the Rotationally "Thermal" Vibrational Populations. The model (□) has been produced by a contribution of 14 percent branching fraction from reaction (14a), (-_-), and 30 percent of the rotationally excited model, shown separately as direct (--) and statistical contributors (·-·). The relative populations have been normalized to the sum of the rotationally excited vibrational populations. The rotationally excited component is also shown (· · ·).

The determined contribution from CO(A) radiative cascade is about a factor of 2 lower than the recalculated branching ratio of Piper.[23] Our result could be consistent if the branching ratio for reaction (17a) decreases somewhat at lower temperatures. Conversely, the requirement of 30 percent thermalization of the initially formed rotationally excited component is larger than the established bound. Inclusion of v>8 of the rotationally excited component in the fits decreases the v>4 thermal populations by ~40 percent which reduces the fractional thermalization proportionately. Even with this reduction, we still require rotational relaxation processes to be faster than our estimates or the nascent distributions to be bimodal. Bimodel rotational distributions have been observed in HF under near-nascent conditions.[46] These studies clearly indicate that determination of rotational relaxation must take the nature of the excited complex into account. The important factors are the rate of rotation and the relative velocities of the fragments. If the velocities are low and rate of rotation high, rapid rotational thermalization will occur. The similarities between the thermal and rotationally excited vibrational distributions strongly suggest a direct correlation. Whether the observed bimodal distributions arise from excitation followed by multi-collisional thermalization or near-nascent relaxation of the excited complex cannot be distinguished at these experimental conditions.

In summary, the results of surprisal analysis indicates two dynamic mechanisms are responsible for the rotationally excited component, one producing the low vibrational levels and another, more statistical mechanism contributing to all vibrational levels. CO(A) radiative cascade and a fixed fraction of the rotationally excited component are sufficient to account for the thermalized populations.

The dynamics of the $N_2(a')$ + CO quenching process are worthy of some comment. The interaction must satisfy conservation of angular momentum and energy,

$$(2\mu E_i)^{1/2} b_i = (2\mu E_f)^{1/2} b_f + Jh/2\Pi \qquad (17)$$

$$E_i + \Delta E = E_f + E_v + BJ^2 \qquad (18)$$

where μ is the reduced mass, E_i and E_f are the initial and final center-of-mass collision energies, b_i and b_f are the initial and final impact parameters, ΔE is the exoergicity of the process, and BJ^2 approximates the product rotational energy after the collision. High rovibrational excitation of CO from $N_2(a')$ quenching is certainly energetically permissible. The observed CO rovibrational excitation of ~3.7 eV represents only 45 percent of the total exoergicity; the remainder will be manifested in the N_2 internal modes. The manifestation of fractional energies of this magnitude in internal modes is common to many processes containing a large energy defect.

From Eq. (17), large values of J can be achieved through highly attractive collisions with large initial impact parameters and small final impact parameters with the concurrent requirement that the final center-of-mass kinetic energy is small.[47] Large initial impact parameters have been

---

46. Clark, W.G. and Setser, D.W. (1980) Energy Transfer Reactions of $N_2(A^3\Sigma_u^+)$V: Quenching by Hydrogen Halides, Methyl Halides and Related Molecules, *J. Phys. Chem.* **84**:2225.

47. Poppe, D. (1987) Rotational Excitation of Diatomic Molecules in Exothermic Processes, *Chem. Phys.* **111**:17; Classical Dynamics of Rotationally Inelastic Scattering of Atoms with Molecules, *Chem. Phys.* **111**:21.

determined for the quenching of Na(3^2P) + CO which is 2.1 eV exoergic. Two mechanisms were identified, a "direct" process involving colinear Na--CO approach with an impact parameter of $16a_0$ and a "complex" formation mechanism from colinear NA--OC approach with an impact parameter $13a_0$. Both mechanisms produce rovibrational excitation of CO with up to 0.8 eV in rotation. Extensive molecular orbital calculations of the Na* + CO interaction indicated the source of the rotational excitation to be a strong angular anisotropy of the potential energy surface. There are similarities between the Na* + process and the $N_2(a')$ + CO quenching process observed here. However, these similarities cannot be considered more than qualitative until extensive potential energy surface calculations can be performed.

8. CONCLUSIONS

We have observed extensive rovibrational excitation in carbon monoxide from quenching of discharged nitrogen in a low pressure cryogenic apparatus. The CO fundamental emission spectra exhibit bimodal distributions; 14 rotationally thermalized levels and 8 rotationally excited vibrational levels have been identified. The spectral features due to the rotationally excited component are best fit by a statistical distribution, E = 3.7 eV. this distribution provides sufficient population in the region oi the Fortrat reversal, J ~ 90, to account for the observed R-branch band head formation. The energy transfer process of ~3.5 eV is sufficient to account for the vibrational extent of the thermal component. These two energetic limits are not different in our analysis.

Analysis of the data has identified a contribution to CO(v=1,2) of the thermalized component from

$$N_2(v) + CO \rightarrow N_2(v-1) + CO(v=1)$$

$$N_2(v) + CO \rightarrow N_2(v-2) + CO(v=2).$$

Based on kinetic and energetic arguments we have determined the energy transfer process

$$N_2(a'^1\Sigma_u^-) + CO \rightarrow N_2(X,v) + CO(A^1\Pi)$$

$$\rightarrow N_2(X,v) + CO(v,J)$$

to be responsible for the observed rovibrational excitation. The branching ratio for CO($A^1\Pi$) formation is 30±8 percent. In order to account for emissions observed here, CO(v,J) excitation must account for the remainder.

The energy transfer mechanism producing the rotationally excited component exhibits dynamic similarities to that determined for Na(^2P) + CO; two mechanisms have been identified, one responsible for the low vibrational levels and another that contributes to all accessible vibrational levels. Rigorous potential energy surface calculations will be required, however, to determine the true dynamics of the $N_2(a')$ + CO interaction.

Acknowledgements

The authors would like to acknowledge advice provided by B.D. Green, W.A.M. Blumberg, K.W. Holtzclaw, L.G. Piper, and W.J. Marinelli, and assistance provided by H.C. Murphy, M. Gouveia, and M. DeFaccio. This work was performed under contact F19628-85-C-0032 with the Air Force Geophysics Laboratory, and was sponsored by the U.S. Air Force Office of Scientific Research under Task 2310G4 and by the Defense Nuclear Agency under Project SA, Task SA, Work Unit 115.

References

1. Rawlins, W.T., Fraser, S.M., and Miller, S.M. (1989) Rovibrational Excitation of Nitric Oxide in the Reaction of O_2 with Metastable Atomic Nitrogen, *J. Phys. Chem.* **93**:1097.
2. Houston, P.L. (1987) Vector Correlations in Photodissociation Dynamics, *J. Phys. Chem.* **91**:5388.
3. Woodbridge, E.L., Fletcher, T.R., and Leone, S.R. (1988) Photofragmentation of Acetone at 193 nm: Rotational- and Vibrational-State Distributions of the CO Fragment by Time-Resolved FTIR Emission Spectroscopy, *J. Phys. Chem.* **92**:5387.
4. Bamford, D.J., Filseth, S.V., Foltz, M.F., Hepburn, J.W., and Moore, C.B. (1985) Photofragmentation Dynamics of Formaldehyde: CO(v,J) Distributions as a Function of Initial Rovibronic State and Isotopic Substitution, *J. Chem. Phys.* **82**:3032.
5. Debarre, D., Lefebvre, M., Péalat, M., and Taran, J.-P.E. (1985) "Photofragmentation Dynamics of Formaldehyde: H_2(v,J) Distributions, *J. Chem. Phys.* **83**:4476.
6. Harding, D.R., Weston, R.E., and Flynn, G.W., *J. Phys. Chem.*, in press.
7. Shortridge, R.G. and Lin, M.C. (1976) The Dynamics of the $O(^1D_2) + CO(X^1\Sigma^+, v=0)$ Reaction, *J. Chem. Phys. Lett.* **42**:4076.
8. Hsu, D.S.Y. and Lin, M.C. (1976) Electronic-to-Vibrational Energy Transfer Reactions: $Na(3^2P) + CO(X^1\Sigma^+, v=0)$, *Chem. Phys. Lett.* **42**:78.
9. Reiland, W., Tittes, H.U., Hertel, I.V., Bonacic-Koutecky, V., and Persico, M. (1982) Stereochemical Effects in the Quenching of Na*(32P) by CO: Crossed Beam Experiment and Ab Initio C1 Potential Energy Surfaces, *J. Chem. Phys.* **77**:1908.
10. Lin, M.C. and Shortridge R.G. (1974) Electronic-to-Vibrational Energy Transfer Reactions: X* + CO(x=0, I and Br), *Chem. Phys. Lett.* **29**:42.
11. Horiguchi, H. and Tsuchiya, S. (1979) Vibrational Distribution of CO and NO Excited by Electronic-to-Vibrational Energy Transfer Collisions with $Hg(6^3P_1$ and $6^3P_0)$, *J. Chem. Phys.* **70**:762.
12. De Benedictis, S. and Cramarossa, F. (1987) Vibrational Analysis of $N_2(B^3\Pi_g$ and $C^3\Pi_u)$ and CO(X) Excited in N_2 Discharge and Post Discharge, *Chem. Phys.* **112**:363.

13. De Benedictis, S., Capitelli, M., Cramarossa, F., D'Agostino, R., and Gorse, C. (1984) Vibrational Distributions of CO in N_2 Cooled Radio frequency Post Discharges, *Chem. Phys. Lett.* **112**:54.
14. Treanor, C.E., Rich, J.W., and Rehm, R.G. (1967) Vibrational Relaxation of Anharmonic Oscillators with Exchange-Dominated Collisions, *J. Chem. Phys.* **48**:1798.
15. Caledonia, G.E. and Center, R.E. (1971) Vibrational Distribution Functions in Anharmonic Oscillators, *J. Chem. Phys.* **55**:552.
16. Piper, L.G., Cowles, L.M., and Rawlins, W.T. (1986) State-to-State Excitation of NO($A^2\Sigma^+$, v'=0,1,2) by N_2($A^3\Sigma_u^+$, v=0,1,2), *J. Chem. Phys.* **85**:3369
17. Dreyer, J.W., Perner, D., and Roy, C.R. (1974) Rate Contestants for the Quenching of N_2($A^3\Sigma_u^+$ v_A = 0-8) by CO, CO_2, NH_3, NO, and O_2, *J. Chem. Phys.* **61**:3164.
18. Rawlins, W.T., Murphy, H.C., Caledonia, G.E., Kennealy, J.P., Robert, F.X., Corman, A., and Armstrong, R.A. (1984) COCHISE:Laboratory Studies of Atmospheric IR Chemiluminescence in a Cryogenic Environment, *Applied Optics* **23**:3316.
19. Legay-Sommaire, N. and Legay, F. (1970) Vibrational Distribution of Populations and Kinetics of the CO-N_2 System in the Fundamental and Harmonic Regions, *Can. J. Phys.* **48**:1966.
20. Washida, N., Bandow, H., and Inoue, G. (1983) Chemiluminescences in the Carbon Monoxide-Active Nitrogen System, *Bull. Chem. Soc. Japan* **56**:3748.
21. Farrenq, R., Rossetti, C., Guelachvili, G., and Urban, W. (1985) Experimental Rovibrational Populations of CO up to v=40 from Doppler-Limited Fourier Spectra of the Sequences $\Delta V=1,2$ and 3 Emitted by a Laser Type Source, *Chem. Phys.* **92**:389.
22. Fraser, M.E., Rawlins, W.T., and Miller, S.M. (1988) *J. Chem. Phys.* **88**:538.
23. Huber, K.P. and Herzberg, G. (1979) *Molecular Spectra and Molecular Structure IV. Constants of Diatomic Molecules*, Van Nostrand Reinhold, New York.
24. Chackerian, C., Farrenq, R., Guelachvili, G., Rossetti, C., and Urban, W. (1984) Experimental Determination of the $^1\Sigma^+$ State Electric Dipole Moment Function of Carbon Monoxide up to a Large Internuclear Separation, *Can. J. Phys.* **62**:1579.
25. Piper, L.G. and Marinelli, W.J. (1988) Determination of Non-Boltzmann Vibrational Distributions of N_2(X,v'') in He/N_2 Microwave-Discharge Afterglows, *J. Chem. Phys.* **89**:2918.
26. Chawla, G.K., McBane, G.D., Houston, P.L., and Schatz, G.C. (1988) State-Selective Studies of T→R, V Energy Transfer: The H+CO System, *J. Chem. Phys.* **88**:5481.
27. Haugen, H.K., Pence, W.H., and Leone, S.R. (1984) Infrared Double Resonance Spectroscopy of V-T, R Relaxation of HF(v=1): Direct Measurement of the High-J Populations, *J. Chem. Phys.* **80**:1839.
28. Yang, X.F. and Pimentel, G.C. (1984) HF Multiquantum V→R Relaxation Rates with N2 and CO, *J. Chem. Phys.* **81**:1346.
29. Caledonia, G.E. and Green, B.D. (1979) A Study of Vibrational Level Dependent Quenching of CO(v=1-16) by CO_2, *J. Chem. Phys.* **71**:4369.
30. Stewart, B., Magill, P.D., Scott, T.P., Derouard, J., and Pritchard, D.E. (1988) Quasiresonant Vibration ↔ Rotation Transfer in Atom-Diatom Collisions, *Phys. Rev. Lett.* **60**:282.
31. Rawlins, W.T., Piper, L.G., Fraser, M.E., and Murphy, H.C. (Feb. 1989) *CANOES II: Dynamics of Atmospheric Infrared Thermochemical Excitation*, PSI 9032/TR-901, Final Report, Contract F19628-85-C-0032.
32. Piper, L.G., Donahue, M.E., and Rawlins, W.T. (1987) Rate Coefficients for N(^{2}D) Reactions, *J. Chem. Phys.* **91**:3883.
33. Thomas, J.M., Kaufman, F., and Golde, M.F. (1987) Rate Constants for Electronic Quenching of N_2($A^3\Sigma_u^+$, v=0-6) by O_2, NO, CO, N_2O and C_2H_4, *J. Chem. Phys.* **86**:6885.
34. Marinelli, W.J., Kessler, W.J., Green, B.D., and Blumberg, W.A.M., The Radiative Lifetime of N_2($a^1\Pi_g$, v=0-2), *J. Chem. Phys.*, in press.

35. Piper, L.G. (1987) Quenching Rate Coefficients for $N_2(a'^1\Sigma_u^-)$, *J. Chem. Phys.* **87**:1625.

36. Slanger, T.G. and Black, G. (1975) Electronic-to-Vibrational Energy Transfer Between Molecules, *J. Photochem.* **4**:329.

37. Ionikh, Y.Z., Kuranov, A.L., Lobanov, A.N., and Starenkova, L.S. (1986) Vibrational Excitation of CO Molecules in the Reaction $CO^*(a^3\Pi) + CO \rightarrow CO^v + CO^v$, *Opt. Spectrosc.* (USSR) **60**:444.

38. Taylor, G.W. and Setser, D.W. (1973) Quenching Rate Constants for $CO(a^3\Pi$: $v'=0,1,2)$, *J. Chem. Phys.* **58**:4840.

39. Clark, W.G. and Setser, D.W. (1975) Comparison of Quenching Rate Constants of $CO(a^3\Pi)$ at 300 and 77 K, *Chem. Phys. Lett.* **33**:71.

40. Slanger, T.G., Wood, B.J., and Black, G. (1973) Temperature-Dependent $N_2(A^3\Sigma_u^+)$ Quenching Rate Coefficients , *J. Photochem.* **2**:63.

41. Marinelli, W.J., Kessler, W.J., Green, B.D., and Blumberg, W.A.M. (1989) Quenching of $N_2(a^1\Pi_g$, $v'=0)$ by N_2, O_2, CO, CO_2, CH_4, H_2, and Ar, submitted to *J. Chem. Phys.*

42. Bernstein, R.B. and Levine, R.D. (1975) Role of Energy in Reaction Molecular Scattering: An Information-Theoretical Approach, in *Advances in Atomic and Molecular Physics II*, edited by D.R. Bates and B. Bederson, Academic, New York, 216.

43. Levine, R.D. and Bernstein, R.B. (1975) Thermodynamic Approach to Collision Processes, in *Modern Theoretical Chemistry, Vol. II: Dynamics of Molecular Collisions Part B*, edited by W.H. Miller, Plenum, New York, Chapter 7.

44. Ho, P. and Smith, A.V. (1982) Rotationally Excited CO from Formaldehyde Photodissociation, *Chem. Phys. Lett.* **90**:407.

45. Brechignac, Ph. (1978) Transfer of Rotational Population in CO by IR Laser Double Resonance *Opt. Commun.* **25**:53.

46. Clark, W.G. and Setser, D.W. (1980) Energy Transfer Reactions of $N_2(A^3\Sigma_u^+)V$: Quenching by Hydrogen Halides, Methyl Halides and Related Molecules, *J. Phys. Chem.* **84**:2225.

47. Poppe, D. (1987) Rotational Excitation of Diatomic Molecules in Exothermic Processes, *Chem. Phys.* **111**:17; Classical Dynamics of Rotationally Inelastic Scattering of Atoms with Molecules, *Chem. Phys.* **111**:21.

Contents

1. Introduction and Overview 59
  1.1 Description of Solid State Photomultiplier (SSPM) 59
2. First Generation SSPM Package in COCHISE 61
3. Second Generation SSPM Package 68
References 74

5. Solid State Photomultiplier Results

by

S.M. Miller

1. INTRODUCTION AND OVERVIEW

In April 1986, representatives of Rockwell International made a presentation at AFGL concerning new infrared detector technology. Reported in this briefing was the development of a new infrared detector, capable of counting individual infrared photons, called a Solid Sate Photomultiplier (SSPM). Two of the critical operating conditions, low detector temperature and low blackbody background, were already satisfied by the COCHISE facility. So, an agreement was made with Rockwell that some of these new devices would be tested utilizing the COCHISE facility.

Over the next several months, both a detector housing and amplifier were designed and built. Preliminary testing began in October 1986. A description of an SSPM and the subsequent testing of this device is presented next.

1.1 Description of Solid State Photomultiplier (SSPM)

An SSPM is a solid state device made from Si:As. Unlike a traditional Si:As photoconductor, it possesses enough inherent gain to increase the pulse of current from an individual photon above the bias current of the device itself. The detailed operation of an SSPM can best be described using the schematic in Figure 1. Working from right to left the device is made from a silicon substrate with a

SSPM OPERATING PRINCIPLE

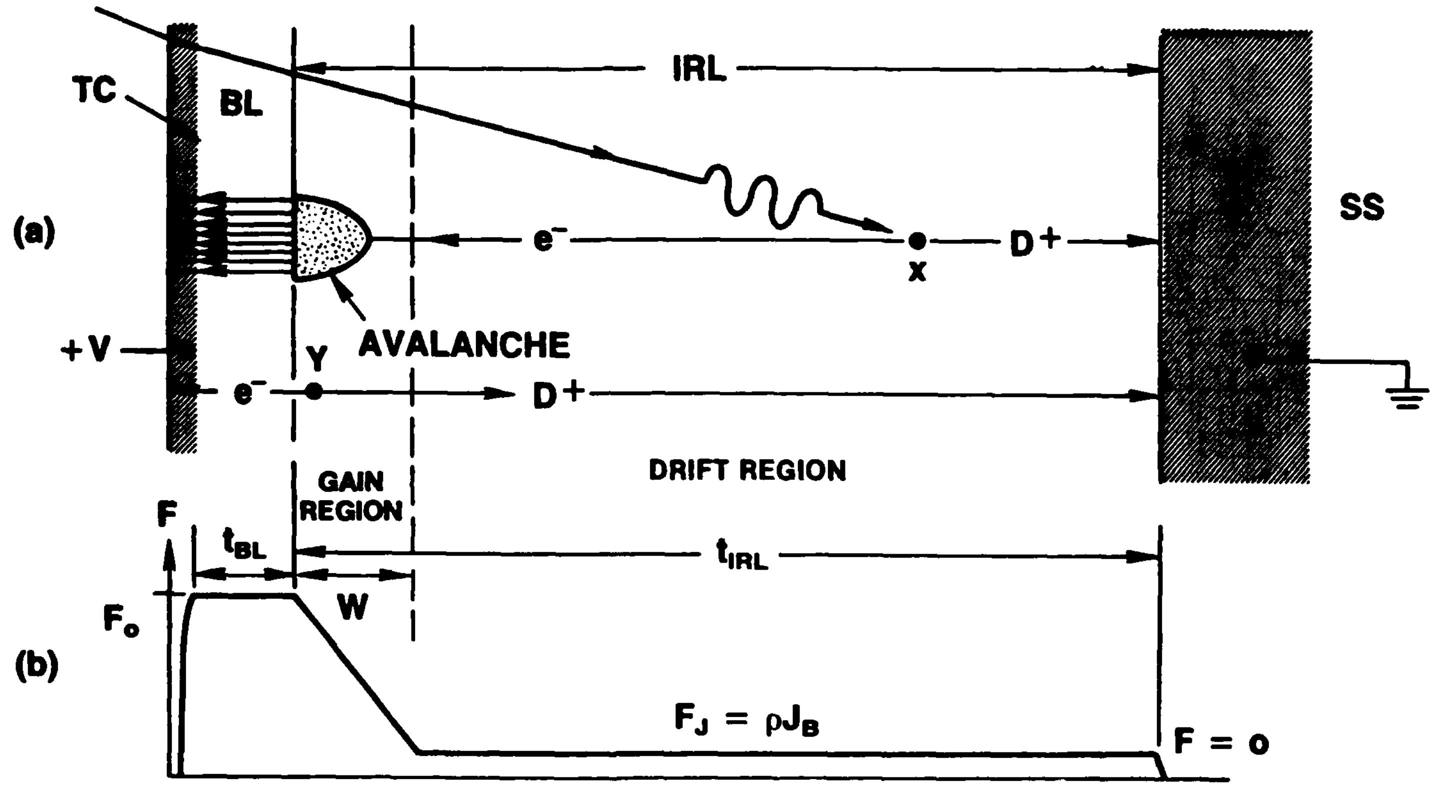

(a) SSPM LAYER CONFIGURATION WITH SCHEMATIC REPRESENTATION OF THE GENERATION OF BIAS CURRENT AND THE EFFECTS FOLLOWING ABSORPTION OF A PHOTON.
(b) ELECTRIC-FIELD PROFILE

Figure 1. Schematic Diagram of a Solid State Photomultiplier

layer of arsenic implant for the negative contact. Next comes the infrared active layer of arsenic doped silicon with an acceptor concentration profile that produces the drift and gain regions of this layer. At the far left is another layer of silicon substrate acting as a blocking layer. This blocking layer is implanted with arsenic for the positive electrode.

A bias voltage of a few volts applied across the device produces the electric field profile shown in Figure 1b. A photon entering from the front (left) of the device is absorbed in the IR active layer and creates an ion-electron pair from the arsenic-created impurity levels. The electron drifts to the left under the influence of the low electric field until it reaches the gain region. Here it is accelerated until it possesses enough energy to create a second ion electron pair. This avalanche process continues until the blocking layer is reached where the resulting electrons drift in a high field region to the positive contact. The much heavier ions drift slowly in the low field region until they recombine to create impurity levels once again.[1]

This process produces a gain of approximately 50,000, reduced at high photon flux by the recombination rate of the ions. The resulting pulses of electrons can be observed by connecting the SSPM to a current to voltage device such as a a transimpedance amplifier with the output of the amplifier connected to an oscilloscope. The height and width of the pulses are mainly limited by the amplifier. The amplifier circuit will be described later. Typical SSPM pulses are shown in Figure 2.

The main characteristics of the SSPM that make it unique are the low noise equivalent power, $< 10^{-18}$ W/Hz$^{1/2}$ at 10 μm, the bandwidth, potentially > 100 MHz, and the spectral range, $0.4\ \mu m < \lambda < 20\ \mu m$ (in different physical configurations). These each have the potential to significantly improve the quality and variety of data taken with the COCHISE facility. The improved NEP could provide orders of magnitude improvement of signal to noise on very weak signals. The added bandwidth could provide a means to take time dependent data on the microsecond time scale and the spectral range could allow spectral scans in the visible as well as the infrared.

2. FIRST GENERATION SSPM PACKAGE IN COCHISE

The first COCHISE SSPM detector housing was made from a large block of oxygen free copper and is shown in Figure 3. This was bolted to the monochromator with a nylon spacer between to provide thermal insulation. A copper strap connected this housing and thus the SSPM to the liquid helium reservoir. The copper cold finger to which the SSPM was mounted is shown in Figure 4. Along with the $1 \times 1.2\ mm^2$ detector, a platinum RTD and a heating resistor were mounted to the cold finger to provide first order temperature control. A transimpedance amplifier was designed and built to convert the pulsed current output of the SSPM to voltage. A schematic of this amplifier is shown in Figure 5. This equipment along with additional amplifiers and pulse counters interfaced to a computer represents the hardware necessary for the initial SSPM testing in COCHISE.

The first COCHISE run utilizing the SSPM was performed in the short wavelength infrared (SWIR). This was done to preclude any potential high background due to light leaks. After a cooldown

---

[1] Petroff, M.D., Stapelbroek, M.G., and Kleinhans, W.A. (19??) Detection of Individual 0.4 - 28 μm Wavelength Photons via Impurity-Impact Ionization in a Solid-State Photomultiplier, *Appl. Phys. Lett.* **51**(6):401.

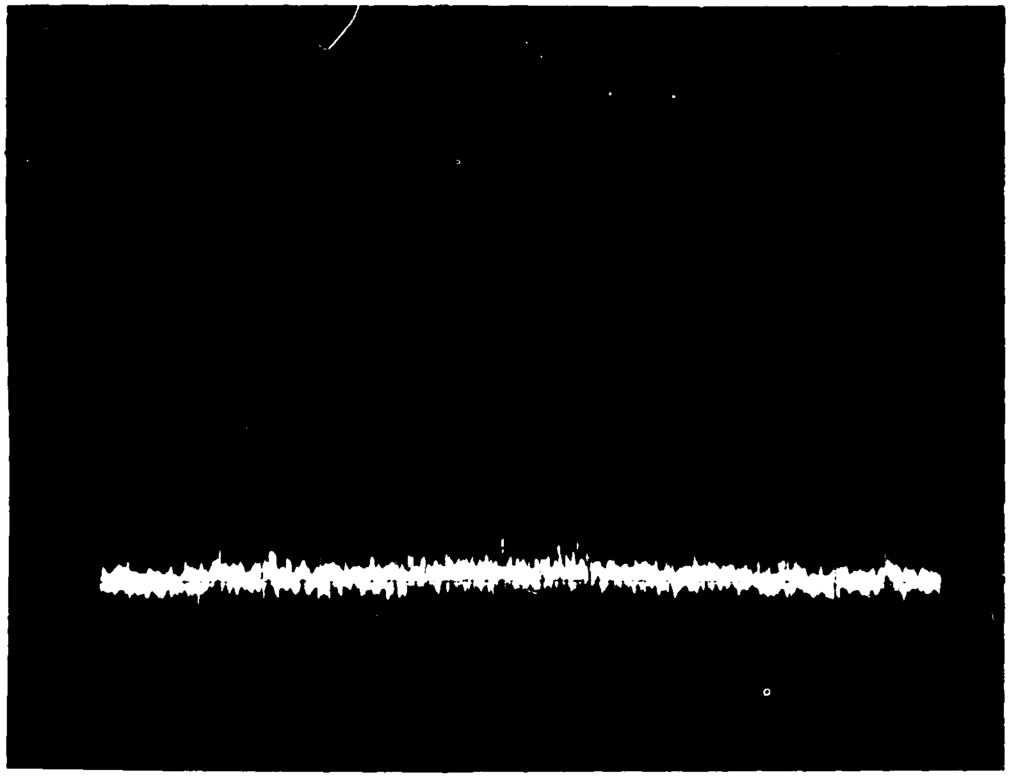

Figure 2. Typical SSPM Pulses

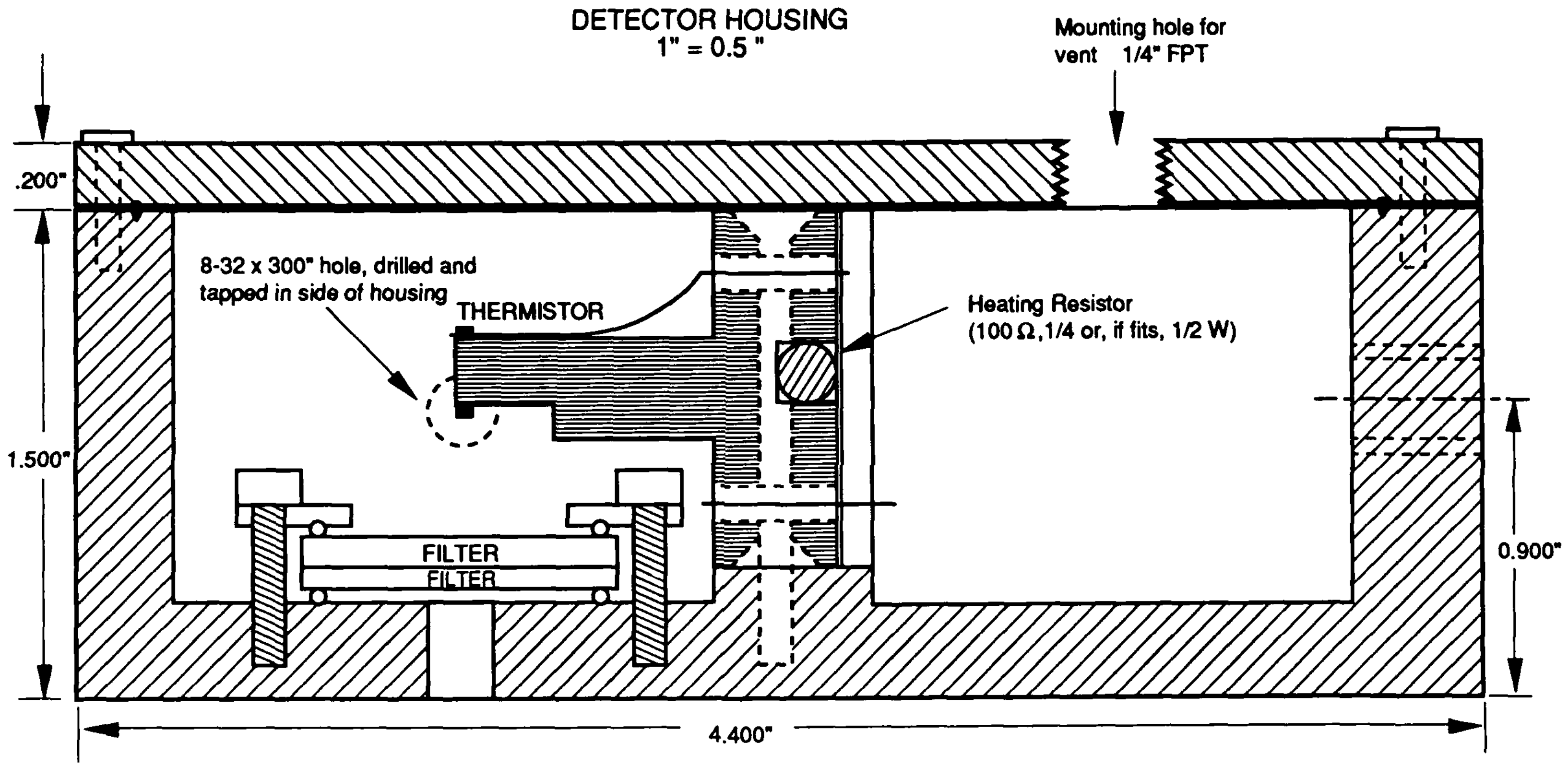

Figure 3. SSPM Detector Housing

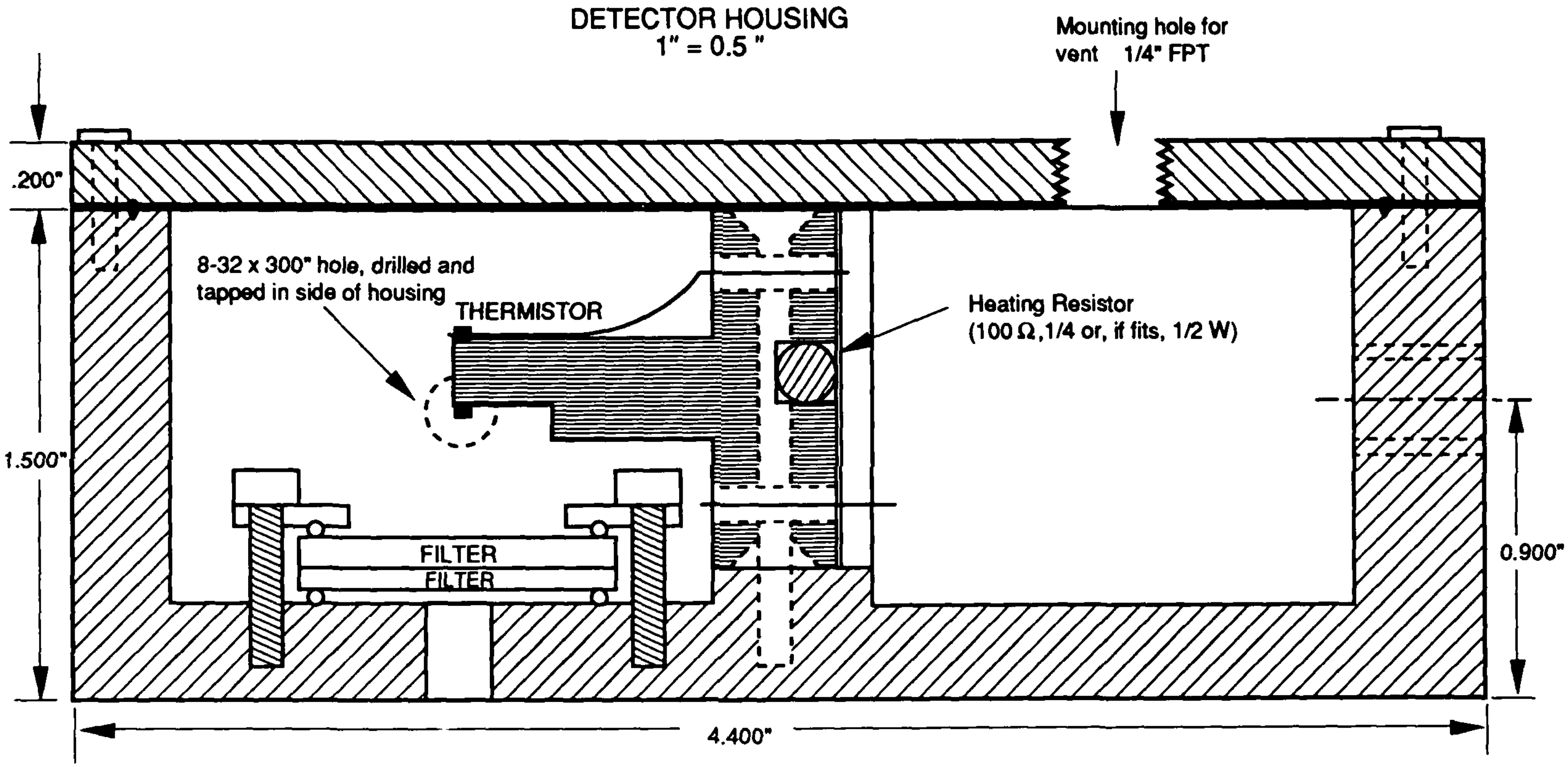

Figure 3. SSPM Detector Housing

SSPM SYSTEM

BLOCK DIAGRAM

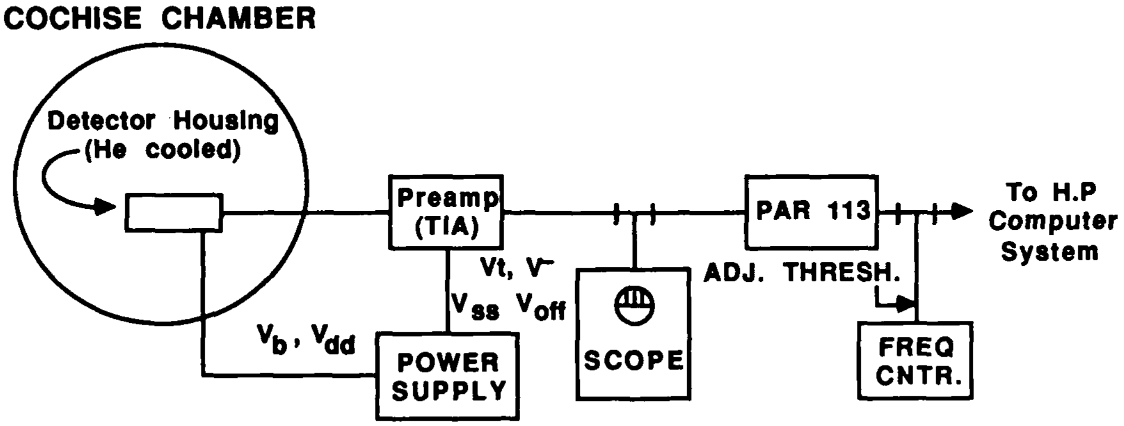

DETECTOR - PREAMP SCHEMATIC

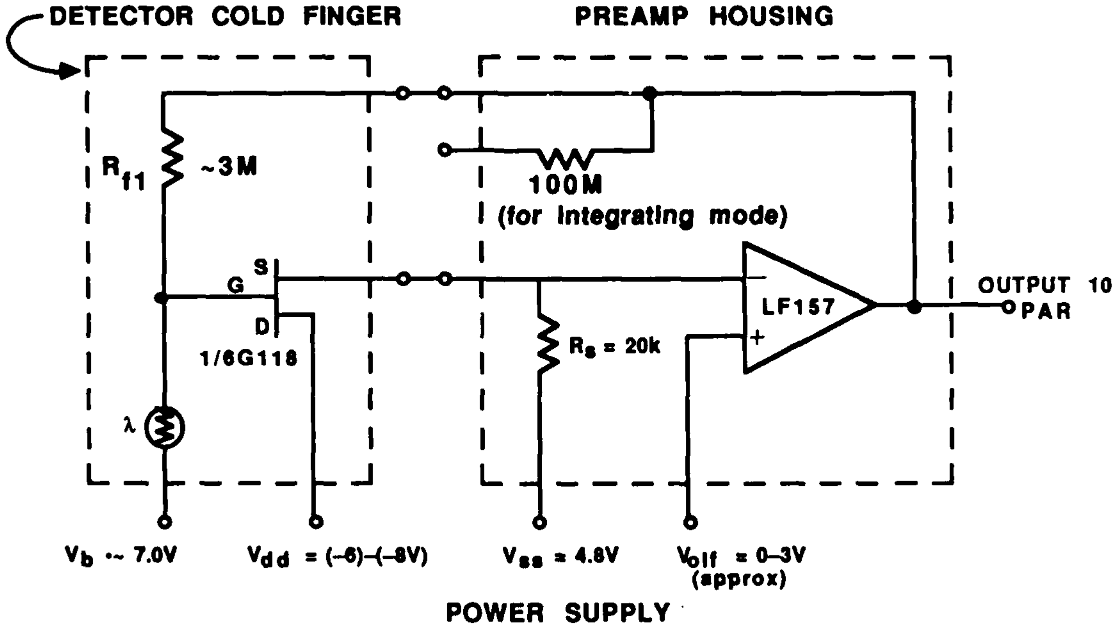

Figure 5. Block Diagram of SSPM System and Schematic of the Detector and Preamplifier

period of 3 days the detector reached an operating temperature of 7 K. At this point the SSPM operated properly as an integrating detector but no photon pulses were observed. This was later determined to be due to excessive capacitance from the long leads connecting the SSPM to the amplifier. The sensitivity of the detector was then examined utilizing COCHISE's blackbody calibration source. The results show that when the transmission loss due to the bandpass filters and the lack of a collection mirror is taken into consideration, the SSPM, operated in photoconductive mode, had approximately the same sensitivity as a conventional Si:As detector.

Several modifications were made during the next series of runs. These included the addition of a collection mirror to increase photo collection efficiency, the installation of a FET on the cold finger to drive the long output line to the amplifier and the installation of an InAs photodiode to provide an amplitude modulated source of light at 3.2 μm. Additional cold straps were also mounted to the SSPM housing for faster cooling.

The first COCHISE SSPM pulses were detected in January 1987. The first test was to determine if any background light from the COCHISE reaction cell could be detected in this 2 - 4 micron band. The SSPM output pulse count with the monochromator slits open and closed was compared to that measured at Rockwell in their test dewar. In this way, it was determined that no background radiation from the reaction cell was detectable in the 2 to 4 micron band. For the second test, a data acquisition program was written to simulate a multichannel analyzer (MCA). For the SSPM to be a true photon counter, it must obey Poisson statistics. The MCA allowed us to model the statistics of the incoming data and determine if they were Poisson. The results, displayed in Figure 6, show that at low photon fluxes, < 50 kHz, the pulses were essentially Poisson in nature while at higher count rates, >70 kHz, the statistics deviated significantly from Poisson. This problem was traced to a pulse pileup problem where two overlapping pulses were being counted as one. This in turn was caused by the long wires from the SSPM to the amplifier. These wires provided additional capacitance which reduced the effective bandwidth to less than 100 kHz. Although this reduced the dynamic range to about 10, it provided us with a working photon counting system to observe chemiluminescence.

Another problem became apparent at this time. During a typical 30 minute spectral scan, the detector would "drop out". That is, an avalanche too large for the detector's capacity would essentially short it out. This could be rectified by reducing the bias voltage monentarily to zero. This breakdown was more prominent at higher temperatures, > 7K and with larger area detectors. A related and potentially more serious problem occurs when the COCHISE microwave discharges are lighted with a tesla coil. The tesla coil induces a large bias across the SSPM, causing many ion electron pairs to develop. The number of ions is so high that it takes many hours for recombination to occur. Warming the detector to 12 K reduces this time to about 3 hours. Up to this point the solution to this problem has been to shut the SSPM bias and amplifier power off when the discharges are lighted. A better solution must be found for the long term.

Chemiluminescence studies with the SSPM began in June 1987. For these studies the 2 - 4 μm bandpass filter was replaced with a BaF_2 window to take spectra in the mid wavelength infrared (MWIR). The background photon flux test was repeated for the 4 to 8 micron band. No background was observed. The first set of runs confirmed that one could indeed collect chemical spectra with the SSPM in the photon counting mode. Typical spectra of carbon monoxide and nitric oxide are shown

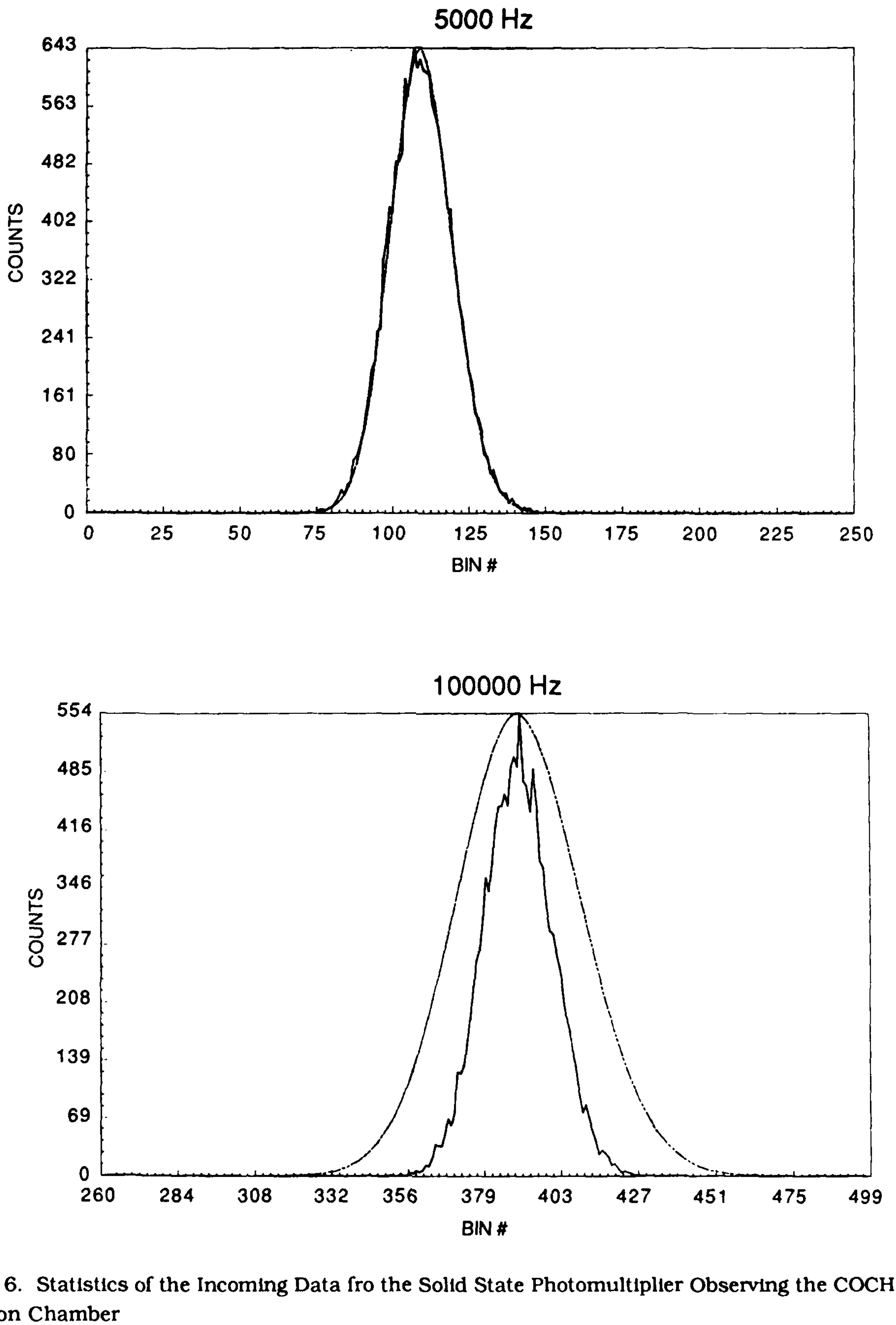

Figure 6. Statistics of the Incoming Data fro the Solid State Photomultiplier Observing the COCHISE Reaction Chamber

in Figures 7a and 7b, respectively.[2] The signal to noise of these spectra turned out to be good but not exceptional, similar to the Si:As detector.

Several experimental changes were made for the last series of SSPM COCHISE runs. These included the installation of two pulse counters, longer integration times, and lower detector temperatures. The dual pulse counters provided us with the ability to either count double pulses and thus increase dynamic range or simultaneously collect both in-phase and out-of-phase data. The longer integration times increased the signal to noise by the square root of the time and the lower detector temperature (6.4 K from 7 K) reduced the detector dark count by an order of magnitude.

These changes resulted in a significant increase in signal to noise as can be seen in the higher resolution NO spectra of Figure 8. These spectra provided the first glimpse of the P branches of the NO hot bands[3], thus confirming the identification of the NO band heads. The final COCHISE SSPM test utilized the 3.2 μm LED and the N_2 (W, v = 2) → N_2 (B, v = 1) band to compare the signal to noise ratio obtainable with the SSPM to that of the Si:As photoconductor. These comparisons are shown in Figures 9 and 10. A proper signal to noise analysis was used to determine that the SSPM possesses a factor of 3 better signal to noise than the Si;As photoconductor. The major caveat in the result is the collection efficiency of optics in the SSPM package compared to that of the Si:As detector package. Taking this collection efficiency factor (× 10) into consideration the SSPM detector tested in COCHISE is capable of signal to noise improvements over the SI:As detector of a factor 30.

3. SECOND GENERATION SSPM PACKAGE

To improve upon the performance of the SSPM in COCHISE, a major redesign of the detector/ amplifier package was made. The parameters that can be readily improved are dynamic range, detector dark counts and therefore signal to noise, and optical collection efficiency. The dynamic range improvement requires that the amplifier be placed as close to the SSPM detector as possible. This should allow the LF157 operational amplifier to operate near its 1 MHz bandwidth, over a factor of 10 improvement. The major challenge here is to provide the detector with a 7-10K operating environment thermally and radiationally isolated from the amplifier 2 cm away which requires at least an 80K operating environment. This will be accomplished by building a detector housing with two isolated chambers. The detector dark count can be reduced by using a smaller detector and by obtaining a new quieter version of the SSPM from Rockwell which trades off pulse height dispersion for NEP. Finally the optical collection will be improved by coupling the detector to the focal length of the collection mirror. This package is presently being prepared for testing in a small test dewar. When this package is found to be operating optimally, it will be placed back into COCHISE and additional chemiluminescence studies will be performed. They will include examination of the nitric oxide overtone band heads in the 2.7 to 4 μm band, long wavelength infrared measurements of ozone in the

---

[2] For future spectral comparisons, it should be noted that throughout the SSPM testing in COCHISE only discharges 2 and 4 worked properly, thus reducing the absolute signal level by about a factor of two.

[3] Refer to Chapter 2 for a thorough discussion of all aspects of the COCHISE nitric oxide chemistry.

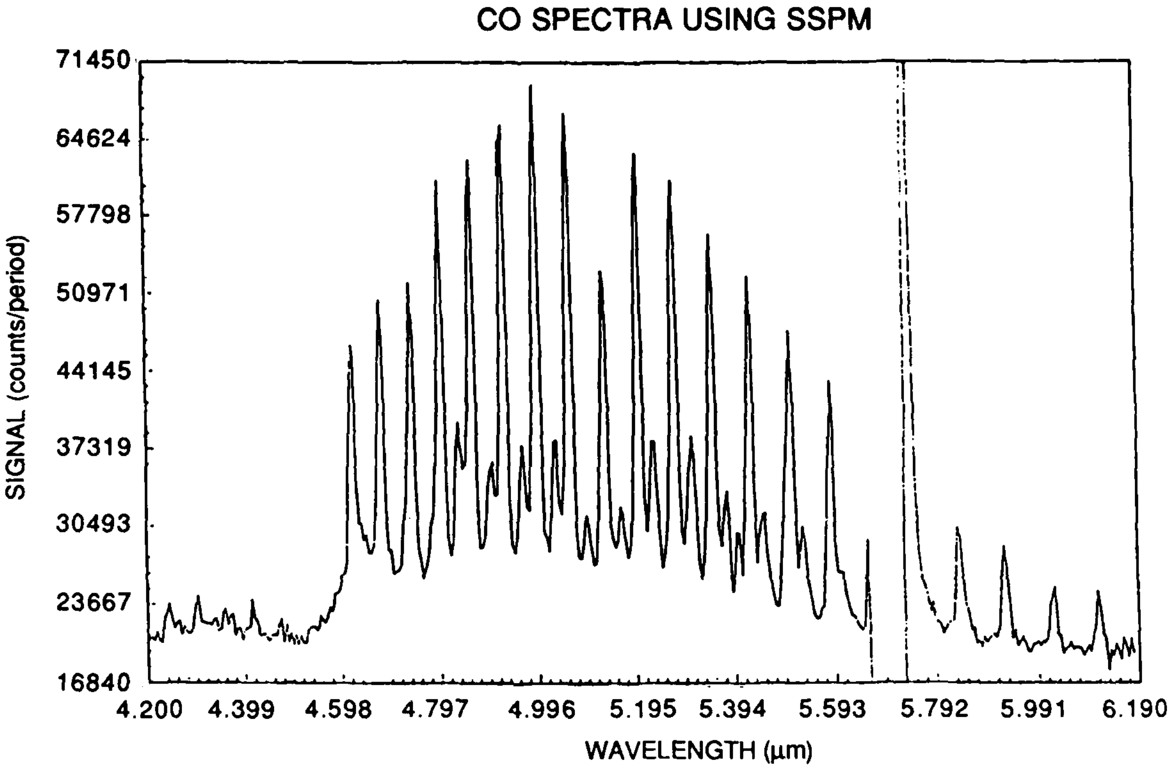

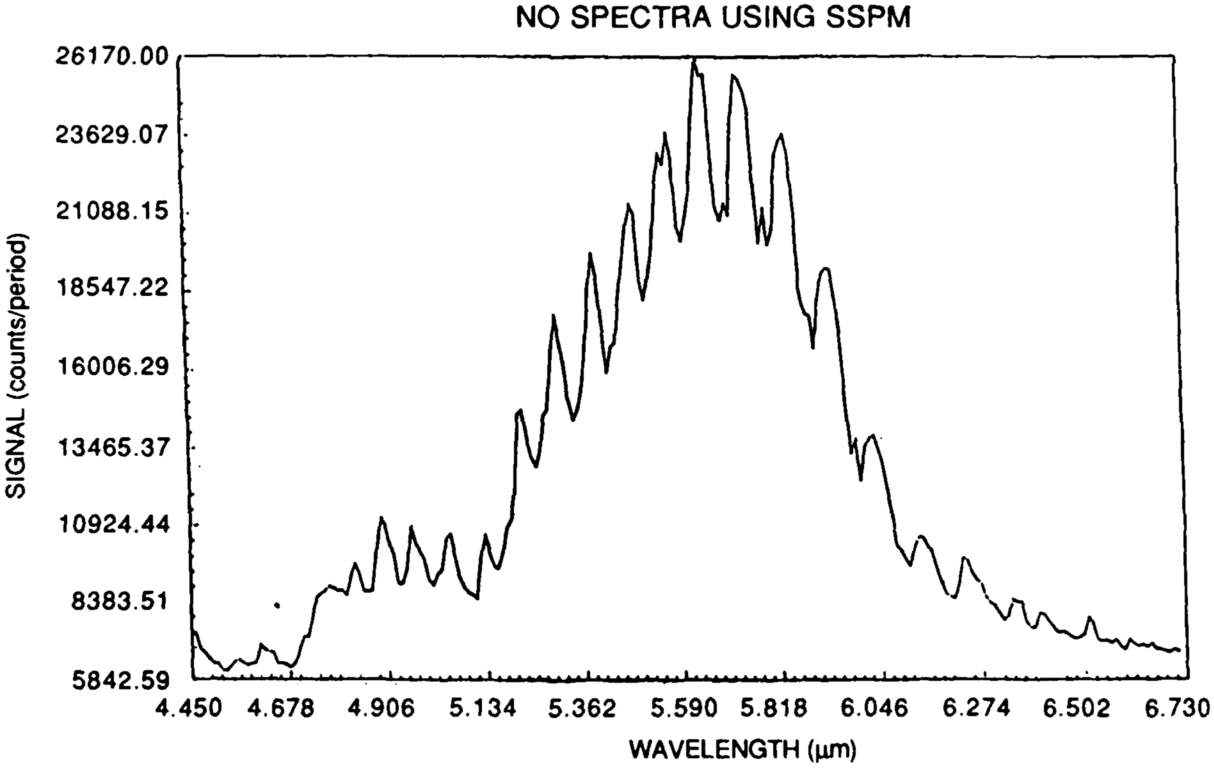

Figure 7. Typical Spectra of (a) Carbon Monoxide and (b) Nitric Oxide

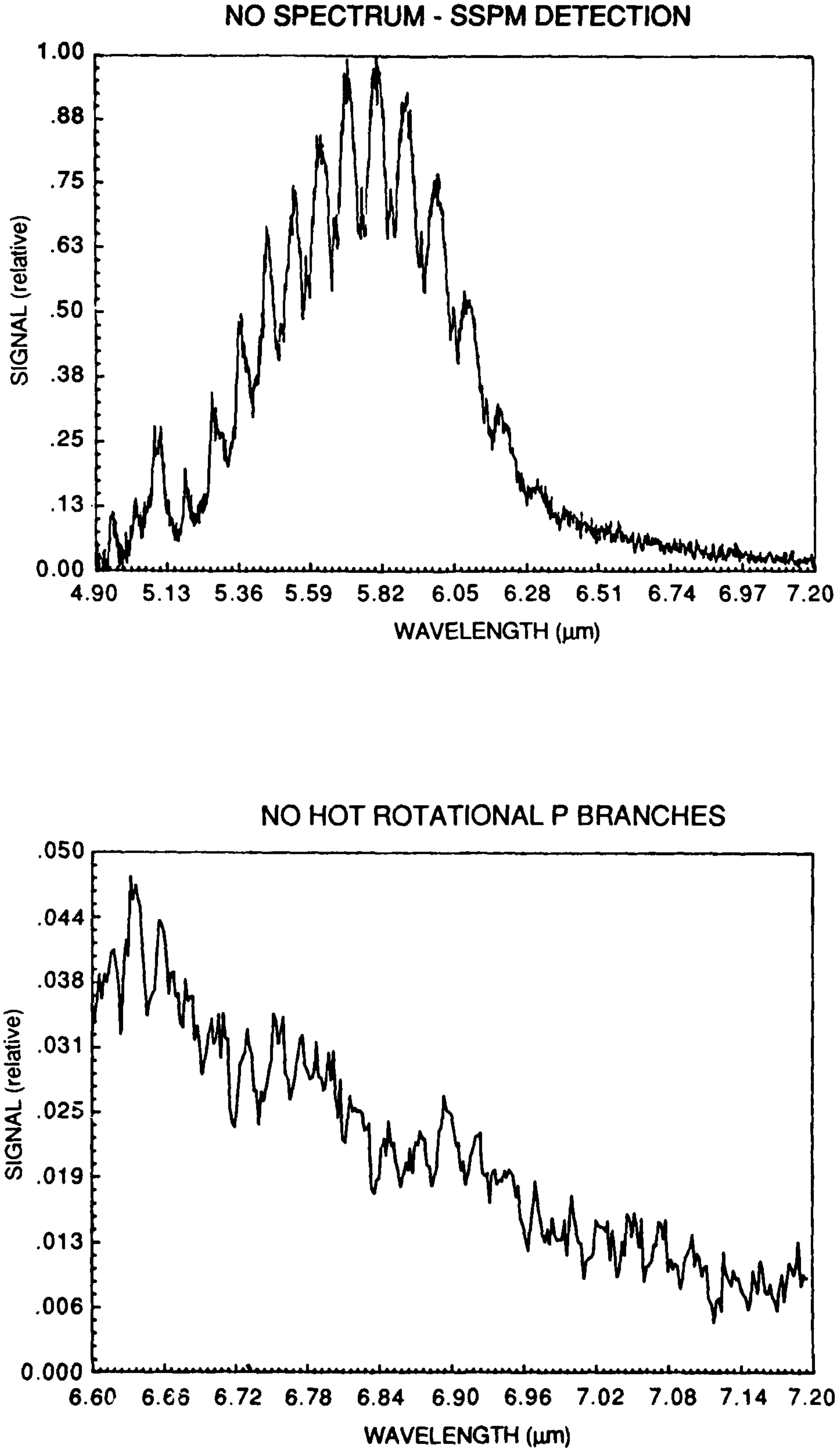

NO SPECTRUM - SSPM DETECTION

NO HOT ROTATIONAL P BRANCHES

Figure 8. Higher Resolution NO Spectra Obtained from Improvements to the SSPM Detector. Top, 4.9 to 7.2 μm spectrum (note improvement over spectrum in Figure 7b); Bottom spectrum between 6.6 and 7.2 μm showing NO hot rotational P branches.

InAs Photodiode Signal - Si:As detection

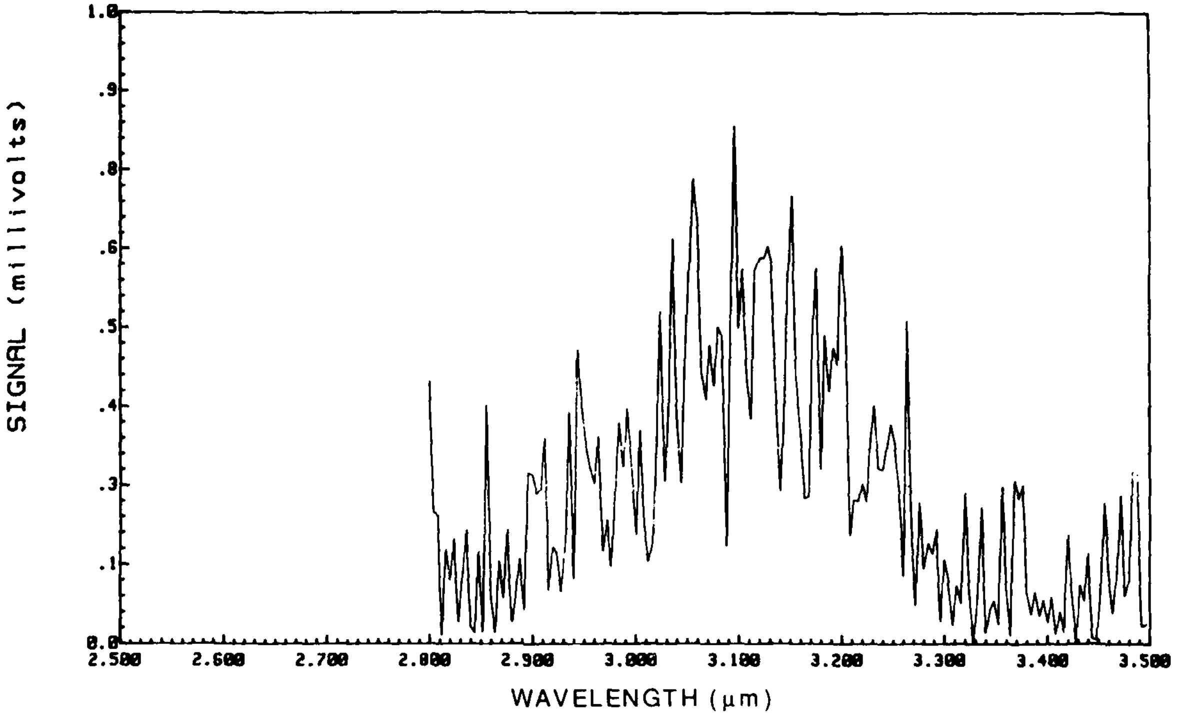

InAs Photodiode Signal - SSPM detection

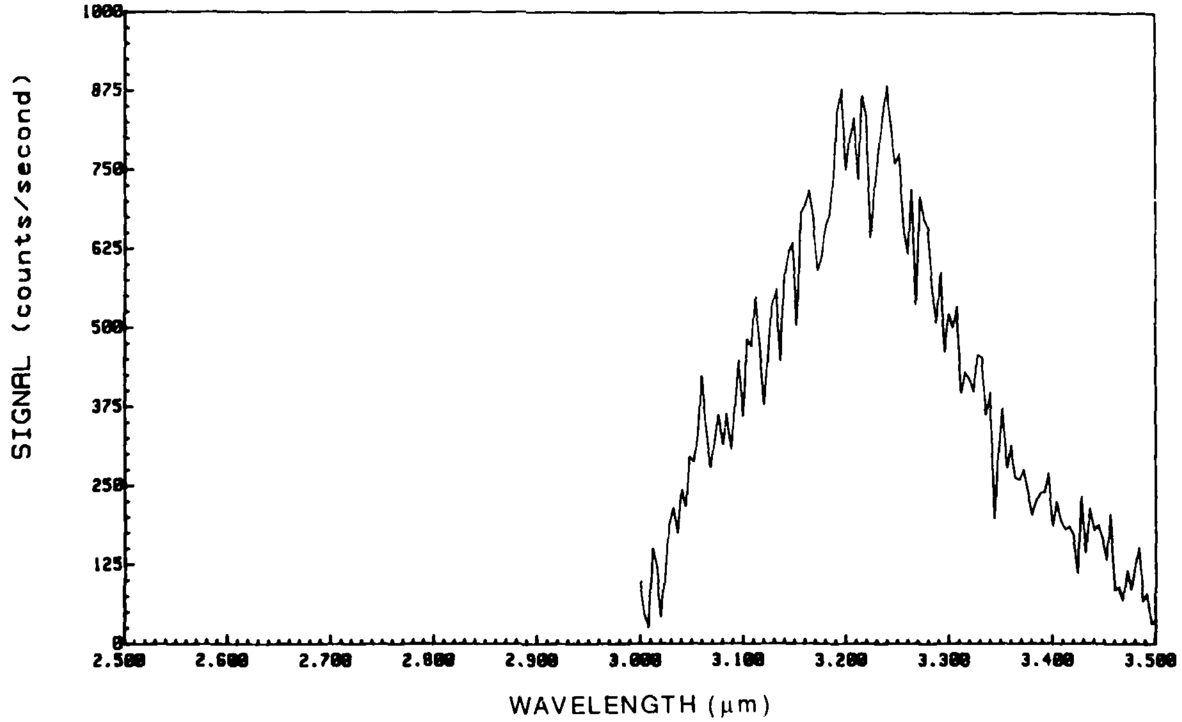

Figure 9. Signal Strength from (Top) a Si:As Photoconductor, vs (Bottom) a Solid State Photomultiplier Detector

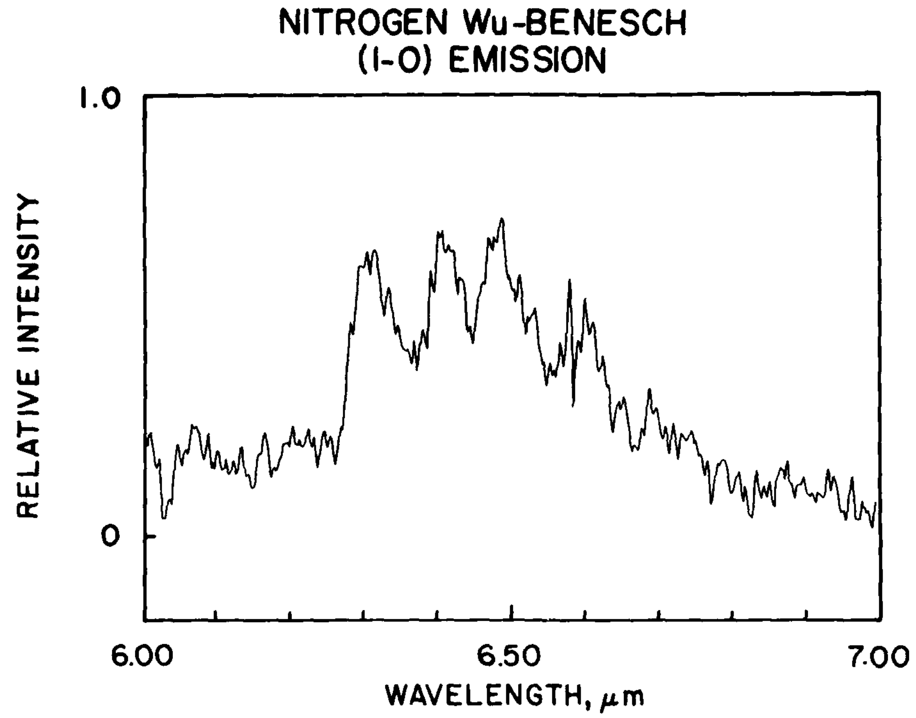

TRADITIONAL Si:As DETECTION

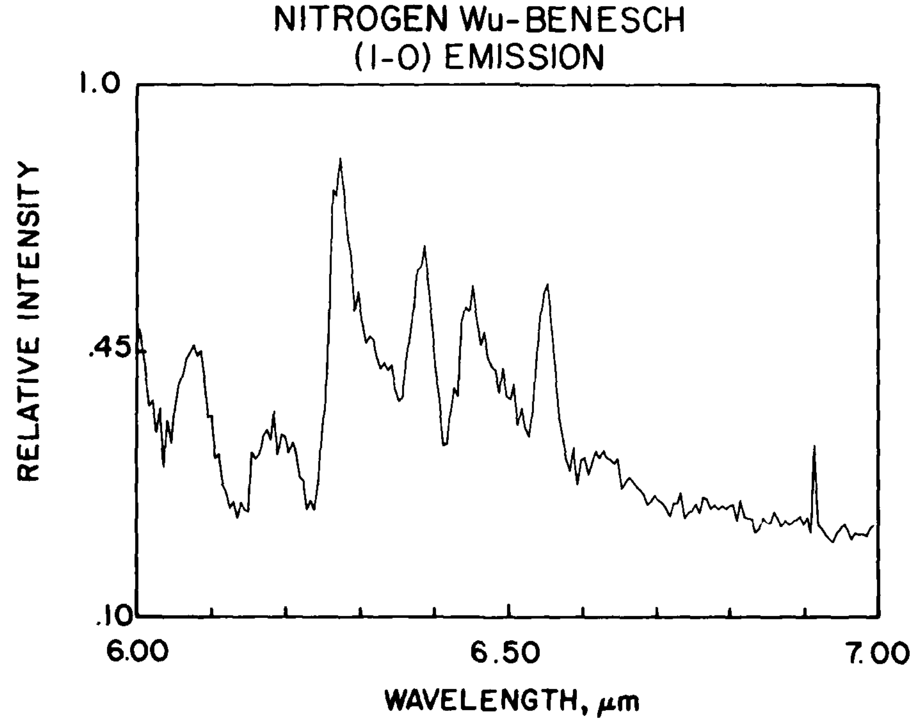

SOLIDSTATE PHOTOMULTIPLIER DETECTION

Figure 10. Relative Signal Strengths from (Top) a Si:As Photoconductor, vs a Solid State Photomultiplier Detector, (Bottom), for a Radiation from Nitrogen Wu-Benesch (1-0) Emission

11 to 12 μm band to search for higher vibrational states and a general survey from 2 to 16 μm to search for previously undetected states of a variety of atmospherically related molecules.

References

1. Petroff, M.D., Stapelbroek, M.G., and Kleinhans, W.A. (19??) Detection of Individual 0.4 - 28 μm Wavelength Photons via Impurity-Impact Ionization in a Solid-State Photomultiplier, *Appl. Phys. Lett.* **51**(6):401.
2. For future spectral comparisons, it should be noted that throughout the SSPM testing in COCHISE only discharges 2 and 4 worked properly, thus reducing the absolute signal level by about a factor of two.
3. Refer to Chapter 2 for a thorough discussion of all aspects of the COCHISE nitric oxide chemistry.

6. Infrared (2 to 8 μm) Fluorescence of the $W^3\Delta_u \rightarrow B^3\Pi_g$ and $W^1\Delta_u \rightarrow a^1\Pi_g$ Systems of Nitrogen

by

M.E. Fraser, W.T. Rawlins, and S.M. Miller

Infrared (2 to 8 μm) fluorescence of the $W\,^3\Delta_u \rightarrow B\,^3\Pi_g$ and $w\,^1\Delta_u \rightarrow a\,^1\Pi_g$ systems of nitrogen

Mark E. Fraser and Wilson T. Rawlins
Physical Sciences Inc., Research Park, Andover, Massachusetts 01810
Steven M. Miller
Infrared Technology Division, Air Force Geophysics Laboratory, Hanscom AFB, Massachusetts 01731

(Received 20 July 1987; accepted 23 September 1987)

Eleven transitions in the $W\,^3\Delta_u \rightarrow B\,^3\Pi_g$ (*W–B*) and $w\,^1\Delta_u \rightarrow a\,^1\Pi_g$ (*w–a*) systems of nitrogen have been observed in the infrared including the previously unobserved (1,0) and (2,1) *W–B* features at 6.5 and 7.65 μm, respectively. The fluorescence spectra were observed in a cryogenic reaction chamber at pressures of ~3 mTorr (0.4 Pa), following expansion of flowing N_2/Ar mixtures excited by microwave discharges at ~1 Torr. Einstein coefficients for the *w–a* system, calculated using a published transition moment function, predict the radiative lifetimes of the lower vibrational levels of the $w\,^1\Delta_u$ state to be a factor of 3 longer than earlier estimates. Using a spectral simulation and linear least-squares fitting technique, the published *W–B* and calculated *w–a* branching ratios are verified for the transitions observed across the 2 to 4 μm region. The observed vibrational/electronic state distributions are not characteristic of those expected for direct excitation, but appear to result from extensive collisional coupling among excited states of nitrogen which occurs in the high pressure region prior to expansion.

INTRODUCTION

There are several nitrogen electronic transitions which give rise to emission in the 2 to 8 μm infrared region.[1-9] These systems include $W\,^3\Delta_u \leftrightarrow B\,^3\Pi_g$, $w\,^1\Delta_u \rightarrow a\,^1\Pi_g$, and $a\,^1\Pi_g \rightarrow a'\,^1\Sigma_u^-$. Emissions from the $B'\,^3\Sigma_u^- \rightarrow B\,^3\Pi_g$ and $B\,^3\Pi_g \rightarrow A\,^3\Sigma_u^+$ systems also extend into this spectral region. These systems are commonly observed in nitrogen discharge plasmas and several have been indicated as potential infrared auroral transitions.[10] The detailed excited state populations and vibrational distributions responsible for the observed fluorescence provide information on mechanisms of excitation and energy disposal in excited nitrogen. Interpretation of auroral or plasma spectra for these band systems, however, requires prior verification of the transition branching ratios. We report here observation of emission from several vibrational levels in $W\,^3\Delta_u \rightarrow B\,^3\Pi_g$ ($v' = 1$–5) and in $w\,^1\Delta_u \rightarrow a\,^1\Pi_g$ ($v' = 0$–2), and verification of their radiative branching ratios across the 2 to 4 μm region.

EXPERIMENTS

These experiments were performed in the COCHISE (cold chemiexcitation infrared stimulation experiment) cryogenic discharge afterglow apparatus, which is described in detail elsewhere.[11] Excitation of nitrogen electronic states is produced in four parallel microwave discharges (2450 MHz, 50 W) of flowing N_2/Ar mixtures at ~1 Torr total pressure. A diagram of the reaction chamber is shown in Fig. 1. After exiting the discharge tubes the gas expands into a low pressure (~3 mTorr), cryogenically pumped chamber (~20 K) where the molecules enter the collimated field of view of a scanning monochromator/infrared detector assembly. Residence times in the discharge tubes are on the order of 3 to 5 ms; an average time of flight of 500 ± 100 μs is required for the gases to exit the discharge tubes and enter the field of view. Opposing flows of argon are used to create a quasistatic interaction region along the centerline of the field of view, resulting in partial rethermalization of the expansion-cooled rotational distributions. The gas residence time in the field of view is ~0.3 ms. Gaseous helium refrigerant maintains all internal temperatures at 20 K, excepting the gas lines and optics which are held at 80 and 40 K, respectively.

The infrared emissions are observed by a cryogenic 0.5 m Czerny–Turner monochromator equipped with a liquid-helium-cooled arsenic doped silicon detector and a grating blazed at 3 μm. The discharges are chopped with a 23 Hz, 50% duty cycle square wave, and data collection is performed with a computer-interfaced lock-in amplifier. Data

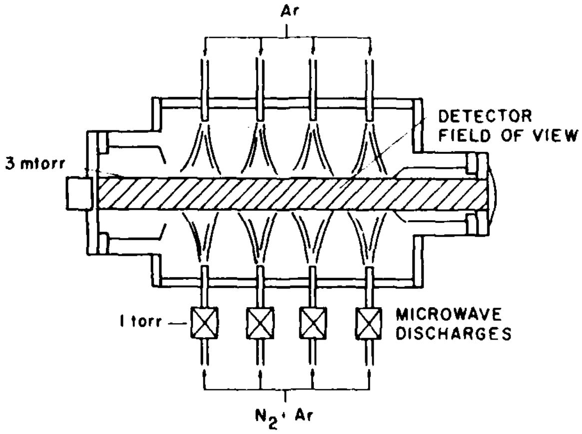

FIG. 1. Diagram of the COCHISE reaction chamber. The physical dimensions of the cell are 0.6 m in length and 0.4 m in diameter.

0021-9606/88/020538-07$02.10

over the 2 to 4 μm region were taken with the phase shift between reference and signal waveforms locked in at the 3.3 or 3.6 μm features. The phase shift for the 4 to 8 μm spectra was locked at the emissions at 6.5 or 7.5 μm.

The absolute uncertainty in the wavelengths (due to monochromator drive error) of the spectral scans is ± 0.003 μm. The data were corrected for instrument responsivity using blackbody calibration spectra taken in the 300 to 370 K range. The uncertainty in the accuracy of the blackbody temperature is ± 3 K, which results in a relative uncertainty of $\pm 20\%$ in the measured 2.5/5.0 μm intensity ratios. This method of calibration has been verified in studies of the fundamental/overtone ratios for NO(v) vibraluminescence.[12]

Spectra were taken for N_2/Ar mixtures with N_2 mole fractions of 0.006 to 0.12, with a mass-balanced counterflow of argon added to thermalize the observed emissions. Spectra were also taken without nitrogen to identify the background ArI Rydberg emission.[13] The data were taken typically at a resolution of 0.013 μm in the 2 to 4 μm region and 0.040 μm for the 4 to 8 μm region.

SPECTRAL ANALYSIS

The interpretation of the 2 to 4 μm discharged nitrogen data is complicated due to the coincidence of several of the $W\,^3\Delta_u \rightarrow B\,^3\Pi_g$ (W–B) and $w\,^1\Delta_u \rightarrow a\,^1\Pi_g$ (w–a) features. The transitions that are not distinguishable from each other at a resolution of 0.013 μm include the W–B (4,1) and w–a (2,1) at 2.4 μm, the W–B (3,1) and w–a (0,0) at 3.6 μm, and the W–B (4,2) and w–a (2,2) at 4.0 μm. These overlapping bands cannot be identified or quantified by inspection, therefore a spectral fitting technique is required.

The spectral analysis technique used for these studies has also been successfully applied to the analysis of NO($A\,^2\Sigma$),[14] N_2 electronic emission,[15] and IF($B\,^3\Pi_{0^+}$).[16] The synthetic spectra are generated by a computer code based upon the work of Kovacs[17] and implemented through major modification of a program written by Whiting *et al.*[18,19] The program considers singlet–singlet, doublet–doublet, and triplet–triplet dipole transitions for diatomic molecules in the optically thin limit. Line-by-line transition frequencies are computed from energy eigenvalues determined by exact solution of the Schrödinger equation, where the matrix elements of the upper and lower state Hamiltonians are specified from tabulated spectroscopic constants. Following well-established procedures,[17,20] the eigenfunctions of the states are described as linear combinations of eigenfunctions of hypothetical pure Hund's case (a) eigenstates. The transition amplitudes are given by the transformation of the dipole moment function between the upper and lower states.[17,20] The computed infinite resolution emission spectrum is convolved with the instrument scan function (in this case, a symmetric triangle with full width at half-maximum as the spectral resolution) to create basis sets for each vibrational level which are then fit to the experimental spectrum using a linear least squares method. The fitting procedure yields a determination of the product of the upper state number density and the spontaneous emission coefficient of the transition. Rotational distributions are treated by simple Boltzmann expressions, so that band-integrated vibrational state number densities and transition probabilities may be used.

Lambda doubling, which is on the order of 1 cm^{-1} for the $W\,^3\Delta_u \rightarrow B\,^3\Pi_g$ system,[21] is not treated in this analysis. The $W\,^3\Delta_u \rightarrow B\,^3\Pi_g$ emission system totals 27 branches without lambda doubling. Furthermore, the coupling for the W state is close to Hund's case (b) while the B state coupling exhibits transition from (a) to (b) at higher rotational levels. Despite these complexities, comparison of the line positions of the synthesized $W\,^3\Delta_u \rightarrow B\,^3\Pi_g$ (2,0) feature to published high resolution data[21] indicates the positions of the principal lines are reproduced to within 1 cm^{-1}. Similarly, the agreement between the synthesized and high resolution[22] $w\,^1\Delta_u \rightarrow a\,^1\Pi_g$ (0,0) transition is excellent, $\leqslant 0.1$ cm^{-1}. Since most of the data presented here have been taken and fit to a resolution of 0.013 μm (12 cm^{-1} at 3.3 μm), deficiencies in the spectral synthesis program on the order of 1 cm^{-1} or less are too small to be observed. The spectroscopic data sources for the considered N_2 states were Huber and Herzberg[23] and Roux *et al.*[22] for $w\,^1\Delta_u$ and $a\,^1\Pi_g$, Cerny *et al.*[24] for $W\,^3\Delta_u$ and Effantin *et al.*[25] for $B\,^3\Pi_g$.

Each vibrational transition is treated as an independent basis function in a linear least-squares fit to the total spectrum to determine the band-integrated intensities, $N_{v'}A_{v'v''}$. To determine the excited state number densities, accurate values for $A_{v'v''}$ are needed. The transition probabilities used for the W–B system are the *ab initio* values calculated by Werner *et al.*[26] and shown in Table I. These values are more than a factor of 2 smaller than the empirical estimates of Covey, Saum, and Benesch,[27] but exhibit essentially the same branching ratios; we prefer the results of Werner *et al.*[26] owing to their use of a more accurate transition moment function. There are no published transition probabilities for the $w\,^1\Delta_u \rightarrow a\,^1\Pi_g$ system. Consequently, we calculated them using the Franck–Condon and r-centroid data tabulated in Lofthus and Krupenie[28] and the transition moment function determined by Yeager and McKoy.[29] The results are shown in Table II. The radiative lifetimes for the first five vibrational levels are predicted to be 1500, 830, 470, 430, and 360 μs, respectively, at variance with earlier estimates[28] of 500 to 100 μs. These radiative lifetimes are more than an order of magnitude longer than those used by Cartwright[10] for auroral modeling predictions.

Using the spectral synthesis linear least-squares fitting technique described above, 11 bands from the $N_2(W\,^3\Delta_u \rightarrow B\,^3\Pi_g)$ and $N_2(w\,^1\Delta_u \rightarrow a\,^1\Pi_g)$ systems have

TABLE I. Einstein coefficients for the $W\,^3\Delta_u \rightarrow B\,^3\Pi_g$ transitions (in 10^3 s^{-1}) as calculated by Werner *et al.* (Ref. 26).

$v' \setminus v''$	0	1	2	3	4	5	6
0	0.000						
1	0.221						
2	0.735	0.084					
3	0.868	0.764	0.014				
4	0.649	1.525	0.457	0.000			
5	0.377	1.619	1.554	0.183	0.000		
6	0.187	1.222	2.311	1.157	0.043	0.000	

TABLE II. Computed Einstein coefficients for the $w\,^1\Delta_u \rightarrow a\,^1\Pi_g$ transitions (in $10^3\ \mathrm{s}^{-1}$).

$v'\backslash v''$	0	1	2	3	4	5	6
0	0.636	0.013					
1	0.979	0.206	0.013				
2	0.660	1.03	0.444	0.010			
3	0.308	1.199	0.767	0.002	0.006		
4	0.117	0.797	1.415	0.466	0.004	0.004	
5	0.040	0.394	1.284	1.362	0.237	0.017	0.002
6	0.013	0.164	0.800	1.600	1.13	0.095	0.028

been indentified. Inclusion of the $B\,^3\Pi_g \rightarrow A\,^3\Sigma_u^+$, $B'\,^3\Sigma_u^- \rightarrow B\,^3\Pi_g$, $a\,^1\Pi_g \rightarrow a'\,^1\Sigma_u^-$, and $B\,^3\Pi_g \rightarrow W\,^3\Delta_u$ systems of nitrogen in the fits indicated no evidence of emission from these systems in the observed spectra. This is consistent with the rapid radiative decay expected for the $N_2(B,B',a)$ states in transit from the discharge exits to the field of view.

The rotational temperatures, T_r, used in the fits were determined empirically by comparison of intensity distributions and branch structures of the data with theoretical spectra. The (2,0) band was used for the *W–B* system with the result $T_r = 100$ K, indicating this emission system is nearly rotationally thermalized. With the rotational temperatures of the *W–B* system fixed at 100 K, simultaneous *W–B* and *w–a* fits were used to determine the rotational temperature for the *w–a* sytem. The optimal T_r was chosen as that which best reproduced the intensity distribution of the first two branches of the 3.6 μm emission feature which corresponds, in large part, to the *R* and *Q* branches of the *w–a* (0,0) emission. The result for *w–a* was $T_r = 300$ K, although 200 K produced better fits in some data taken at low nitrogen mole fraction. The deviation in the calculated populations incurred using *w–a* basis sets with $T_r = 200$ K vs $T_r = 300$ K is < 10% in the *w–a* populations and < 5% in the *W–B* populations.

RESULTS

Identification of the observed spectral features was facilitated by a variation of the relative *W–B* and *w–a* intensities as a function of nitrogen mole fraction. At low nitrogen mole fraction the *w–a* features are more prominent allowing unambiguous identification. Under these conditions the dominant spectral feature at 3.6 μm is the (0,0) *w–a* transition. Figure 2 shows the data and best fit to the 3.5 to 3.9 μm region of data obtained at a nitrogen mole fraction of 1.2×10^{-2}. The figure also shows the contributions to the fit from each of the *w–a* and *W–B* basis sets. The best fit was obtained for a *w–a* basis set with $T_r = 200$ K. At higher nitrogen mole fractions the *W–B* features predominate, in particular the (2,0) feature at 3.3 μm. Figure 3 shows data taken at high nitrogen mole fraction and fit to both *W–B* and *w–a* systems over the full 2 to 4 μm region. Six transitions in the *W–B* system are identified, three from the $\Delta v = 3$ series and three from the $\Delta v = 2$ series. The *W–B* (5,3) band at 4.5 μm cannot be distinguished from the noise level, in keeping with its small transition probability relative to that for the (5,2) band (cf. Table I). No *W–B* emission from vibrational levels higher than $v' = 5$ is observed under any nitrogen mole fraction condition. Five transitions in the *w–a* system are also identified, the (1,0) and (2,1) bands in the $\Delta v = 1$ sequence and the (0,0), (1,1), and (2,2) bands in the $\Delta v = 0$ sequence. No clearly identifiable emission from $v' = 3$ in the *w–a* system is observed. All additional features in Fig. 3 are due to ArI Rydberg emission, which appears as scattered light from the discharges. We have reported on these emissions previously.[13]

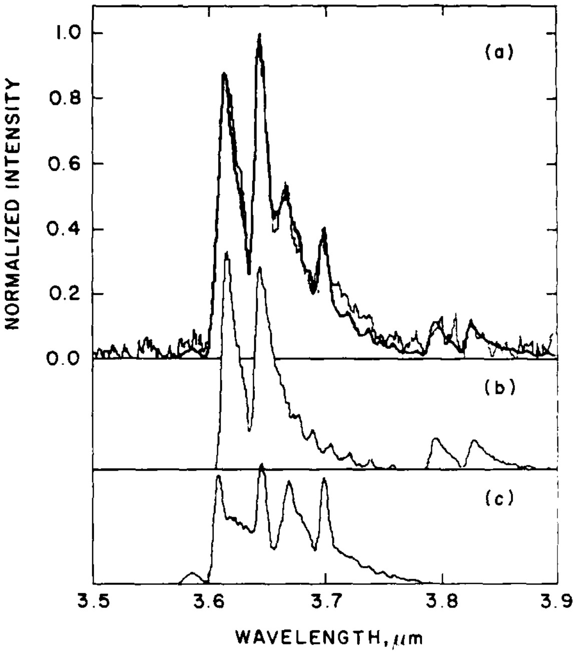

FIG. 2. Data (light line) and best fit (dark line) (a) to the (0,0) and (1,1) $N_2(w\,^1\Delta_u \rightarrow a\,^1\Pi_g)$ and (3,1) $N_2(W\,^3\Delta_u \rightarrow B\,^3\Pi_g)$ emission systems at rotational temperatures of 200 and 100 K, respectively. The spectrum was obtained at a discharge nitrogen mole fraction of 1.2×10^{-2} and a resolution of 0.0067 μm. The maximum intensity of the spectrum is 3.45×10^{-7} W cm^{-2} sr^{-1} μm^{-1}. The *w–a* and *W–B* basis sets which comprise the best fit in (a) are shown in (b) and (c), respectively.

Spectra taken of discharged nitrogen in the 6 to 8 μm region also show evidence of *W–B* features. Fits to the data provide unambiguous identification of the previously unobserved (1,0) and (2,1) transitions at 6.2 to 6.8 μm and 7.4 to 8 μm, respectively. Figures 4(a) and 4(b) show data and fit to the *W–B* (1,0) and (2,1) *W–B* features, respectively. The *W–B* (2,1) feature is the only emission observed with this apparatus in the 7 to 8 μm wavelength range.

Figure 5 shows the detemined populations in the $v' = 3$ level of the $W\,^3\Delta_u$ state and $v' = 0$ of the $w\,^1\Delta_u$ state as a function of nitrogen mole fraction. The *W–B* and *w–a* emission systems coexist in the effluent of a microwave discharge under all nitrogen mole fraction conditions. Both systems exhibit similar kinetic behavior except at N_2 mole fractions in excess of 10%. Under these conditions the $w\,^1\Delta_u$ ($v' = 0$) population drops off more rapidly than the $W\,^3\Delta_u$ ($v' = 3$). The *W–B* (2,0) feature exhibits dissimilar and variable temporal behavior as measured by phasing relative to the other *W–B*, *w–a* emission features as a function of nitrogen mole

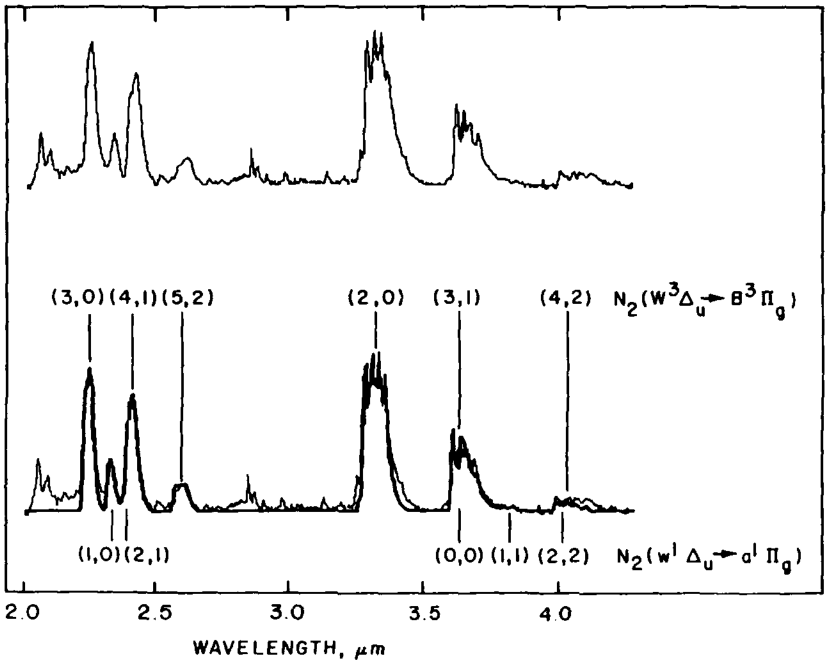

FIG. 3. Data (light line, shown with the best fit and separately above) and best fit (dark line) to the indicated $N_2(w\,^1\Delta_u \rightarrow a\,^1\Pi_g)$ and $N_2(W\,^3\Delta_u \rightarrow B\,^3\Pi_g)$ emission systems at rotational temperatures of 300 and 100 K, respectively, and at a spectral resolution of 0.013 μm. The spectrum was obtained at a discharge nitrogen mole fraction of 9.1×10^{-2}. The maximum intensity of the spectrum is 3.4×10^{-7} W cm^{-2} sr^{-1} μm^{-1}. The observed features not accounted by the fit are due to ArI Rydberg emission (Ref. 13).

fraction. The *W–B* (2,0) feature is in phase only at the higher nitrogen mole fractions. At the lower N_2 mole fractions, the phase lag of the (2,0) band is on the order of π (22 ms), corresponding to cessation of the discharge pulse. Since the radiative lifetime of the $W\,^3\Delta_u$ ($v' = 2$) level is short (1200 μs) compared to the modulation frequency (23 Hz), and is comparable to the radiative lifetimes of other observed states which exhibit no phase lags, radiative decay effects have been ruled out as the cause. Investigations of the (1,0) and (2,1) *W–B* bands also indicate variable phasing between these emissions. These two emissions are in phase with each other only at low nitrogen mole fractions. No phase shift effects are encountered with *w–a* emissions or with the *W–B* ($v' \geqslant 3$) bands.

The relative population distributions for the vibrational levels of the $W\,^3\Delta_u$ and $w\,^1\Delta_u$ states are shown in Figs. 6(a) and 6(b), respectively. Also shown in Figs. 6(a) and 6(b) are the distributions backcorrected for the 500 μs radiative decay which is incurred during transit from the end of the discharge tubes to the field of view. In the absence of collisional feed sources in the reaction cell, the corrected distributions are those which would exist at the discharge exits. Both $W\,^3\Delta_u$ and $w\,^1\Delta_u$ states exhibit strongly relaxed distributions, with the maximum population occurring at the lowest vibrational levels. Also shown in Figs. 6(a) and 6(b) are the determined upper limit relative populations for $W\,^3\Delta_u$ ($v' = 6$) and $w\,^1\Delta_u$ ($v' = 3$). The value for $W\,^3\Delta_u$ ($v' = 6$) corresponds to the noise level of the data. The *w–a* (3,2) band corresponds to a distinguishable feature which lies at 2.5 μm, but the observed intensity appears to be principally attributable to a coincident ArI Rydberg line.[13] [The *w–a* (3,3) band at 4.2 μm is not observable owing to its very small relative transition probability (cf. Table II).]

Emission from $v' > 1$ levels in the $N_2(a\,^1\Pi_g \rightarrow a'\,^1\Sigma_u^-)$ system also occurs in the 2 to 4 μm region. Owing to the short radiative lifetime of the $a\,^1\Pi_g$ state (~ 100 μs), observation of this band system in the field of view due to discharge excitation is unlikely. Fits to the data of the *a–a'*

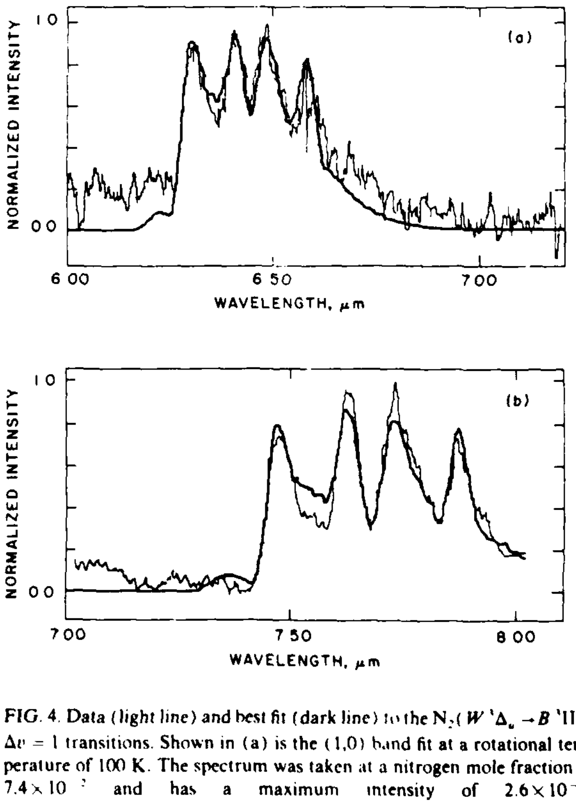

FIG. 4. Data (light line) and best fit (dark line) to the $N_2(W\,^3\Delta_u \rightarrow B\,^3\Pi_g)$ $\Delta v = 1$ transitions. Shown in (a) is the (1,0) band fit at a rotational temperature of 100 K. The spectrum was taken at a nitrogen mole fraction of 7.4×10^{-2} and has a maximum intensity of 2.6×10^{-10} W cm^{-2} sr^{-1} μm^{-1}. Shown in (b) is the (2,1) band fit at a rotational temperature of 120 K. The spectrum was taken at a nitrogen mole fraction of 1.2×10^{-1} and has a maximum intensity of 3.6×10^{-10} W cm^{-2} sr^{-1} μm^{-1}.

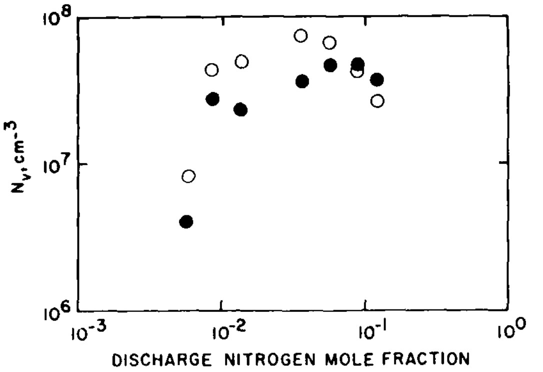

FIG. 5. Determined populations for $W\,^3\Delta_u$ ($v' = 3$) (●) and $w\,^1\Delta_u$ ($v' = 0$) (○) vs discharge nitrogen mole fraction. Absolute number densities pertain to the 3 mTorr interaction region in the center of the reaction volume.

($v' = 1$–3) features indicate none of these features are distinguishable from the noise level in the data, with determined upper limit populations of $\leqslant 2 \times 10^6\ cm^{-3}$. This is consistent with the anticipated production of $N_2(a,v' \geqslant 1)$ in the field of view by the observed *w–a* radiative cascade. Similarly, the absence of identifiable emission in the $B'\,^3\Sigma_u^- \rightarrow B\,^3\Pi_g$ system gives an upper bound of $\sim 10^6\ cm^{-3}$ for the $N_2(B')$ number density in the field of view.

DISCUSSION

In comparison of the data and the predictions of the spectral synthesis code, we observe only minor disagreements in spectral position and branch intensity distribution. Discrepancies in the reproduction of the branch head positions are within the spectrometer drive error of 0.003 μm. Failure to exactly match the relative branch intensities within a given band may be partially due to non-Boltzmann rotational temperature distributions. Assumption of a single Boltzmann distribution may also cause discrepancies in the detailed reproduction of the relative branch intensities. The magnitude of these descrepancies is small, and at low resolution ($\delta\lambda > 0.013\ \mu m$) the band shapes and integrated intensities are relatively well reproduced. Because the *w–a* and *W–B* systems can be discriminated at different nitrogen mole fractions, the fits confirm the (3,0)/(3,1), (4,1)/(4,2) *W–B* and (1,0)/(1,1), (2,1)/(2,2) *w–a* branching ratios, obtained from Tables I and II, to ± 20%.

The observed vibrational and electronic state distributions are quite different from those one might expect for discharge-flow excitation under the conditions of these expriments. Typically, at low N_2 mole fractions, the residence time in the active discharge plasma (~ 2800 cm/s at 1.4 Torr in each tube) is 3 to 5 ms, with the discharge region extending essentially to the end of the tube. For N_2 mole fractions near 0.1, the discharge region "shrinks" to about 2 ms, allowing 1 to 2 ms of flow time downstream of the dosed volume prior to expansion into the observation volume. For typical conditions of this type of discharge ($[e^-] \sim 10^{11}\ cm^{-3}$, $E/N \sim 10^{-16}\ V\ cm^2$, characteristic electron energy ~ 6 to 8 eV), we expect the principal excitation mechanism for $N_2(W,w)$ to be via direct electron impact on ground state nitrogen. This production term would be balanced by losses due to electron impact processes (dissociation, superelastic deexcitation), collisional deactivation, radiative loss, and flow out of the discharge.[30]

For the discharge conditions used in these studies, the dominant loss terms are dissociation, surface quenching, and flow, which should not affect the vibrational/electronic state distribution formed in the excitation process. Since electron impact excitation gives rise to Franck–Condon vibrational distributions relative to ground state nitrogen, we would expect to observe significant fluorescence from higher vibrational levels ($v' = 4$–9) of the *W* and *w* states, with a preponderance of the triplet over the singlet, qualitatively similar to the state distributions predicted by Cartwright[10] for an aurora. In contrast, however, we observe relatively "cold" vibrational distributions with roughly equal populations in the triplet and singlet states, despite their 1.5 eV energy difference. These observations suggest that there are rapid collisional "scrambling" reactions occurring in the discharge which can significantly alter the excited state population distributions. A possible example of such a reaction

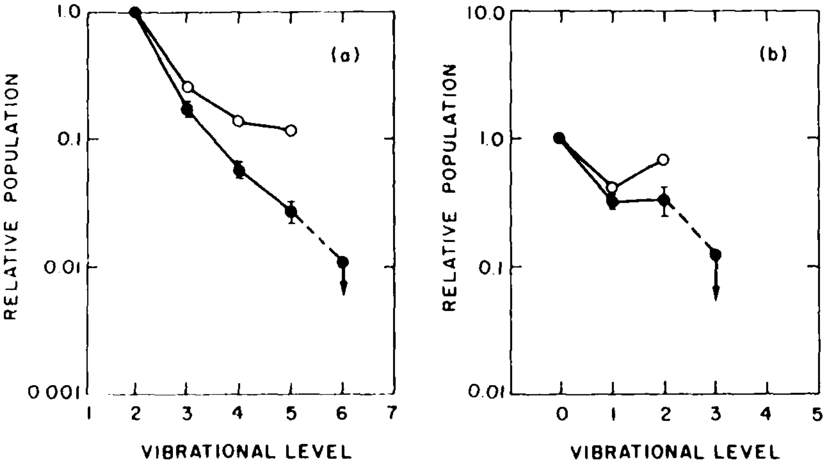

FIG. 6. (a) Relative vibrational population distribution for $W\,^3\Delta_u$ at a discharge nitrogen mole fraction of 1.2×10^{-1} (●) normalized to $v' = 2$. Also shown are the data back-corrected for a 500 μs radiative decay (○). (b) Relative vibrational population distribution for $w\,^1\Delta_u$ at a discharge nitrogen mole fraction of 1.2×10^{-1} (●) normalized to $v' = 0$. Also shown are the data backcorrected for a 500 μs radiative decay (○).

would be the enhancement of the lower levels of the W state by fast reaction of nitrogen atoms with singlet metastables:

$$N(^4S) + N_2(a'\,^1\Sigma_u^-) \to N_2(W\,^3\Delta_u, v \leqslant 5) + N(^4S).$$

Similar rapid intersystem crossings may occur through collisions of excited N_2^* with N_2 and Ar. Indeed, previous observations of fluorescence from $N_2(B\,^3\Pi_g)$ excited by an electron beam gave evidence of strong collisional coupling between the neighboring vibrational levels of the B and W states.[31]

The excitation mechanism for $N_2(w)$ is less apparent owing to its high energy relative to the neighboring states of N_2^*. The nonthermal rotational distributions we observe for the $w \to a$ transitions suggest formation of $N_2(w)$ by a reactive collision, although direct energy transfer to N_2 cannot be ruled out. In the latter case, however, the precursor states would have to be medium to high vibrational levels of one or more of the neighboring N_2^* electronic states. An intriguing possibility is excitation of $N_2(w)$ via metastable–metastable interactions, e.g., $N_2^* + N_2^*$ or $N^* + N_2^*$; precursor number densities on the order of 10^{12} cm^{-3} (in the active discharge at 10^{17} cm^{-3} total number density) and a near gas-kinetic rate coefficient would be sufficient to account for the quantity of $N_2(w)$ observed in the field of view.

The large phase lag between $N_2(W, v' = 1,2)$ and the remainder of the excited N_2 states is difficult to understand. Evidently these states are not formed as rapidly (and/or are destroyed more rapidly) in the active discharge as $W(v' = 3\text{–}5)$ and $w(v' = 0\text{–}2)$, but are rapidly formed by collisional energy transfer following cessation of the discharge. This could occur through a relatively inefficient process such as energy transfer with N_2, such that at lower N_2 mole fractions a substantial amount of $N_2(W, v = 1,2)$ cannot be formed until after the precursor and $N_2(W)$ loss processes in the active discharge are terminated. The precursor may then be a sufficiently energetic afterglow species such as $N_2(A, v \geqslant 9)$ or $N_2(X, v \geqslant 33)$.

The collisional processes for energy redistribution among the states of N_2^* implied by these data must occur with relatively high efficiency, with collision efficiences ranging from near unity for atom–metastable and metastable–metastable reactions to perhaps 1% for collisions with $N_2(X, v = 0)$. Such processes will clearly affect the energy flow in N_2 plasma systems at pressures of a few Torr or greater. Furthermore, some of the collisional energy shuffling reactions may be fast enough to affect N_2^* state distributions in the auroral upper atmosphere, particularly in the 80 to 100 km altitude regime where collisional quenching competes with radiative deactivation of excited species. This possibility could be tested by observations of altitude-dependent $N_2(W, w)$ fluorescence in a strong aurora and comparison of the observed vibrational/electronic distributions with those expected for direct auroral excitation.

CONCLUSIONS

We have observed infrared (2 to 8 μm) fluorescence from nitrogen in the $\Delta v = 0$ and 1 progressions of the $w\,^1\Delta_u \to a\,^1\Pi_g$ band system and in the $\Delta v = 1, 2,$ and 3 progressions of the $W\,^3\Delta_u \to B\,^3\Pi_g$ band system resulting from microwave discharge excitation of N_2/Ar mixtures. Using a spectral synthesis procedure with literature values for the spectroscopic constants provides adequate description of the observed spectra for spectral resolutions with full width at half-maximum greater than or equal to 0.007 μm (6.4 cm^{-1} at 3.3 μm). Experimental observations of relative intensities of different transitions arising from a common upper state support the theoretical predictions for the dipole moment functions of Werner[26] for W–B and Yeager and McKoy[29] for the w–a system. We report w–a Einstein coefficients calculated from the data given in Ref. 29; these values differ markedly from those used by Cartwright[10] in his estimation of the relative $N_2(w\,^1\Delta_u)$ auroral number densities. Recalculation with the new w–a Einstein coefficients leads to an increase in the predicted high-altitude $N_2(w\,^1\Delta_u)$ relative number density by an order of magnitude.

The identification of the (1,0) and (2,1) W–B bands represents the first time these bands have been experimentally observed. The observed W–B and w–a vibrational distributions provide evidence of complex collisional coupling of the discharge-excited states of N_2, in particular a collisional feed of $W\,^3\Delta_u$. More detailed time-resolved kinetic studies will be required to resolve this issue.

ACKNOWLEDGMENTS

The authors would like to acknowledge advice provided by W. J. Marinelli, L. G. Piper, B. D. Green, and W. A. M. Blumberg, and assistance by H. C. Murphy, M. A. DeFaccio, and M. Clawson. The spectral generation code was developed at PSI in large part by P. F. Lewis. This work was performed under Contract F19628-85-C-0032 with the Air Force Geophysics Laboratory, and was sponsored by the U. S. Air Force Office of Scientific Research under Task 2310G4 and by the Defense Nuclear Agency under Project 5A, Task 5A, Work Unit 115.

[1] R. A. McFarlane, IEEE J. Quantum Electron. **QE-2**, 229 (1966).
[2] H. L. Wu and W. Benesch, Phys. Rev. **172**, 31 (1968).
[3] W. M. Benesch and K. A. Saum, J. Quant. Spectrosc. Radiat. Transfer **12**, 1129 (1972).
[4] R. A. McFarlane, Phys. Rev. **140**, A1070 (1965).
[5] R. A. McFarlane, Phys. Rev. **146**, 37 (1966).
[6] K. A. Saum and W. M. Benesch, Appl. Opt. **9**, 195 (1975).
[7] E. M. Gartner and B. A. Thrush, Proc. R. Soc. London Ser. A **346**, 103 (1975).
[8] H. Sakai, P. Hansen, M. Esplin, R. Johansson, M. Peltola, and J. Strong, Appl. Opt. **21**, 228 (1982).
[9] W. M. Benesch, J. Chem. Phys. **78**, 2978 (1983)
[10] D. Cartwright, J. Geophys. Res. **83**, 517 (1978).
[11] W. T. Rawlins, H. C. Murphy, G. E. Caledonia, J. P. Kennealy, F. X. Robert, A. Corman, and R. A. Armstrong, Appl. Opt. **23**, 3316 (1984).
[12] W. T. Rawlins, M. E. Fraser, and S. M. Miller (in preparation).
[13] W. T. Rawlins, A. Gelb, and R. A. Armstrong, J. Chem. Phys. **82**, 681 (1985).
[14] L. G. Piper and L. M. Cowles, J. Chem. Phys. **85**, 2419 (1986)
[15] L. G. Piper, L. M. Cowles, and W. T. Rawlins, J. Chem. Phys. **85**, 3369 (1986).
[16] L. G. Piper, W. J. Marinelli, W. T. Rawlins, and B. D. Green, J. Chem. Phys. **83**, 5602 (1985).
[17] I. Kovacs, *Rotational Structure in the Spectra of Diatomic Molecules* (Adam Hilger, London, 1969)
[18] J. O. Arnold, E. E. Whiting, and G. C. Lyle, J. Quant. Spectrosc. Radiat. Transfer **9**, 775 (1969).

[19] E. E. Whiting, J. O. Arnold, and G. C. Lyle, NASA TN-D5088, NASA/Ames, Distributed as Cosmic Progam #ARC-10221.

[20] J. T. Hougen, *The Calculation of Rotational Energy Levels and Rotational Line Intensities in Diatomic Molecules*, Natl. Bur. Stand. Monogr. 115 (U. S. GPO, Washington, D.C., 1970).

[21] C. Effantin, J. D'Incan, and R. Bacis, J. Mol. Spectrosc. **76**, 204 (1979).

[22] F. Roux, C. Effantin, and J. D'Incan, J. Mol. Spectrosc. **91**, 238 (1982).

[23] K. P. Huber and G. Herzberg, *Molecular Spectra and Molecular Structure. IV. Constants of Diatomic Molecules* (Van Nostrand, New York, 1979).

[24] C. Cerny, F. Roux, C. Effantin, J. D'Incan, and J. Verges, J. Mol. Spectrosc. **81**, 216 (1980).

[25] C. Effantin, C. Amiot, and J. Verges, J. Mol. Spectrosc. **76**, 221 (1979).

[26] H. J. Werner, J. Kalcher, and E. A. Reinsch, J. Chem. Phys. **81**, 2420 (1984).

[27] R. Covey, K. A. Saum, and W. Benesch, J. Opt. Soc. Am. **63**, 592 (1973).

[28] A. Lofthus and P. H. Krupenie, J. Phys. Chem. Ref. Data **6**, 117 (1977).

[29] D. L. Yeager and V. McKoy, J. Chem. Phys. **67**, 2473 (1977).

[30] G. E. Caledonia, S. J. Davis, B. D. Green, L. G. Piper, W. T. Rawlins, G. A. Simons, and G. Weyl, Analysis of Metastable State Production and Energy Transfer, AFWAL-TR-86-2078, Air Force Wright Aeronautical Laboratories, Wright Patterson AFB, OH 45433-6563.

[31] B. D. Green, W. J. Marinelli, L. G. Piper, and W. A. M. Blumberg (in preparation).

7. Dynamics of Vibrationally Excited Ozone Formed by Three-Body Recombination: I. Spectroscopy

by

W.T. Rawlins and R.A. Armstrong

Dynamics of vibrationally excited ozone formed by three-body recombination. I. Spectroscopy

W. T. Rawlins
Physical Sciences Inc., Research Park, P. O. Box 3100, Andover, Massachusetts 01810
R. A. Armstrong[a]
Infrared Technology Division, Air Force Geophysics Laboratory, Hanscom AFB, Massachusetts 01731

(Received 19 June 1987; accepted 21 July 1987)

Spectrally resolved infrared fluorescence near 10 μm from vibrationally excited $O_3(\nu_3)$ has been observed in a cryogenic reactor facility at low pressure. The excited $O_3(v)$ is formed principally by three-body recombination of O and O_2 in flowing, microwave-discharged O_2/Ar mixtures at 1 Torr and 80 K. The spectral resolution is sufficient to permit identification and assignment of band centers for up to five quanta of stretching excitation. The observed transition frequencies are consistent with those predicted from a Darling–Dennison perturbation treatment. The spectra, which sample the recombination/deactivation sequence in its early to middle stages, indicate surprisingly little intermode coupling, being predominantly ν_3 in character. There is also evidence of $O_3(v)$ excitation by near-resonant V–V coupling between O_3 and $O_2(v = 2)$. The spectroscopic analysis of the data is described, and considerations for scaling the spontaneous transition probabilities with vibrational level are discussed.

I. INTRODUCTION

The three-body recombination of atomic and molecular oxygen to form ozone,

$$O + O_2 + M \rightarrow O_3 + M, \qquad (1)$$

has long been a problem of special interest in the study of recombination reactions in polyatomic systems. The large negative temperature coefficient and relatively small room-temperature rate coefficient for this reaction offer intriguing questions which have not yet been answered in terms of reaction rate theory. In addition to its relevance to fundamental reaction rate theory, reaction (1) is a crucial component of the oxygen/ozone photochemical cycle which governs the chemistry of the Earth's atmosphere.

The presence of recombined vibrationally excited ozone $O_3(v)$ in the upper atmosphere is a matter of considerable interest. A significant fraction of vibrationally excited molecules can lead to a red shift in the Hartley continuum ultraviolet absorption spectrum, resulting in increased solar photodissociation of atmospheric ozone. In addition, $O_3(v)$ may be an important energy carrier in the upper atmosphere, and could exhibit enhanced reactivity over vibrationally cold O_3. At high altitudes (90 ± 20 km), airglow from $O_3(v)$ is one of the dominant sources of infrared radiation in the upper atmosphere, its variations in intensity and spectral distribution reflecting the complex interplay of the O_2/O_3 photochemical cycle.

Direct observation of $O_3(v)$ infrared chemiluminescence from reaction (1) is difficult owing to the need to make high-sensitivity emission measurements at relatively long wavelengths (approximately 10 μm for the ν_3 band, the strongest of the O_3 bands—see Table I). The first such measurements were reported by von Rosenberg and Trainor[1-3] in an excellent series of flash photolysis studies at room temperature and relatively high pressures ($[M] = 2\text{–}13 \times 10^{18}$ cm^{-3}). However, this work involved only bandpass observations of the infrared emissions, and the extent of collisional intermode and intramode coupling was clearly rather large. The extension of the data base to lower pressures and higher spectral resolution has required rather extreme measures, namely the construction of a totally cryogenic discharge-flow apparatus to eliminate thermal infrared backgrounds.

We have previously reported on spectrally resolved $O_3(v)$ chemiluminescence observed from reaction (1) at ~1 Torr and 80–120 K.[4] These experiments utilized the cryogenic COCHISE (cold chemiexcitation infrared stimulation experiment) reactor/spectrometer facility[5] at the Air Force Geophysics Laboratory, and constitute the first laboratory measurements of spectrally resolved infrared emission from vibrationally excited O_3. We have subsequently applied the spectroscopic and kinetic information developed

TABLE I. Ozone fundamental and overtone vibrational bands.[a]

Band	Band origin (μm)	Einstein coefficient (s^{-1})
ν_1	9.07	0.61
ν_2	14.27	0.23
ν_3	9.60	11.4
$2\nu_3$	4.86	0.35
$3\nu_3$	3.29	0.77
$\nu_1 + \nu_3$	4.74	3.8
$\nu_2 + \nu_3$	5.79	0.12
$\nu_1 + \nu_2$	5.57	0.55
$\nu_1 + \nu_2 + \nu_3$	3.59	0.14

[a] Data from Ref. 11.

---

[a] Present address: Mission Research Corporation, 1 Tara Blvd., Suite 302, Nashua, NH 03062.

5202 J. Chem. Phys. 87 (9), 1 November 1987 0021-9606/87/215202-07$02.10

in that work to the analysis and kinetic interpretation of high altitude $O_3(v)$ infrared emission spectra.[6-8] However, a number of key issues remained unresolved in the laboratory measurements. Principally, the spectroscopic description of the $O_3(v)$ emission was only approximate, and the detailed excited state distributions and number densities could not be determined unambiguously. Furthermore, because of the limited spectral resolution, it was not possible to assess the degree of intermode coupling via spectral contributions from combination states.

We have now acquired an extensive data base for $O_3(v)$ chemiluminescence over a wide range of kinetic effects (i.e., initial O_2/Ar mixing ratio, gas temperature, etc.) and at sufficiently high spectral resolution to permit conclusive spectroscopic analysis. These results support and extend the preliminary conclusions of our earlier work. Studies of the kinetics and mechanisms for $O_3(v)$ formation and destruction are presented in a companion paper[9] (paper II). In the present paper, we present a spectroscopic analysis of the observed $O_3(v)$ fluorescence near 10 μm. The results show that: (1) observed vibrational transition frequencies are close to those predicted from a Darling–Dennison perturbation treatment; (2) little intermode ($\nu_3 \rightarrow \nu_1, \nu_2$) coupling occurs in the early stages of the recombination sequence, with evidence only for weak contributions from the lowest excited ν_1 level; and (3) the possibility of near-resonant V–V energy transfer from molecular O_2 is indicated. The assumptions for scaling the band-integrated Einstein transition probabilities with vibrational quantum number are examined in detail to assess the uncertainties in transforming the observed band intensities into vibrational state number densities.

II. EXPERIMENTAL MEASUREMENTS

The design and operation of the COCHISE facility have been described in detail elsewhere.[5] In brief, the entire radiative environment of the experiment is maintained at a base temperature of approximately 20 K, which effectively eliminates background radiation within the 2–20 μm operating range of the apparatus. The detection system consists of a scanning grating monochromator and a liquid-helium-cooled Si:As detector. Reagent gases are introduced through temperature-controlled feedlines to the reaction cell as shown in Fig. 1. A flowing O_2/Ar mixture at approximately 1 Torr passes through four parallel microwave discharges (2450 MHz, 50 W) prior to expanding into a low-pressure (approximately 3 mTorr), cryogenically pumped interaction volume. A counterflow gas (usually O_2 or Ar) enters the volume from the opposite side to combine with the discharged gas in a stagnation region near the axis of the cell, which coincides with the axis of the cylindrical field of view of the detector. In some cases (e.g., Ref. 10), this interaction consists of a chemical reaction under nearly single-collision conditions. However, in the present experiments, reaction (1) is too slow to occur significantly in the interaction zone at 3 mTorr, and all the O_3 emission observed arises from processes occurring in the discharge sidearms. This is readily confirmed by substituting nonreactive counterflow gases and obtaining no change in the observed emission intensity.

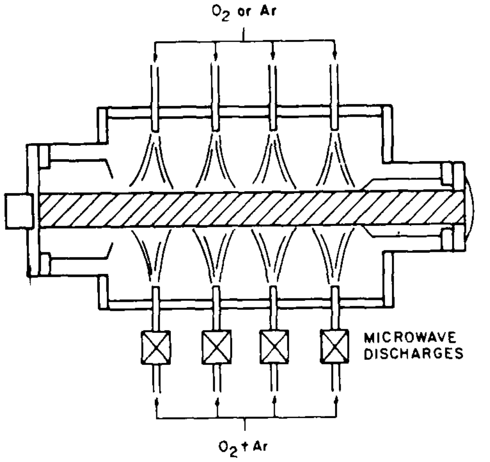

FIG. 1. COCHISE reaction chamber. The cross-hatched region delineates the field of view of the detector (not shown).

In the experiments reported here and in paper II, the reagent gases were introduced at temperatures of 80–150 K; most of the experiments were conducted at 80-90 K. In the discharged gas, the Ar flow rate was held at 640 μmol/s, and the O_2 flow rate was varied from 2.3 to 86 μmol/s (0.3% to 12% O_2). Under these conditions, the residence time in the chemically active portion of the sidearm is approximately 2 ms, and vibrational deactivation of $O_3(v)$ occurs mainly via collisions with O and to a lesser extent with Ar and the surface of the discharge tube.[4,9] The transit time through the expansion regime from the discharge exit to the field of view is ~0.5 ms; the gas residence time in the field of view is ~0.3 ms.

Vibraluminescence from $O_3(v)$ was observed with spectral resolutions of 0.027 to 0.080 μm (2.7 to 8.0 cm^{-1}). Some 45 spectra were obtained with sufficient signal/noise for meaningful analysis. A typical higher-resolution spectrum is shown in Fig. 2, illustrating the readily identifiable (001)-(000) transition centered at 9.6 μm and the characteristic extension to longer wavelengths due to $\Delta v_3 = 1$ fluorescence from higher vibrational states. All spectral data were acquired by an on-line computer and were corrected to radiometric units using blackbody calibrations of the spectral responsivity of the detection system. Detailed spectroscopic analyses were restricted to the data with high spectral resolution, intermediate O_2 mole fraction, and low reagent temperature (~10 spectra). However, the results of the analysis were applied to all the data and were found to provide consistent representations of the observed spectra over the entire range of experimental conditions.

III. METHOD OF SPECTRAL ANALYSIS

The $O_3(v_3)$ spectral data are analyzed by a least-squares spectral fitting procedure[5] originally applied to O_3 spectra in Ref. 4. In this formulation, the transition frequencies and band strengths for the appropriate vibration-rotation transitions are computed or estimated from spectroscopic data in the literature, are convolved with the instrumental scan function, and are fit to the observed spec-

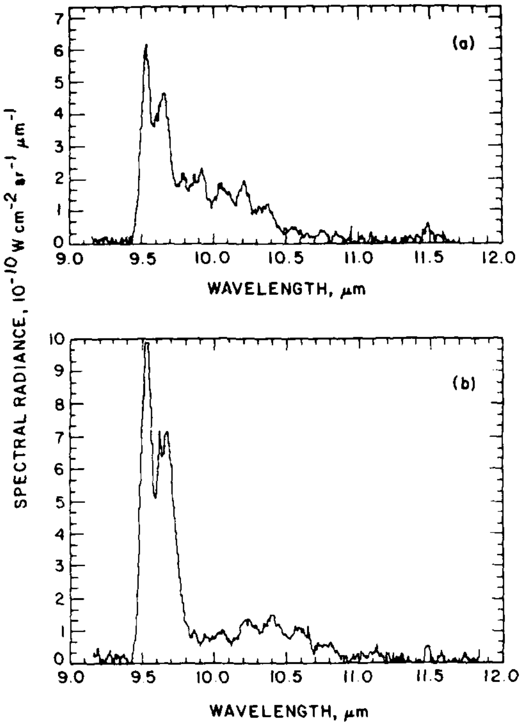

FIG. 2. Observed $O_3(v)$ chemiluminescence spectra, medium resolution. $T = 80$ K, spectral resolution = 0.04 μm. (a) 1.0% O_2 in Ar; (b) 10.0% O_2 in Ar.

tra to determine number densities of $O_3(v)$ in various emitting vibrational states. A complete spectral analysis would treat all $\Delta v_3 = 1$ transitions for all possible (v_1, v_2) combinations; however, such a treatment is extremely difficult owing to the overlap between adjacent emission bands and to the lack of spectroscopic data on highly vibrationally excited ozone (above two quanta). As will be shown in the next section, the spectral resolution of the present data is sufficient to allow clear identification of contributions and band center frequencies for emission from $(00v_3)$ and $(10v_3)$ states with up to five quanta of excitation. This result permits a more definitive representation of the emission spectrum than was possible in the previous work.

Detailed information on the rotational line positions and strengths of the (001)–(000), (002)–(001), (101)–(100), and (011)–(010) transitions is available from the absorption line parameter compilation of the Air Force Geophysics Laboratory[11]; these data are collected from the results of many recent high resolution absorption measurements.[12-15] To describe the band shapes for $\Delta v_3 = 1$ emission from higher-lying vibrational states, it is necessary to estimate the upper state emission band centers $\tilde{\nu}_0(v_1v_2v_3)$ from some description of the anharmonicity of the molecule. In our previous work,[4] the band centers were estimated from the simple first-order anharmonicity formula:

$$\tilde{\nu}_0(00v_3) = \tilde{\nu}_0(001) - 2x_{33}(v_3 - 1) \qquad (2)$$

with $x_{33} = 12.3\ \mathrm{cm}^{-1}$ after the results of Barbe *et al.*[16] However, since O_3 exhibits Darling–Dennison resonance, a second-order coupling between upper levels of the symmetric and asymmetric stretching modes,[17] a more precise description of the vibrational energy levels can be obtained from the perturbation treatment presented by Barbe *et al.*[12] Adler-Golden and Armstrong[18] extended this treatment to incorporate additional high-lying states relevant to the present study. The transition frequencies at band center as determined from the vibrational state energies predicted by Adler-Golden and Armstrong[18] are used in the present analysis, with only slight adjustments as required to improve the comparison between observed and computed spectral features (see the next section).

With the band center frequencies chosen as described above, the rotational line spacings and relative strengths within each band are taken to be the same as those given by Ref. 11 for the (001)–(000) band. This treatment thus neglects the effects of vibration–rotation interactions, an approximation which has no obvious impact on the analysis of the data reported here. The rotational population distributions are described by the usual Boltzmann factor using a single assumed rotational temperature. The assumed values of rotational temperature are adjusted to optimize the fit to the envelope of the R branch of the (001)–(000) band, where there are no underlying contributions from other states. The contribution to the total integrated intensity due to each $\Delta v_3 = 1$ band is then given by

$$I_{v'} = hc\tilde{\nu}_{0v'} N_{v'} A_{v'v''}, \qquad (3)$$

where v' and v'' denote the upper and lower $(v_1v_2v_3)$ states, $N_{v'}$ is the number density of species in each upper state, and $A_{v'v''}$ *is the band-integrated* Einstein coefficient for each transition. The sum of the $dI_{v'}/d\lambda$ contributions, convolved with the instrumental slit function, is matched to each experimental spectrum by a linear least-squares fit in which the quantities $\{N_{v'}A_{v'v''}\}$ are the solutions which minimize the sum of the squares of the intensity differences between experimental and computed spectra. The values of $N_{v'}$ can then be determined if values for $A_{v'v''}$ can be specified. The estimation of $A_{v'v''}$ is discussed in the next section.

IV. RESULTS AND DISCUSSION

A. Spectral analysis

A representative comparison between observed and computed high-resolution spectra is illustrated in Fig. 3. Also shown in Fig. 3 are the individual contributions of the identifiable vibrational bands to the total spectral intensity. At the present spectral resolution of 0.027 μm, the P, Q, and R branch structures of many of the individual vibrational bands can be clearly identified, especially with the aid of the spectral fitting analysis. Spectral fits incorporating only $(00v_3)$ transitions are clearly inadequate at this resolution, failing to account for the spectral intensity observed near 10.0, 10.3, and 10.7 μm. Incorporation of $(10v_3)$ bands into the calculations provides a good match to the observed spectral structure. Further incorporation of other (v_1v_2) combinations is unnecessary to explain the data, and leads to an overspecification of the least-squares fitting due to extensive band overlap. Indeed, spectral calculations show that if the ν_1 and ν_2 modes are excited to the extent observed for ν_3, the

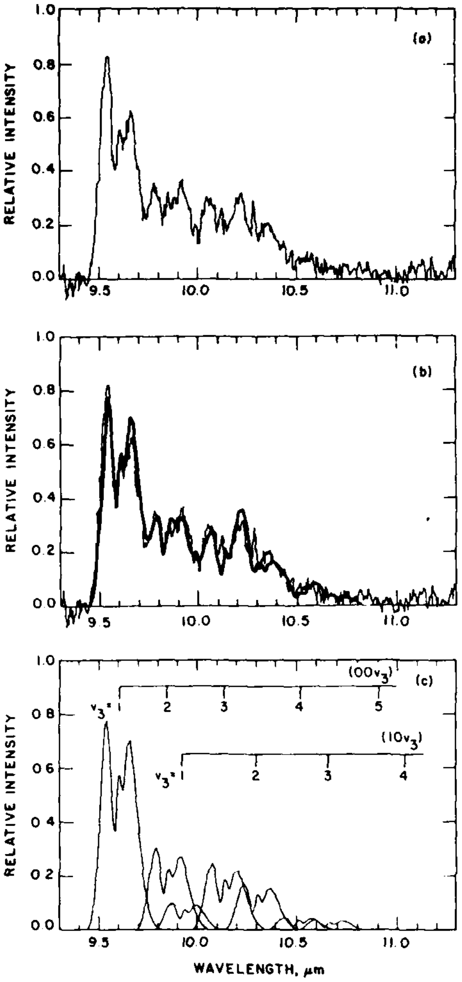

FIG. 3. Observed and computed $O_3(v)$ chemiluminescence spectra, high resolution. (a) Experimental spectrum, 1.0% O_2 in Ar, $T = 80$ K, spectral resolution = 0.027 μm, corrected for spectral responsivity. (b) Computed spectrum, least-squares fit, $T_{ROT} = 50$ K. The heavy line is the computed fit; the light line is the observed spectrum. (c) Contributions from individual vibrational bands. Data for the five-quantum states are available in spectral scans of lower resolution and better S/N near 11.0 μm.

resulting band overlap would cause a smoothing effect on the total spectrum, i.e., the vibrational structure would be more "washed out" than we observe. Thus we conclude that the ν_1 and ν_2 modes are not significantly excited in these experiments.

From the comparison of best fit and experimental spectra, it is possible to deter nine the band center frequencies which provide the best alignment. The values of $\nu_{0v'}$ determined from calculations of Ref. 18 (i.e., Darling–Dennison perturbation of a harmonic oscillator, fit to the spectroscopic data of Barbe *et al.*[12]) provide a reasonable fit to the data; however, we find it necessary to adjust these values slightly to give the best results. The band centers determined in this fashion are listed in Table II, along with the harmonic Darling–Dennison values. The values reported in Table II represent an optimization for the entire data base, but are most sensitively determined by comparison of the Q branch positions for the highest resolution spectra. For the 0.027 μm resolution, differences in Q branch positions of 2 to 3 cm^{-1} are readily identifiable in the comparisons. The observed values agree with the results of Barbe *et al.*[12] and the predictions of Adler-Golden and Armstrong[18] within approximately 3 cm^{-1}, i.e., well within the uncertainties of both the present experiment and the predictions. Also listed in Table II, and in significant disagreement with the present results, are values of $\nu_{0v'}$ as determined from: (1) the simple anharmonic oscillator approximation of Eq. (2) (used in our previous work)[4]; and (2) a fit to the data of Imre *et al.*[19] using an algebraic formulation for coupled anharmonic modes.[20]

TABLE II. Band origins (cm^{-1}) for observed $\Delta v_3 = 1$ transitions.

State	This work ($\pm 3\ cm^{-1}$)	Darling–Dennison perturbation[a]	Algebraic Hamiltonian[b]	Anharmonic oscillator[c]
001	1042	1042.1	1040.94	1042
002	1016	1015.8	1013.32	1018
101	1008	1007.6	1003.96	···
003	987	987.3	983.57	993
102	971	974.5	969.81	···
004	952	955.4	949.59	968
103	939	941.6	935.37	···
005	916	918.8	910.61	944
104	904	907.1	899.64	···
006	···	878.6	868.86	919
105	···	871.0	862.54	···
007	···	837.7	827.35	···
106	···	833.6	824.45	···

[a] Reference 18, fit to spectroscopic data of Ref. 12.
[b] Reference 20, fit to spectroscopic data of Ref. 19.
[c] Approximation used in Ref. 4, spectroscopic data of Ref. 16.

An additional factor which aids in spectral separation of the vibrational bands is the low rotational temperature observed in the experiments ($T_{ROT} \sim 50$ K in Fig. 3). The temperature of the discharge sidearm is typically 80 K or higher. As the discharged gas expands into the reaction chamber (Fig. 1), it undergoes a free expansion where rotational energy is partially converted to translation. When an equal mass flow of opposing counterflow gas is admitted to the reaction cell, a stagnation region develops along the axis, and most of the initial rotational energy is recovered.[21] This is confirmed by observation of rotational temperatures consistent with the sidearm temperature, as reported previously.[4] However, when no opposing counterflow is introduced, there is no well-defined quasistatic region within the field of view, and the recovery of rotational energy is incomplete. This results in lower rotational temperatures and correspondingly reduced spectral overlap between adjacent vibrational bands. Indeed, close examination of the P and R branch structure of the (001) → (000) band (Fig. 3) reveals that the observed rotational distribution is multimodal and is not adequately represented by our Boltzmann approximation. The higher-energy wings of the band are well fit by the value 50 ± 5 K, but the ratio of the R and P branch maxima is characteristic of a much higher rotational temperature near that of the discharge gas prior to expansion. Thus the lower rotational levels appear to be collisionally thermalized on the time scale of the measurement, while the higher levels are not. For comparison, the transit time from the discharge tube outlet to the field of view is approximately 0.5 ms and the residence time in the field of view is approximately 0.2–0.3 ms. The 50 K distribution found for the higher rotational levels suggests that R → T transfer in the expansion is collision limited for our apparatus. Thus the observed rotational structure is not fully accounted for in the spectral analysis. However, as we have observed for other molecular systems,[5-10] minor discrepancies in the rotational fine structure of the spectrum do not significantly affect the analysis of the much coarser vibrational envelope, so the results of the spectral fitting are not sensitive to the above uncertainties in the rotational distribution.

B. Estimation of band Einstein coefficients

As described above [Eq. (3)], values of the band-integrated Einstein coefficients $A_{v' \to v''}$ are required to transform the spectral fitting solutions into $O_3(v)$ number densities. Values for low-lying vibrational states accessible in thermal absorption measurements are well documented and are available in the literature.[11] However, no such data exist for the higher vibrational states of O_3 (i.e., three quanta or more). It is therefore necessary to estimate values for the higher states based on possible scalings of $\Delta v_3 = 1$ transition probabilities with vibrational energy.

The Einstein coefficients for the $\Delta v_3 = 1$ emissions observed here may be scaled from the well-known[11] values for (001) → (000) and (101) → (100) transition via the relationship

$$\frac{A_{v'v''}}{A_{10}} = \left(\frac{\nu_{v'v''}}{\nu_{10}}\right)^3 \left(\frac{R_{v'v''}}{R_{10}}\right)^2, \tag{4}$$

where $R_{v'v''}$ is the transition moment matrix element connecting states v' and v'', and the subscript 10 denotes the (001)–(000) or (101)–(100) transitions as appropriate. If the system is electrically harmonic, Eq. (4) reduces to

$$A_{v'v''} = v' A_{10} \left(\frac{\nu_{v'v''}}{\nu_{10}}\right)^3. \tag{5}$$

In this case the transition probabilities scale with vibrational quantum number, but are moderated by the mechanical anharmonicity of the oscillator. We have used this scaling formula in our previous work.[4] However, it is highly likely that this approximation will break down at some point for higher vibrational levels. This could occur by one or more of several mechanisms, including electrical anharmonicity, near-resonant intermode coupling (e.g., Darling–Dennison coupling or accidental resonance vibronic coupling with a possible bound electronically excited triplet state,[22] or the approach to ergodic behavior[23] near the dissociation limit. With the possible exception of electrical anharmonicity, these effects will tend to reduce the transition probabilities from the values predicted by Eq. (5). We expect vibronic coupling and ergodic behavior, if they occur, to be more significant for vibrational levels higher than those observed here; indeed, such effects may be partially responsible for our failure to observe emission from O_3 states near the dissociation limit.

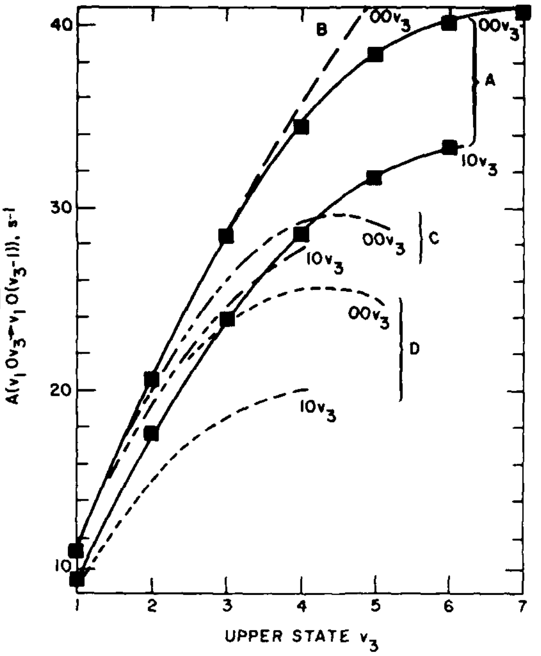

FIG. 4. Estimated Einstein coefficients for $O_3(\nu_3)$ emission. A: Equation (5) with observed band origins, used in this work; B: Eq. (5) with anharmonic oscillator estimation of band origins, used in Ref. 4; C: Darling–Dennison + electrical harmonicity, derived in Ref. 18 from data of Ref. 12; D: Darling–Dennison + theoretical dipole moment of Ref. 24, reported in Ref. 25.

The effects of Darling–Dennison coupling and transition moment variations have been investigated theoretically by Adler-Golden and co-workers.[18,24,25] Adler-Golden and Armstrong[18] report $(R_{v'v''}/R_{10})^2$ values determined from the first-order matrix elements obtained from overlap integrals of the perturbed harmonic oscillator wave functions of Barbe *et al.*[12] These calculations predict lower values of $A_{v'v''}$ than Eq. (5), the deviation being less than 10% for $v_{3'} < 3$ but more substantial at higher $v_{3'}$. The two sets of values are compared in Fig. 4. Also shown in Fig. 4 are values of $A_{v'v''}$ determined from the perturbed harmonic oscillator wave functions together with a theoretical dipole moment function.[24,25] These latter calculations indicate that the effects of electrical anharmonicity may be substantial for $v_3 > 5$. However, it should be noted that the quartic potential surface[12] used in these calculations is accurate only near the bottom of the potential well, and may not be adequate for treatment of the higher vibrational levels.

For the range of vibrational levels observed in our experiments, we have elected to use the $A_{v'v''}$ values given by Eq. (5). It appears upon comparison to complex theoretical calculations[25] that the uncertainty in these values is minimal for $v_{3'} < 3$, and that Eq. (5) provides, at worst, upper bounds to $A_{v'v''}$ for higher $v_{3'}$. Thus the vibrational state number densities inferred from our analysis may actually be lower bounds for $v_{3'} = 4$–5, the values being perhaps 50% low for $v_{3'} = 5$. We await definitive measurements of either $A_{v'v''}$ or $(R_{v'v''}/R_{10})^2$ to resolve this remaining uncertainty.

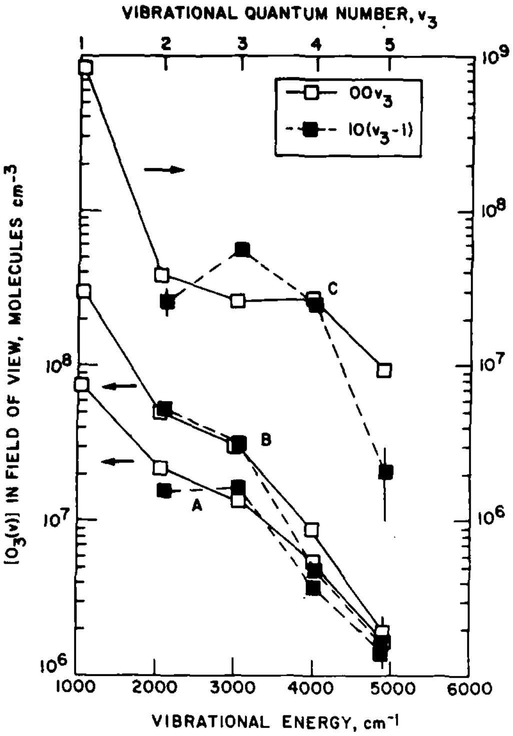

FIG. 5. Example $O_3(v)$ vibrational population distributions, $T = 80$ K. A: 0.24% O_2 in Ar; B: 1.46% O_2 in Ar; C: 10.1% O_2 in Ar.

C. Vibrational population distributions

The values of $N_{v'}A_{v'v''}$ obtained from the spectral fitting analysis were transformed into vibrational state number densities using $A_{v'v''}$ values estimated from Eq. (5). Representative vibrational distributions obtained for different initial O_2 mole fractions are shown in Fig. 5. The error bars, indicated where larger than the data point symbols, are the statistical standard deviations in the least-squares solutions (67% confidence) as determined from the variance–covariance matrix for each spectral fit. (It should be noted that this error analysis assumes Gaussian statistics, which may not be strictly correct for nonorthogonal solutions as pertain here.) The variations in both absolute number density and relative distribution as functions of initial O_2 mole fraction in the discharges are clearly seen. For low O_2 levels, the vibrational distributions are roughly Boltzmann in character, with the relative contribution from higher levels increasing as the O_2 is reduced. In contrast, at high O_2 mole fraction, the distribution is sharply bimodal. In our previous work,[4] we interpreted similar observations to represent steady-state distributions resulting from excitation and deactivation processes occurring in the discharge tubes: (1) Three-body recombination of O and O_2 at low O_2 levels, with deactivation by O and Ar; and (2) one or more additional $O_3(v)$ excitation processes at high O_2. These interpretations are supported and amplified by more detailed kinetic measurements of this type, as described in paper II.

Another effect can be seen upon examination of the combination state number densities. The $\nu_1 + (n-1)\nu_3$ states lie closer in energy to the corresponding $n\nu_3$ levels than any of the other vibrational levels of O_3. Indeed, they are the only levels within $\sim kT$ at the bath temperature of 80 K, having Boltzmann factors at that temperature, $N_{10(v_3-1)}/N_{v_3}$, of 0.39, 0.52, 0.62, and 0.77 for $v_3 = 2$, 3, 4, and 5, respectively. Within the statistical fitting uncertainties, the observed population ratios for the $v_3 = 4$, 5 states match the 80 K Boltzmann factors for the low O_2 mole fraction cases (i.e., the recombination-dominated regime). This observation is consistent with population of the 103 and 104 states by rapid, near-resonant collisional V → T energy transfer from the 004 and 005 states initially populated in the recombination/deactivation sequence. However, the 102 and 101 populations are significantly larger than dictated by Boltzmann factors; in particular, the population of the 102 state is enhanced by as much as a factor of 3, giving rise to its prominence in the spectrum as discussed above. This type of observation indicates a direct source of $O_3(102)$ other than deactivation of higher states. We note that $O_3(102)$, which lies at an energy of 3085 cm^{-1}, is nearly resonant with O_2 $(v = 2)$ at 3089 cm^{-1}. Since $O_2(v)$ is surely an important species in discharged oxygen effluents, it is possible that $O_3(102)$ is efficiently produced by the rapid V–V exchange:

$$O_2(v=2) + O_3(000) \rightarrow O_3(102) + O_2(v=0). \qquad (6)$$

We then expect $O_3(101,002,003)$ to be formed by collisional deactivation of $O_3(102)$.

The ν_2 mode does not appear to be significantly populated by collisional energy transfer in our experiments; this is consistent with the slow rates for transfer from the stretching to the bend modes observed by other workers.[26-30] Perhaps more surprisingly, higher levels of the ν_1 mode $(v_1 > 1)$ are also not observed in the spectra. These results imply that the recombination/deactivation sequence is mode selective, with only near-resonant transfer to $v_1 = 1$ states branching into the symmetric stretch mode. This point will be examined in more detail in paper II.

V. SUMMARY AND CONCLUSIONS

In summary, we have obtained moderate-resolution spectra of infrared emission from vibrationally excited ozone, formed principally by three-body recombination of O and O_2 [reaction (1)] in flowing, microwave-discharged O_2/Ar mixtures near 1 Torr and 80 K. The observed emission occurs entirely in the ν_3 mode fundamental band near 10 μm. The ν_1 and ν_2 bands at 9 and 14 μm, respectively, are too weak to be observed in our experiments.

From the emission spectra, we are able to identify the band centers for $\Delta v_3 = 1$ transitions from $(00v_3)$ and $(10v_3)$ vibrational levels with up to five quanta of stretching excitation. The band center frequencies for these transitions are consistent with those predicted from a Darling–Dennison coupling analysis.[18]

We have determined individual vibrational state number densities from a least-squares spectral fitting analysis. Central to this determination is the description of the variation of the Einstein transition probabilities with vibrational quantum number. This is fairly reliable near the bottom of the potential well but becomes highly uncertain for levels above those identified here.

The results presented here are consistent with those of our previous work,[4] which was performed over a less extensive range of experimental conditions. In that work, a simple kinetic analysis was used to establish that reaction (1) is responsible for the observed emission for most conditions; furthermore, evidence for a secondary excitation of the $v'_3 = 4, 5$ levels is observed at larger O_2 mole fractions. In addition to these effects, the improved spectral resolution of the present work reveals that $O_3(102)$ appears to be selectively excited relative to the other vibrational levels; we take this to be evidence for a rapid, near-resonant V–V exchange between $O_3(000)$ and $O_2(v=2)$ [reaction (6)]. The detailed excitation and deactivation kinetics of $O_3(v)$ are the subject of a companion paper (paper II).[9]

As a final point, the absence of higher vibrational levels deserves comment. The O_3 potential well can accommodate up to eight or nine bound vibrational levels in the ν_3 mode; however, under no conditions do we observe more than five quanta of excitation. Thus the chemiluminescence spectrum never extends substantially beyond approximately 11 μm (at our spectral resolution and low rotational temperatures). The five-quantum level occurs at an energy of 4919 cm^{-1}, or about 58% of the dissociation energy of O_3. Possible explanations for this apparent spectral "cutoff" include kinetic interference of the long-postulated triplet excited state of O_3,[22,31] or a catastrophic loss of transition strength at high energies due to anharmonic or resonance effects or quantum "chaos"[23] as discussed above. If any of these hypotheses are correct, then the 11–12 μm fluorescence from higher vibrational levels of O_3 may never be observable, even in the rarefied conditions of the upper atmosphere. However, it is clear that collisional deactivation by both Ar and O is important in our experiments, and the "hottest" vibrational distributions are obtained at low initial O_2 mole fractions where the total fluorescence signal is very small, so the fluorescence from the higher states may simply lie below our detection limit because of rapid collisional deactivation. In that case, 11–12 μm fluorescence may be detectable at low pressures if sufficient detector sensitivity can be attained. The kinetic data and analysis presented in paper II[9] address this issue.

ACKNOWLEDGMENTS

We are grateful for many productive discussions with B. D. Green, G. E. Caledonia, A. Gelb, and S. M. Adler-Golden, and for the assistance of H. C. Murphy and R. H. Krech in the experimental work. This research was supported by the Defense Nuclear Agency and the Air Force Office of Scientific Research.

---

[a] Present address: Mission Research Corporation, 1 Tara Blvd., Suite 302, Nashua, NH 03062.

[1] C. W. von Rosenberg and D. W. Trainor, J. Chem. Phys. **59**, 2142 (1973).
[2] C. W. von Rosenberg and D. W. Trainor, J. Chem. Phys. **61**, 2442 (1974).
[3] C. W. von Rosenberg and D. W. Trainor, J. Chem. Phys. **63**, 5348 (1975).
[4] W. T. Rawlins, G. E. Caledonia, and J. P. Kennealy, J. Geophys. Res. **86**, 5247 (1981).
[5] W. T. Rawlins, H. C. Murphy, G. E. Caledonia, J. P. Kennealy, F. X. Robert, A. Corman, and R. A. Armstrong, Appl. Opt. **23**, 3316 (1984).
[6] W. T. Rawlins, G. E. Caledonia, J. J. Gibson, and A. T. Stair, Jr., J. Geophys. Res. **40**, 2896 (1985).
[7] B. D. Green, W. T. Rawlins, and R. M. Nadile, J. Geophys. Res. **91**, 311 (1986).
[8] W. T. Rawlins, J. Geophys. Res. **90**, 12283 (1985).
[9] W. T. Rawlins, G. E. Caledonia, and R. A. Armstrong, J. Chem. Phys. **87**, 5209 (1987).
[10] J. P. Kennealy, F. P. DelGreco, G. E. Caledonia, and B. D. Green, J. Chem. Phys. **69**, 1574 (1978).
[11] L. S. Rothman, R. R. Gamache, A. Barbe, A. Goldman, J. R. Gillis, L. A. Brown, R. A. Toth, J. M. Flaud, and C. Camy-Peyret, Appl. Opt. **22**, 2247 (1983).
[12] A. Barbe, C. Secroun, and P. Jouve, J. Mol. Spectrosc. **49**, 171 (1974).
[13] A. Barbe, C. Secroun, P. Jouve, N. Monnanteuil, J. C. Depannemaecker, B. Duterage, J. Bellet, and P. Pinson, J. Mol. Spectrosc. **64**, 343 (1977).
[14] J. M. Flaud, C. Camy-Peyret, A. Barbe, C. Secroun, and P. Jouve, J. Mol. Spectrosc. **80**, 185 (1980).
[15] A. Barbe, C. Secroun, P. Jouve, A. Goldman, and D. G. Murcray, J. Mol. Spectrosc. **86**, 286 (1981).
[16] A. Barbe, C. Secroun, and P. Jouve, C. R. Acad. Sci. (Paris) **274**, 615 (1972).
[17] G. Herzberg, *Infrared and Raman Spectra of Polyatomic Molecules* (Van Nostrand, New York, 1945).
[18] S. M. Adler-Golden and R. A. Armstrong, AFGL-TR-82-0231, Air Force Geophysics Laboratory, Hanscom AFB, MA (1982).
[19] D. G. Imre, J. L. Kinsey, R. W. Field, and D. H. Kateyama, J. Phys. Chem. **86**, 2564 (1982).
[20] I. Benjamin, R. D. Levine, and J. L. Kinsey, J. Phys. Chem. **87**, 727 (1983). See also comments by K. K. Lehmann, *ibid.* **88**, 1047 (1984) and authors' reply.
[21] G. E. Caledonia, B. D. Green, G. A. Simons, J. P. Kennealy, F. X. Robert, A. Corman, and F. P. DelGreco, AFGL-TR-77-0281, Air Force Geophysics Laboratory, Hanscom AFB, MA (1977).
[22] C. W. Wilson, Jr. and D. G. Hopper, J. Chem. Phys. **74**, 595 (1981).
[23] K. D. Hansel, *Laser-Induced Processes in Molecules*, edited by K. L. Kompa and S. D. Smith, Springer Series in Chemical Physics (Springer, Berlin, 1979), Vol. 6.
[24] S. M. Adler-Golden, S. R. Langhoff, C. W. Bauschlicher, Jr., and G. D. Carney, J. Chem. Phys. **83**, 255 (1985).
[25] S. M. Adler-Golden, SSI-TR-54, Spectral Sciences, Inc., Burlington, MA (1984).
[26] D. I. Rosen and T. A. Cool, J. Chem. Phys. **59**, 6097 (1973).
[27] D. I. Rosen and T. A. Cool, J. Chem. Phys. **62**, 466 (1975).
[28] K. K. Hui, D. I. Rosen, and T. A. Cool, Chem. Phys. Lett. **32**, 141 (1975).
[29] S. M. Adler-Golden and J. I. Steinfeld, Chem. Phys. Lett. **76**, 479 (1980).
[30] J. A. Jones, J. B. Burkholder, and E. J. Bair, J. Chem. Phys. **76**, 5902 (1982).
[31] N. Swanson and R. J. Celotta, Phys. Rev. Lett. **35**, 783 (1975).

8. Dynamics of Vibrationally Excited Ozone Formed by Three-Body Recombination: II. Kinetics and Mechanism

by

W.T. Rawlins, G.E. Caledonia, and R.A. Armstrong

Dynamics of vibrationally excited ozone formed by three-body recombination. II. Kinetics and mechanism

W. T. Rawlins and G. E. Caledonia
Physical Sciences Inc., Research Park, P. O. Box 3100, Andover, Massachusetts 01810
R. A. Armstrong[a]
Infrared Technology Division, Air Force Geophysics Laboratory, Hanscom AFB, Massachusetts 01731

(Received 19 June 1987; accepted 21 July 1987)

Spectrally resolved infrared chemiluminescence from vibrationally excited ozone, $O_3(v)$, has been used to study the reaction kinetics of $O_3(v)$ in discharged O_2/Ar mixtures at ~ 1 Torr and 80–150 K. Dependences of the excited state number densities on temperature and O_2 mole fraction indicate $O_3(v)$ is formed primarily by three-body recombination of O with O_2 and is destroyed by rapid chemical reaction with O. Several secondary excitation reactions involving vibrationally and electronically excited O_2 are also indicated. The data are treated with a detailed steady-state analysis of the discharge kinetics, to extract estimates for rate coefficients of the key elementary reactions. The effective "quasinascent" state distribution in recombination is also inferred; this distribution shows selective recombination into the asymmetric stretching mode, but an apparently statistical (i.e., collisionally scrambled) behavior among the vibrational states within that mode. The results are discussed in terms of the detailed dynamics of three-body recombination.

I. INTRODUCTION

The chemical kinetics of vibrationally excited ozone, $O_3(v)$, is a complex problem of fundamental importance in studies of atmospheric photochemistry as well as in basic molecular dynamics. Experimental observations of $O_3(v)$ formed during the three-body recombination sequence

$$O + O_2 \rightleftarrows O_3^{\ddagger}, \tag{1a}$$

$$O_3^{\ddagger} + M \rightarrow O_3(v) + M, \tag{1b}$$

$$O_3(v) + M \rightarrow O_3(v-n) + M \tag{1c}$$

can provide insight to the detailed dynamics of the initial formation of $O_3(v)$ and to the subsequent vibrational deactivation and intermode exchange. In particular, low-pressure observations of discrete $O_3(v)$ states formed in early stages of the recombination sequence can provide a unique data base on a marginally understood problem in chemical kinetics: the molecular dynamics and mechanisms of recombination and energy transfer in polyatomic systems.[1]

The kinetics of $O_3(v)$ formation and deactivation have been addressed by a number of investigators. In general, $O_3(v)$ is usually formed by laser excitation of the ν_3 mode or by three-body recombination following flash photolysis, and is detected by ultraviolet absorption or broadband infrared fluorescence. Rosen and Cool[2-4] studied the quenching of infrared fluorescence from low-lying, laser-excited vibrational states of O_3 by several reagents, and showed that vibration-to-translation (V→T) energy transfer near the bottom of the potential well is rate limited by deactivation from the well-coupled symmetric (ν_1) and asymmetric (ν_3) stretching modes through the poorly coupled bending (ν_2) mode. Using similar techniques, West *et al.*[5,6] studied the deactivation of low levels of $O_3(v)$ by O, concluding that the deactivation pathway was primarily V→T energy transfer rather than chemical conversion to O_2.

Von Rosenberg and Trainor[7-9] were the first to observe $O_3(v)$ formed in three-body recombination, reporting on the production and deactivation of broadband infrared fluorescence in the ν_3, $\nu_1 + \nu_3$, and ν_2 bands. Working at total pressures of 100 to 400 Torr, they found greater excitation in the bending than in the stretching modes, presumably because of the extensive collisional deactivation and intermode transfer by both V→T and V→V [$O_3(v) + O_3$ intermode equilibration] processes that occurred under these conditions. More recently, the kinetics of laser-initiated and recombination-generated $O_3(v)$ have been reinvestigated using ultraviolet absorption in the Hartley bands as the diagnostic for $O_3(v)$.[10-15] These studies are somewhat less definitive than the infrared fluorescence measurements owing to the greater difficulty of resolving contributions from different modes to the observed absorption spectra. However, the results are generally consistent with the analogous infrared fluorescence data. It is noteworthy that Joens *et al.*,[15] investigating recombination under conditions of V→T-dominated collisional deactivation, inferred initial formation of $O_3(v)$ in the stretching modes followed by kinetically limited collisional transfer to the bending mode, in contrast to the results of von Rosenberg and Trainor.[7-9]

Except for the $O + O_3(v)$ studies,[5,6] all of the above experiments were performed in a flash-photolysis mode, with relatively high pressures of order 10^2 Torr, observation times of 10 to 100 μs, and room temperature. Thus the newly formed $O_3(v)$ molecules experienced on the order of 10^4–10^6 collisions on the time scale of the observations. In many cases, O_3 was a significant collision partner, providing the avenue of rapid V→V equilibration. In contrast, in the upper atmosphere [e.g., altitudes of 80 to 100 km, where $O_3(v)$ effects are most pronounced], an excited $O_3(v)$ molecule

---

[a] Present address: Mission Research Corporation, 1 Tara Blvd., Suite 302, Nashua, NH 03062.

0021-9606/87/215209-13$02.10

suffers only about 10^2–10^3 collisions in the time scale of its radiative lifetime; the principal collision partners are N_2 and O_2, which we expect to induce simple $V \rightarrow T$ cascade down the vibrational ladder, and O, which may give more complex deactivation pathways. Thus it is important to probe the earliest possible stages of the recombination sequence, where the effects of $V \rightarrow T$ cascade [reaction (1c)] are minimized, in order to determine the range of vibrational levels which are likely to be populated in high-altitude atmospheric conditions.

We report here on studies of the $O + O_2$ recombination sequence in flowing, microwave-discharged O_2/Ar mixtures near 1 Torr and at low temperatures, 80 to 150 K. Prior to their observation, the $O_3(v)$ molecules experience $\sim 10^4$ collisions, primarily with Ar, a relatively inefficient $V \rightarrow T$ transfer partner. Thus collisional effects are significant but are not severe enough to destroy information about the early stages of the recombination sequence. The measurements were made by directly observing the spectrally resolved infrared chemiluminescence from $O_3(v)$ in the ν_3 band near 10 μm, using the cryogenic COCHISE (cold chemiexcitation infrared stimulation experiment) infrared reactor/spectrometer facility[16] at the Air Force Geophysics Laboratory. Our earlier investigation,[17] with a limited set of experimental conditions, produced the first laboratory spectra of $O_3(v)$ fluorescence, attributed this fluorescence to three-body recombination in steady state with collisional deactivation, demonstrated the effects of deactivation by atomic oxygen, and hinted at the possibility of other discharge-related excitation mechanisms. We have now reinvestigated this problem with greater dynamic range so that more definitive conclusions can be made regarding both spectrosopic and kinetic/mechanistic issues which arose in the earlier work. The detailed spectroscopic observations have been reported in a companion paper (paper I).[18] We report here on the results and interpretations of kinetic/spectroscopic experiments whose objectives are to: (1) determine a quasiinitial state distribution from the recombination reaction, for use in atmospheric modeling; (2) assess the kinetic effects of deactivation by atomic oxygen; and (3) characterize and identify other $O_3(v)$ excitation mechanisms arising in the discharged gas. The results of this work are generally consistent with those from the initial studies,[17] and serve to validate and extend our interpretations[19-21] of the high-altitude chemistry of vibrationally excited ozone.

II. EXPERIMENTS AND SPECTRAL DATA

The COCHISE facility is described in detail elsewhere,[16] and the configuration of the $O_3(v)$ experiments is described thoroughly in paper I.[18] $O_3(v)$ is produced in four parallel microwave discharges (2450 MHz, 50 W) of rapidly flowing O_2/Ar mixtures at ~ 1 Torr total pressure and selected temperatures between 80 and 150 K. The discharge effluents expand into a low-pressure (~ 3 mTorr), cryogenically pumped chamber, where they enter the collimated field of view of a scanning monochromator/infrared detector assembly. Optional opposing flows of O_2 or Ar may be used to create a quasistatic interaction region along the centerline of the field of view. The use of this counterflow thus gives some increase in the observed effluent fluorescence intensities, but also causes partial rethermalization of the expansion-cooled rotational distributions. Thus in most of the experiments, counterflows were not employed in order to keep the rotational temperatures lower and minimize spectral overlap. The use of O_2, Ar, and N_2 counterflows give essentially identical results; the absence of a counterflow gives the same vibrational spectral distributions but colder rotational distributions and about half the total intensity. These results confirm the expectation that measurable $O_3(v)$ is formed only in the discharge tubes and not in the low-pressure viewing region. Typical gas residence times are ~ 2 ms for the high-pressure (1 Torr) discharge region, 0.5 ms for the expansion region between the discharge exit and the field of view, and ~ 0.3 ms for the viewing volume.

Vibraluminescence from $O_3(v)$ was observed with spectral resolutions of 0.027 to 0.080 μm (2.7 to 8.0 cm^{-1}). For convenience and optimized signal-to-noise (S/N) ratio, the lower resolution was employed for most of the measurements. Higher resolution scans for selected conditions were used to develop and verify the spectroscopic model used in the analysis as described in paper I.[18]

The primary thrust of these experiments is to examine the variation in $O_3(v)$ number densities and relative population distributions with varying O_2 mole fraction in the discharge gas. Our previous work[17] showed: (1) at low O_2 mole fractions, $\chi_{O_2} \leqslant 10^{-2}$, the relative contributions of the higher-lying states increased as χ_{O_2} decreased, presumably due to reduced collisional deactivation by atomic oxygen formed in the discharge; and (2) for $\chi_{O_2} \sim 10^{-1}$, bimodal vibrational distributions were obtained, implying the onset of another excitation reaction pumping the higher vibrational states. Accordingly, in the present experiments, the Ar flow rate was maintained at 640 μmol s^{-1} and the O_2 flow rate was varied from 2.3 to 86 μmol s^{-1} (0.3% to 12% O_2), all at a constant discharge tube temperature of 80 K. The dynamic range of χ_{O_2} was limited by poor S/N at the low end and difficulty of remote discharge ignition (inside the cryogenic chamber) at the upper end of the range. The variations in spectral distribution over this range are illustrated in Fig. 1.

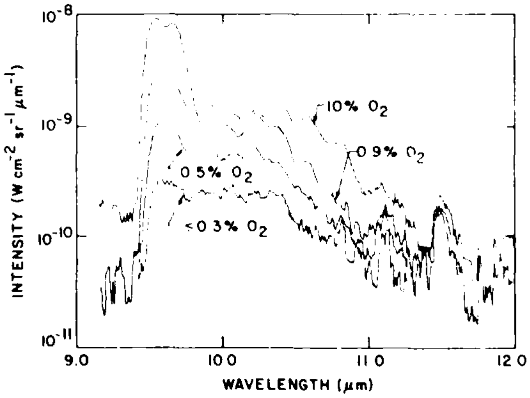

FIG. 1. Effect of O_2 level in discharged O_2/Ar mixtures on observed spectral distributions (no counterflow, 80 K, 640 μmol/s Ar, 0.08 μm resolution).

For selected constant O_2 and Ar flow velocities, the discharge sidearm and gas supply temperatures were varied systematically from 80 to 150 K. The effect on the observed spectra is illustrated in Fig. 2. The spectral distribution is seen to be invariant with temperature, however, the total intensity exhibits a strong negative temperature coefficient. These data lend credence to the interpretation that the observed $O_3(v)$ derives either directly or indirectly from ozone formed in three-body recombination, which follows a similar temperature dependence.[22] We will pursue this point further in the next section.

Prior to analysis of the spectral data, it was necessary to correct the observed spectra for atomic argon Rydberg lines appearing as scattered light from the discharge tubes.[23] This was a straightforward procedure involving subtraction of background spectra obtained with no O_2 added to the discharges. This contamination was at worst only a minor effect near 10.0 and 10.3 μm, with stronger features near 11.1, 11.4, and 12.3 μm lying generally beyond the maximum spectral extent of the $O_3(v)$ emission.

During the course of the measurements, spectral surveys were conducted over the entire 2 to 16 μm range of the apparatus in search of other ozone emission bands besides the prominent ν_3 band reported here. The only other O_3-related feature we could detect was the $\nu_1 + \nu_3$ combination band, which originates near 4.7 μm. The ν_1 and ν_2 bands, which are factors of 22 and 45 weaker than ν_3,[24] were not observable under any conditions of flow, temperature, or spectral resolution. Based on blackbody calibrations of the spectral responsivity, examination of the S/N of the ν_3 data, and the results of the spectral fitting analysis described below, we estimate a minimum detection limit for $O_3(001)$ of 5×10^6 molecules cm^{-3}, which in turn corresponds to detection limits of 1×10^8 and 3×10^8 cm^{-3} for $O_3(100)$ and $O_3(010)$, respectively. Also unobservable was any O_3-related fluorescence near 6.6 and 8 μm, observed at high pressure by von Rosenberg and Trainor[9] and attributed by them to electronic and vibrational transitions of electronically excited triplet ozone.

III. ANALYSIS AND RESULTS

Individual excited state number densities were determined from the spectral data using the linear least-squares spectral fitting method described in paper I.[18] As discussed there, high resolution spectra showed evidence for emission from $(00v_3)$ and $[10(v_3-1)]$ states up to $v_3 = 5$, with no observable features from states with $v_1 > 1$ or $v_2 > 0$. Accordingly, the $(00v_3)$ and $[10(v_3-1)]$ states were included in all the spectral fits. An important aspect of this fitting procedure is that the solutions are values of $N_{v'}A_{v'v''}$, where $N_{v'}$ is the number density for the emitting state and $A_{v'v''}$ is the Einstein coefficient for the radiative transition to the lower state v''. As discussed in paper I,[18] the scaling of $A_{v'v''}$ with v' is highly uncertain, and we have chosen a course which could result in underestimates of the values of $N_{v'}$. We believe these estimates are reasonably accurate for up to three quanta of stretching excitation, but become progressively more uncertain for the higher levels, with perhaps as much as 50% uncertainty for five quanta. The error bars shown in the following figures reflect only statistical uncertainties from the fitting unless otherwise stated.

An example least-squares fit to spectral data is illustrated in Fig. 3. The slight mismatch between observed and computed rotational distributions, most noticeable in the *P*/*R* branch structure of the prominent (001) → (000) band near 9.6 μm, appears to be due to a non-Boltzmann rotational distribution resulting from collision-limited R↔T transfer in the low-pressure expansion region of the reaction chamber. However, since the vibrational state number densities are determined from the much coarser band integrals, the results are insensitive to such small discrepancies in the fine structure of the spectrum. Examples of the detailed vibrational state number densities determined from such fits are shown in Fig. 5 of paper I.[18]

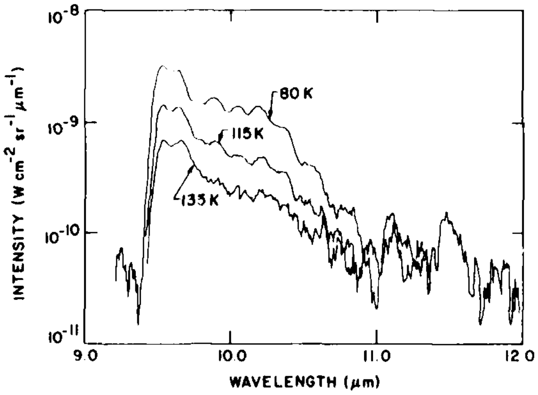

FIG. 2. Effect of temperature, low-O_2 case (no counterflow, 640 μmol/s Ar, 1% O_2, 0.08 μm resolution).

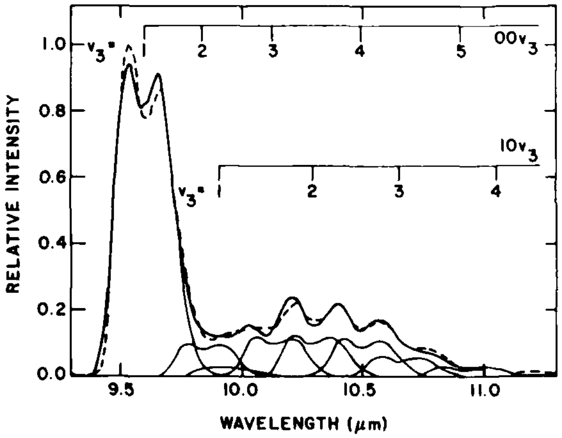

FIG. 3. Comparison of observed and computed (least-squares fit) spectra (11.8% O_2 in Ar, $T = 80$ K, spectral resolution = 0.08 μm. ---, experimental spectrum; —, computed spectrum and individual vibrational bands, $T_{rot} = 60$ K).

A. Temperature dependence

The $O_3(v)$ temperature dependence was studied from 80 to 150 K for initial O_2 mole fractions of 0.0067, 0.030, 0.109, and 0.118. In all cases, the individual relative vibrational state populations did not change with temperature, but the total absolute number densities varied by almost an order of magnitude. Accordingly, the total vibrationally excited number densities, $\Sigma_{v>1}[O_3(v)]$, were normalized to a common value at 100 K in order to collapse the data onto a single temperature dependence curve. The results are shown in Fig. 4.

The normalized $\Sigma[O_3(v)]$ values can be fit quite well by a T^{-n} dependence, where $n = (3.2 \pm 0.3)$ at the 95% confidence level. This is considerably larger than $n \cong 2$ as commonly observed for $O + O_2$ recombination with Ar near 300 K.[22] However, in Arrhenius form, as plotted in Fig. 5, the COCHISE data extrapolate well to the higher temperature results for the recombination reaction,[25-28] with approximate asymptotes of $e^{500/T}$ at high T and $e^{250/T}$ at low T. The close correspondence of the temperature dependence of $O_3(v)$ and that of the three-body recombination reaction

$$O + O_2 + Ar \rightarrow O_3 + Ar \tag{2}$$

is evidence that the $O_3(v)$ observed in COCHISE is formed either directly in reaction (2) or by excitation of ground-state O_3 formed in that reaction.

Since the observed $O_3(v)$ is actually in steady state with collisional deactivation processes, one might expect the temperature dependencies of those processes to influence the behavior of either the relative distributions or the net number densities. The apparent absence of such effects indicates that the overall temperature dependence is controlled by that of the O_3 production rate. For V→T deactivation processes, viz. $Ar + O_3(v)$, one might expect a weak positive temperature coefficient, perhaps $T^{1/2}$. However, the downward curvature in the data at low T indicates a decreasing $O_3(v)$ production efficiency rather than a decreasing deactivation rate. Thus it appears that the reactions controlling $O_3(v)$ deactivation are not strongly temperature dependent.

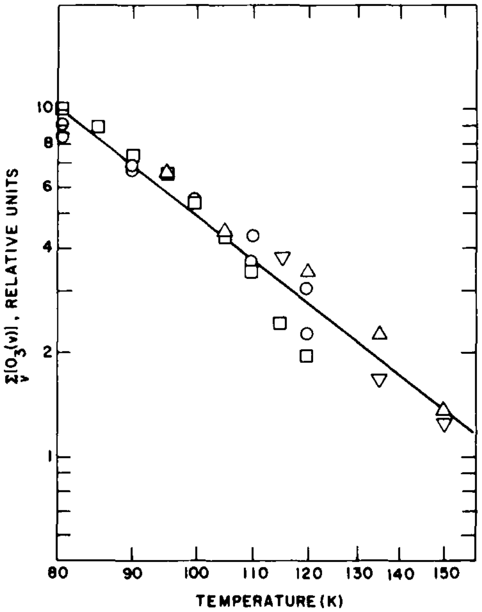

FIG. 4. Temperature dependence of total $[O_3(v)]$ (∇, 0.67% O_2; ○, 3.0% O_2; △, 10.9% O_2; □, 11.8% O_2. The solid line is a least-squares fit to the data, $\Sigma_v[O_3(v)] \propto T^{-3.2 \pm 0.3}$ (95% confidence level).

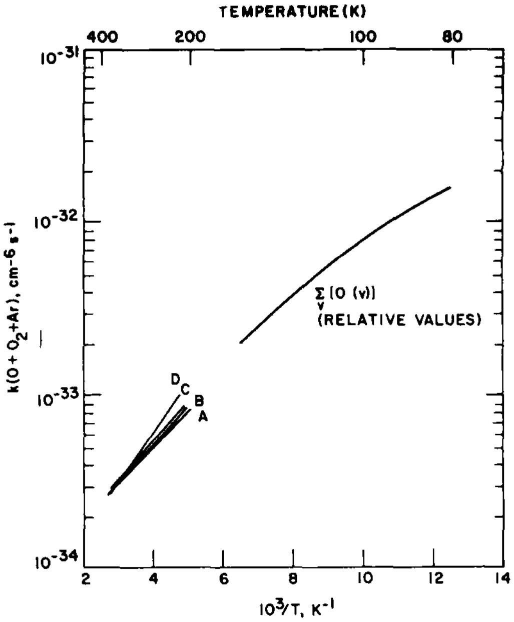

FIG. 5. Arrhenius plot comparing the observed $\Sigma_v[O_3(v)]$ temperature dependence to that observed for the recombination rate coefficient (A: Ref. 25; B: Ref. 26; C: Ref. 27; D: Ref. 28).

B. Variation of O_2 mole fraction

$O_3(v)$ number densities were determined for a variation of χ_{O_2} over slightly more than two orders of magnitude for constant discharge pressure (1.3 Torr) and temperature (80 K). For clarity, we display the results in three figures, Figs. 6 through 8. The overall results, comparing $\Sigma[O_3(v)]$, $[O_3(001)]$, and $\Sigma[O_3(v>1)]$, are plotted in Fig. 6. Break-

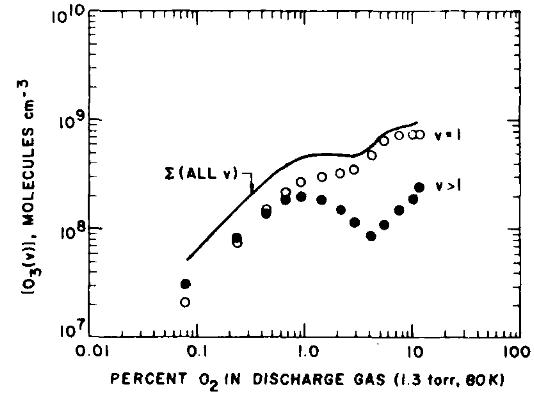

FIG. 6. Observed $O_3(v)$ number densities for all v, $v = 1$, and $v > 1$ (number densities are those observed in the field of view at 3 mTorr).

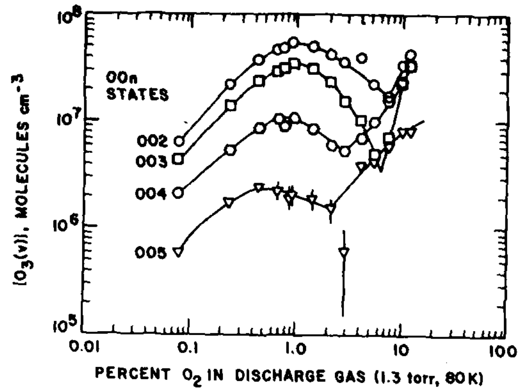

FIG. 7. Observed $O_3(v)$ number densities in field of view, $(00v_3, v_3 > 2)$ only.

downs of the individual $(00v_3)$ and $[10(v_3-1)]$ number densities for $v_3 > 1$ are plotted in Figs. 7 and 8, respectively. In general, the data show a roughly first-order dependence on O_2 at low χ_{O_2}, a strong quenching effect for the higher levels above $\chi_{O_2} \sim 0.01$, and a striking increase in $O_3(v)$ production near $\chi_{O_2} \sim 0.1$ which results in population inversions among the higher levels.

The first-order behavior below $\chi_{O_2} = 0.01$ is consistent with our earlier view[17] of $O_3(v)$ formation by reaction (1) balanced by destruction principally by atomic oxygen. The regime above $\chi_{O_2} \sim 0.01$ exhibits a substantial increase in the $O_3(v)$ loss rate, especially for the higher levels; the implication is the onset of another reaction with some discharge-produced species which reaches large concentration at this O_2 level. As we will discuss in the next section, we do not expect O, O_3, or O_2 to be responsible for this behavior.

The increase in $O_3(v)$ production at large χ_{O_2} seems to originate in the highest observed levels, $v_3 = 4$–5. The production of these levels begins to increase at substantially lower χ_{O_2} than for the lower levels, $v_3 = 2$–3, as if the high levels are directly excited and the lower levels are increasingly populated from above by collisional cascade as χ_{O_2} is increased. Since $O_3(006)$ is not observed even though there is sufficient sensitivity $\{[O_3(005)]/[O_3(006)] > 10\}$, the excitation reaction responsible for these observations must have an energetic limit in the 5000–6000 cm^{-1} range. Furthermore, since the temperature dependence of $O_3(v)$ tracks with that of recombination even in this regime of χ_{O_2}, the reaction must involve excitation of ground-state O_3, formed from deactivation of recombination-generated $O_3(v)$. The dramatic increase with χ_{O_2} points to an energetic excitation partner which is formed from electron-irradiated O_2. The possibilities then are V→V transfer to O_3 from $O_2(v)$, or E→V transfer from an electronic metastable species. The energy defect we require, ~4900 to 5800 cm^{-1}, is significantly off resonance with the states of $O_2(v)$; for example, the $v = 3$ and 4 states of O_2 lie at energies of 4598 and 6085 cm^{-1}, respectively. However, the observed energetics correspond well to the energy difference between $O_2(b\,^1\Sigma_g^+)$ and $O_2(a\,^1\Delta_g)$ of 5238.5 cm^{-1}. We therefore invoke the reaction

$$O_2(b\,^1\Sigma_g^+) + O_3 \rightarrow O_2(a\,^1\Delta_g) + O_3(005). \tag{3}$$

The quenching of $O_2(b)$ by O_3 has been observed to occur at room temperature with a rate coefficient of 2.2×10^{-11} cm^3 $molecule^{-1}$ s^{-1} and a branching fraction of 2/3 for dissociation of O_3.[29] As will be discussed in the next section, if the remaining 1/3 of the quenching proceeds by reaction (3), we anticipate that there is sufficient $O_2(b)$ produced in the discharge to account for the observations at large χ_{O_2}.

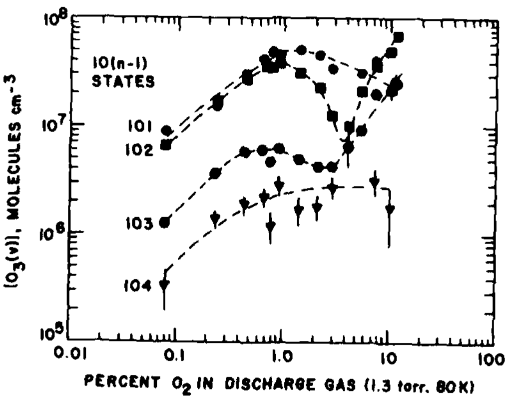

FIG. 8. Observed $O_3(v)$ number densities in field of view $[(10v_3)$ states$]$.

As discussed in paper I,[18] in the recombination-dominated regime of χ_{O_2}, we observe population of the combination states (103) and (104) in thermal equilibrium with the "pure-ν_3" states (004) and (005), and have interpreted this observation in terms of initial recombination into the ν_3 mode followed by rapid, near resonant V→T transfer with Ar to populate the nearby $[10(v_3-1)]$ states. In addition (also in paper I[18]), we observe a strong enhancement of $[O_3(102)]$ and a minor enhancement of $[O_3(101)]$ which is most likely the result of resonant V→V exchange with O_2 $(v=2)$:

$$O_2(v=2) + O_3(000) \rightarrow O_2(v=0) + O_3(102), \tag{4}$$

$$O_3(102) + M \rightarrow O_3(101) + M. \tag{5}$$

It is also likely that $O_3(002, 003)$ are enhanced to some extent by deactivation of $O_3(102)$. We have attempted to estimate a lower bound to the total $O_3(v)$ formed from V→V exchange by computing from the data the total amount of $O_3(101, 102)$ in excess of the thermal equilibrium with $O_3(002, 003)$ expected for recombination. These values are plotted in Fig. 9. For $[O_3(000)]$ estimated by extrapolation of the observed $O_3(v)$ distributions, a value of $\sim 10^{-11}$ cm^3 s^{-1} for rapid V→V exchange, and deactivation by O as described below, the levels of $O_3(v)$ observed in Fig. 9 require an $O_2(v)$ vibrational temperature of $\sim 10^3$ K, which is well within the range expected for microwave discharges such as those used here. In addition, the behavior with χ_{O_2} shown in Fig. 9, i.e., a first-order dependence below $\chi_{O_2} = 0.01$ and constant within experimental scatter above that point, has a bearing on the formation kinetics of $O_3(000)$; this point will be addressed in the next section.

We now wish to isolate the effect of recombination kinetics on the vibrational distributions at low χ_{O_2}. In the recombination-dominated regime of χ_{O_2}, we view the observed

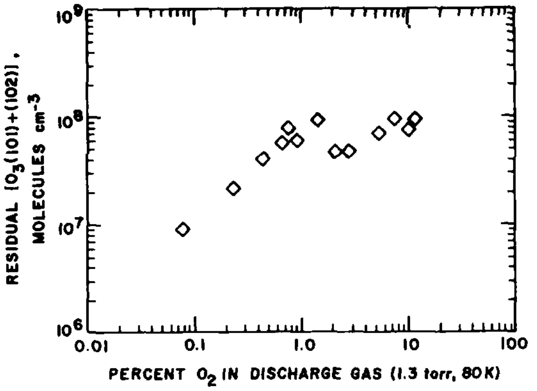

FIG. 9. Estimated contribution from $O_2(v) + O_3$ exchange [number densities (field of view values) represent sum of (102) and (101) values, corrected for their estimated levels due to recombination/deactivation (see the text)].

$O_3(v)$ as being populated by collisional cascade from higher levels which are formed directly in recombination, and destroyed primarily by atomic oxygen. In the steady-state approximation, we have

$$[O_3(v)] = \frac{k_F(v)[O][O_2][Ar]}{k_D(v)[Ar] + k_0(v)[O]} \cong \frac{k_F(v)}{k_0(v)}[O_2][Ar]. \quad (6)$$

As discussed in the next section, the direct formation term $k_F(v)$ does not apply to the relatively low vibrational states observed here, but rather to much higher states which are rapidly deactivated to the lower levels. In this analysis the cascade production rates cannot be treated on a state-to-state basis, so collisional scrambling effects among the lowest five levels are inherent in the values of $k_F(v)$. There is also some contribution from the V→V exchange reaction (4), which can be subtracted from the data using the results of Fig. 9. [Note that there is probably some residual contribution from reaction (4) in the (003) and perhaps (002) populations which we cannot evaluate.] Finally, we correct for resonant V→T transfer to the combination states by adding the population of each $[10(v_3-1)]$ state to that of the corresponding $(00v_3)$ state. A plot of the resulting relative vibrational state populations, $[O_3(00v_3)]/\Sigma_{v_3>1}[O_3(00v_3)]$, as functions of χ_{O_2} is shown in Fig. 10. For $\chi_{O_2} < 0.01$, the data fit well to an exponential empirical expression, with well-defined intercepts at $\chi_{O_2} = 0$. Since [Ar] is constant throughout, the slopes of the lines reflect variations in the atomic oxygen deactivation rates with χ_{O_2}; variation in the slopes suggests a vibrational level-dependent rate coefficient which increases with v_3. The intercepts reflect an effective vibrational distribution which is affected only by collisions with argon. A least-squares analysis of the $\chi_{O_2} = 0$ vibrational distribution gives a vibrational "temperature" of $2070 \pm 210(1\sigma)$ K. In the next section, we will attempt to extract from these data further details about the atomic oxygen deactivation and about the nascent or quasinascent $O_3(v)$ distribution from three-body recombination.

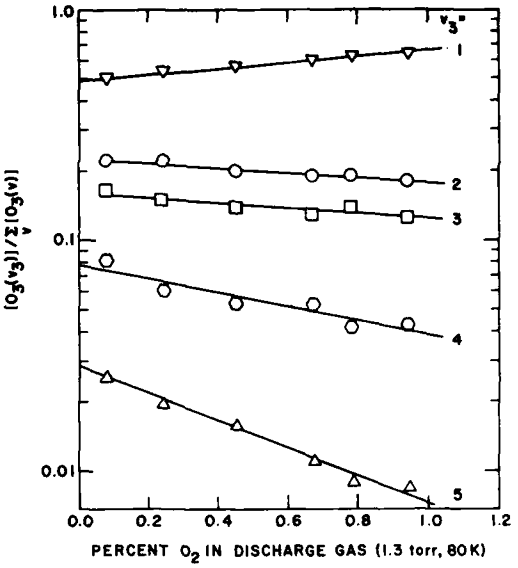

FIG. 10. Dependence of relative vibrational distributions from recombination upon O_2 mole fraction in discharge gas (the solid lines are least-squares fits to the data points).

As a final point in the data analysis, we note the striking difference between the kinetic behavior of O_3 (001) and that of the higher levels (cf. Figs. 6 and 10). The relative (001) contribution increases steadily with χ_{O_2}, showing none of the sensitivity to O_2-related loss processes that are evident in the data for higher v. While a number of hypotheses might account for this, the simplest explanation which satisfies both the reaction order and temperature dependence is that significant O_3 (001) might be formed by secondary electron impact excitation of O_3 (000), which undoubtedly accumulates in the recombination process. If this is true, then O_3 (001) and O_3 (000) might well be in a quasiequilibrium, especially at higher χ_{O_2} where O_3 (000) buildup is more substantial. Similar excitation of the higher levels may also occur, however, from inspection of the data, this does not seem to be a dominant contribution.

IV. KINETIC INTERPRETATIONS

In order to fully interpret the data in terms of production and loss mechanisms for $O_3(v)$, we must assess species number densities, rate coefficients, and scalings with χ_{O_2} and T for the relevant reactions which we expect to occur in the microwave discharges. In this section, we first address the physics and chemistry of the discharge in order to estimate number densities of the key species. We then apply these values in a comparative assessment of the various possible $O_3(v)$ production and loss processes. This leads to the derivation of a rigorous steady-state kinetic analysis, which we can then use to interpret the experimental results.

A. Discharge conditions

The COCHISE discharges are of the conventional microwave type, whose operating conditions are governed by ambipolar diffusion.[30,31] For the conditions of these experiments, we estimate an electric field/density ratio of $E/N \sim 3 \times 10^{-16}$ V cm^2; from energy balance considerations, this leads to an estimated electron number density of $\sim 10^{11}$ cm^{-3}. We have solved the Boltzmann transport equation, treating all the inelastic processes occurring in the discharge to the accuracy with which their cross sections are known, to obtain a characteristic electron energy of ~ 8 eV for dilute O_2/Ar mixtures. This characteristic energy is roughly constant from $\chi_{O_2} = 0$ to 0.01, and then decreases with increasing χ_{O_2} due to increasing collision frequency of electrons with O_2, approaching a value of ~ 2 eV for 100% O_2. Application of the electron energy distributions obtained in this fashion to energy-dependent excitation cross sections available in the literature gives the effective excitation rate coefficients as functions of E/N and χ_{O_2}.

We have used this treatment to estimate rate coefficients for the key electron impact processes, including O_2 dissociation (O formation), excitation of $O_2(v)$ and of the O_2 metastables $a\,^1\Delta_g$, $b\,^1\Sigma_g^+$, $c\,^1\Sigma_u^-$, and dissociation of O_3 (a key O_3 loss process). An important aspect of these calculations is that, since the electron energy distribution is unaffected by O_2 at low χ_{O_2}, the excitation rate coefficients are constant below $\chi_{O_2} = 0.01$, i.e., in the recombination-dominated regime. This means that the production rates for O, $O_2(v)$, and $O_2(a,b,c)$ are linearly dependent upon $[O_2]$ in this regime. We will use these rate coefficients in the steady-state analysis presented below. Further details on the Boltzmann transport solutions are given in the Appendix.

B. Excitation of $O_3(v)$

We wish to evaluate and compare the $O_3(v)$ production rates for the most likely reactions: three-body recombination; electron-impact excitation, resonant V→V transfer from $O_2(v=2)$; resonant E–V transfer from $O_2(b\,^1\Sigma_g^+)$; and the possible chemical reaction between O_2 and one or more of the high-lying metastables $O_2(A\,^3\Sigma_u^+$, $A'\,^3\Delta_u$, $c\,^1\Sigma_u^-)$. The reactions considered are listed in Table I, along with their estimated rates for $\chi_{O_2} = 10^{-3}$, 10^{-2}, and 10^{-1}.

To estimate the three-body recombination rate, we use values of [O] given by the discharge analysis. O is formed by electron-impact dissociation of O_2, and its number density is limited by the residence time t in the discharge. Thus we have $[O]/[O_2] = 2k_E^{O_2}[e^-]/t$. For $k_E^{O_2}$ as determined for the COCHISE discharges, we get $[O]/[O_2] \sim 1$ for $\chi_{O_2} < 10^{-2}$ and $[O]/[O_2] \sim 0.2$ for $\chi_{O_2} = 10^{-1}$. From Fig. 5, we estimate a recombination rate coefficient of $k_R \sim 2 \times 10^{-32}$ cm^6 s^{-1} at 80 K; this then gives a product $k_R[O][O_2][Ar] = 2 \times 10^{13}$, 2×10^{15}, and 4×10^{16} cm^{-3} s^{-1} for $\chi_{O_2} = 10^{-3}$, 10^{-2}, and 10^{-1}, respectively.

The next three reactions in Table I involve excitation by energy transfer to $O_3(000)$, whose number density must be estimated from the discharge calculations. The only efficient means of forming $O_3(000)$ in the discharge is by the recombination/vibrational relaxation pathway; the above total $O_3(v)$ production rates provide an upper bound for $O_3(000)$ formation. The principal loss process for $O_3(000)$ is most likely by electron-impact dissociation; we estimate a loss rate on the order of 10^3 s^{-1} based on the discharge predictions. Dissociation of O_3 by metastables of O, O_2, or Ar proves to be more than an order of magnitude slower by comparison. Thus we estimate upper-bound values for $[O_3(000)]$ of 2×10^{10}, 2×10^{12}, and 4×10^{13} cm^{-3} for $\chi_{O_2} = 10^{-3}$, 10^{-2}, and 10^{-1}. The value at $\chi_{O_2} = 10^{-2}$ is consistent with extrapolation of the observed vibrational distribution and correction for the expansion pressure ratio, i.e., $[O_3(000)]/[O_3(001)] \sim 25$. The actual $[O_3(000)]$ value may be considerably less than this owing to incomplete vibrational relaxation.

Vibrational excitation of O_3 by low-energy electrons is difficult to assess since its cross section is unknown and the effective electron density is ill defined. If we describe the process in terms of the total electron density and an effective rate coefficient of 10^{-9} cm^3 s^{-1}, the upper-bound excitation rates are about an order of magnitude smaller than those for recombination. Thus this reaction may compete with recombination for formation of $O_3(001)$, but does not appear to be effective for general excitation of $O_3(v)$.

$O_2(v)$ is formed in the active discharge by electron-impact excitation of O_2, and is removed by deactivation by O and electron-impact dissociation. For low vibrational levels, the O-atom reaction is the dominant loss process by one to two orders of magnitude. From the discharge predictions and a likely $O + O_2(v)$ rate coefficient of $\sim 10^{-11}$ cm^3 s^{-1}, we expect $[O_2(v=2)] = 8 \times 10^{12}$, 8×10^{12}, and 4×10^{13} cm^{-3} at $\chi_{O_2} = 10^{-3}$, 10^{-2}, and 10^{-1}, corresponding to vibrational "temperatures" of about 1700, 900, and 800 K, respectively. The actual temperatures could be significantly higher due to V↔V self-pumping by O_2, not considered here. For an O_2–O_3 V→V transfer rate coefficient of $\sim 10^{-11}$ cm^3 s^{-1}, we obtain $O_3(102)$ production rates which are competitive with those expected for recombination. The values listed in Table I are also consistent within a factor of 2 with the apparent $O_3(102)$ production rate determined from the data of Fig. 9 using the deactivation rates derived below. The $O_2(v) + O_3$ hypothesis therefore appears to be quite credible in terms of both the data and the expected discharge kinetics.

$O_2(b\,^1\Sigma_g^+)$ is formed and dissociated by electron impact. The dissociation cross section is not known, but the effective rate coefficient can be scaled from the $O_3(v)$ data. From the onset of the $O_3(v)$ enhancements shown in Fig. 7,

TABLE I. Estimated rates[a] of $O_3(v)$ formation in microwave discharges of O_2/Ar, 1.3 Torr, 80 K.

Reaction	$\chi_{O_2} = 10^{-3}$	10^{-2}	10^{-1}
$O + O_2 + Ar \rightarrow O_3(v) + Ar$	2 (13)[b]	2 (15)	4 (16)
$e + O_3 \rightarrow O_3(001) + e^-$	<2 (12)	<2 (14)	<4 (16)
$O_2(v=2) + O_3 \rightarrow O_3(102) + O_2$	2 (12)	2 (14)	2 (16)
$O_2(b\,^1\Sigma) + O_3 \rightarrow O_3(005) + O_2$	1 (11)	1 (14)	6 (15)
$O_2(c\,^1\Sigma) + O_2 \rightarrow O_3(001,002) + O$	···	1–10 (13)	···

[a] Rates are in units of molecules cm^{-3} s^{-1}.

[b] 2 (13) represents 2×10^{13}.

together with an E→V rate coefficient of 7×10^{-12} cm^3 s^{-1} (in keeping with the results of Slanger and Black[29]), we estimate $[O_2(b)]$ values which, taken with the discharge-predicted $O_2(b)$ production rates, correspond to an $O_2(b)$ dissociation rate coefficient which is about five times larger than that for $O_2(X\,^3\Sigma_g^-)$. This gives $[O_2(b)] = 10^{12}$, 10^{13}, and 2×10^{13} cm^{-3} for $\chi_{O_2} = 10^{-3}$, 10^{-2}, and 10^{-1}. The resulting O_3 (005) production rates, shown in Table I, are seen to be competitive with recombination only at large χ_{O_2}.

Lastly, we consider the reaction

$$O_2^* + O_2 \rightarrow O_3(v) + O, \tag{7}$$

where O_2^* is one of the Herzberg states: $A\,^3\Sigma_u^+$, $A'\,^3\Delta_u$, and $c\,^1\Sigma_u^-$. This type of reaction was implicated in high altitude auroral measurements,[19,21] but has yet to be demonstrated in the laboratory. The reaction with $O_2(A,v=0)$ is exoergic enough to form O_3 with up to two quanta of stretching vibration. For $\chi_{O_2} = 10^{-2}$, we estimate from the discharge predictions for $O_2(c)$ an O_2^* production rate of $\sim 6\times10^{16}$ cm^{-3} s^{-1}. By analogy with the other metastables, the loss rate by dissociation is probably 10^4–10^5 s^{-1}, so we expect $[O_2^*] = \sim 10^{11}$–10^{12} cm^{-3}. This means that reaction (7) may compete successfully with recombination if the rate coefficient is in the 10^{-13} cm^3 s^{-1} range, a value which is consistent with quenching measurements at room temperature for $O_2(A)$.[32] However, the strong negative temperature coefficient observed for all $O_3(v)$ under all χ_{O_2} conditions argues against the contribution of reaction (7) in the COCHISE measurements at cryogenic temperatures.

C. Deactivation of $O_3(v)$

The principal loss of $O_3(v)$ occurs through collisions with Ar, the wall of the discharge tube, and atomic oxygen. Deactivation by O_2 is not important at these dilutions. In addition, we will consider dissociation of $O_3(v)$ by electrons, $O_2(a\,^1\Delta_g)$, and $O_2(b\,^1\Sigma_g^+)$. The relevant reactions are listed in Table II.

The deactivation of low levels of $O_3(v)$ by Ar has been studied at room temperature.[2–4,12] We have scaled those data by $vT^{1/2}$ to apply to our conditions. Based on the state distributions we observe, it appears that the deactivation occurs mainly by $\Delta v_3 = 1$ changes until the (001) state is reached, after which it may proceed through (010) into (000) as suggested by Rosen and Cool.[2,3] For this type of V→T transfer, we expect single quantum cascade down the vibrational ladder. The assumed Ar deactivation rates are therefore in the 10^3 s^{-1} range, with a significant dependence on vibrational level.

TABLE II. Estimated loss rates[a] for $O_3(v)$ in microwave discharges of O_2/Ar, 1.3 Torr, 80 K.

Reaction		$\chi_{O_2} = 10^{-3}$	10^{-2}	10^{-1}
$O_3(v) + Ar \rightarrow O_3(v-1) + Ar$		$700v$	$700v$	$700v$
$O_3(v) \xrightarrow{\text{wall}} O_3(v-n)$		<300	<300	<300
$O_3(v) + O \rightarrow 2O_2$	or	1 (3)[b]	1 (4)	2 (4)
$O_3(v-n) + O$				
$O_3(v) + e \rightarrow O_2 + O$		1 (3)	1 (3)	1 (3)
$O_3(v) + O_2(a\,^1\Delta) \rightarrow 2O_2 + O$		1–10 (2)	1–10 (3)	4–40 (4)
$O_3(v) + O_2(b\,^1\Sigma) \rightarrow 2O_2 + O$		···	1 (2)	···

[a] Rates are in units of molecules s^{-1}.

[b] 1 (3) represents 1×10^3.

Deactivation of $O_3(v)$ on the wall of the discharge tube was estimated from lowest mode diffusion[30] by analogy to CO_2,[17,33] assuming unit deactivation efficiency. This gives an upper bound of ~ 300 s^{-1}, which is of minor importance for our conditions. This value is comparable to 500 s^{-1} corresponding to the inverse of the residence time in the active discharge prior to expansion, so little influence of wall collisions on the vibrational distributions is expected.

Deactivation of $O_3(v)$ by O is a critical reaction which is difficult to treat. West *et al.*[5] studied this reaction for $O_3(v=1)$ and found efficient removal of $O_3(v)$ by O, with a rate coefficient of either $\sim 10^{-11}$ or $\sim 10^{-12}$ cm^3 s^{-1}, depending upon whether chemical reaction or V→T transfer occurred. These same investigators[6] later reported no significant loss of O in the process, implicating V→T transfer as the dominant pathway, at least for $O_3(v=1)$. The behavior for higher v is not known, although statistical arguments[34] favor deactivation by multiquantum energy transfer. For reasons discussed later in this paper, we suspect that the chemical reaction pathway plays a role in our experiments. For the present purposes, we invoke a rate coefficient of 10^{-11} cm^3 s^{-1} with no dependence upon vibrational level. For this value, we can see that deactivation by O is competitive with Ar at the lowest χ_{O_2} and faster for larger χ_{O_2}. In the analysis to follow, we will use the data to obtain better estimates for the rate of this process.

The rate of dissociation of $O_3(v)$ by electrons was estimated by analogy with $O_3(000) + e^-$ rates determined above, assuming no large increase in the rate with O_3 vibrational energy. This loss process may be a minor factor at low χ_{O_2}, but does not appear to be generally important except to determine the overall loss rate of total ozone.

The dissociation of $O_3(v)$ by $O_2(a\,^1\Delta_g)$ is an interesting possibility and may provide an explanation for the anomalously large loss rates for $O_3(v\geqslant2)$ which are evident in the data (Figs. 6 through 8) for $\chi_{O_2} > 10^{-2}$. Quenching of vibrationally cold $O_2(a)$ by ground state O_3 is known to be slow[22]; however, excitation of at least one vibrational quantum of either partner would permit dissociation of the O_3, and might therefore lead to a substantial increase in the reaction cross section. Based on the discharge predictions, we estimate $[O_2(a)] \sim 10^{14}$ to 4×10^{15} cm^{-3} for $\chi_{O_2} = 10^{-2}$ to 10^{-1}. Thus we can account for the observations with a rate coefficient in the 10^{-11} to 10^{-10} cm^3 s^{-1} range. We know of no other possible hypotheses to explain the observed depletion in $O_3(v\geqslant2)$ above $\chi_{O_2} = 10^{-2}$.

Finally, we have evaluated the dissociation of $O_3(v)$ by $O_2(b\,^1\Sigma_g^+)$ using the discharge predictions given above for $[O_2(b)]$ and the total quenching constant of Slanger and Black[29] for ground-state O_3. As shown in Table II, this turns out to be an insignificant loss process for $O_3(v)$.

D. Steady-state kinetic analysis

Comparison of the estimated $O_3(v)$ production and loss rates in Tables I and II allows us to confidently verify our initial belief that, for $\chi_{O_2} < 10^{-2}$, $O_3(v)$ is formed primarily through three-body recombination and is removed by collisions with O and Ar. The values of Tables I and II give predicted steady-state $O_3(v)$ number densities in the field of view of $\sim 3\times 10^7$, 7×10^8, and $3\times 10^9\ \mathrm{cm}^{-3}$ for $\chi_{O_2} = 0.001$, 0.01, and 0.1, respectively. The first two values are within a factor of ~ 2 of the observations (cf. Fig. 6), which is well within the uncertainty of the calculations. The predicted value at $\chi_{O_2} = 0.1$ is high by a factor of ~ 3, suggesting that we may have underestimated some of the loss rates for this discharge condition.

The excited ozone observed in these experiments is in low vibrational states, $v \leqslant 5$, which are unlikely to have been formed directly upon stabilization of the O_2–O collision complex. We define here a true nascent distribution, $O_3(v^*, J^*)$, as being the earliest rotational–vibrational distribution for which collisional redissociation is insignificant compared to radiative and/or collisional deactivation. This distribution is likely to encompass vibrational states in the upper third or half of the potential well, and is also probably extremely short lived, perhaps surviving for only 100 collisions. On this time scale there will evolve a secondary vibrational distribution, $O_3(v)$, which is the quasiinitial distribution that precedes the deactivation observed here. The states within this distribution are populated by downward collisional cascade, not by direct recombination. Thus for each state there are several production terms involving higher-lying states, which in turn have more production terms. For algebraic simplicity, we treat the $O_3(v)$ states collectively, such that collisional "scrambling" among the individual states is an inherent part of the distribution. In terms of the steady-state analysis for collective $[O_3(v)]$, it is easy to show that a steady-state assumption of $O_3(v^*, J^*)$ formation by three-body recombination and removal by Ar gives the same form for the production rate for $O_3(v)$ as if we assume direct recombination into $O_3(v)$. We can therefore write the level-dependent steady-state equations [cf. Eq. (6)]:

$$[O_3(v)] = \frac{k_v^R[O][O_2][Ar]}{k_v^0[O] + R_v}, \tag{8}$$

$$\sum_v [O_3(v)] = \frac{\Sigma_v k_v^R[O][O_2][Ar]}{k_L^0[O] + R_1}, \tag{9}$$

where k_v^R is the apparent rate coefficient for "direct" recombination into state v, k_v^0 is the rate coefficient for collisional removal of state v by O, and R_v represents the removal of state v by all oxygen-independent processes, mainly Ar and wall collisions. In Eq. (9), k_L^0 represents the rate-limiting step for removal of all $O_3(v)$ by O. For example, if the $O + O_3(v)$ step proceeds by single quantum cascade, this is given by $k_L^0 = k_1^0$; if the process is a chemical reaction or involves total multiquantum deactivation to $O_3(v=0)$, we have $k_L^0 = \Sigma_v k_v^0[O_3(v)]/\Sigma[O_3(v)]$.

Several important conclusions can now be stated upon examination of the reaction orders observed in Figs. 6 through 8. First, the observed number densities of $\Sigma[O_3(v)]$ and $[O_3(v)]$ are first order in O_2 even at the lowest χ_{O_2}, corresponding to $[O_2] = 1.3\times 10^{14}\ \mathrm{cm}^{-3}$. From the discharge predictions, we expect $[O]/[O_2]$ to be constant throughout this regime, with an estimated ratio of unity. From the condition required for first-order behavior, $k_v^0[O] > R_v$ and R_v given by Table II, we conclude $k_1^0 > 8\times 10^{-12}\ \mathrm{cm}^3\,\mathrm{s}^{-1}$, etc., up to $k_5^0 > 3\times 10^{-11}\ \mathrm{cm}^3\,\mathrm{s}^{-1}$. Further information on the deactivation step can be gleaned from the V→V transfer results plotted in Fig. 9. From the discharge predictions, we expect $(O_2^{\cdot}(v=2)]$ to be constant from $\chi_{O_2} = 10^{-3}$ to 10^{-2}. The first-order behavior in $[O_3(102)]$ exhibited in Fig. 9 must therefore be due to a similar dependence in $[O_3(v=0)]$. First-order behavior of $[O_3(v=0)]$ cannot occur if there is significant formation of $O_3(v=0)$ by $O + O_3(v)$. This, together with the large values of k_v^0, indicates that the major route of the $O + O_3(v)$ step is chemical reaction to form O_2.

To assess the level-dependent kinetic effects, we examine the relative vibrational distributions

$$\frac{[O_3(v)]}{\Sigma_v[O_3(v)]} = \frac{k_v^R}{\Sigma_v k_v^R}\,\frac{k_L^0[O] + R_1}{k_v^0[O] + R_v}. \tag{10}$$

It can be shown after considerable algebra that, over the range of [O] and relative population observed here, Eq. (10) is approximated by the empirical exponential form plotted in Fig. 10. The empirical slopes are related to the kinetic parameters via

$$\frac{d\ln\{[O_3(v)]/\Sigma_v[O_3(v)]\}}{d[O_2]} \cong \frac{fk_L^0}{R_1} - \frac{fk_v^0}{R_v} \tag{11}$$

to within $\sim 30\%$, where $f = [O]/[O_2] \approx 1$. The first-order kinetics in $[O_2]$ provides us with the lower bound $k_L^0/R_1 > 8\times 10^{-15}\ \mathrm{cm}^3$. Using the Ar and wall deactivation rate coefficients from Table II, and the empirical slopes from Fig. 10, we can evaluate lower bounds for k_v^0: $(0.8, 1.4, 2.0, 2.7,\ \text{and}\ 3.6)\times 10^{-11}\ \mathrm{cm}^3\,\mathrm{s}^{-1}$ for $v = 1, 2, 3, 4$, and 5, respectively.

The $\chi_{O_2} = 0$ intercepts from Fig. 10 can be used to determine the quasiinitial $O_3(v)$ distribution from recombination. From Eq. (10) at $[O] = 0$, we obtain

$$\left(\frac{[O_3(v)]}{\Sigma_v[O_3(v)]}\right) = \frac{k_v^R}{\Sigma_v k_v^R}\,\frac{R_1}{R_v}, \tag{12}$$

where $k_v^R/\Sigma_v k_v^R$ are the quantities we seek. The observed intercepts and the values corrected for R_v/R_1 are plotted in Fig. 11. The error bars reflect the combined uncertainties in R_v/R_1 (i.e., with and without wall collisions) and in the Einstein coefficients used in the spectral analysis. Also plotted in Fig. 11 is the statistical nascent distribution which would obtain if the entropy change of the reaction were maximized, i.e., if all final states within the ν_3 mode were equally probable. In the language of surprisal theory,[35] this is called the "prior" or "zero surprisal" distribution of states, and is given by[36]

$$P^0(v) = \frac{(1 - E_v/E)^{3/2}}{\Sigma_v(1 - E_v/E)^{3/2}}, \tag{13}$$

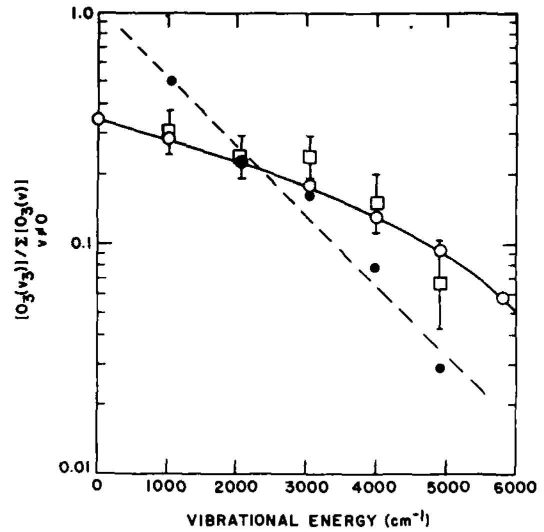

FIG. 11. Quasiinitial vibrational distribution of $O_3(v)$ formed in recombination [---●---, $\chi_{O_2} = 0$ intercepts, with least squares-fit [T_{vib}] $= 2070 \pm 210(1\sigma)$ K]; □, zero-O_2 values adjusted for Ar deactivation; –O–, computed statistical distribution (including $v = 0$)].

where E_v is the energy of vibrational state v and E is the total energy available ($E = 8468 \pm 140$ cm^{-1}). The close correspondence between the COCHISE quasiinitial distribution and the zero surprisal distribution is striking. It appears from this that the energy contained in the truly nascent O_3 (v^*,J^*) states is rapidly randomized throughout the asymmetric stretching mode of the molecule in collisions with the Ar bath gas.

V. DISCUSSION

The detailed dynamics of three-body recombination are summarized in Table III. In the energy transfer or association/deactivation mechanism, we envision the formation of an unbound but associated O---O_2 complex which can live long enough to collide with an Ar atom. This collision results in either dissociation of the complex or formation of slightly bound O_3(*). Further collisions of O_3(*) result in either redissociation or stepwise deactivation until finally the nondissociative nascent distribution O_3 (v^*,J^*) is attained. The state distribution continues to evolve downwards by collisional cascade, at first rapidly through V,R → T transfer until the rotational distribution is thermalized, and then more slowly by conventional V → T transfer thereafter. Within the framework of this model, we require rapid scrambling of the recombination energy throughout the ν_3 mode. This is not unreasonable, since trajectory calculations for Ar + O_3 (v,J) collisions indicate efficient energy transfer with large ΔE for excited ozone molecules with high rotational energy.[37,38] The observed preference for asymmetric stretching motion is also striking; it seems that the newly formed molecules (probably in a quasicontinuum of states) are deactivated into the nonchaotic portion of the potential well so rapidly that they retain "memory" of the original approach configuration. The decrease in the recombination rate with increasing temperature can be ascribed, qualitatively at least, to less efficient complex formation and increased collisional redissociation prior to formation of the nascent distribution.

TABLE III. Dynamics of three-body recombination.

(1) Association/deactivation mechanism		
Complex formation:	$O + O_2 \to O{-}{-}{-}O_2 \to O + O_2$	
	$O{-}{-}{-}O_2 + M \to O + O_2 + M$	
	$O{-}{-}{-}O_2 + M \to O_3(^*) + M$	
Stabilization:	$O_3(^*) + M \to \to \to O + O_2 + M$	
	$O_3(^*) + M \to \to \to O_3(v^*,J^*) + M$	
Deactivation	$O_3(v^*,J^*) + M \to \to \to O_3(v) + M$	
	$O_3(v) + M \to \to \to$	Rotational thermalization Vibrational cascade
(2) Chaperon mechanism		
	$O + M \rightleftarrows OM$	
	$O_2 + OM \to O_2 + O + M$	
	$O_2 + OM \to O_3(v^*,J^*) + M$	
	$O_3(v^*,J^*) + M \to \to \to$	Rotational thermalization Vibrational cascade

In an alternative recombination scheme, the chaperon or radical-molecule complex mechanism, O and Ar may exist in equilibrium with the weakly bound van der Waals molecule ArO, which can react with O_2 to either dissociate or form excited O_3. Troe[39] has suggested that this mechanism may be responsible for the anomalously low values for the three-body and high-pressure rate coefficients observed for the reaction at room temperature. We can find no evidence in our data to preclude the occurrence of this mechanism. A detailed study of these mechanisms using classical trajectory calculations is currently under way in our laboratory; preliminary results indicate an O_3 (v) production rate by the chaperon mechanism which is much smaller than that obtained from Fig. 5.[40]

The elusive triplet excited state of ozone[41,42] may also be involved in the recombination sequence, perhaps as a collisional precursor to the quasiinitial O_3 (v) distribution. Our data neither support nor contradict this, however, there is no spectral evidence for significant triplet ozone,[18] nor do we need to invoke its presence to account for the results.

The COCHISE data have profound significance in the interpretation and modeling of high-altitude O_3 (v) chemistry.[19-21] We expect the observed quasiinitial distribution to correspond fairly well to the three-body recombination reaction in the upper atmosphere. The effects of N_2 and O_2 as third bodies and V → T collisional deactivation partners should be similar to those observed here for Ar. Furthermore, the large rate coefficients we find for reaction of O_3 (v) with O indicate that the atomic oxygen reaction will be important between 80 and 100 km for some (but not all) atmospheric conditions. Finally, the characterization of other discharge-related O_3 (v) excitation processes has an important bearing on the interpretation and scaling of auroral observations.

VI. CONCLUSIONS

By a detailed analysis of spectrally resolved O_3 (v) fluorescence data over a wide range of experimental conditions, we have been able to characterize completely the kinetics of $O_3(v)$ formed in microwave discharges of dilute, flowing O_2/Ar mixtures. The primary result of this effort is the determination of the quasiinitial distribution of $O_3(v)$ states formed in three-body recombination of O with O_2,

$$O + O_2 + Ar \rightarrow O_3(v) + Ar.$$

The results indicate statistical behavior in the asymmetric stretch mode, but little or no transfer into the other modes on the time scale of the measurements. An analysis of the change in vibrational distribution with changing O_2 mole fraction leads to the conclusion that deactivation of $O_3(v)$ by O proceeds via chemical reaction:

$$O + O_3(v) \rightarrow O_2 + O_2$$

with rate coefficients in excess of 10^{-11} cm^3 s^{-1} and increasing with v. As an interesting aside, this reaction can lead to considerable vibrational and electronic excitation in O_2, including the formation of the metastables $A\,^3\Sigma_u^+$, $A'\,^3\Delta_u$, and $c\,^1\Sigma_u^-$.

Additional evidence was obtained for other $O_3(v)$ excitation processes. These include: resonant V→V transfer from $O_2(v)$,

$$O_2(v=2) + O_3 \rightarrow O_2(v=0) + O_3(102);$$

resonant E→V transfer from $O_2(b\,^1\Sigma_g)$,

$$O_2(b\,^1\Sigma_g^+) + O_3 \rightarrow O_2(a\,^1\Delta_g) + O_3(005);$$

and possibly electron-impact excitation of O_3,

$$e^- + O_3 \rightarrow O_3(001) + e^-.$$

Finally, indirect evidence suggests rapid dissociation of $O_3(v_3 > 1)$ by $O_2(a\,^1\Delta_g)$:

$$O_3(v_3 > 1) + O_2(a\,^1\Delta_g) \rightarrow O + O_2 + O_2.$$

Much of the information presented here was inferred from indirect and often circuitous analysis of a complex data base. For this reason, these results are by no means definitive. Nevertheless, they represent the current state of the art for this difficult problem, and the development of a more definitive data base will undoubtedly prove to be extraordinarily difficult. We eagerly await the testing of the concepts and models presented here by advanced theoretical and experimental methods.

ACKNOWLEDGMENTS

The authors thank B. D. Green and A. Gelb for many stimulating discussions, H. C. Murphy for assistance with the experiments, and L. M. Cowles and J. F. Cronin for portions of the data analysis. This research was supported by the Defense Nuclear Agency and the Air Force Office of Scientific Research.

APPENDIX: THE PREDICTION OF EXCITATION RATE CONSTANTS IN O_2/Ar DISCHARGES

We present here predictions for excitation rates in O_2/Ar microwave discharges. These calculations not only incorporate the collective effects of ground-state excitation of O_2 but also include excitation of discharge created species such as cross sections for O-atom excitation, ozone dissociation, and ionization of argon metastable states.

We have used a computer model which solves the Boltzmann transport equation to evaluate the excitation rates characteristic of the O_2/Ar discharges used in the COCHISE ozone studies. Discharge predictions were performed for various O_2/Ar mixtures as a function of E/N (electric field per unit length normalized by total number density). The inputs to these calculations are the electron energy dependent cross sections for the inelastic processes occurring in the discharge while the outputs include discharge characteristics such as characteristic electron energy and drift velocity as well as excitation rate constants. The calculational techniques are straightforward and well understood (see, e.g., Ref. 43).

The predictions are, of course, only as accurate as the cross sections employed. In the case of argon all the cross sections are well known with the exception of those for electronic excitation. We have characterized electronic excitation with two processes representing *s* state excitation with an energy loss of 11.6 eV and *p* state excitation with an energy loss of 13.1 eV. These cross sections were used with the more standardly accepted cross sections for momentum transfer and ionization for Ar[43,44] to predict the transport properties of argon discharges. Predicted values of drift velocity, characteristic energy, and ionization coefficient as functions of E/N gave good agreement with experimental measurements for argon discharges.

For the case of O_2 the cross section data base discussed extensively by Phelps and co-workers[46-48] has been used. These cross sections provided reasonable agreement with O_2 discharge data and limited measurements of O_2 metastable state excitation rates.[46,47] The processes considered include momentum transfer, rotational and vibrational excitation, electronic excitation of several states, dissociation, dissociative attachment, and ionization.

Several excitation processes involving O and O_3 have also been included in the analysis. These species have been treated as traces and thus do not affect the discharge electron energy distribution. Electron-impact excitation of $O(^3P)$ to $O(^1D)$ and $O(^1S)$ has been specified by the cross sections recommended by Jackman *et al.*,[49] and dissociation of O_3 by the analysis of Keto.[50] The latter treatment is theoretical with no experimental validation.

Similarly, electron-impact ionization of the Ar(4*s*, 4*p*) states has also been incorporated. These cross sections have been taken from the theoretical treatment in Ref. 51. The cross sections for Ar(4*s*) have been validated experimentally. Ar metastables were only treated as a trace in the calculations. Note, however, that this stepwise ionization process can change the discharge operating conditions if the Ar metastable state concentration becomes sufficiently large.

These cross sections have been used to calculate discharge properties and excitation/deexcitation rate coefficients of various O_2/Ar mixtures as a function of E/N. Some of the predictions are shown in Figs. 12 through 16. These rate coefficients were used in the kinetic analysis presented in Sec. IV. More detailed tabulations and plots of the relevant cross section data and predicted rate coefficients are available from the authors upon request.

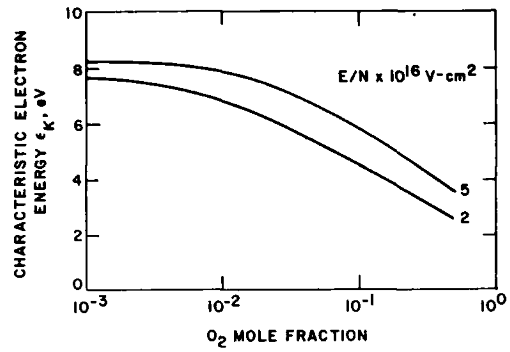

FIG. 12. Predicted characteristic energies in microwave excited mixtures of O_2/Ar.

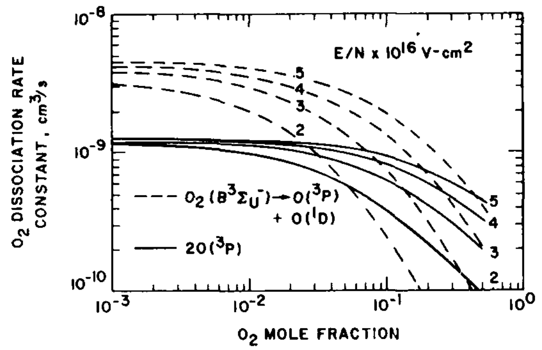

FIG. 13. Predicted rate constants for O_2 dissociation in microwave excited O_2/Ar discharges.

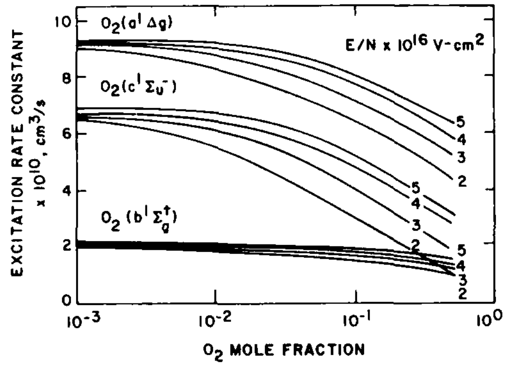

FIG. 14. Rate constants for electron-impact excitation of ground state O_2 to several metastable states for microwave excited O_2/Ar mixtures.

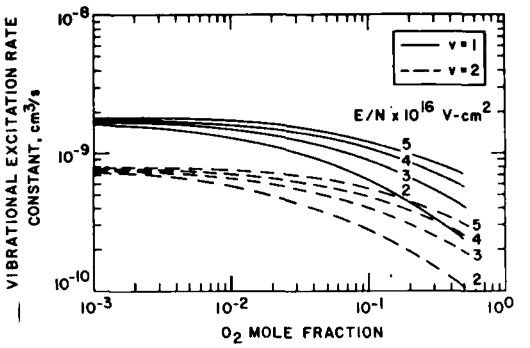

FIG. 15. Predicted rate constants for direct excitation of vibrational levels $v = 1$ and 2 of O_2 in microwave excited mixtures of O_2/Ar.

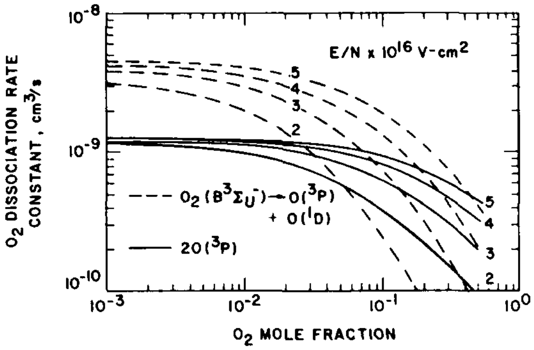

FIG. 16. Predicted rate constants for electron-impact dissociation of O_3 in microwave excited O_2/Ar mixtures.

It must be noted that these predictions should not be considered to be exact. Indeed, at these high characteristic energies the adequacy of the first-order expansion of the transport equation is in question. In addition, superelastic collisions have not been accounted for and it has been assumed that the O and O_3 concentrations are traces relative to those for O_2. If the latter assumption is valid, and given the accuracy of the cross sections, we expect the rate constants to be accurate to within a factor of 2. Furthermore, at very high excitation levels additional processes should be considered, e.g., electron-impact dissociation of the metastable states of O_2.

[1] J. Troe, Annu. Rev. Phys. Chem. **29**, 223 (1978).
[2] D. I. Rosen and T. A. Cool, J. Chem. Phys. **59**, 6097 (1973).
[3] D. I. Rosen and T. A. Cool, J. Chem. Phys. **62**, 466 (1975).
[4] K. K. Hui, D. I. Rosen, and T. A. Cool, Chem. Phys. Lett. **32**, 141 (1975).
[5] G. A. West, R. E. Weston, Jr., and G. W. Flynn, Chem. Phys. Lett. **42**, 488 (1976).
[6] G. A. West, R. E. Weston, Jr., and G. W. Flynn, Chem. Phys. Lett. **56**, 429 (1978).
[7] C. W. von Rosenberg and D. W. Trainor, J. Chem. Phys. **59**, 2142 (1973).
[8] C. W. von Rosenberg and D. W. Trainor, J. Chem. Phys. **61**, 2442 (1974).
[9] C. W. von Rosenberg and D. W. Trainor, J. Chem. Phys. **63**, 5348 (1975).
[10] I. C. McDade and W. D. McGrath, Chem. Phys. Lett. **72**, 432 (1980).
[11] I. C. McDade and W. D. McGrath, Chem. Phys. Lett. **73**, 413 (1980).
[12] S. M. Adler-Golden and J. I. Steinfeld, Chem. Phys. Lett. **76**, 479 (1980).
[13] S. M. Adler-Golden, E. L. Schweitzer, and J. I. Steinfeld, J. Chem. Phys. **76**, 2201 (1982).
[14] T. Kleindienst, J. B. Burkholder, and E. J. Bair, Chem. Phys. Lett. **70**, 117 (1980).
[15] J. A. Joens, J. B. Burkholder, and E. J. Bair, J. Chem. Phys. **76**, 5902 (1982).
[16] W. T. Rawlins, H. C. Murphy, G. E. Caledonia, J. P. Kennealy, F. X. Robert, A. Corman, and R. A. Armstrong, Appl. Opt. **23**, 3316 (1984).

[17] W. T. Rawlins, G. E. Caledonia, and J. P. Kennealy, J. Geophys. Res. **86**, 5247 (1981).

[18] W. T. Rawlins and R. A. Armstrong, J. Chem. Phys. **87**, 5202 (1987).

[19] W. T. Rawlins, G. E. Caledonia, J. J. Gibson, and A. T. Stair, Jr., J. Geophys. Res. **40**, 2896 (1985).

[20] B. D. Green, W. T. Rawlins, and R. M. Nadile, J. Geophys. Res. **91**, 311 (1986).

[21] W. T. Rawlins, J. Geophys. Res. **90**, 12283 (1985).

[22] D. L. Baulch, R. A. Cox, R. F. Hampson, Jr., J. A. Kerr, J. Troe, and R. T. Watson, J. Phys. Chem. Ref. Data **13**, 1259 (1984).

[23] W. T. Rawlins, A. Gelb, and R. A. Armstrong, J. Chem. Phys. **82**, 681 (1985).

[24] L. S. Rothman, R. R. Gamache, A. Barbe, A. Goldman, J. R. Gillis, L. A. Brown, R. A. Toth, J. M. Flaud, and C. Camy-Peyret, Appl. Opt. **22**, 2247 (1983).

[25] R. E. Huie, J. T. Herron, and D. D. Davis, J. Phys. Chem. **76**, 2653 (1972).

[26] I. Arnold and F. J. Comes, Chem. Phys. **42**, 231 (1979).

[27] O. Klais, P. C. Anderson, and M. J. Kurylo, Int. J. Chem. Kinet. **12**, 469 (1980).

[28] C. L. Lin and M. T. Leu, Int. J. Chem. Kinet. **14**, 417 (1982).

[29] T. G. Slanger and G. Black, J. Chem. Phys. **70**, 3434 (1979).

[30] F. Kaufman, Adv. Chem. Ser. **80**, 29 (1969).

[31] S. C. Brown, in *Encyclopedia of Physics, Vol. XXII Gas Discharges II*, edited by S. Flugge (Springer, Berlin, 1956), pp. 531-575.

[32] R. D. Kenner and E. A. Ogryzlo, Int. J. Chem. Kinet. **12**, 501 (1980).

[33] J. O. Hirschfelder, C. F. Curtiss, and R. B. Bird, *Molecular Theory of Gases and Liquids* (Wiley, New York, 1954).

[34] M. Quack and J. Troe, Ber. Bunsenges. Phys. Chem. **79**, 179 (1975).

[35] R. B. Bernstein and R. D. Levine, in *Advances in Atomic and Molecular Physics II*, edited by D. R. Bates and B. Bederson (Academic, New York, 1975), pp. 216–297; R. D. Levine and R. B. Bernstein, in *Modern Theoretical Chemistry, Vol. II: Dynamics of Molecular Collisions, Part B*, edited by W. H. Miller (Plenum, New York, 1975), Chap. 7.

[36] J. P. Kennealy, F. P. Del Greco, G. E. Caledonia, and B. D. Green, J. Chem. Phys. **69**, 1574 (1978).

[37] A. J. Stace and J. N. Murrell, J. Chem. Phys. **68**, 3028 (1978).

[38] A. Gelb, J. Phys. Chem. **89**, 4189 (1985).

[39] A. E. Croce de Cobos and J. Troe, Int. J. Chem. Kinet. **16**, 1519 (1984).

[40] A. Gelb and W. T. Rawlins, Physical Sciences Inc., TR-567, under Air Force Contract No. F19628-85-C-0032, 1986.

[41] N. Swanson and R. J. Celotta, Phys. Rev. Lett. **35**, 783 (1975).

[42] C. W. Wilson, Jr. and D. G. Hopper, J. Chem. Phys. **74**, 595 (1981).

[43] L. S. Frost and A. V. Phelps, Phys. Rev. A **136**, 1538 (1969).

[44] J. Dutton, J. Phys. Chem. Ref. Data **4**, 577 (1975).

[45] L. J. Kieffer, JILA Information Center Report, September 30, 1973, Vol. 13.

[46] S. A. Lawton and A. V. Phelps, J. Chem. Phys. **29**, 1055 (1978).

[47] K. Tachibana and A. V. Phelps, J. Chem. Phys. **75**, 3315 (1981).

[48] A. V. Phelps (private communication, 1982).

[49] C. H. Jackman, R. H. Garvey, and A. E. S. Green, J. Geophys. Res. **82**, 5081 (1977).

[50] J. W. Keto, J. Chem. Phys. **74**, 4445 (1981).

[51] J. Bretagne, J. Godart, and V. Peuch, J. Phys. D **15**, 2205 (1982).

Contents

1. Introduction 105
2. Apparatus 106
3. Kinetics 109
4. Results and Discussion 109
5. Conclusion 110
References 114

9. Quenching of Metastable Nitrogen Atoms (^2D,^2P) by O(^3P)

by

S.M. Miller and C.P. Fell

1. INTRODUCTION

Metastable nitrogen atoms are important constituents of the mesosphere and thermosphere. Atmospheric modelling studies[1] indicate that the reaction of N(^2D) with molecular oxygen is the primary source of the large NO concentrations observed in rocket experiments.[2] A recent measurement of the rate coefficient for quenching of N(^2D) by O(^3P)[3] reported a value of $\approx 3\exp(-145/T) \times 10^{-11}$ cm^{3}s^{-1}, considerably in excess of currently accepted experimental and theoretical estimates[4]

---

1. Caledonia G.E. and Kennealy, J.P. (1982) *Planet. Space Sci.* **30**:1043.
2. Meira, L.G. (1971) *J. Geophys. Res.* **76**:202.
3. Jusinski, L. and Slanger, T. *J. Phys. Chem.* , (in press).
4. Lin, C.L., Parkes, D.A., and Kaufman, F. (1970) *J. Chem. Phys.* **53**:3896.

(Figure 1). This would have serious implications for models of NO production in the upper atmosphere, and consequently, this rate of coefficient was remeasured to resolve this issue.

The quenching of N(^{2}D/^{2}P) has been studied in the FACELIF afterglow reactor. The O(^{3}P) atoms were generated by titrating NO directly into the main flow where it rapidly reacts with N(^{4}S) to generate O(^{3}P) with unit efficiency. Measurements have been taken over a wide range of mixing times with residual NO concentrations explicitly monitored.

2. APPARATUS

The data reported here were obtained with a Nd:YAG-pumped dye laser with wavelength extension optics (Quanta-Ray DCR-2A, PDL-1, WEX-1) in conjunction with the FACELIF flowing afterglow reactor[5] represented schematically in Figure 2. Matheson research-grade He and N_2 (99.9999 percent pure), and North Shore Cryogenics O_2 (99.9999 percent) were used in this work. Matheson NO (98 percent pure) was used for calibrations after flowing it through a purification manifold that included an ascarite trap and cryogenic trap consisting of a liquid nitrogen/methanol slurry.

N_2 gas passed through a 600°C Cu gettering furnace (modified Centorr model 28-20) and He passed through a 800°C Ti gettering furnace before entering the microwave discharge tube. The NO and He entering the flow through the circular injector shown in Figure 2 were used without further purification. The pressure during these measurements was in the range 0.5 - 4 Torr, as monitored by a 0-10 Torr Baratron Capacitance monometer. The flow rates of the individual gases were measured with mass flow meters (Tylan model FM360) calibrated with a bubble meter and stop watch.

Nitrogen atoms were produced by flowing a mixture of the scrubbed He and N_2 through a 30 watt 2450 MHz microwave discharge (Opthos model MPG-4M). The nitrogen atom number densities used for these measurement were 2.5×10^{13} to 1.3×10^{14} cm^{-3} as determined by standard NO titration methods.[6,7] A 0.5 m spectrometer (Spex model 1870B) equipped with a photomultiplier tube (RCA P28) was used for the titration measurements.

The NO/He mixture was introduced into the flow upstream of the discharge port and two Ni wire grid electrodes biased at 9V situated perpendicular to the flow with 1 cm separation.

The UV output from the WEX-1 was focused between the detector grids with a 250 mm focal length lens and passed through the detection region of the flow tube perpendicular to the flow direction. After exiting the flow tube, the laser beam struck a calibrated pyroelectric joulemeter (Molectron J3-05). The ion current produced by the focused beam and detected by the biased grids was dropped across a 100 MΩ resistor amplified (×100) by a PAR 113 amplifier and then fed into the A channel of boxcar integrator (PAR 165). Under our experimental conditions the ion current displayed a quadratic

---

5. Piper, L.G. (1988)
   J. Phys. Chem., in press EOS **69**.
6. Gerard, C., Feser, C.G., and Rusch, D.W.
7. Kaufmann, F. and Kelso, J.R. (1958) 7th International Symposium on Combustion, Oxford, p. 53.

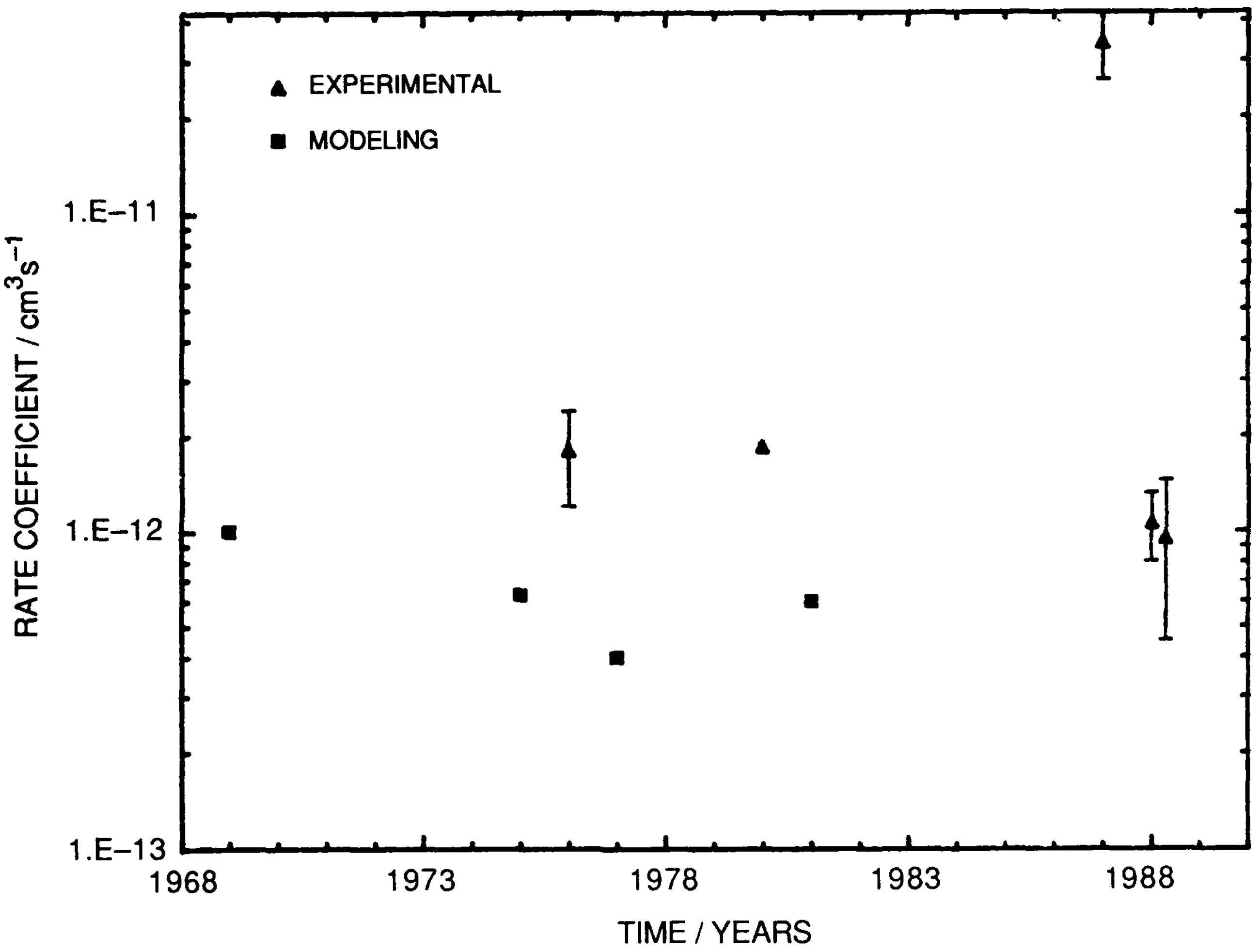

Figure 1. Some Previous Determinations of k_O

EXPERIMENTAL

SCHEMATIC DIAGRAM OF EXPERIMENTAL SET-UP

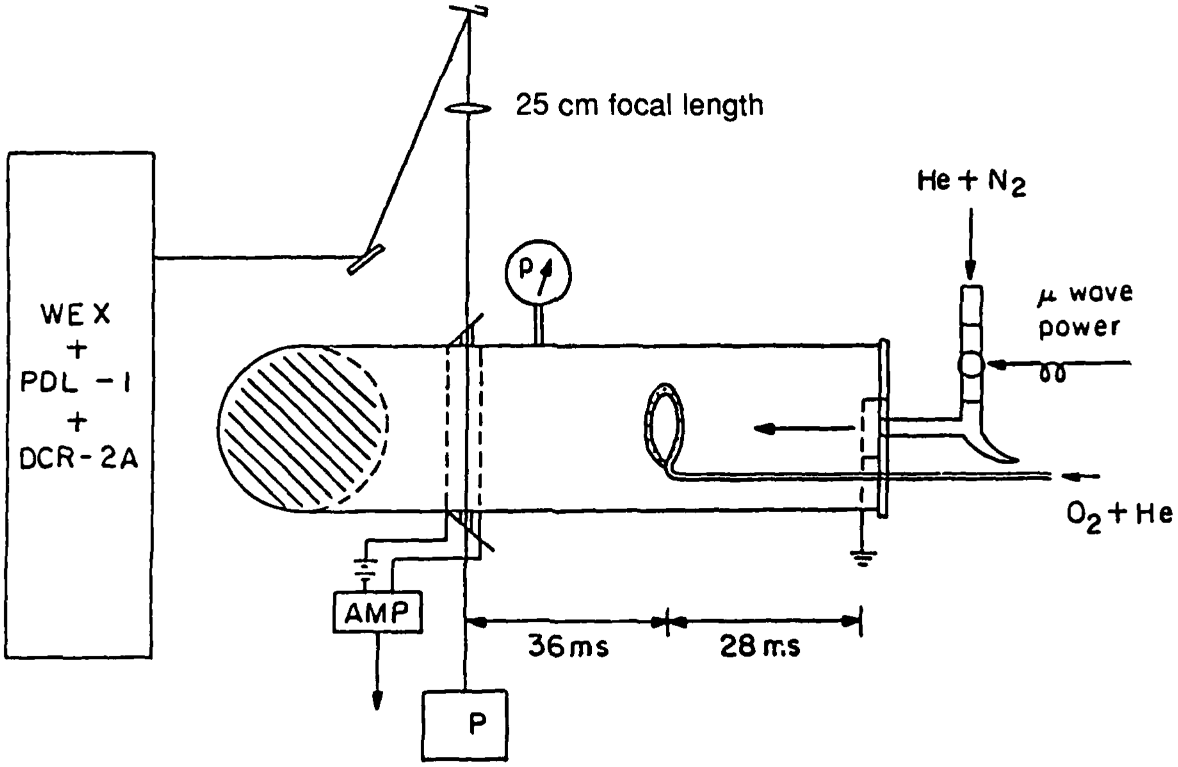

Generation of $O(^3P)$ atoms [Slarger et al. J. Phys. Chem. (in press)].

$$N(^4S) + NO \xrightarrow{fast} N_2 + O(^3P)$$

$$N(^2D/^2P) + O(^3P) \xrightarrow{k_O} N(^4S) + O$$

Figure 2. Schematic Diagram of Experimental Set-Up

dependence on the laser fluence. The output of the joulemeter was fed into the B channel on the same boxcar (PAR 165). The ion and laser power signals were then displayed on a chart recorder (HP 7132A).

3. KINETICS

The excited nitrogen species may be quenched by $O(^3P)$ and NO, both of which will be present in concentrations that vary along the length of the flowtube. The rate equation for the decay of N^* is

$$\frac{-d[N^*]}{dt} = K_{NO}[N_*] + K_O[N_*][O] + K_w[N^*] \text{ ,} \tag{1}$$

where K_w is the first order rate constant for wall deactivation. Integration of this equation between t = 0 and t gives

$$-\ln\frac{[N^*]}{[N^*]} = K_{NO}\int_0^t [NO]\,dt + K_O\int_0^t [O]\,dt + K_w t \text{ ,} \tag{2}$$

where $[N^*]_O$ is the initial concentration of $[N^*]$. The concentration of [O] at any given time t, is given by

$$[O]_t = [NO]_O - [NO]_t \tag{3}$$

where $[NO]_O$ is the initial concentration of NO. Equation (2) may then be rewritten as

$$-\ln[N^*] = K_{NO}\int_0^t [NO]\,dt + K_O\int_0^t \{[NO]_O - [NO]\}dt + \text{const.} \tag{4}$$

The NO concentration, assuming a large excess of $N(^4S)$ and $N(^4S) >> N^*$, is given by

$$[NO] = [NO]_O e^{-Kn[N]t} \tag{5}$$

where K_N is the well-known rate constant for the reaction $N(^4S)$ + NO.[4] Substituting this expression into Eq. (4) and integrating gives

$$-\ln[N^*] = K_O[NO]_O t + \frac{(K_{NO} - K_O)}{K_N[N]} 1 - e^{-K_N[N]t}[NO] \tag{6}$$

4. RESULTS AND DISCUSSION

The above analysis assumes that No is introduced uniformly across the flowtube. A crucial assumption used in obtaining the rate coefficient in Reference 3 was that the residence time of the NO in the flowtube was sufficiently short that No quenching of N^* atoms could be neglected. Here, we have explicitly measured the extent of completion of the $N(^4S)$ + NO reaction for a wide range of mixing times. This was done by monitoring the NO $\gamma(0,0)$ MPI-signal and titrating the NO, first with no microwave discharge (and hence no $N(^4S)$ atoms) and then repeating the titration with the microwave discharge on. The ratio of the two slopes gives the percentage completion of the reaction.

For the shorter mixing times, significant concentrations of NO were measured at the detection point. It was possible to vary the mixing time over a limited range by adjusting the injector to detector distance. In order to obtain the required wider range, it was also necessary to alter the pumping rate. The results, shown in Figure 3, display approximately exponential behavior and it is apparent that the NO is sufficiently long-lived to contribute significantly to the N* quenching. Comparative studies were performed using a perforated ball injector, as in Reference 3, with results indicating a marginally slower decay in the NO concentration.

The preliminary result are shown in Figure 4. The rate coefficients are calculated assuming, as in Reference 3, that the NO is uniformly converted to O(^{3}P) before making any contribution to the quenching. The form of the curve closely follows that for the NO decay. It is apparent from these results that the large apparent rate coefficients measured for short mixing times are primarily attributable to rapid quenching of N* by residual NO. The measurements at shorter mixing times therefore represent a lower limit to the NO quenching rates with the long mixing time measurements providing an upper limit to the O(^{3}P) quenching rates.

Examination of Eq. (6) shows that, to recover the true rate coefficient for the N* + O(^{3}P) reactions, it is necessary to know K_{no}, K_N and [N]. From Figures 4 and 5 it is apparent that the NO quenching rates are approximately an order of magnitude larger that the corresponding O(^{3}P) quenching rates. For the shorter mixing times the O(^{3}P) contribution may therefore be neglected, and if K_N and [N] are known, K_{NO} may be obtained directly. K_N has been measured previously[4] and , in theory, [N] may be obtained by a standard NO titration technique. For faster flows, and consequently lower pressures, the endpoint of the titrations become indistinct, precluding an accurate determination of [N]. To overcome this problem, the NO (0,0) MPI signal was measured as a function of mixing time (varied by adjusting the injector to detector distance). A plot of the logarithm of the NO (0,0) MPI signal versus time gives a slope of K_N [N]. The signal level initially displays the expected exponential decay before assuming a constant finite value. This is believed to be a physical effect brought about by the geometry of the flowtube. The diameter of the flowtube increases dramatically just downstream of the microwave discharge. As the injector is withdrawn towards the expansion point it begins to interfere with the flow in such a way that the gas from the injector does not become fully mixed until a certain distance downstream, characteristic of the flow speed. Consequently, results were only taken with the injector in the region exhibiting exponential behavior.

5. CONCLUSION

The results obtained in this study show that while measurements of the same magnitude, as in Reference 3, may be obtained for the N(^{2}D) + O(^{3}P) rate coefficient, these are associated with the presence of significant concentrations of NO in the flowtube. Preliminary results indicate that the true rate is of the order of $(6.9 \pm 1.0) \times 10^{-13}$ cm^3-s^{-1}. This is in excellent agreement with the results of a recent measurement by L. Piper[5], which derived a value of $(1.06 \pm 0.26) \times 10^{-12}$ cm^{3}s^{-1}. The O atoms in this instance were generated by three separate methods and the N(^{2}D) detected by resonance fluorescence. The close agreement obtained between these two studies, using different techniques, adds further weight to the validity of these results. The most recent modelling study[6] of NO and N(^{2}D) distributions in the mesosphere and thermosphere also favors a value of 1×10^{-12} cm^{3}s^{-1} for the N(^{2}D) + O(^{3}P) quenching rate coefficient, therefore obtaining, for the first time, agreement between modelling and experiment to within the limits of experimental error.

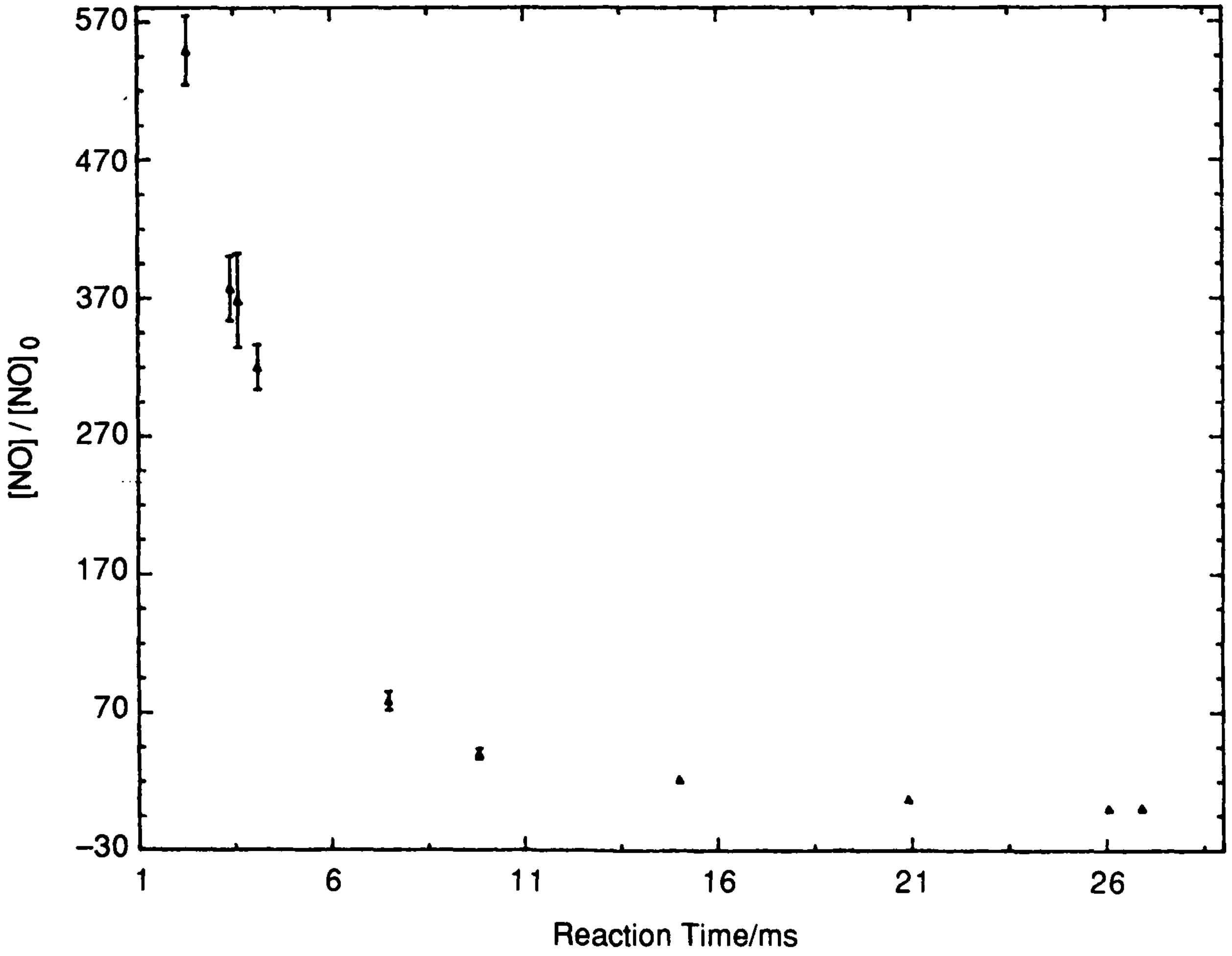

Figure 3. Residual NO Concentration vs Reaction Time

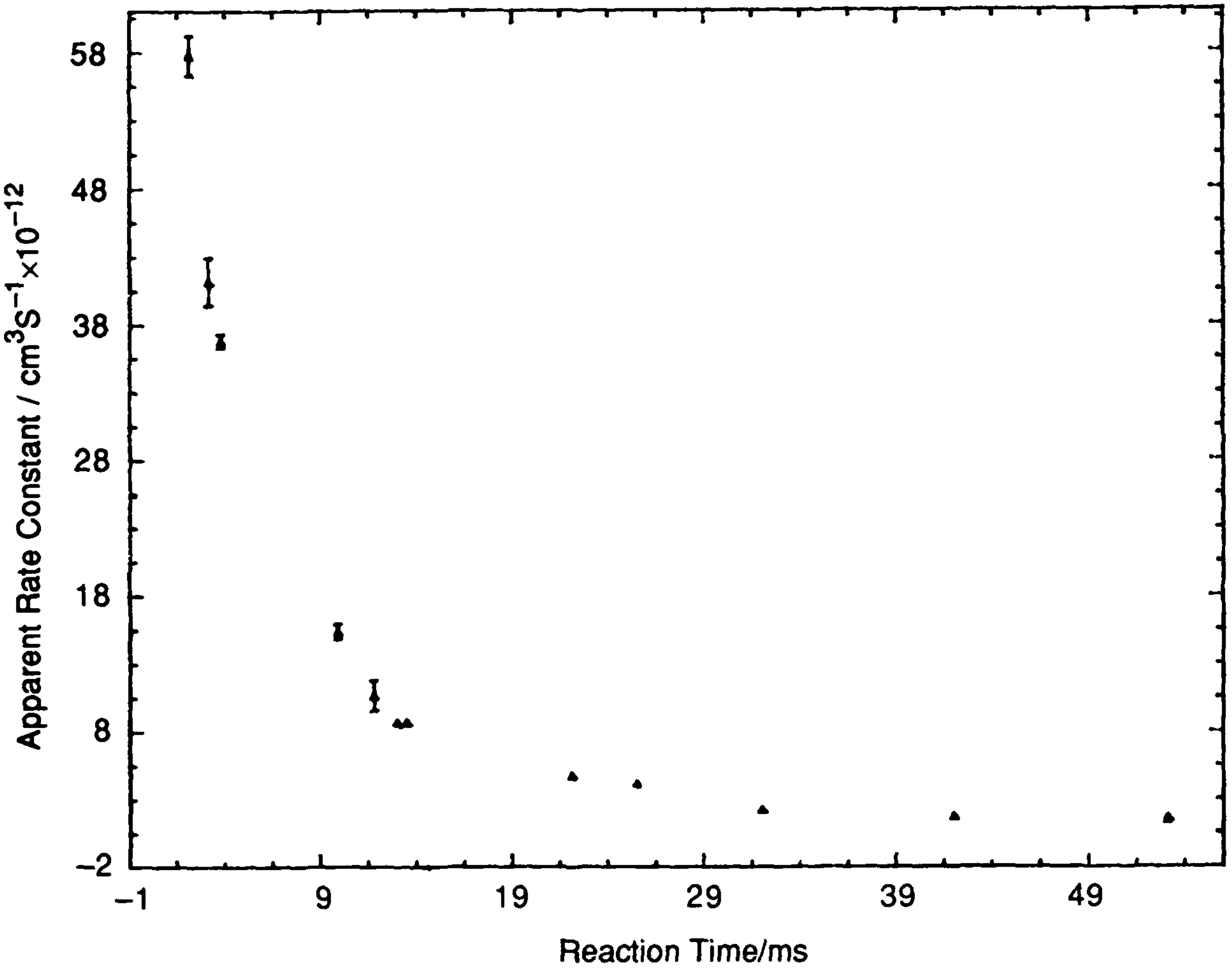

Figure 4. Variation in Apparent Rate Constant with Reaction Time $N(^2D) + O(^3P)$

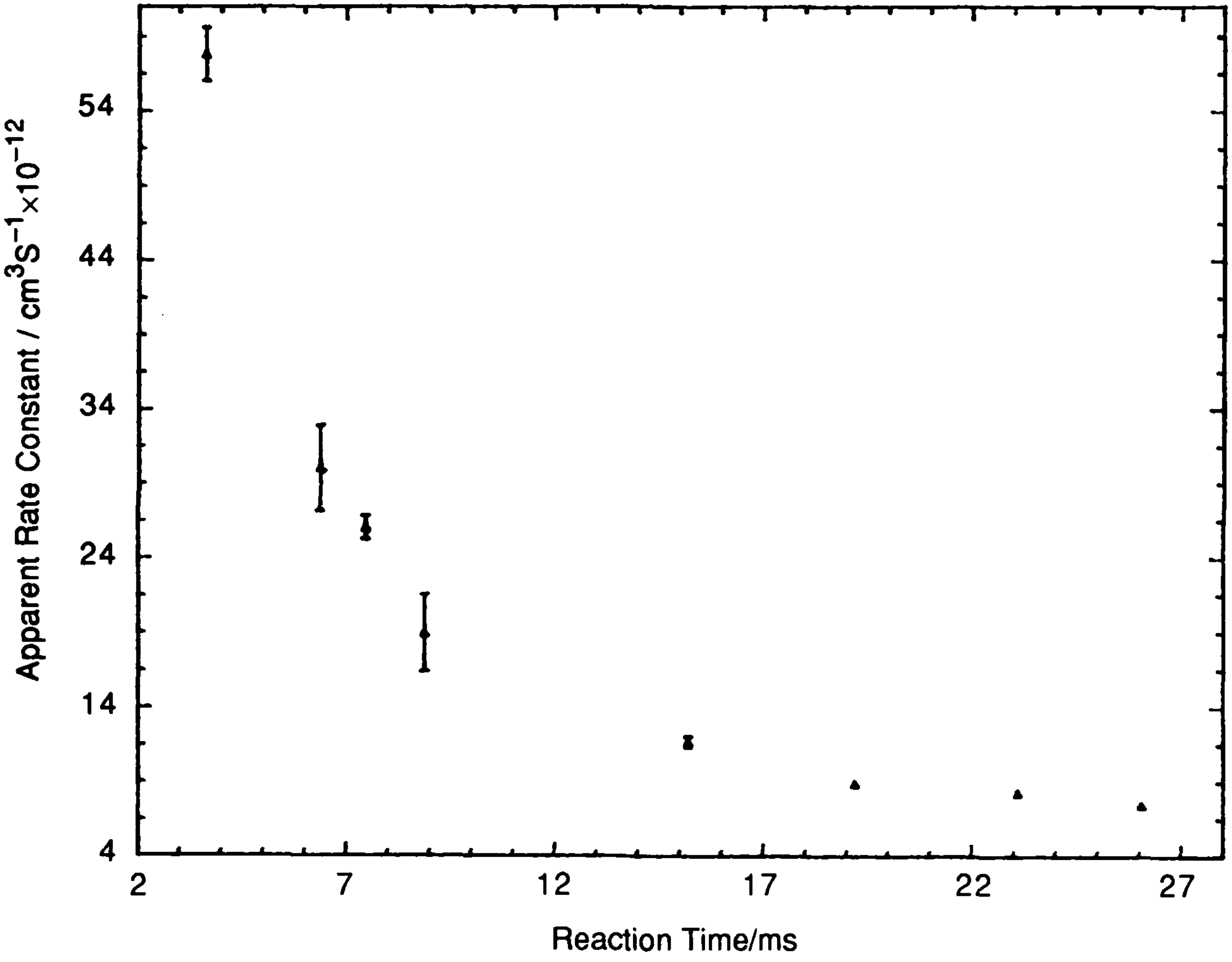

Figure 5. Variation in Apparent Rate Constant with Reaction Time $N(^2P) + O(^3P)$

References

1. Caledonia G.E. and Kennealy, J.P. (1982)
   Planet. Space Sci. **30**:1043.
2. Meira, L.G. (1971)
   J. Geophys. Res. **76**:202.
3. Jusinski, L. and Slanger, T.
   J. Phys. Chem. , (in press).
4. Lin, C.L., Parkes, D.A., and Kaufman, F. (1970)
   J. Chem. Phys. **53**:3896.
5. Piper, L.G. (1988)
   J. Phys. Chem., in press EOS **69**.
6. Gerard, C., Feser, C.G., and Rusch, D.W.

7. Kaufmann, F. and Kelso, J.R. (1958) 7th International Symposium on Combustion, Oxford, p. 53.

10. Determination of NO(V = 0-7) Product Distribution from the N(^4S) + O_2 Reaction Using Two-Photon Ionization

by

I.C. Winkler, R.A. Stachnik, J.I.Steinfeld, and S.M. Miller

Determination of NO ($v = 0$–7) product distribution from the N(^4S) + O$_2$ reaction using two-photon ionization

I. C. Winkler,[a] R. A. Stachnik,[b] and J. I. Steinfeld
Department of Chemistry, Massachusetts Institute of Technology, Cambridge, Massachusetts 02139
S. M. Miller
Air Force Geophysics Laboratory, Hanscom Air Force Base, Bedford, Massachusetts 01731

(Received 25 February 1986; accepted 7 April 1986)

The product vibrational state distribution for the reaction N(^4S) + O$_2$→NO($^2\Pi$,v) + O has been measured using saturated multiphoton ionization spectroscopy to determine NO electronic ground-state distributions. The fraction of the reaction exothermicity appearing in product vibration is $\langle f_v \rangle = 0.34$; however, the *even* vibrational levels ($v = 0,2,4,6$) are relatively overpopulated with respect to the *odd* vibrational levels ($v = 1,3,5$). It is not possible to obtain a good linear-surprisal fit to all the data, but the even and odd subsets fit quite well to individual surprisal plots. The results are compared with previous measurements, including a reanalysis of laser-excited fluorescence data corrected for electronic transition moment and Franck–Condon factor variations. Collisional relaxation is observed at high O$_2$ pressures for NO levels $v = 4$ through 7, and is fit with a phenomenological relaxation model.

I. INTRODUCTION

The elementary atom-transfer reaction

$$\mathrm{N}(^4S) + \mathrm{O}_2(^3\Sigma_g\ ) \rightarrow \mathrm{NO}(^2\Pi_r,v) + \mathrm{O}(^3P) \qquad (1)$$

has been the subject of numerous investigations. In addition to its fundamental interest, reaction (1) is important as a source of infrared emission from the upper atmosphere, since the NO molecules formed in vibrationally excited states can radiate their energy in either the fundamental

$$\mathrm{NO}(v) \rightarrow \mathrm{NO}(v-1) + h\nu(5\text{–}6\,\mu\mathrm{m}) \qquad (2)$$

or first overtone bands

$$\mathrm{NO}(v) \rightarrow \mathrm{NO}(v-2) + h\nu(2.5\text{–}3\,\mu\mathrm{m}). \qquad (3)$$

The determination of the vibrational product distribution in reaction (1) is therefore of considerable importance.

The absolute rate coefficient of reaction (1) at 300 K has been determined[1,2] to be

$$k_1 = \sum_{v=0}^{v_{\max}} k_1(v)$$
$$= (1.1 \pm 0.1) \times 10^{-16}\,\mathrm{cm}^3\,\mathrm{molecule}^{-1}\,\mathrm{s}^{-1}. \qquad (4)$$

The exothermicity $D_0^0\,(\mathrm{O}_2) - D_0^0\,(\mathrm{NO}) = -1.381$ eV $= 31.85$ kcal/mol; when this is added to the activation energy of 7–8 kcal/mol,[1] there is sufficient energy released to populate $v = 0$ through 7 of NO, and possibly $v = 8$ from higher-energy reactive collisions.

The product branching ratio

$$f(v) = k_1(v)/k_1 \qquad (5)$$

has been previously measured using several different techniques. Whitson *et al.*[3] and Rahbee and Gibson[4] used overtone chemiluminescence [reaction (3)] to determine relative final-state distributions for $v = 2$–7. Herm *et al.*[5] used laser-excited fluorescence (LEF) of NO to measure $f(v)$ for the full range of $v = 0$–7. There are numerous inconsistencies between these data sets, particularly as regards the populations of the higher v levels. The rate coefficient[6] and product distribution[7] for the reaction analogous to reaction (1) taking place with metastable excited nitrogen atoms, i.e.,

$$\mathrm{N}(^2D,^2P) + \mathrm{O}_2(^3\Sigma_g^-) \rightarrow \mathrm{NO}(^2\Pi_r,v) + \mathrm{O}(^3P) \qquad (6)$$

have also been determined. The role of this reaction in the kinetics will be discussed later.

Several recent developments have made it appropriate and advisable to remeasure $f(v)$. The v dependence of the electronic transition moment $M_{\mathrm{el}}(\bar{r})$ for the NO $A \leftrightarrow X$ system has been recalculated,[8] which permits a more accurate analysis of measurements using optical detection techniques. In addition, resonant multiphoton ionization (MPI) has been shown[9,10] to be a sensitive and state-specific technique for measuring small quantities of NO, and which is free of some of the systematic errors present when using LEF.

In this paper, we report the vibrational product distribution of NO produced in reaction (1) measured using resonant (1 + 1) MPI. The experimental method is described in Sec. II, and a kinetic analysis is presented in Sec. III. In Sec. IV, results are given for the $v = 0$–7 levels of the NO product. These results are compared with earlier measurements and are discussed in terms of available potential surfaces and dynamic models for the reaction in Sec. V.

II. APPARATUS AND EXPERIMENTAL METHOD

A. Apparatus

The data reported here were obtained with a Nd:YAG-pumped dye laser with wavelength extension optics (Quan-

---

[a] Present address: Massachusetts Institute of Technology Lincoln Laboratory, Lexington, Massachusetts.

[b] Present address: Jet Propulsion Laboratory, California Institute of Technology, Pasadena, California.

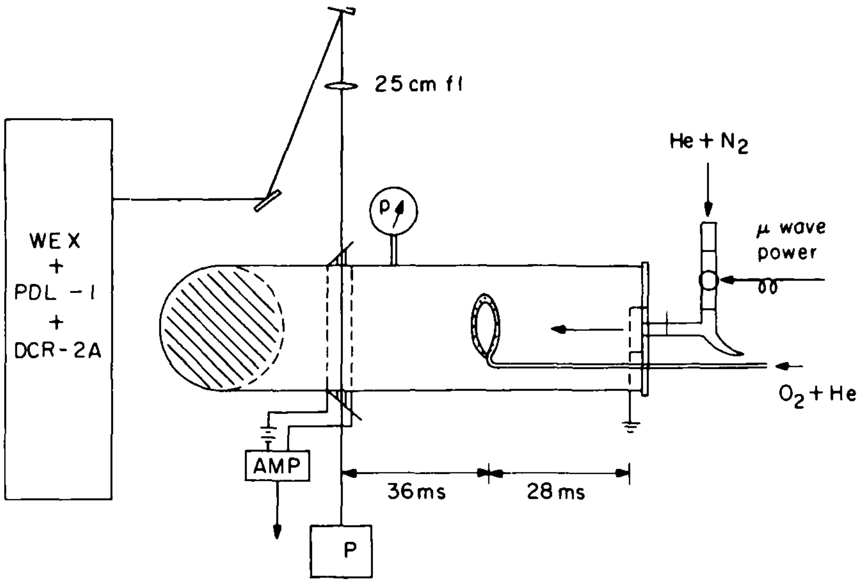

FIG. 1. Schematic of FACELIF experimental apparatus, modified for multiphoton ionization detection. Flow times from the N/N_2/He injection point to the O_2/He injection point, and thence to the MPI detection region, are indicated just under the flow tube. p is a capacitance manometer and P is a laser power/energy meter; the shaded area represents a right-angle connection to the pumping system.

ta-Ray DCR-2A, PDL-1, WEX-1) in conjunction with the FACELIF flowing afterglow reactor[11] represented schematically in Fig. 1. Matheson research-grade He and N_2 (99.9999% pure), and North Shore Cryogenics O_2 (99.9999%) were used in this work. Matheson NO (98% pure) was used for calibrations after flowing it through a purification manifold that included an ascarite trap and cryogenic trap consisting of a liquid nitrogen/methanol slurry.

N_2 gas passed through a 600 °C Cu gettering furnace (modified Centorr model 28-20) and He passed through a 800 °C Ti gettering furnace before entering the microwave discharge tube. The O_2 and He entering the flow through the circular injector shown in Fig. 1, were used without further purification. The average pressure during these measurements was 1.2 Torr and was monitored with a 0–10 Torr capacitance manometer (MKS Baratron). The flow rates of the individual gases were measured with mass flow meters (Tylan model FM360) calibrated with a bubble meter and stop watch.

Nitrogen atoms were produced by flowing a mixture of the scrubbed He and N_2 through a 30 W 2450 MHz microwave discharge (Opthos model MPG-4M). The nitrogen atom number densities used for these measurements were 2.5×10^{13} cm^{-3} and 5.6×10^{13} cm^{-3} as determined by standard NO titration methods.[12] A 0.5 m spectrometer (Spex model 1870B) equipped with a photomultiplier tube (RCA 31034A) in a cooled housing (Products for Research Model TE 182TSRF) was used for the titration measurements.

The flow tube was 5 cm in diameter and operated at a linear flow velocity of ~600 cm s^{-1}. These parameters ensured plug-flow conditions at the pressures used in these experiments. The O_2/He mixture was introduced into the flow 17 cm downstream, corresponding to 28 ms of flow time; this was varied in a few experiments to establish different measurement times. A pair of two Ni wire grid electrodes, situated perpendicular to the flow, spaced 1 cm apart, and biased at 45 V, were located 22 cm downstream of the O_2 injector at a point corresponding to an additional 36 ms of flow time. A grounded fine mesh Ni grid was placed just downstream of the nitrogen atom inlet to prevent charged species produced in the discharge from reaching the detector grids. The maximum ion density present in the reaction zone was estimated to be no greater than 10^8 cm^{-3}.

The UV radiation was generated by mixing the Nd:YAG fundamental (1.06 μm) with the frequency-doubled output of the YAG-pumped dye laser in the WEX-1. The output of the WEX was focused between the detector grids with a 250 mm focal length quartz lens and passed through the detection region of the flow tube perpendicular to the flow direction. After exiting the flow tube, the laser beam struck a calibrated pyroelectric joulemeter (Molectron J3-05). The ion current produced by the focused beam and collected by the biased grids was amplified ($\times10^{10}$) by a current to voltage amplifier mounted directly on the flow tube then fed into the A channel of a boxcar integrator (PAR 164/162). Under our experimental conditions the ion current was on the order of picoamps and was linearly dependent on the laser fluence. The output of the joulemeter was fed into the B channel of the same boxcar (PAR 165) which was operated in the A/B mode for shot-to-shot normalization of the ion signal to the laser power. The normalized signal was displayed on one channel of a chart recorder (HP 7132A). The joulemeter was coupled to a second boxcar whose output was displayed on the second channel of the chart recorder. This provided a record of the laser output.

The normalization procedure was checked by monitoring the ion current and laser power separately. The vibrational distribution measured by this method agreed well with the data collected using the boxcar operating in the A/B mode.

B. Experimental method

The NO γ bands used to measure the ground state populations are given, along with their wavelengths, in Table I. These bands were chosen because they were situated in con-

TABLE I. $\gamma(v',v'')$ P_{11} bandhead wavelengths.[a]

v',v''	λ(nm)
0,0	226.28
1,1	223.92
2,2	221.62
3,3	219.40
3,4	228.38
0,5	284.93
1,6	280.10
1,7	294.18

[a] Data are taken from R. Engleman, Jr., P. E. Rouse, H. M. Peak, and V. D. Balamonte, *β and γ band systems of NO*, Los Alamos Scientific Laboratories Report LA-4364 (1970), and are accurate to ± 0.01 nm.

venient wavelength regions and were free from overlap with other bands. The spectral feature chosen for kinetic measurements was the P_{11} bandhead since it was the most intense feature in most of the γ-band spectra; however, the relative intensity of this feature varies among the γ bands. To correct for this variation, the ratios of P_{11} bandhead intensity to the integrated band intensity were determined for each band by fitting calculated spectra to the observed spectra. The spectroscopic constants employed in this fitting procedure are given in Ref. 13.

A measured two-photon ionization spectrum and a synthesized one photon absorption spectrum are shown in Fig. 2. The synthesized spectrum was calculated without Hönl–London factors. This is appropriate for an NO spectrum in which the $A \leftarrow X$ transition is saturated[10] and provides further evidence that the laser fluence used in the kinetic measurements was sufficient to insure a linear dependence of the ion signal on the laser fluence. The linear fluence dependence was checked for each γ band listed in Table I by measuring the unnormalized ion signal as the laser power was varied. Operating in the saturation regime eliminates the need to correct the kinetic data for variations in the γ-band absorption strengths due to Franck–Condon factors or a v dependence of the electronic transition moment.

The ionization probabilities of the intermediate $A\,^2\Sigma^+$ states must also be considered when measuring NO ground state populations with two-photon ionization. Since only one such cross section has been reported to date,[14] we assume these cross sections are all equal. Support for this assumption is provided by a measurement of the $v = 6$ populatin via $\gamma(0,6)$ and $\gamma(1,6)$; the results agreed to within approximately 15%. Moreover, no intensity anomalies were observed in the eight γ bands recorded, indicating that at least within the 200 cm^{-1} scan the ionization probabilities are equal. Further details on the quantitative use of two-photon ionization are given in Ref. 10.

The kinetic measurements were made by scanning the laser to the peak of the P_{11} bandhead, then varying the O_2 pressure while the laser wavelength remained fixed at the peak. Since the bandhead is broad compared to the laser linewidth, small changes in the laser wavelength during data acquisition had no detectable effect on the signal strength. The system response was calibrated for NO($v = 0$) by measuring the intensity of the P_{11} bandhead as a function of purified NO added to the flow. The resulting calibration curve is shown in Fig. 3; the response is linear over a factor of 30 in NO density, with a lower limit of detection on the order of 10^7 molecule cm^{-3}.

III. KINETIC ANALYSIS

The kinetic model used to interpret these measurements is the same as that used in previous work,[5] with the explicit addition of a phenomenological relaxation term for NO(v). That is, we consider reaction (1),

$$N + O_2 \rightarrow NO(v) + 0$$

along with a rapid reaction which consumes NO,

$$NO(v) + N \xrightarrow{k_2} N_2 + O.$$

These two elementary steps yield a steady-state solution for

$$[NO(v)]_{ss} = \frac{k_1(v)}{k_2}[O_2] \tag{7}$$

when $k_2 \gg k_1$ and is assumed to be independent of v.

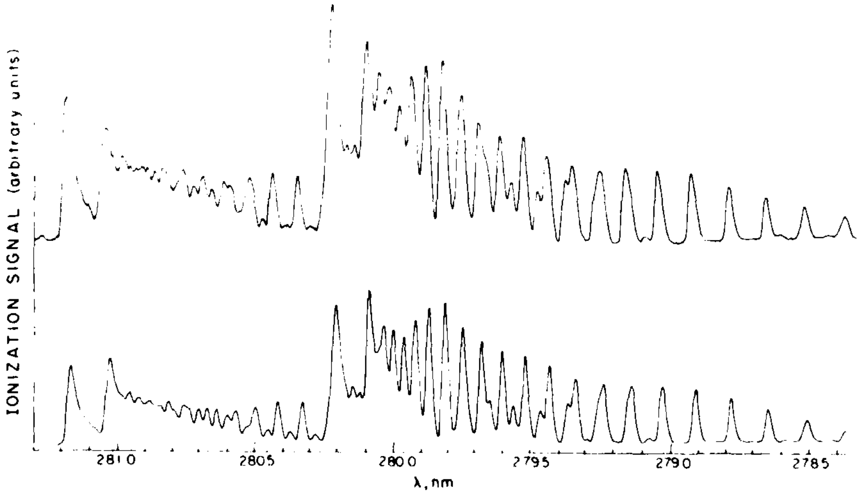

FIG. 2. MPI spectrum of the γ(1,6) band of NO produced in the flowing afterglow apparatus. Upper trace: experimental spectrum. Lower trace: synthesized spectrum calculated for saturated two-photon resonant ionization.

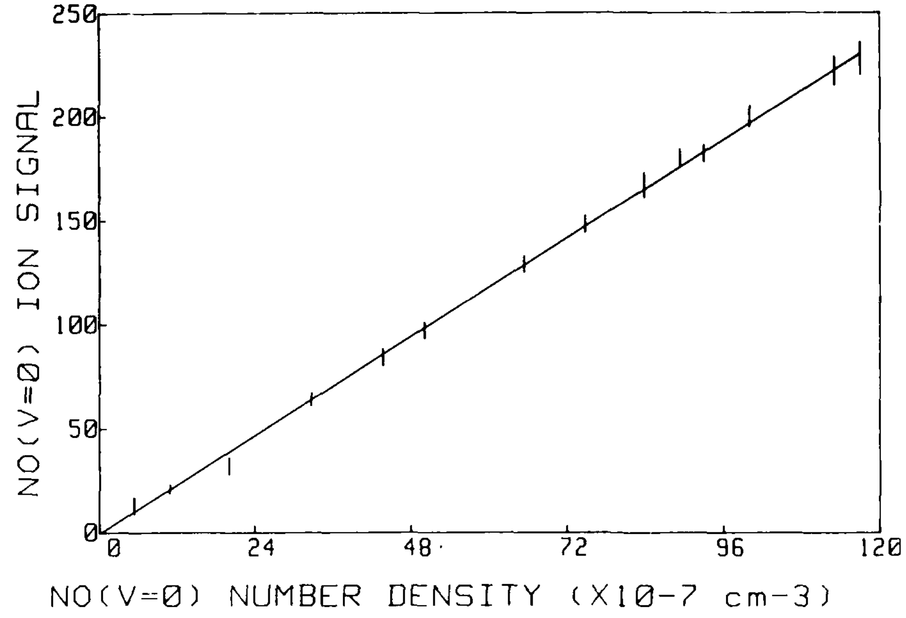

FIG. 3. Multiphoton ionization signal vs number density of NO added to the flow. The $\gamma(0,0)$ band is used as the resonant transition.

Collisional deactivation of vibrationally excited NO may be represented by

$$\mathrm{NO}(v) + \mathrm{M} \xrightarrow{k'} \mathrm{NO}(v' \neq v) + \mathrm{M}. \tag{8}$$

Oxygen molecules are expected to be the most efficient relaxation partner in the reaction system[15]; other species present, such as N atoms or N_2, possess deactivation rates at least an order of magnitude smaller. If we take $\mathrm{M} = O_2$, the steady-state treatment yields

$$[\mathrm{NO}(v)]_{ss} = \frac{k_1(v)[\mathrm{N}][O_2]}{k_2[\mathrm{N}] + k'[O_2]} = \frac{k_1(v)[O_2]}{k_2 + k''[O_2]}, \tag{9a}$$

where $k'' = k'/[\mathrm{N}]$, and may be v dependent. The approach taken in the analysis of the kinetic data presented in the following section has been to fit the empirical values of k'' to the $[\mathrm{NO}(v)]$ vs $[O_2]$ plots. This yields an effective net deactivation rate when the linear relationship predicted by Eq. (7) is not obeyed, and allows us to extract corrected values of $k_1(v)$ in the limit of $[O_2] \to 0$. For those values of v for which $k''[O_2] \ll k_2$, a linear dependence is obtained, and only an upper limit on k'' can be determined. It should be emphasized that values obtained in this way are themselves lower bounds to the true deactivation rates, since they represent the net effect of deactivation to lower v levels and cascade population from higher levels.

A more detailed kinetic model was also analyzed, using a nonlinear least-squares fit to the form

$$[\mathrm{NO}(v)]_{ss} = \frac{k_1(v)[\mathrm{N}][O_2] + k'(v+1)[O_2]}{k_2[\mathrm{N}] + k'(v)[O_2]}. \tag{9b}$$

Equation (9b) accounts for both deactivation to lower v levels and cascade population from higher levels. Values of $k'(v)$ derived in this way agreed within 50% with the values determined using the simple phenomenological expression, Eq. (9a).

The possible role of electronically excited nitrogen atoms (^2P, ^2D) in the overall kinetics has been considered by us as well as by other workers. Under our experimental conditions, the mean lifetime of $\mathrm{N}(^2D)$ with respect to loss at the walls is on the order of 2 ms.[6] Metastable nitrogen atoms from the discharge therefore make a negligible contribution to the observed $\mathrm{NO}(v)$. At high $\mathrm{N}(^4S)$ concentration, however, a steady-state concentration of $\mathrm{N}(^2P)$ can be established by the energy-pooling reactions[16]

$$\mathrm{N} + \mathrm{N} + \mathrm{M} \to N_2(A\,^3\Sigma) + \mathrm{M}$$

$$k_{10} = 3.8\times 10^{-33}\ \mathrm{cm^6\,s^{-1}}, \tag{10}$$

$$\mathrm{N} + N_2(A\,^3\Sigma) \to \mathrm{N}(^2P) + N_2(X\,^1\Sigma)$$

$$k_{11} = 5\times 10^{-11}\ \mathrm{cm^3\,s^{-1}}, \tag{11}$$

and

$$N_2(A\,^3\Sigma) + O_2 \to \text{products}$$

$$k_{12} = 3\times 10^{-12}\ \mathrm{cm^3\,s^{-1}}. \tag{12}$$

The steady-state concentration is given by

$$[\mathrm{N}(^2P)]_{ss} = \frac{k_{10}k_{11}[\mathrm{M}][\mathrm{N}]^3}{(k_6[O_2] + k_w(P))(k_{11}[\mathrm{N}] + k_{12}[O_2] + k_w(A))}, \tag{13}$$

where the rate coefficient[6] for reaction (6) is $k_6 = 3.5\times 10^{-12}\ \mathrm{cm^3\,s^{-1}}$ and $k_w(P)$ and $k_w(A)$ are the wall loss rate constants for $\mathrm{N}(^2P)$ and $N_2(A\,^3\Sigma)$, respectively. Under the conditions of these measurements, evaluation of Eqs. (13) and (7) indicates that $\mathrm{N}(^2P)$ makes at most a 10% contribution to the NO concentration in the low O_2 limit. The absence of a pronounced [N] dependence, and

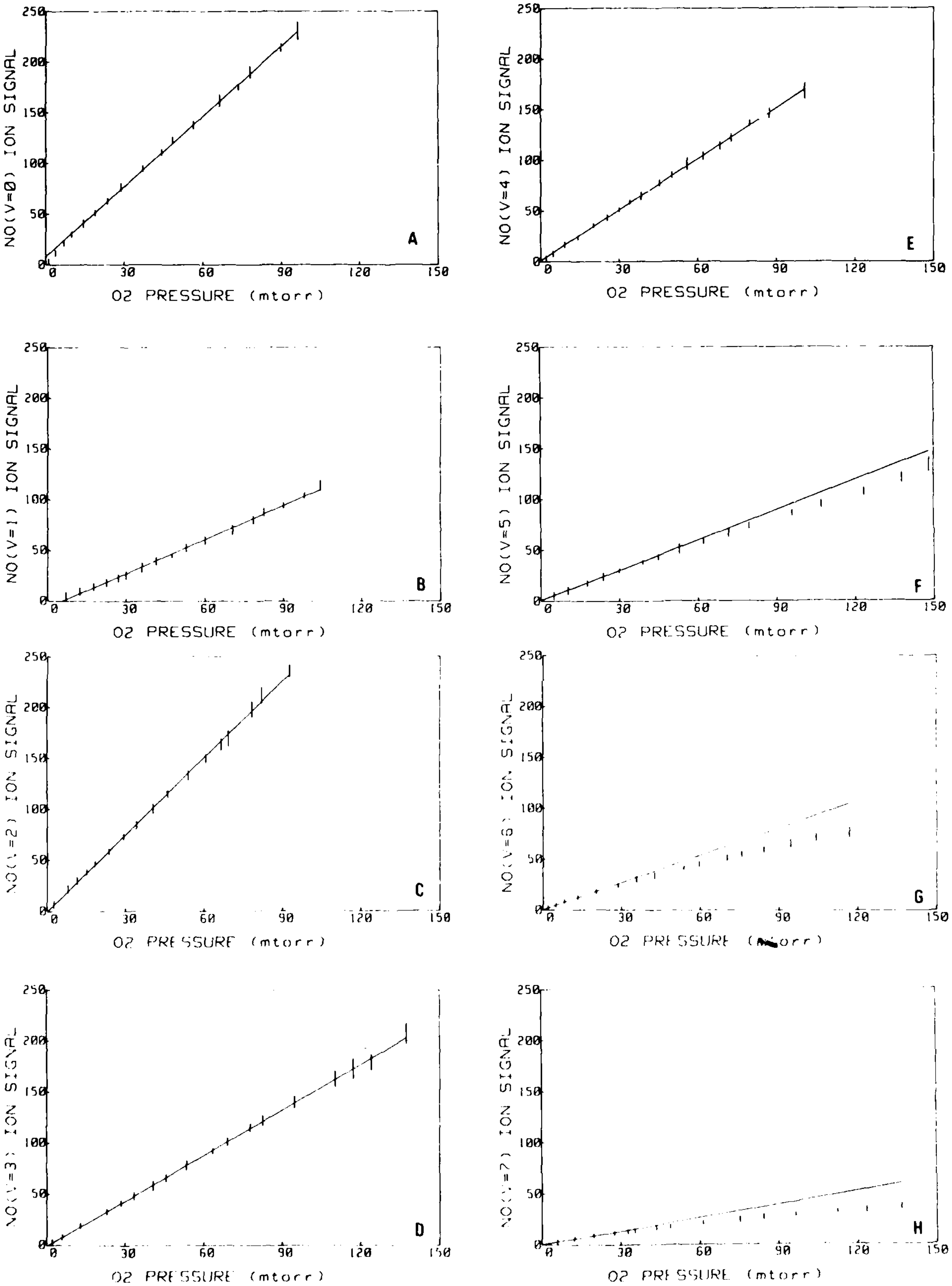

FIG. 4. NO(*v*) multiphoton ionization signal vs partial pressure of added O_2. Panels (A)–(H) give data for $v = 0$ through 7, respectively. N atom density is 5.6×10^{11} cm^{-3}.

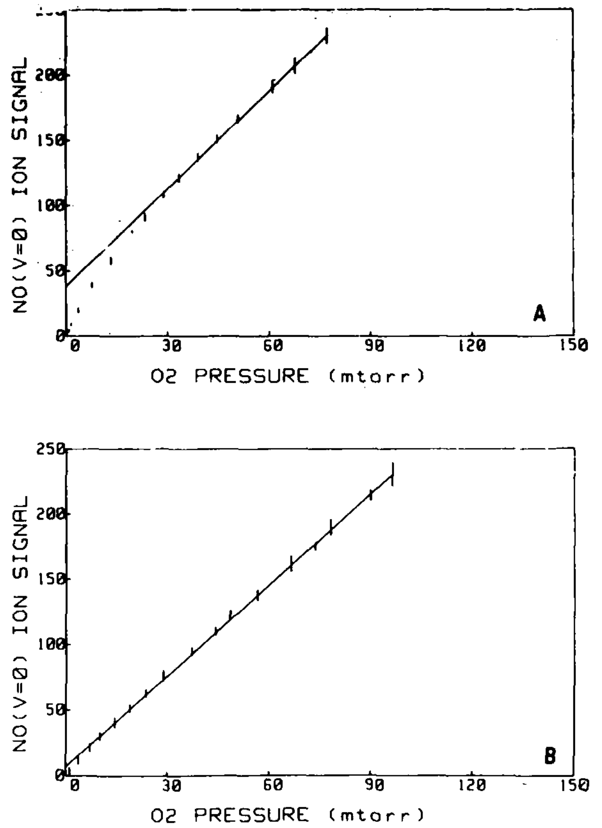

FIG. 5. NO($v=0$) multiphoton ionization signal vs partial pressure of added O_2 for (A) low N atom density (2.5×10^{13} cm^{-3}) and (B) high N atom density (5.6×10^{13} cm^{-3}).

absence of NO molecules in $v>8$ (next section), both suggest that reaction (6) does not make a significant contribution to the observed NO signals. Similar conclusions were reached in previous studies.[5,16]

IV. RESULTS

The plots of NO(v) ion signal vs O_2 pressure shown in Fig. 4 illustrate the range of O_2 pressures for which the simple steady-state analysis given in Sec. III is applicable. Equation (7) predicts a linear relationship between [NO] and [O_2] at low [O_2], and this is observed for NO($v=1$) through NO($v=7$). For higher O_2 pressures, the data points for $v=4$ and above begin to fall below the straight line which describes the low pressure behavior. This will be discussed later in this section.

The NO($v=0$) data show some curvature at low O_2 pressure. This effect is more pronounced when the N-atom concentration is lowered, as shown in Fig. 5. We also note, however, that the limiting slopes are the same within the measurement uncertainties. This curvature at low [O_2], which was also observed in Ref. 5, is not due to residual ground-state NO present in either the N_2 discharge or the added O_2. The NO produced in the discharge from O_2 and H_2O impurities makes a constant ([O_2] independent) contribution to the $v=0$ signal, and has already been subtracted from the data presented in Fig. 5; in no case was the correction greater than 10% of the maximum signal. Moreover, no signals were observed from NO($v=1$–7) prior to addition of O_2. There was no NO signal present when O_2 was flowed into the detection region in the absence of the discharge. The curvature also does not appear to be due to N(^2D,^2P), produced either in the discharge or by the energy-pooling reactions discussed in the previous section. Evaluation of the kinetics including Eqs. (6) and (10)–(12) indicates that a contribution from metastable nitrogen atoms would contribute a *negative* curvature at low [O_2], which cannot account for the data represented in Fig. 5. Furthermore, a search was made for populations in $v>8$, which should be populated by the N(^2D, ^2P) + O_2 reaction, but no signals could be detected. Based on detection limits imposed by interfering features from other bands, an upper limit for $f(8)<0.5\%$ can be estimated.

We do not have a satisfactory explanation for the curvature in NO($v=0$) at low [O_2]. There may possibly be ions or electrons from the discharge getting through the first set of grids, which could provide additional reactive pathways to NO until quenched by added O_2; however, the reaction $N^+(^3P) + O_2 \rightarrow O^+ + NO(X,v')$ is known[17,18] to constitute only 5% of the total ion–molecule reaction rate, and with the

TABLE II. Branching ratios and rate coefficients for the $N(^4S) + O_2 \rightarrow NO(^2\Pi,v) + O$ reaction.

	$k_1(v)$ (cm^3 $molecule^{-1}$ $s^{-1}\times10^{17}$)			
v	[N] = 2.5×10^{13} cm^{-3} reaction time = 36 ms average of three runs	[N] = 2.5×10^{13} cm^{-3} reaction time = 46 ms one run	[N]5.6×10^{13} cm^{-3} reacton time = 36 ms average of two runs	$f(v)\times100$
0	1.54 ± 0.41	1.43	1.28	21.0 ± 1.7
1	0.82 ± 0.02	0.60	0.59 ± 0.06	10.4 ± 1.3
2	1.55 ± 0.30	1.10	1.44 ± 0.01	21.8 ± 2.0
3	0.76 ± 0.03	0.62	0.90 ± 0.02	11.6 ± 2.7
4	1.13 ± 0.10	0.72	1.10 ± 0.16	16.3 ± 2.2
5	0.57 ± 0.03	0.32	0.59 ± 0.01	8.5 ± 1.2
6	0.48 ± 0.07	0.31	0.55 ± 0.04	7.4 ± 1.2
7	0.31 ± 0.02	0.22	0.32 ± 0.02	4.6 ± 0.7
8	...	...	...	<0.5
$k_1 = \sum_{v=0}^{7} k_1(v) = 7.20\pm0.97$		5.31	6.52 ± 0.32	

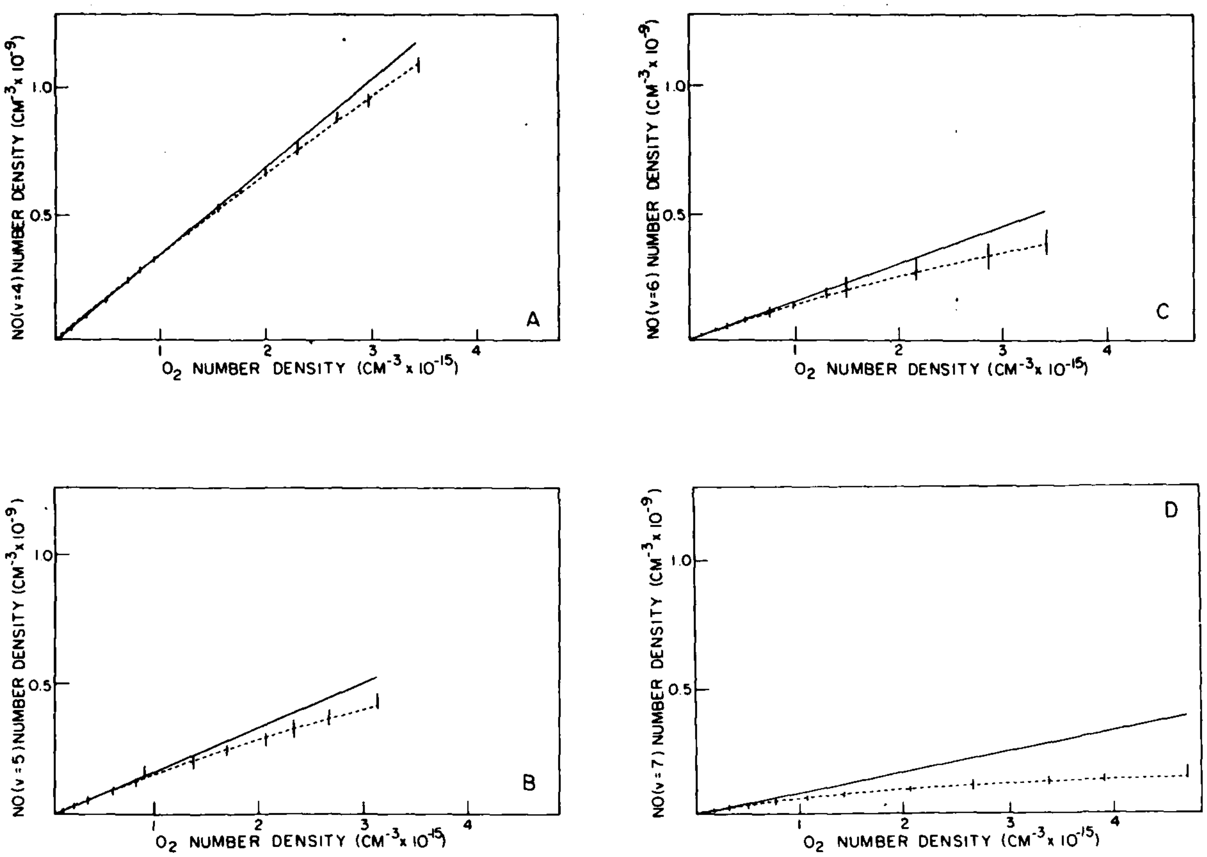

FIG. 6. NO(v) number density, obtained from multiphoton ionization signal, vs partial pressure of added O$_2$ at low N atom density (2.5×10^{13} cm^{-3}). Panels (A)–(D) give data for $v = 4$ through 7,; respectively. The solid straight line is the prediction of Eq. (7), i.e., setting $k'' = 0$ in Eq. (9); the dashed curves are obtained using Eq. (9) with $k''(v) =$ (A) 9.0×10^{-28} ($v = 4$); (B) 3.2×10^{-27} ($v = 5$); (C) 3.6×10^{-27} ($v = 6$); and (D) 1.3×10^{-26} ($v = 7$).

total ion density less than 10^8 cm^{-3}, this is unlikely to make a significant contribution to the observed NO signals. It may be that the steady-state condition (7) is not reached at the low O$_2$ concentrations. In any case, we have chosen the linear portion of the [NO] vs [O$_2$] curve as representative of the $v = 0$ rate coefficient, in part because the limiting slope gives self-consistent values over a range of N atom concentrations.

The branching ratios $f(v)$ and absolute rate coefficients $k_1(v)$ in Table II were calculated from the linear slopes of the curves in Fig. 4, and from similar curves obtained under a range of experimental conditions. The branching ratios may be obtained directly from the relative slopes normalized to 100%, and the uncertainties are the statistical variations among the data. Changing the N atom concentration from 2.5×10^{13} to 5.6×10^{13} cm^{-3} has little effect on the observed distribution. The detection time was varied from 36 to 46 ms by withdrawing the O$_2$ injector from the MPI detection region (see Fig. 1); this resulted in a slightly more relaxed distribution of NO(v).

Absolute rate coefficients $k_1(v)$ were calculated from the slopes of the NO signal vs [O$_2$] curves, according to Eq. (7). The MPI signals were converted to NO concentrations using the calibration data appropriate to the specific experimental conditions. The value of $k_2 = (3.4 \pm 0.9)\times 10^{-11}$ cm^3 molecule^{-1} s^{-1} was taken from Ref. 19.

Data obtained at the lower N atom concentration for NO($v = 4$–7) are shown in Fig. 6. The dashed curve is a plot of Eq. (9a) used to account for the nonlinear behavior at high O$_2$ pressure. The value of $k_1(v)$ is calculated from the slope of the straight line fit (solid line) of the data taken at low O$_2$ pressure, k_2 is taken from Ref. 17 and k'' is an adjustable parameter. The values of k'' fit to the data are 9.0×10^{-28}, 3.2×10^{-27}, 3.6×10^{-27}, and 1.3×10^{-26} (cm^6 s^{-1}) for $v = 4$, 5, 6, and 7, respectively. These values scale with v as expected.[15] For $v = 1$, 2, and 3, the plot of NO(v) vs [O$_2$] is linear, and only an upper limit on $k'' < 10^{-28}$ cm^6 s^{-1} can be inferred.

V. DISCUSSION

A. Product vibrational distributions

The product branching ratios $f(v)$ from Table II are plotted in Fig. 7 against f_v, the fraction of the total available reaction energy appearing in product vibration. The total energy was estimated by adding the reaction exothermicity (32 kcal/mol), the experimental activation energy (~ 7 kcal/mol),[1] and reactant thermal energy (~ 2 kcal/mol) to

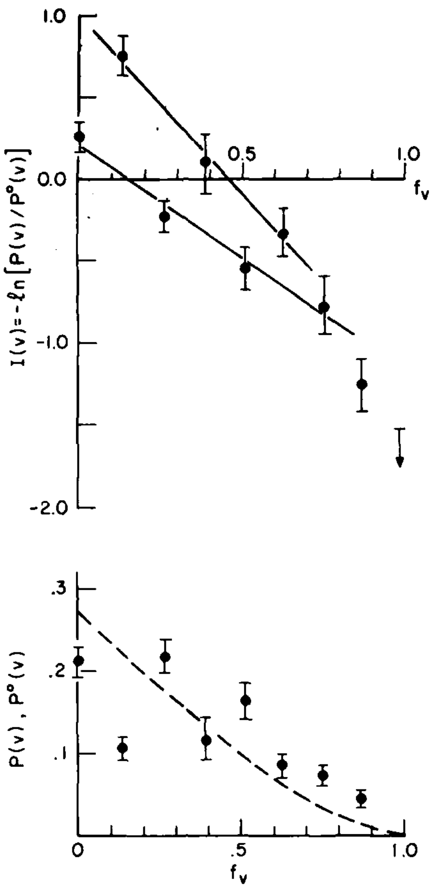

FIG. 7. Product vibration distributions for the reaction $N(^4S) + O_2 \rightarrow NO(^2\Pi, v) + O$. The lower panel shows the experimental $P(v)$ values as points with associated error limits, and the calculated prior $P^0(v)$ as the dashed curve. The upper panel is a linear surprisal plot of the data, with separate fits for even v (0,2,4,6) and odd v (1,3,5).

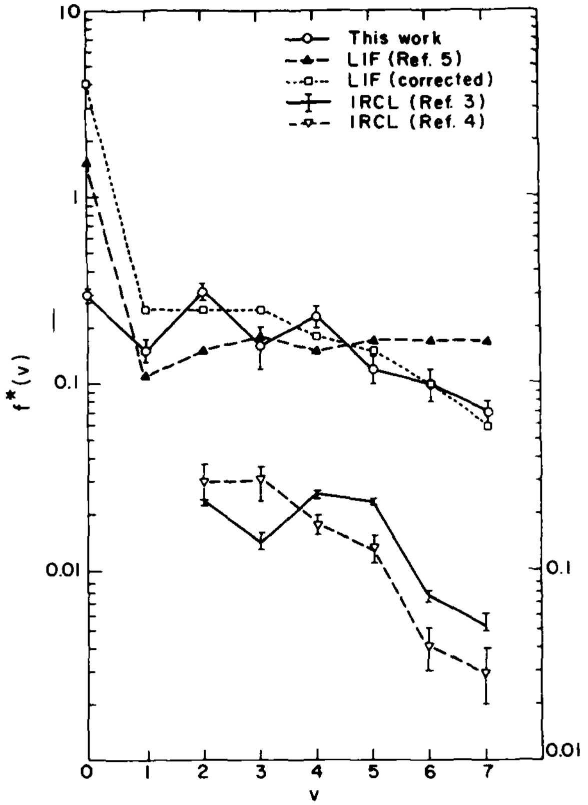

FIG. 8. Comparison of $N(^4S) + O_2 \rightarrow NO(v) + O$ branching ratios from IR chemiluminescence,[3,4] LEF,[5] and MPI (present work) measurements. Also shown are the reanalyzed LEF data corrected for $R_e(\bar{r})$ and Franck–Condon variations. The IRCL data are offset for clarity.

give a total approximately 41 kcal/mol. NO vibrational term energies were calculated using the spectroscopic constants in Ref. 13. The average amount of energy in product vibration is found as

$$\langle f_v \rangle = \sum_{v=0}^{7} f(v) f_v = 0.34, \qquad (14)$$

i.e., about one-third of the total energy appears in product vibration.

The results obtained in this work are compared with the previous LEF[5] and IR chemiluminescence[3,4] measurements in Fig. 8. In order to facilitate comparison with the latter data, we define a renormalized distribution function

$$f^*(v) = \frac{k(v)}{\Sigma_{v=2}^{7} k(v)}, \qquad (15)$$

which enables the data for v = 2 through 7 to be directly compared. The LEF data have been reanalyzed taking into account the variation of the electronic transition moment with r centroid[8] and a reevaluation of Franck–Condon factors for the A–X transition. The $R_e(\bar{r})$ correction is relatively small, but the $q_{v'v''}$ values[20] used in Ref. 5 do not agree with the generally accepted ones.[21,22] The result of this reanalysis may be seen in Fig. 8: the corrected LEF results are in much better agreement with both the IR chemiluminescence and the present MPI results, particularly at the high v levels. The major discrepancy is in the $v = 0$ rate coefficient; this results from the choice of limiting slope in the NO signal versus O_2 pressure plots, as discussed previously. The total reaction rate coefficient

$$k_1 = \sum_{v=0}^{7} k_1(v) = (7.2 \pm 0.97) \times 10^{-17}\ \mathrm{cm^3\,s^{-1}}$$

is somewhat smaller than the value $[(1.1 \pm 0.1) \times 10^{-16}]$ determined in Refs. 1 and 2.

An additional feature of these results is an apparent alternation of rates, and therefore level populations, for $v = 0$ through 5. The even vibrational levels appear to be overpopulated relative to adjacent odd v levels. A suggestion of such alternation is present in one of the chemiluminescence measurements: Whitson *et al.*[3] found a distribution in $v = 2$, 3, and 4 quite similar to the present results. Measurements on the $N(^2D) + O_2$ reaction[7] have also given a product distribution oscillating around the statistical prior distribution (see below), but did not show a regular even–odd alternation. A remeasurement out of the product vibrational distribution in the $N(^2D) + O_2$ reaction would be very useful at this time.

The population alternation is made even more clear by an information-theoretic analysis[23] of the data. In this analysis, the prior or statistical distribution is given by

$$P^0(v) \propto \frac{5}{2}(1-f_v)^{3/2} \tag{16}$$

with the prior normalized to unity,

$$\sum_{v=0}^{7} P^0(v) = 1. \tag{17}$$

The surprisal is defined as

$$I(v) = -\ln[P(v)/P^0(v)] \tag{18}$$

with $P(v) \equiv f(v)$. The resulting surprisal plot of $I(v)$ vs f_v is shown in the upper part of Fig. 7. It is not possible to obtain a good linear surprisal fit

$$I(v) = -\lambda^0 - \lambda_v f_v \tag{19}$$

to all the points; however, the individual subsets $v = 0,2,4,6$ and $v = 1,3,5$ lie along separate straight lines with slopes $\lambda_v = -1.38 \pm 0.36$ and $\lambda_v = -2.17 \pm 0.74$, respectively. The difference between these values is marginally significant, but is consistent with the observed excess population in even as compared with odd v levels. The even v levels, which can evidently access a larger available phase space, are more statistical (less constrained) in their product energy disposition, while the odd v levels are more constrained (larger negative λ_v). A product distribution of this sort has not been observed in any other exothermic atom-transfer reaction. A "sawtooth" or oscillating vibrational-state distribution has been predicted[24,25] for certain levels of CO_2 under nonequilibrium conditions, and indeed a gasdynamic CO_2 laser has been made to operate[26] between a pair of such inverted levels, $03^10 \rightarrow 10^00$. In this case, however, the alternating distribution arises from a Treanor-type[27] V–V pumping mechanism.

The question remains as to the nature of the dynamical bias which favors production of even v levels in the $N(^4S) + O_2$ reaction. A possible origin for such a dynamical bias may be found in the anharmonic coupling model of Darling and Dennison.[28,29] In this model, strong coupling exists between levels in which the symmetric stretch (ν_1) and antisymmetric stretch (ν_3) modes differ by two quantum numbers, i.e., the matrix elements

$$\langle v_1+2, v_2, v_3-2 | \mathfrak{H}_{\text{anh}} | v_1, v_2, v_3 \rangle$$

are large. If the $[N \cdots O \cdots O]^\ddagger$ activated complex begins to break up with the thermodynamic limit of eight quanta in the asymmetric stretching vibration (which corresponds to the reaction coordinate), then one might expect to see the even levels of the symmetric stretch mode preferentially populated by this coupling mechanism, which would ultimately produce excess population in even vibrational levels of the final NO product. A quantitative explanation must, however, await detailed dynamical calculations on an accurate potential surface for the reaction. The existing calculations[30–32] of the N–O–O potential surface predict the transition state to be bent ($^2A'$) and give roughly the correct barrier height, but do not appear to be sufficiently accurate to give the harmonic frequencies and anharmonic coupling terms required for such a calculation.

B. Product relaxation

The values of k'' derived from the curvatures of the kinetic plots for $NO(v = 4–7)$ at high $[O_2]$ furnish some information about vibrational relaxation of NO in these levels. Multiplying the phenomenological k'' values by the density of N atoms in the experiment (2.5×10^{13} cm^{-3}) gives effective bimolecular deactivation constants k'. These are $k'(4) = 2.2 \times 10^{-14}$, $k'(5) = 8.0 \times 10^{-14}$, $k'(6) = 9.0 \times 10^{-14}$, and $k'(7) = 3.2 \times 10^{-13}$, all in units of cm^3 molecule^{-1} s^{-1}. As noted previously, values of $k(v)$ derived from a more detailed cascade model agree to within 50% with these values, and the alternation in $k_1(v)$ remains in the results of fitting to Eq. (9b). It may also be noted that the $k'(v)$ values given above show approximately the same scaling with v as the values derived from electron-impact-excitation measurements,[15] and the values for $v = 7$ in fact agree within 30%. Further work, which is currently in progress, on state-specific V–V and V–T rates in NO should help to clarify these results.

ACKNOWLEDGMENTS

This research was supported by contract F19628-83-K-0003 from the Air Force Geophysics Laboratory (AFGL). We thank Dr. Russell A. Armstrong, (Mission Research Control) and Dr. Terry Rawlins (Physical Sciences, Inc.) for discussion and assistance. Dr. C. M. Phillips assisted with the calculations and experiments; Dr. J. W. Rich and Professor R. D. Levine provided valuable suggestions concerning the theoretical analysis.

[1] M. A. A. Clyne and B. A. Thrush, Proc. R. Soc. London Ser. A **261**, 259 (1961).

[2] I. D. Clark and R. P. Wayne, Proc. R. Soc. London Ser. A **316**, 539 (1970).

[3] M. E. Whitson, Jr., L. A. Darnton, and R. J. McNeal, Chem. Phys. Lett. **41**, 552 (1976).

[4] A. Rahbee and J. J. Gibson, J. Chem. Phys. **74**, 5143 (1981).

[5] R. R. Herm, B. J. Sullivan, and M. E. Whitson, Jr., J. Chem. Phys. **79**, 2221 (1983).

[6] C. L. Lin and F. Kaufman, J. Chem. Phys. **55**, 3760 (1971).

[7] J. P. Kennealy, F. P. del Greco, G. E. Caledonia, and B. D. Green, J. Chem. Phys. **69**, 1574 (1978).

[8] L. Piper, Report No. PSI-0761-TR-518 (1985).

[9] H. Zacharias, M. M. T. Loy, P. A. Roland, and Aa. S. Sudbo, J. Chem. Phys. **81**, 3148 (1984).

[10] I. C. Winkler, R. Stachnik, J. I. Steinfeld, and S. Miller, Spectrochim. Acta Part A **42**, 339 (1986).

[11] R. A. Armstrong, J. P. Kennealy, F. X. Robert, A. Corman, W. T. Rawlins, L. G. Piper, G. E. Caledonia, B. D. Green, H. C. Murphy, J. I. Steinfeld, R. Stachnik, and S. M. Adler-Golden, COCHISE Report No. AFGL-TR-82-0305 (1982).

[12] F. Kaufman and J. R. Kelso, *7th International Symposium on Combustion* (Oxford University, Oxford, 1958), p. 53.

[13] R. Engleman, Jr. and P. E. Rouse, J. Mol. Spectrosc. **37**, 240 (1980).

[14] H. Zacharias, R. Schmiedl, and K. H. Welge, Appl. Phys. **21**, 127 (1980).

[15] B. D. Green, G. E. Caledonia, R. E. Murphy, and F. X. Robert, J. Chem. Phys. **76**, 2441 (1982).

[16] T. Rawlins (private communication).

[17] A. O'Keefe, G. Mauclaine, D. Parent, and M. T. Bowers, J. Chem. Phys. **84**, 215 (1986).

[18] D. L. Albritton, A. A. Vigiano, I. Dotan, and F. C. Fehsenfeld, J. Chem. Phys. **71**, 3295 (1979).

[19] J. H. Lee, J. V. Michael, W. A. Payne, and L. J. Stief, J. Chem. Phys. **69**, 3069 (1978).

[20] D. J. Flinn, R. J. Spindler, S. Fifer, and M. Kelly, J. Quant. Spectrosc. Radiat. Transfer **4**, 271 (1964).

[21] R. W. Nicholls, J. Res. Natl. Bur. Stand. Sect. A **68**, 535 (1964).

[22] D. C. Jain and R. C. Sahni, Trans. Faraday Soc. **64**, 3169 (1968).

[23] R. D. Levine and J. L. Kinsey, in *Atom–Molecule Collision Theory. A Guide for the Experimentalist*, edited by R. B. Bernstein (Plenum, New York, 1979), pp. 693–750.

[24] A. A. Likal'ter, Sov. J. Quantum Electron. **5**, 1307 (1976).

[25] V. N. Faizulaev, Zhur. Prikl. Mekh. i Tekhn. Fiz. **6**, 9 (1982).

[26] A. A. Vedeneev, A. Yu. Volkov, A. I. Demin, E. M. Kudriavtsev, J. Stanco, J. Milewski, and M. Brunné, Appl. Phys. Lett. **38**, 199 (1981).

[27] C. E. Treanor, J. W. Rich, and R. G. Rehm, J. Chem. Phys. **48**, 1798 (1968).

[28] B. T. Darling and D. M. Dennison, Phys. Rev. **57**, 128 (1940).

[29] A. Barbe, C. Secroun, and P. Jouve, J. Mol. Spectrosc. **49**, 171 (1974).

[30] C. W. Wilson, Jr., J. Chem. Phys. **62**, 4842 (1975).

[31] P. A. Benioff, G. Das, and A. C. Wahl, J. Chem. Phys. **67**, 2449 (1977).

[32] G. Das and P. A. Benioff, Chem. Phys. Lett. **75**, 519 (1980).

11. Remeasurement of $N(^2P) + O_2$ Reaction Rate Using Multiphoton Ionization Detection of Nitrogen Atoms

by

C.M. Phillips, J.I Steinfeld, and S.M. Miller

Reprinted from The Journal of Physical Chemistry, 1987, *91*, 5001.

Remeasurement of N(^{2}P) + O$_2$ Reaction Rate Using Multiphoton Ionization Detection of Nitrogen Atoms

Charles M. Phillips,* Jeffrey I. Steinfeld,

Department of Chemistry, Massachusetts Institute of Technology, Cambridge, Massachusetts 02139

and Steven M. Miller

Air Force Geophysics Laboratory, Hanscom Air Force Base, Bedford, Massachusetts 01731
(Received: June 15, 1987)

We have observed photoionization signals in a flowing afterglow reactor arising from the (2 + 1) photoionization of N(^{2}P) and N(^{2}D), resonantly enhanced by the two-photon transitions N[3p ^{2}P^0_J] ← N[2p^3 ^{2}P^0_J] and N[3p ^{2}S$^0_{1/2}$] ← N[2p^3 ^{2}D^0_J], respectively. A diffusion-limited lifetime of 530 μs at 0.22 Torr was observed for N(^{2}P), indicating wall quenching with unit efficiency. Measurement of N(^{2}P) quenching by O$_2$ yielded a rate coefficient of $(1.8 \pm 0.2) \times 10^{-12}$ cm^3 s^{-1}, which is significantly less than values previously obtained by using vacuum-UV resonance detection of the metastable nitrogen.

Introduction

The creation of vibrationally excited nitric oxide through the reaction of nitrogen atoms and molecular oxygen has been the subject of considerable interest due to the importance of NO as an infrared emitter in the upper atmosphere. Above 150 km in the quiescent atmosphere, the reaction

$$\mathrm{N}(^4\mathrm{S}) + \mathrm{O}_2 \rightarrow \mathrm{NO}(v \le 7) + \mathrm{O}(^3\mathrm{P}) \qquad \Delta H^\circ = -1.38\ \mathrm{eV} \quad (1)$$

is a significant contributor to the production of NO(v>1). Several groups[1-4] have investigated this reaction, obtaining the vibrational branching ratio for the energetically allowed levels of the product NO.

Under auroral conditions, the metastable nitrogen atoms N(^{2}P) and N(^{2}D) are the important contributors to the formation of NO in the upper atmosphere. These react with molecular oxygen [reactions 2a-2e] approximately 4 orders of magnitude faster than do ground-state nitrogen atoms [reaction 1].[5-10]

$$\mathrm{N}(^2\mathrm{D}) + \mathrm{O}_2 \rightarrow \mathrm{NO}(v \le 18) + \mathrm{O}(^3\mathrm{P}) \qquad \Delta H^\circ = -3.77\ \mathrm{eV} \quad (2a)$$

$$\rightarrow \mathrm{NO}(v \le 8) + \mathrm{O}(^1\mathrm{D}) \qquad \Delta H^\circ = -1.80\ \mathrm{eV} \quad (2b)$$

$$\mathrm{N}(^2\mathrm{P}) + \mathrm{O}_2 \rightarrow \mathrm{NO}(v \le 26) + \mathrm{O}(^3\mathrm{P}) \qquad \Delta H^\circ = -4.96\ \mathrm{eV} \quad (2c)$$

$$\rightarrow \mathrm{NO}(v \le 14) + \mathrm{O}(^1\mathrm{D}) \qquad \Delta H^\circ = -2.99\ \mathrm{eV} \quad (2d)$$

$$\rightarrow \mathrm{NO}(v \le 3) + \mathrm{O}(^1\mathrm{S}) \qquad \Delta H^\circ = -0.77\ \mathrm{eV} \quad (2e)$$

Product state distributions of NO(v) for reactions of metastable nitrogen atoms with oxygen have been reported for $1 \le v \le 12$ by Kennealy et al.[11] using infrared chemiluminescence (IRCL).

---

(1) Winkler, I. C.; Stachnik, R. A.; Steinfeld, J. I.; Miller, S. M. *J. Chem. Phys.* **1986**, *85*, 890.

(2) Whitson, Jr., M. E.; Darnton, L. A.; McNeal, R. J. *Chem. Phys. Lett.* **1976**, *41*, 552.

(3) Rahbee, A.; Gibson, J. *J. Chem. Phys.* **1981**, *74*, 5143.

(4) Herm, R. R.; Sullivan, B. J.; Whitson, Jr., M. E. *J. Chem. Phys.* **1983**, *79*, 2221.

(5) Lin, C. L.; Kaufman, F. *J. Chem. Phys.* **1971**, *55*, 3760.

(6) Slanger, T. G.; Wood, B. J.; Black, G. *J. Geophys. Res.* **1971**, *76*, 8430.

(7) Husain, D.; Kirsch, L. J.; Wiesenfeld, J. R. *Faraday Discuss. Chem. Soc.* **1972**, *53*, 201.

(8) Husain, D.; Mitra, S. K.; Young, A. N. *J. Chem. Soc., Faraday Trans. 2* **1974**, *70*, 1721.

(9) Young, R. A.; Dunn, O. J. *J. Chem. Phys.* **1975**, *63*, 1150.

(10) Iannuzzi, M. P.; Kaufman, F. *J. Chem. Phys.* **1980**, *73*, 4701.

0022-3654/87/2091-5001$01.50/0

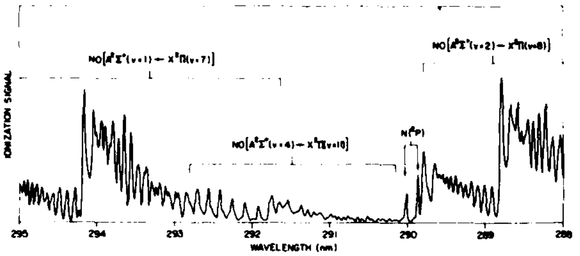

Figure 1. Photoionization signal as a function of the doubled dye wavelength. Shown are signals due to the (1 + 1) photoionization of NO through the $\gamma(1,7)$, $\gamma(4,11)$, and $\gamma(2,8)$ bands as well as the (2 + 1) photoionization of N(^{2}P).

These measurements were subsequently confirmed by electron-beam excitation experiments in the LABCEDE apparatus at Air Force Geophysics Laboratory.[12] In these experiments, however, the total rate of NO(v=0) production cannot be inferred from the data since IRCL obviously cannot probe the ground vibrational state. The FACELIF flowing afterglow reactor[1] is presently being utilized to study this system of reactions since the population of all v levels of NO can be probed directly using (1 + 1) multiphoton ionization (MPI) through the A ← X (γ) system, as was done in the investigation[1] of reaction 1.

Experimental Details

Since the diffusion-limited lifetime of metastable nitrogen atoms in He is on the order of a few milliseconds, the reactants must be introduced to the reaction zone quite rapidly after their creation. In order to accomplish this, modifications were made to the original FACELIF flowing afterglow reactor.[1] A Roots blower (Leybold-Hereaus WS1000) backed by a large displacement forepump (Hereaus-Englehard DK180) allowed linear flow velocities up to 8200 cm s^{-1} at ambient pressures between 0.1 and 0.3 Torr of He. These flow velocities are more than an order of magnitude larger than that of the original configuration of FACELIF. A shortened glass flowtube (~5 cm i.d.) allowed for an overall discharge-to-detection region distance of ~30 cm. Injector loop-to-detection region distances were varied between 12.7 and 18.7 cm, resulting in reaction times as low as 1.6 ms at the maximum flow velocity of 8200 cm s^{-1}. Under our experimental coordinations, the calculated transition length (l = 0.227aR, where a is the tube radius and R is the Reynolds number) was found to be approximately 5 cm. This ensures that a parabolic velocity distribution is established in the reaction zone.

A pair of platinum grids biased between −200 and −300 V was incorporated to trap the large number of ions created in the 2450-MHz microwave discharge. As in the previous studies on FACELIF, the output of a Nd:YAG pumped dye laser/wavelength extender (Quanta-Ray DCR2A, PDL-1, WEX-1; 2.0–2.5 mJ/pulse) was used as the photoionization source.

Results

A portion of the photoionization spectrum of the NO product is shown in Figure 1. All features in the spectrum could be unambiguously assigned to the (1 + 1) photoionization of NO except for two features observed at 290.04 and 289.89 nm. The presence of excited-state nitrogen atoms in the flow tube is suggested by the detection of NO in the v = 8 and v = 11 vibrational states, since these species can be created through reactions 2a, 2c, and 2d. Applying the vacuum correction to the observed wavelengths gave frequencies of 34467.7 and 34485.0 cm^{-1}, respectively, which correlate (within the laser bandwidth of 2 cm^{-1}) with the one-photon frequencies of the two-photon transitions[13,14]

$$\mathrm{N}\left[3\mathrm{p}\ {}^2\mathrm{P}^0_{(1/2,3/2)}\right] \leftarrow \mathrm{N}\left[2\mathrm{p}^3\ {}^2\mathrm{P}^0_{(1/2,3/2)}\right]$$

A power study of these features indicated a second-order intensity dependence, which implies 100% ionization efficiency for every atom excited to the N[3p ^{2}P^0] state. We also observed photoionization signals at the wavelengths 268.95 and 268.98 nm,[14] corresponding to the two-photon transitions[13]

$$\mathrm{N}\left[3\mathrm{p}\ {}^2\mathrm{S}^0_{1/2}\right] \leftarrow \mathrm{N}\left[2\mathrm{p}^3\ {}^2\mathrm{D}^0_{(3/2,5/2)}\right]$$

The diffusion-limited lifetime of N(^{2}P) in our apparatus was determined by monitoring its photoionization signal as a function of the discharge-to-detector distance, equivalent to time at constant flow speed. The 1/e decay time varied from (530 ± 22) μs at P(He) = 0.22 Torr to (2.4 ± 0.1) ms at P(He) = 1 Torr. Using the relationship

$$\tau = \left(\frac{r}{2.405}\right)^2 \frac{P/\mathrm{Torr}}{\mathcal{D}} \tag{3}$$

we find the diffusion coefficient $\mathcal{D}^{\mathrm{He}}{}_{\mathrm{eff}} = (470 \pm 30)$ cm^2 s^{-1}. This has to be multiplied by a nonlaminar flow correction factor for diffusion equal to 1.58,[5] giving $\mathcal{D}^{\mathrm{He}}{}_0 = (740 \pm 40)$ cm^2 s^{-1}. These values are in excellent agreement with those reported by Lin and Kaufman[5] for N(^{2}D), implying that N(^{2}P), as well as N(^{2}P), is deactivated on essentially every encounter with the inner walls of the flow tube. Measurments on N(^{2}P) and N(^{2}D) in N$_2$ also indicate that the diffusion coefficients of these atomic species are equal to each other, within ±1σ error limits.[15]

It has been suggested[16] that N(^{2}P) may also be produced in the flow by an energy-pooling mechanism

$$\mathrm{N}(^4\mathrm{S}) + \mathrm{N}(^4\mathrm{S}) + \mathrm{M} \rightarrow \mathrm{N}_2(\mathrm{A}^3\Sigma_u{}^+) + \mathrm{M} \tag{4}$$

$$k_4 = 3.8 \times 10^{-33}\ \mathrm{cm}^6\ \mathrm{s}^{-1}$$

$$\mathrm{N}_2(\mathrm{A}^3\Sigma_u{}^+) + \mathrm{N}(^4\mathrm{S}) \rightarrow \mathrm{N}(^2\mathrm{P}) + \mathrm{N}_2(\mathrm{X}^1\Sigma_g{}^+) \tag{5}$$

$$k_5 = 5.0 \times 10^{-11}\ \mathrm{cm}^3\ \mathrm{s}^{-1}$$

together with the wall loss processes

$$\mathrm{N}_2(\mathrm{A}^3\Sigma_u{}^+) \xrightarrow{k_6} \mathrm{N}_2(\mathrm{X}^1\Sigma_g{}^+) \tag{6}$$

$$\mathrm{N}(^2\mathrm{P}) \xrightarrow{k_7} \mathrm{N}(^4\mathrm{S}) \tag{7}$$

with rates k_6 = 120 s^{-1} and k_7 = 420 s^{-1} at P(He) = 1 Torr. Processes 4–6 would result in a steady-state concentration of N(^{2}P) in the flow tube given by

$$[\mathrm{N}(^2\mathrm{P})]_{\mathrm{SS}} = \frac{k_4 k_5 [\mathrm{N}(^4\mathrm{S})]^3 [\mathrm{M}]}{k_7(k_5[\mathrm{N}(^4\mathrm{S})] + k_6)} \tag{8}$$

All our measurements of N(^{2}P), at flow speeds between 2000 and 8000 cm s^{-1} and total pressures between 0.2 and 1.0 Torr, showed exponentially decaying concentrations giving consistent diffusion coefficients. Therefore, we conclude that the energy-pooling mechanism does not make a significant contribution to N(^{2}P) concentrations, at least under our conditions.

Quenching of N(^{2}P) by O$_2$. We monitored the N(^{2}P) signal as a function of added O$_2$ in order to determine the overall second-order rate coefficient for

$$\mathrm{N}(^2\mathrm{P}) + \mathrm{O}_2 \xrightarrow{k_9} \mathrm{products} \tag{9}$$

The rate coefficient under plug-flow conditions is given by

$$k_9 = -\alpha\left(\frac{\bar{v}}{d}\right)\frac{\mathrm{d}\ \ln\ [\mathrm{N}(^2\mathrm{P})]}{\mathrm{d}[\mathrm{O}_2]} \tag{10}$$

where $\bar{v}$ is the average flow speed, d is the distance from the O$_2$ injector to the detection region, and α is a nonlaminar flow

---

[11] Kennealy, J. P.; Del Greco, F. P.; Caledonia, G. E.; Green, B. D. *J. Chem. Phys.* **1978**, *69*, 1574.

[12] Green, B. D.; Caledonia, G. E.; Blumberg, W. A. M.; Cook, F. H. *J. Chem. Phys.* **1984**, *80*, 773.

[13] Moore, C. E. *Atomic Energy Levels*; NSRDS-NBS35, Vol. I; U.S. Government Printing Office: Washington, DC, 1971.

[14] Black, G.; Jusinski, L. E. *Chem. Phys. Lett.*, in press.

[15] Cernogora, G.; Sadeghi, N. *Chem. Phys. Lett.* **1980**, *74*, 417.

[16] Rawlins, W. T., private communication.

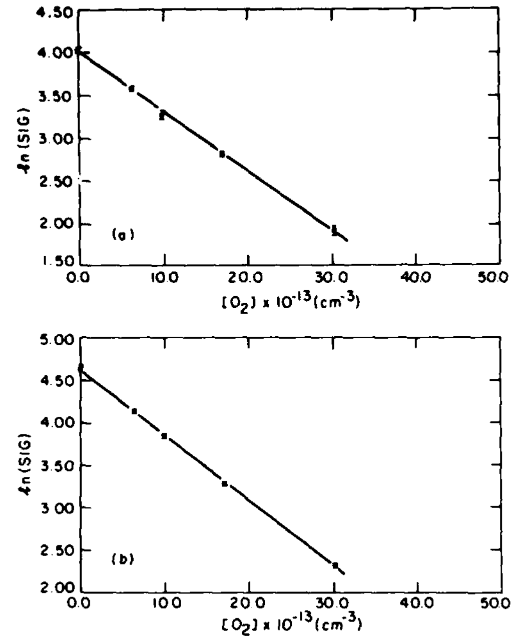

Figure 2. Pseudo-first-order kinetic plots of N(^{2}P) MPI intensity vs. added O_2 at a mean reaction time of 6.5 ms: (a, top) 290.04 nm; (b, bottom) 289.89 nm feature.

correction term for the reaction rate (α = 1.62 for He under our conditions[17]). The flow velocity was reduced in these measurements to permit observations at reaction times from 6 to 9 ms. This was necessary to ensure complete mixing of the O_2 and N(^{2}P) streams; at reaction times shorter than ca. 6 ms, erroneously low values of k_9 were obtained, as a result of incomplete mixing.

A constant value of k_9 was found for reaction times in excess of 6 ms. The value determined by monitoring the feature at 290.04 nm was (1.65 ± 0.2) × 10^{-12} cm^3 s^{-1} (Figure 2a), while from the feature at 289.89 nm it was (1.83 ± 0.2) × 10^{-12} cm^3 s^{-1} (Figure 2b). The reason for the discrepancy appears to be a high-J transition of the $\gamma(4,11)$ band of NO which appears at, and thus contributes to, the signal at 290.04 nm. A simulation of the NO MPI spectrum indicates that no such interference occurs at the 289.89-nm line; therefore, the higher value is taken to be the more accurate determination of k_9. This value is about 30% lower than that reported by Husain et al.[8] [(2.6 ± 0.2) × 10^{-12}] and agrees well with the estimate reported by Young and Dunn [$\leq 2 \times 10^{-12}$], who monitored the N(^{2}P)–N(^{4}S) intercombination line at 346.6 nm. These values are all significantly lower than that found by Iannuzzi and Kaufman[10] [(3.5 ± 0.5) × 10^{-12})], who used vacuum-UV resonance fluorescence to detect N(^{2}P).

Conclusions

Resonant (1 + 1) multiphoton ionization is an accurate and convenient technique for measuring metastable nitrogen atom relative concentrations. Measurements of N(^{2}P) and N(^{2}D) removal, and of formation of NO in vibrationally excited states via reactions 2a–2e, are currently in progress using this technique. The measurements reported here suggest that the rate coefficient for removal of N(^{2}P) by O_2 is less than or equal to 2 × 10^{-12} cm^3 s^{-1}. Atmospheric modelling codes using this rate coefficient may require significant reevaluation.

Acknowledgment. This research was performed under Contract F19628-86-C-0139 with the Air Force Geophysics Laboratory, and sponsored [illegible] the Air Force Office of Scientific Research under Task 2310G4. We thank Drs. G. Black and T. Slanger of SRI International for communicating the results of ref 14 prior to publication, and L. E. Jusinski for several helpful discussions.

---

[17] Ferguson, E. E.; Fehsenfeld, F. C.; Schmeltekopf, A. L. *Adv. At. Mol. Phys.* **1969**, *5*, 1.

12. Evaluation of 2-Photon Ionization Spectroscopy as a Probe of NO Ground State Population Distributions

by

I.C. Winkler, R. Stachnik, J.I. Steinfeld, and S.M. Miller

Spectrochimica Acta, Vol. 42A, No. 2/3, pp. 339–342, 1986.
Printed in Great Britain.
0584–8539/86 $3.00 + 0.00

Evaluation of 2-photon ionization spectroscopy as a probe of NO ground state population distributions

I. C WINKLER,*† R. STACHNIK,*‡ J. I. STEINFELD*§ and S. MILLER‖

*Department of Chemistry, Massachusetts Institute of Technology, Cambridge, Massachusetts 02139, U.S.A. and ‖Air Force Geophysics Laboratory, Hanscom Air Force Base, MA 01731, U.S.A.

(*Received* 16 *August* 1985)

Abstract—We present a critical evaluation of the use of 2-photon ionization spectroscopy as a probe of NO ground state populations. The experimental simplifications which result from saturating the intermediate $A^2\Sigma^+ \leftarrow X^2\Pi$ transition are discussed, as are the criteria for establishing saturation. We also present experimental results which confirm the hypothesis that ionization is the rate limiting step in this 2-photon ionization process and discuss its application to trace impurity analysis in gases.

INTRODUCTION

Since the pioneering experiments of JOHNSON *et al.* [1], molecular multiphoton ionization (MPI) spectroscopy has become a widely used tool for investigating a variety of problems in chemical physics [2, 3]. In particular, the MPI of nitric oxide has been the subject of many such investigations owing to its relatively low ionization potential of 9.26 eV [4] and its inherent chemical importance.

One of the principal difficulties in using MPI as a probe of NO ground state population distributions is normalizing the MPI signal to variations in the laser output. With laser sources capable of generating adequate power only in the visible region of the spectrum, it is necessary to use a 2 + 2 (or 3 + 1) photoionization process [5], i.e. one in which two photons are required to reach the intermediate resonant state and two more photons of the same energy are required to reach the ionization continuum. Since the MPI signal in a 2 + 2 process depends in general on the fourth power of the laser fluence, correction of the MPI signal for fluctuations in laser power introduces considerable uncertainty in the measurement. These fluctuations can also cause the power dependence of the MPI signal to vary since one or more of the transitions involved may move in and out of saturation as the laser power fluctuates.

With the increasing availability of tunable u.v. laser radiation near 226 nm, it has become possible to use a 1 + 1 photoionization process (2-photon ionization) via the $A^2\Sigma^+$ intermediate state to study NO ground state populations [6–9]. Furthermore, at high laser fluence the $A^2\Sigma^+ \leftarrow X^2\Pi$ (γ-band) transition can be saturated. This results in a linear dependence of the MPI signal on the laser power which greatly simplifies the data acquisition and analysis.

In this work we discuss the application of saturated 2-photon ionization spectroscopy to the study of NO ground state population distributions and demonstrate how the rotational structure of the NO $\gamma(0,0)$ band indicates the degree of saturation of the transition. Our results confirm the earlier suggestion [7, 8] that ionization is the rate-limiting step in the 1 + 1 photoionization of NO via $A^2\Sigma^+$, and therefore the $A \leftarrow X$ transition saturates before the ion $\leftarrow A$ step. We also specify the conditions under which saturated 1 + 1 MPI may be used for quantitative determination of NO ground state population distributions, and discuss the application of this technique to trace impurity analysis in gases.

EXPERIMENTAL

The NO used for these measurements was produced in a conventional flowing afterglow reactor from the reaction of ground state nitrogen atoms with oxygen molecules. A detailed description of the apparatus is given elsewhere [9]. The flowtube was equipped with an ionization cell which consisted of two parallel nickel wire grids separated by 1 cm and biased at 45 V. The grids were parallel to the direction of laser beam propagation and perpendicular to the flow. A Nd:YAG pumped dye laser with wavelength extension optics (Quanta-Ray DCR-2A, PDL-1, WEX-1) provided tunable u.v. radiation near 226 nm with pulse energies ~ 0.4 mJ (peak intensity ~ 1.3 MW/cm^2). Spectra were obtained by focussing the laser beam between the detector grids with a 250 mm focal length lens and collecting the ion current as the laser was scanned. The ion current was then amplified ($\times 10^{10}$) with a current to voltage amplifier mounted directly on the flowtube, and normalized for laser power fluctuations on a shot-to-shot basis using a boxcar averager (PAR-162) operating in the *A/B* mode. The output of the boxcar was displayed on a chart recorder (HP 7132A). The signal from a pyroelectric joulemeter (Molectron J3-05), used to monitor the power of the laser beam exiting the cell, was fed into the boxcar for normalization of the ion signal and displayed on an oscilloscope (Tektronix 7834) for direct measurement of the laser output. A razor edge mounted on a high precision *XYZ* translator was used to measure the beam dimensions. Spectra were also recorded without the 250 mm lens.

The dependence of the ion signal on the laser power, at a fixed wavelength, was measured with and without the focussing lens by tuning the laser to the $P_{22} + Q_{12}$ bandhead resonance and monitoring the unnormalized ion current as the laser power was attenuated with quartz plates.

---

† Present address: M.I.T. Lincoln Laboratory, Lexington, Massachusetts 02173, U.S.A.

‡ Present address: Jet Propulsion Laboratory, California Institute of Technology, Pasadena, California 91109, U.S.A.

§ Author to whom correspondence should be addressed.

RESULTS

Log–log plots of the NO ion signal vs laser pulse energy are shown in Fig. 1. Since $S = \sigma I^n$, where S is the ion signal; σ, the absorption across section; I, the laser intensity and n, the order of non-linearity, the slope of these curves gives the values of n. The slope of curve (A) is 1.03 with a correlation coefficient of 0.9946. The data on curve (B) result when the 250 mm lens is removed, and are best fit by a straight line having a slope of 1.29 with a correlation coefficient of 0.9747. The cross sectional area of the unfocussed beam was ~ 1 cm^2; that of the focussed beam was ~ 6×10^{-5} cm^2, and the laser pulse energies ranged from 0.13 to 0.43 mJ/pulse. The average uncertainty in the data points is ± 10% and results from pulse-to-pulse fluctuations in the laser output.

Figure 2 illustrates the dependence of the NO $\gamma(0,0)$ band rotational structure on the laser fluence. The P_{12} and $P_{22} + Q_{12}$ bandhead region of the spectrum is shown. To the right are the same spectral regions calculated with and without the appropriate Hönl–London factors. Spectrum A was traced at a laser fluence that falls within the range of those used to obtain the data shown in Fig. 1A, while spectrum B was traced at a laser fluence used to obtain the data shown in Fig. 1B. The synthesized spectra are those expected for single-photon absorption, and are calculated according to

$$I(\nu) = \sum_{i=1}^{N} F_i(\nu')P(\nu - \nu') \qquad (1)$$

where the intensity of the ith line of the $\gamma(0,0)$ band is

$$F_i(\nu') \propto N_{r,v'',J''}\left(\frac{S_{J'J''}}{2J+1}\right) \qquad (2)$$

and $P(\nu - \nu')$ is the laser spectral profile, assumed here to be Gaussian. $N_{r,v'',J''}$ is the population of the NO $(X^2\Pi_{r,v'',J''})$ level and $S_{J'J''}$ is the appropriate Hönl–London factor [10]. The spectroscopic constants used for NO are those of ENGLEMAN and ROUSE [11]. In the case of saturated MPI, $F_i(\nu')$ is simply proportional to the population factor $N_{r,v'',J''}$, and the Hönl–London factor is omitted.

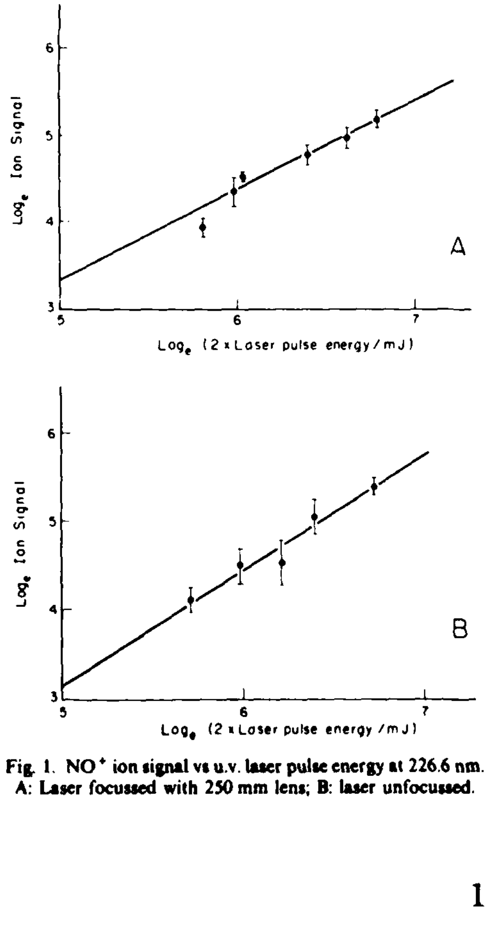

Fig. 1. NO$^+$ ion signal vs u.v. laser pulse energy at 226.6 nm. A: Laser focussed with 250 mm lens; B: laser unfocussed.

DISCUSSION

A linear dependence of the NO ion signal on the focussed laser output is illustrated in Fig. 1(A), since the slope of the straight line fit to the data is 1.03. This indicates that one of the transitions involved in the 2-photon ionization process is saturated. Spectrum A, shown in Fig. 2, was traced using a laser flux which gave a linear power dependence and has a rotational structure best fit by the spectrum calculated without Hönl–London factors. These line strength factors are omitted when calculating a spectrum in which $A \leftarrow X$ is saturated. The populations of the two levels are equal under these conditions, which means that the statistical distribution in the lower level is simply reproduced in the upper level; therefore, only statistical weights are used to calculate the saturated spectrum. From the excellent match between the observed and calculated spectra in Fig. 2(A), we conclude that the $A \leftarrow X$ transition is saturated under our experimental conditions. These observations confirm the earlier suggestion [7, 8] that ionization is the rate limiting step in the 2-photon ionization of NO via the $A^2\Sigma^+$ state.

A greater than linear dependence of the ion signal on the unfocused laser power is shown by the data in Fig. 1(B). The slope of 1.29 indicates a power dependence intermediate between linear and quadratic and is probably due to the pulse to pulse fluctuations in laser power. The spectrum shown in Figure 2(B) was traced with an unfocussed beam and more closely resembles the spectrum calculated with Hönl–London factors, as expected for only partial saturation of the $A \leftarrow X$ transition.

Saturation of the $A \leftarrow X$ transition in the 2-photon ionization of NO can be used to advantage in measuring NO ground state population distributions [9]. In the saturation regime the ion signal need be normalized to only one order of the laser power, reducing the uncertainty associated with a higher order process. Data analysis is also simplified since Hönl–London and Franck–Condon factors are not needed to fit measured spectra. Furthermore, alignment of NO

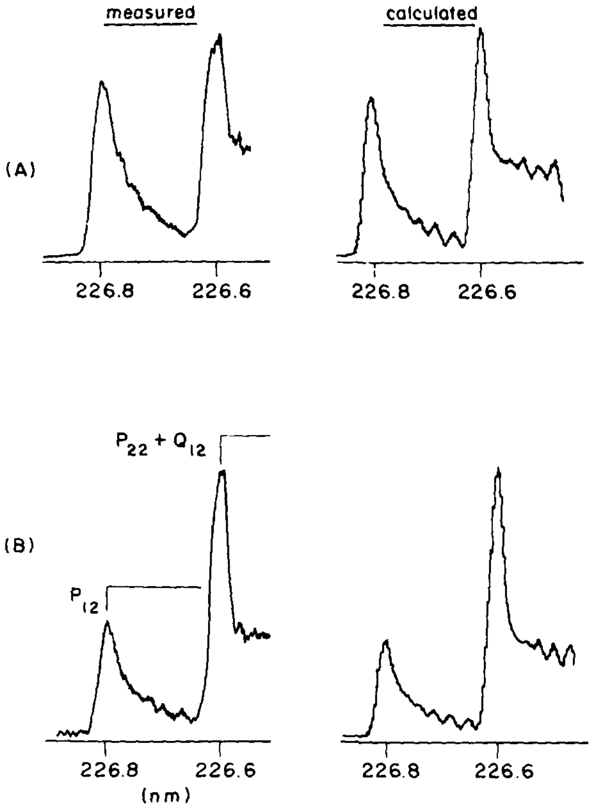

Fig. 2. Dependence of $\gamma(0,0)$ rotational structure on laser power. A: Measured with focussed laser beam and calculated without Hönl–London factors; B: measured with unfocussed laser beam and calculated with Hönl–London factors.

$A^2\Sigma^+$ molecules has recently been shown [12] to alter the rotational structure of the 2-photon ionization spectrum when low laser fluences are used. This complication is avoided when the $A \leftarrow X$ transition is saturated.

In general, quantitative determination of NO ground state populations using 2-photon ionization requires knowledge of the ionization cross sections of NO $A^2\Sigma^+$ molecules. This is perhaps the most significant shortcoming of the method, since only one such cross section has been measured to date [13]. There is some evidence, however, that the ionization cross sections remain fairly constant over the $A^2\Sigma^+$ manifold. Recent measurements of the NO $X^2\Pi$ ($v = 6$) population via two different vibrational states of $A^2\Sigma^+$, using $\gamma(0,6)$ and $\gamma(1,6)$, agree to within the 20% experimental uncertainty [14]. MALLARD *et al.* [15], using laser powers below the saturation limit, found a direct dependence of the photoionization spectrum intensity on the one-photon transition probability, and similar observations have been made by us on the saturated $\gamma(1,1)$, $\gamma(2,2)$, $\gamma(3,3)$, $\gamma(3,4)$, $\gamma(0,5)$ and $\gamma(1,7)$ band spectra [9]. Since the ionization step is rate-limiting, these results also suggest that A state ionization cross sections are nearly equal. The uncertainty due to the lack of NO $A^2\Sigma^+$ ionization cross sections can be surmounted if the same vibrational level of the A state is used in the measurement. For example, to measure the populations of NO $X^2\Pi$ ($v = 0, 1, 2$), the $\gamma(0,0)$, $\gamma(0,1)$ and $\gamma(0,2)$ bands could be used.

Overlap of A state vibrational wave functions with NO$^+$ X state vibrational functions must also be considered in quantitative work. The Franck–Condon propensity rule governing the ionization step is $\Delta v = 0$ [16], where Δv is the difference in vibrational quantum number between the NO A state and NO$^+$ X state. This means the effective ionization potential of an NO molecule is determined by the shape and position of the neutral molecule potential curve relative to the potential curve of the ion. When these curves are displaced or different in shape, deviations from Franck–Condon behavior may be observed and the ionization probability can be distributed over more than one vibrational state of the ion [5(b), 16]. This may not lead to a distortion of the intensity in the 2-photon ionization spectrum if the energy of the photons is sufficient to reach the highest Franck-Condon level in the ion that is overlapped with the neutral molecule. However, if the energy of the photons is not sufficient, a distortion may occur. Since the NO $A^2\Sigma^+$ potential is almost identical to the NO$^+$ X potential, the Franck–Condon propensity rule is expected to hold rigorously until vibrational levels of the NO A state manifold above $v = 3$ become involved in the $1+1$ ionization process. In this region, the A state overlaps with the higher lying $B^2\Pi$ and $C^2\Pi$ states. Non-Franck–Condon behavior due to inter-state mixing has been observed in the $2+2$ ionization via the A state [16] and $3+2$ ionization via the $C^2\Pi$ state [5(b)]. It should be pointed out that similar perturbations may be revealed by a study of the saturated 2-photon ionization spectrum of the A state in the energy region where the A, B and C states overlap. Such perturbations would be observed as anomalous intensity distributions in the spectrum.

APPLICATIONS

The $(1+1)$ photoionization method has been used successfully to measure vibrational and rotational population distributions in ground-state NO, for example as a product of the $N(^4S)+O_2$ reaction [9] and of NO scattered from surfaces [7,17]. Also, due to the high sensitivity of 2-photon ionization spectroscopy ($\sim 5\times10^5$ NO molecules/cm^3) it may be possible to detect extremely low levels of N_2, O_2 and H_2O impurities in gases such as Ar, He, N_2 and O_2. This would be accomplished by passing the gas through a microwave discharge then intercepting the flow upstream with an ionizing laser. If for instance the gas is He, N_2 and O_2/H_2O impurities would produce NO in the discharge which would be subsequently detected using 2-photon ionization. If the gas is N_2, O_2/H_2O levels would be determined. The use of the process for quantitative analysis will require a more detailed understanding of the chemistry occurring in the discharge than is currently available.

Acknowledgements—This work was supported by the Air Force Geophysics Laboratory under Contract F19628-83-K-0003. One of the authors (J.I.S.) is pleased to have this opportunity to express his gratitude to Professor RICHARD C. LORD, who has been a source of both scientific and personal inspiration over many years of pleasant association, beginning as an undergraduate at M.I.T. and now as a colleague in the Department of Chemistry and the G. R. Harrison Spectroscopy Laboratory.

REFERENCES

[1] P. M. JOHNSON, M. R. BERMAN and D. ZAKHEIM, *J. chem. Phys.* **62**, 2500 (1975).
[2] P. M. JOHNSON, *Acc. Chem. Res.* **13**, 20 (1980).
[3] J. H. EBERLY, N. D. PILTCH and J. W. GALLAGHER (eds.), *Multiphoton Bibliography* 1981–1982, Suppl. 4, NBS LP-92.
[4] C. Y. NG, B. H. MAHAN and Y. T. LEE, *J. chem. Phys.* **65**, 1956 (1976).
[5] (a) J. C. MILLER and R. N. COMPTON, *J. chem. Phys.* **75**, 22 (1981); (b) M. G. WHITE, M. SEAVER, W. A. CHUPKA, S. D. COLSON, *Phys. Rev. Lett.* **49**, 28 (1982).
[6] (a) AA. S. SUDBØ and M. M. T. LOY, *J. chem. Phys.* **76**, 3646 (1982); (b) H. ZACHARIAS, M. M. T. LOY, P. A. ROLAND and AA. S. SUDBØ, *J. chem. Phys.* **81**, 3148 (1984).
[7] M. ASSCHER, W. L. GUTHRIE, T.-H. LIN and G. A. SOMORJAI, *Phys. Rev. Lett.* **49**, 76 (1982).
[8] N. GOLDSTEIN, G. D. GREENBLATT and J. R. WIESENFELD, *Chem. Phys. Lett.* **96**, 410 (1983).
[9] I. C. WINKLER, R. J. STACHNIK, J. I. STEINFELD and S. MILLER, in preparation.
[10] L. T. EARLS, *Phys. Rev.* **48**, 423 (1935).
[11] R. ENGLEMAN, JR. and P. E. ROUSE, *J. molec. Spectrosc.* **37**, 240 (1971).
[12] J. P. BOOTH, S. L. BRAGG and G. HANCOCK, *Chem. Phys. Lett.* **113**, 509 (1985).
[13] H. ZACHARIAS, R. SCHMIEDL and K. H. WELGE, *Appl. Phys.* **21**, 127 (1980).
[14] I. C. WINKLER, unpublished results.
[15] W. G. MALLARD, J. H. MILLER and K. C. SMYTH, *J. chem. Phys.* **76**, 3483 (1982).
[16] M. G. WHITE, W. A. CHUPKA, M. SEAVER, A. WOODWARD and S. D. COLSON, *J. chem. Phys.* **80**, 678 (1984).
[17] J. HÄGER, Y. R. SHEN and H. WALTHER, in *Laser Processing and Diagnostics: Proceedings of an International Conference* (edited by D. BAUERLE), *Ser. Chem. Phys.*, Vol. 39, p. 154. Springer, Berlin (1984).

Contents

1. Introduction 137
2. Experimental 138
3. Results 140
   3.1 Photoacoustic 140
   3.2 Fluorescence Excitation 145
   3.3 Absorption 145
   3.4 Fluorescence Spectra 150
4. Spectral Modeling 150
5. Discussion 158
6. Conclusion 159
References 160

13. 2.7/4.3 Micron CO_2 Branching Ratio Measurement

by

S.M. Miller

1. INTRODUCTION

Two rocket infrared measurement programs during the 1970's (ICE CAP and SPIRE) measured significant amounts of radiation in the upper atmosphere at 2.7 microns.[1,2,3,4] Several papers have

---

1. Stair, A.T., Jr., Ulwick, J.C., Baker, K.D., and Baker, D.J. (1975) Rocketborne observations of atmospheric infrared emissions in the auroral region, *Atmospheres of Earth and Planets*, ed. McCormac, B.M., Reidel, D., Dordrecht, Netherlands.

2. Kumer, J.B. (1974) *Analysis of 4.3 Micron ICE CAP Data*, Air Force Cambridge Res. Lab., Bedford, MA, AFCRL-TR-74-0334, ADA014847.

3. Sharma, R.D., Nadile, R., Stair, A.T., Jr., and Gallery, W. (1981)Earthlimb emission analysis of Spectral Infrared Rocket Experiment (SPIRE) data at 2.7 micrometers, Modern Utilization of Infrared Technology, *Proc. Soc. Photo Opt. Instrum. Eng.* **304**:139-142.

4. Stair, A.T., Jr., Sharma, R.D., Nadile, R.M., Baker, D.J., and Grieder, W.F. (1985) Observation of limb radiance with cryogenic Spectral Infrared Rocket Experiment (SPIRE), *J. Geophys. Res.* **90**:(A10).

been published[5,6] which attribute this radiation at 2.7 µm to the hot bands of CO_2. To determine the contribution of 2.7 µm radiation from CO_2, each of these analyses rely on a simple theoretical calculation of the CO_2 branching ratio between 2.7 µm and 4.3 µm:

$$\frac{A(4.3\ \mu m)}{A(2.7\ \mu m) + A(4.3\ \mu m)} = \frac{(v_{4.3})^2 * S_{4.3}}{(v_{2.7})^2 * S_{4.3}(v_{2.7})^2 * S_{4.3}} = 0.96$$

where A is the Einstein A coefficient, v is the frequency in wavenumber and S is the transition line strength.

Examination of Figure 1 shows that there are two assumptions built into this calculation. The line strengths of the 101 → 100 and 021 → 020 have not been measured. Thus it is assumed since only one quanta of asymmetric stretch is changing, that the following matrix elements are equal: $< 101 | u | 100 > = < 021 | u | 020> = < 001 | u | 000 >$, where u is the dipole moment operator. It is also assumed that the line strengths for radiation at 4.26 µm, 2.7 µm, and 2.77 µm are known accurately. Both these assumptions can be avoided by measuring the branching ratio experimentally.

James and Kumer[7,8] attempted to confirm this branching ratio experimentally, first by observing 4.3 µm radiation from a low pressure CO_2 cell when radiated by blackbody radiation and later by observing fluorescence decays when a pulsed laser source at 2.7 µm is used.

An inherent problem with this experiment is its inability to discriminate 4.3 µm radiation from the 101 → 100, and 021 → 020 transitions from the 001 → 000 transition. The 001 energy level becomes populated by collisional excitation which is not important in the upper atmosphere above 50 km but is very important under the 300 mTorr pressures utilized in these experiments. This lack of discrimination prevents the proper determination of the 4.3/2.7 µm branching ratio.

The experiment described here solves this problem by spectrally resolving the direct radiation from the 101 and 021 energy levels from the radiation due to the collisional coupling with the 001 band.

2. EXPERIMENTAL

This project consisted of four experiments. These were an IR absorption measurement to confirm the absorption coefficient (and thus the absorption cross section), a photoacoustic measurement to identify the rotational lines of the absorbed 2.7 µm radiation, a fluorescence excitation experiment to determine the sensitivity of this method, and an interferometry experiment to spectrally resolve the fluorescence from the CO_2. All of these experiments utilized a Burleigh model

---

5. Kumer, J.B. (1977) Theory of the CO_2 4.3 Aurora Related Phenomena, *J. Geophys. Res.* **82**:(16).
6. Sharma, R.D. (1985) CO_2 Component of Daytime Earth Limb Emission at 2.7 Micrometers, *J. Geophys. Res.* **90**:(A10).
7. James, T.C. (1976) *Laboratory Investigation of Infrared Fluorescence of CO_2*, HAES Report No. 60, Final Report to DNA 4238F, Cont. DNA 001-76-C-0017, ADA043524.
8. James, T.C. and Kumer, J.B. (1979) *Fluorescence Experimental and Auroral Data Evaluation to Improve Prediction of Nuclear Atmospheric Infrared Background*, DNA Report LMSC/ D673384, ADA085724.

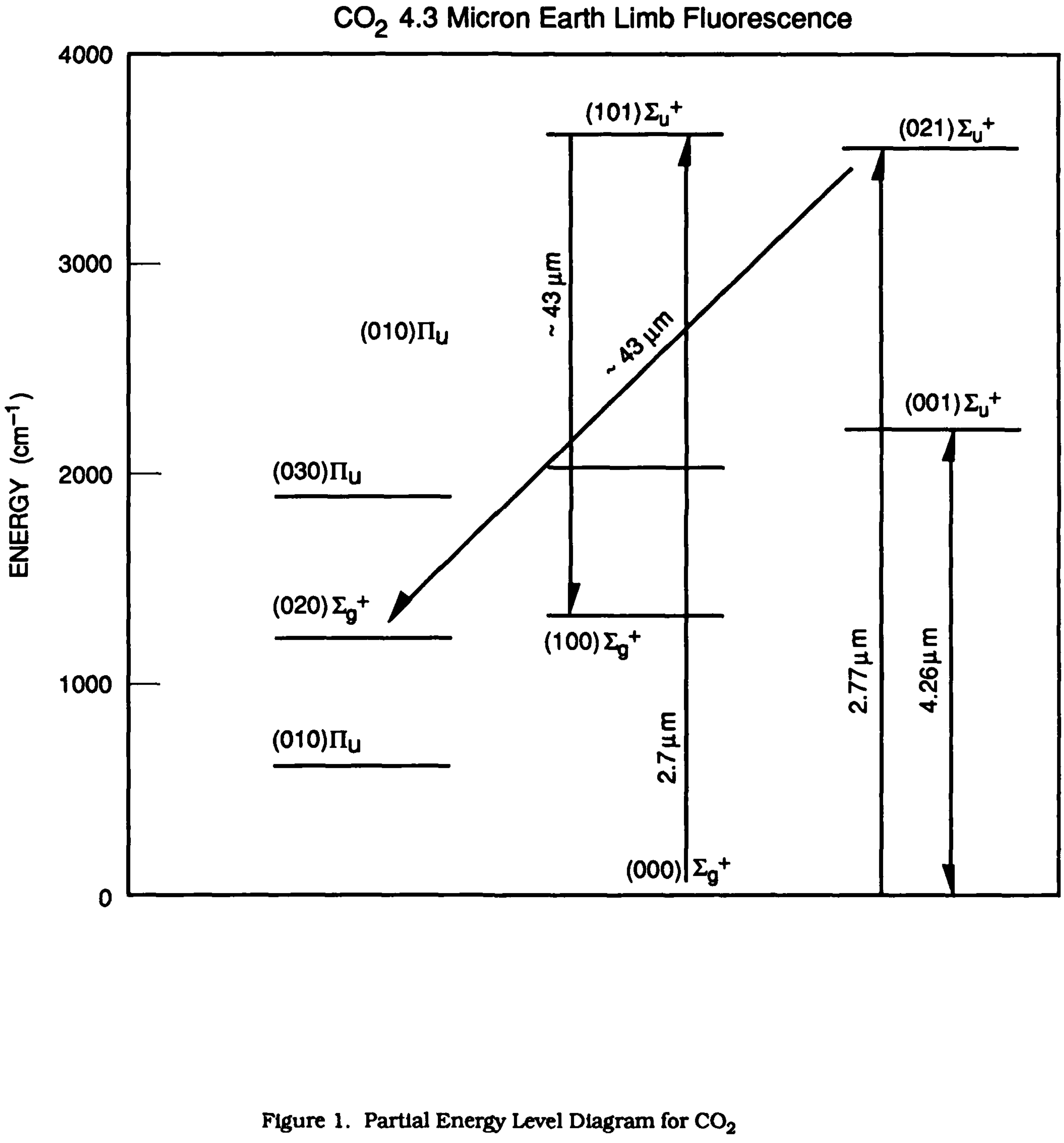

Figure 1. Partial Energy Level Diagram for CO_2

FCL-20 Kr+ laser pumped F-center laser to obtain approximately 50 milliwatts of infrared radiation continuously tunable from 2.5 μm to 2.75 μm. This laser was operated multimode to scan through the 2.7 μm absorption region of CO_2 and was operated in single mode to obtain an absorption measurement on a single rotational line. All data were acquired, displayed, stored and analyzed on a Hewlett-Packard model 9836 computer equipped with a multiprogrammer to scan the laser and acquire data.

The photoacoustic measurements were made using a hearing aid microphone positioned via a "spider" near the center axis of an MDC model 150-4 gas cell equipped with 1 inch sapphire windows. The laser beam was chopped using a PTI model 4000 tuning fork chopper at 400 Hz and passed through the gas cell along a horizontal axis and terminated on a Scientech model 365 power meter. The microphone signal was pre-amplified using a model 747 operational amplifier and fed into a Stanford Research model SR 510 lockin amplifier. The signal from the lockin was sent to the HP computer. Matheson grade CO_2 and UHP grade argon were used throughout without further purification. The photoacoustic signal was obtained at 100 torr of CO_2 with no buffer gas.

The absorption experiment utilized the F-center laser, the photoacoustic gas cell, and the Scientech Power meter. The laser was tuned to the peak of a strong rotational line. Laser power was measured after the beam passed through the gas cell with and without CO_2 in the cell. This provides the relative powers necessary to calculate the absorption cross section.

The equipment arrangement for the photoacoustic and absorption experiment is shown in Figure 2. The fluorescence excitation experiment utilized a fluorescence cell with Brewster angle windows and baffling to reduce laser beam scattering to a minimum, and a recessed observation window capable of holding various bandpass filters and/or lenses to couple to the InSb infrared detector. The laser beam path between the laser and the cell was purged with N_2. The fluorescence from the cell was collected as the F-center laser was tuned through the (021) combination band of CO_2, 2.640 μm to 2.730 μm. The equipment arrangement for this experiment is shown in Figure 3a.

The spectrally resolved fluorescence was observed using a Michelson interferometer with a spectral resolution of 8 cm^{-1} using the arrangement shown in Figure 3b. Both the laser path and the path from the cell to the interferometer were purged with N_2 to eliminate both water vapor and atmospheric CO_2. The interferometer was calibrated using both a blackbody source and a helium lamp for both relative and absolute spectral response. The cell was evacuated and heated and a baseline was taken at least on a daily basis with less than 0.1 μm background pressure. Spectra were collected at several pressures between 10 millitorr and 10 torr with and without Ar buffer gas.

3. RESULTS

3.1 Photoacoustic

A typical photoacoustic spectrum is shown in Figure 4. This represents the nonradiative portion of the energy absorbed by the CO_2 into the (021) combination band. The rotational assignments can be made by identifying the gap between the R and P branches of the spectrum. This spectrum required 100 torr of CO_2 in the cell and 20 - 30 mw of FCL radiation scanned from 2.64 to 2.73 μm. The deviation from regularity on the R branch side results from laser beam absorption by water vapor. Although the

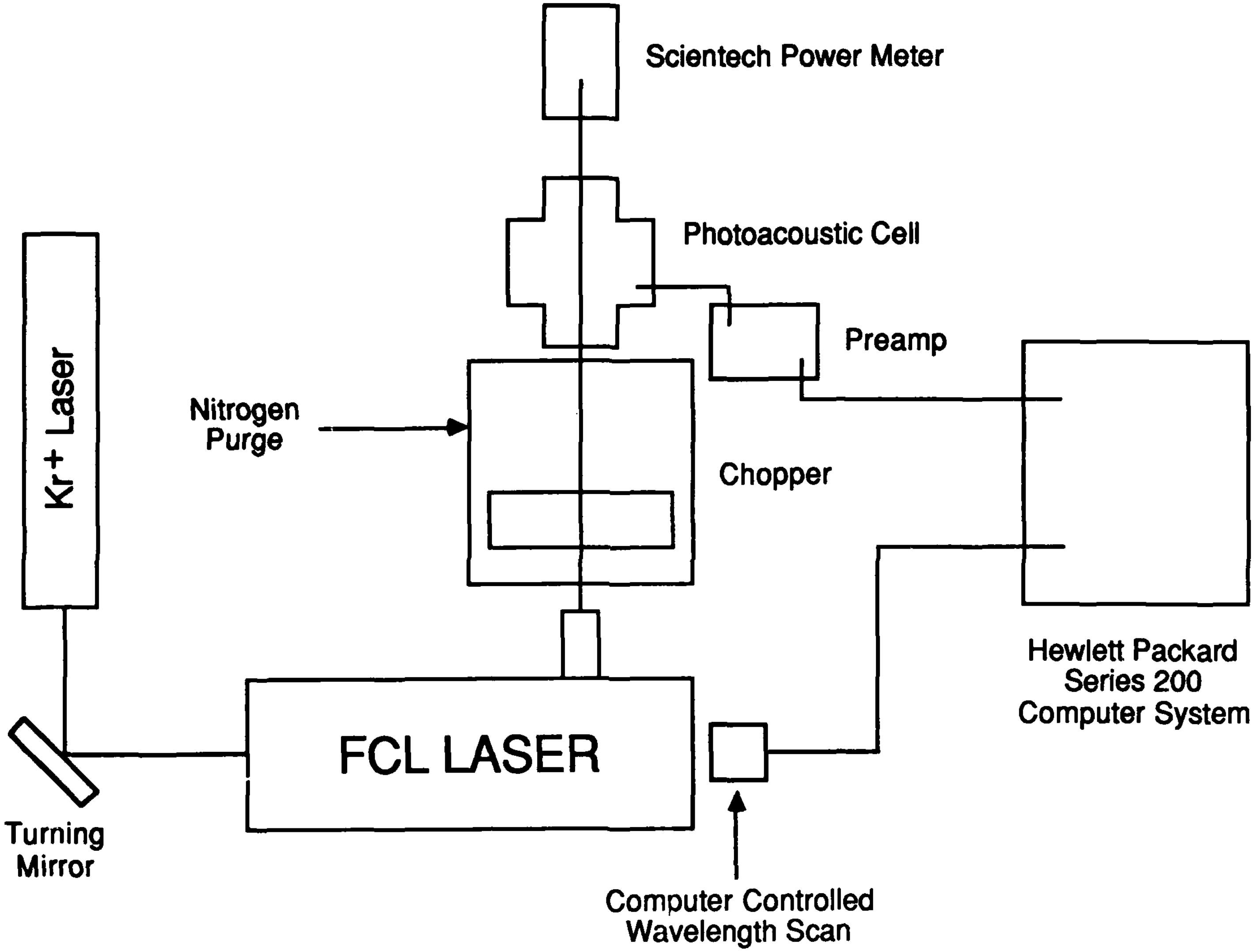

Figure 2. Photoacoustic/Fluorescence Excitation Experimental Setup

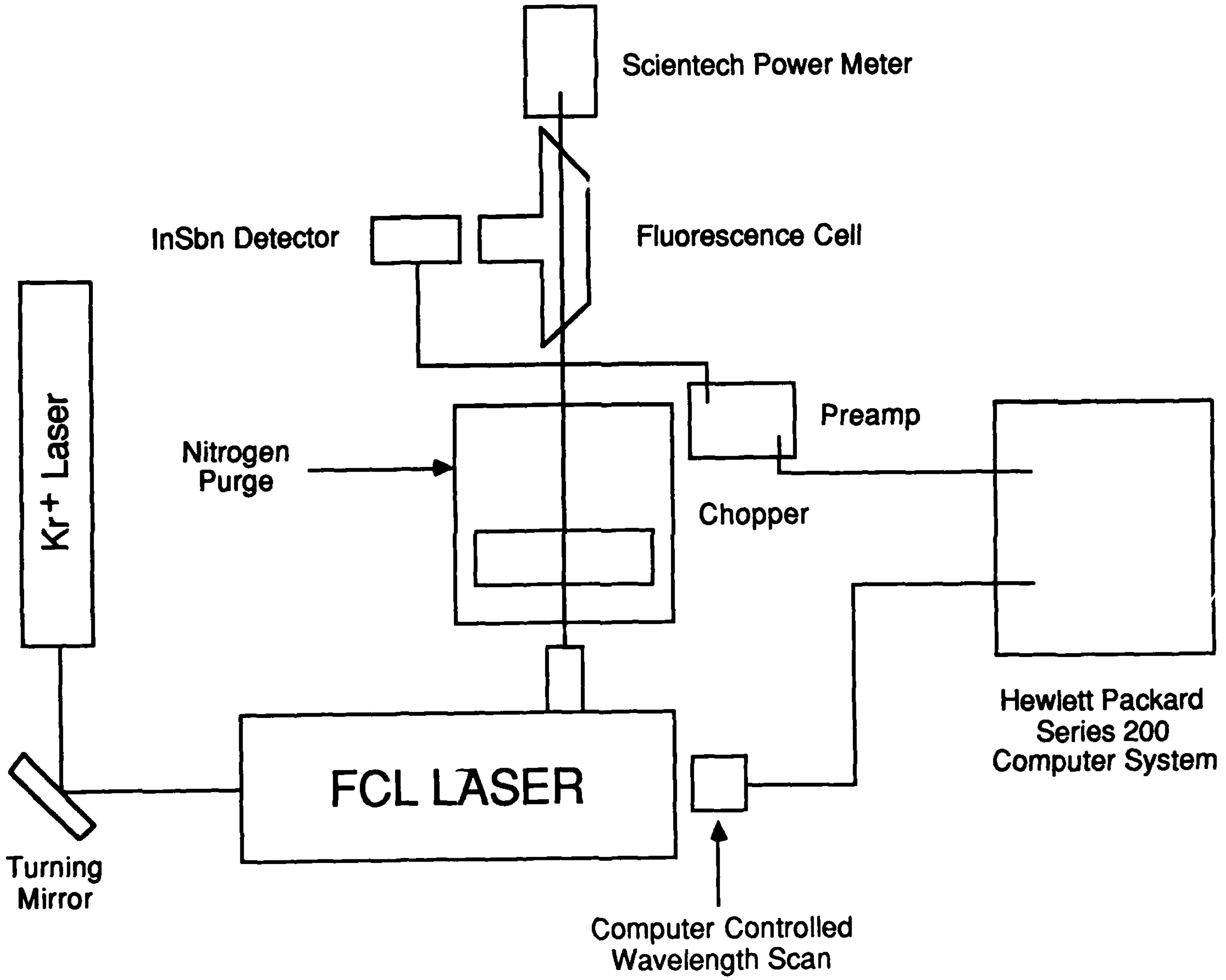

Figure 3a. Fluorescence Excitation Experimental Setup

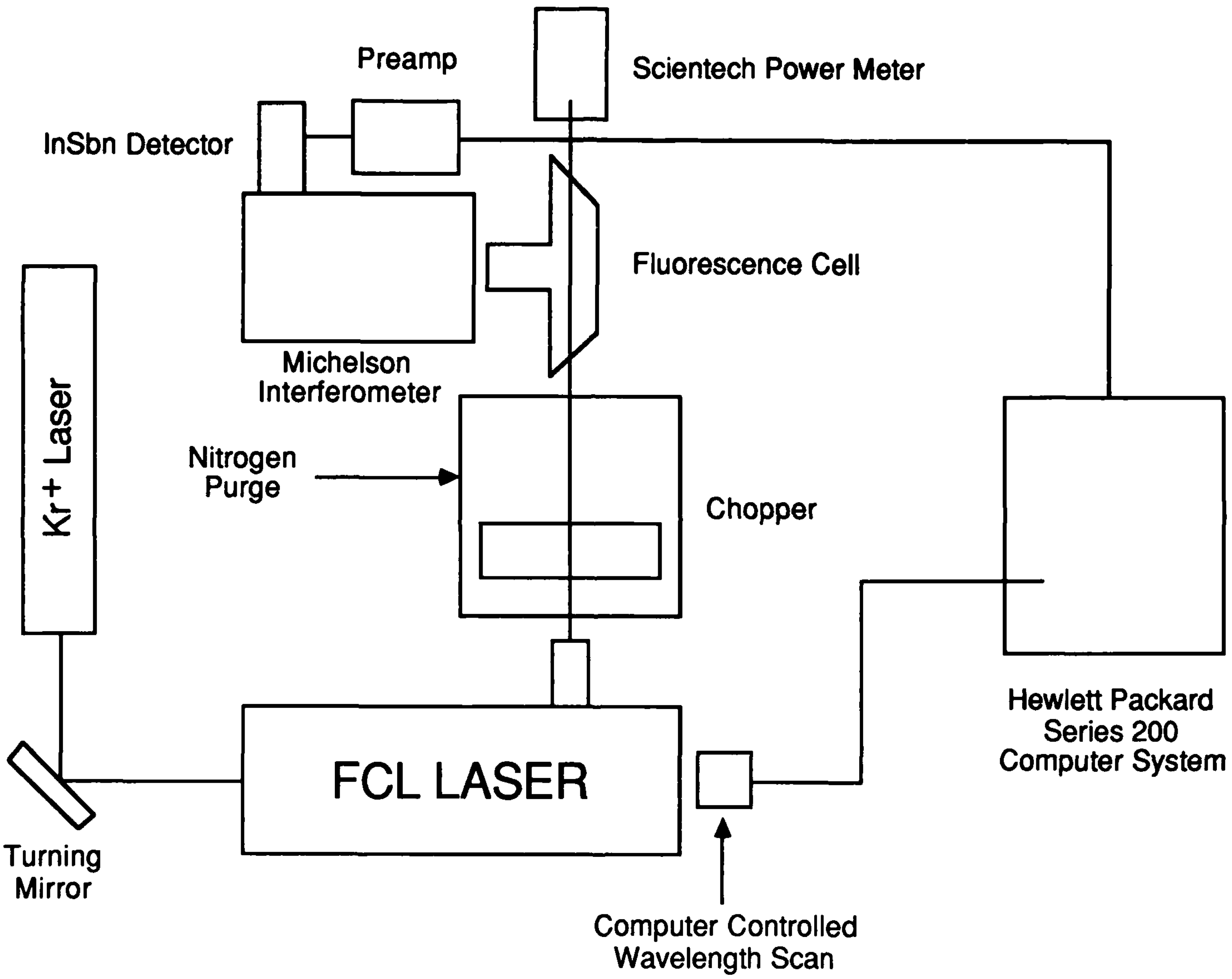

Figure 3b. Interferometric Experimental Setup

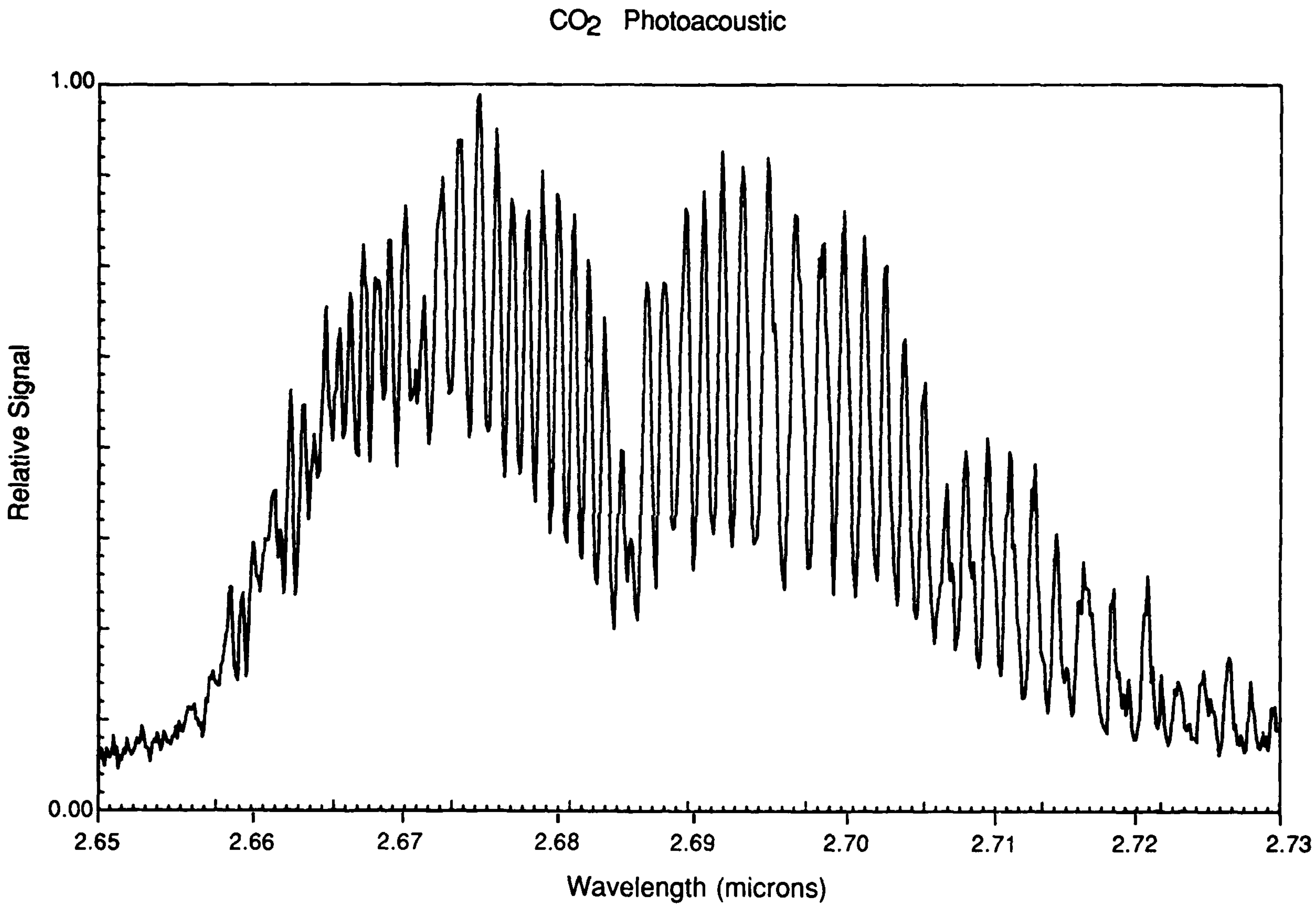

Figure 4. Photoacoustic Spectrum

laser path is purged with N_2, water has a very large absorption coefficient for 2.7 µm radiation. Using this spectrum, the P11 rotational line was chosen for the fluorescence experiments.

3.2 Fluorescence Excitation

The next stage involved observing the total fluorescence in the 4.3 µm bandpass from the absorption of 2.7 µm radiation. Figures 5 and 6 show this 4.3 µm fluorescence as a function of laser wavelength. The first spectrum required 80 mw of laser radiation, 1 torr of CO_2 and 50 torr of Argon buffer gas, while the second required 90 mw of of laser radiation, 20 torr of CO_2 and 50 torr of Argon buffer gas. These spectra clearly show that a pressure range of 10 millitorr to 10 torr of CO_2 could be studied with sufficient signal to noise to determine the CO_2 branching ratio. Fluorescence in the 2.7 µm bandpass was examined with less success. To discriminate 2.7 µm fluorescence from laser radiation, a short wavelength R branch rotational line had to be excited and the longer wavelength P branch fluorescence observed. This ideally requires a bandpass filter with a very sharp short wavelength cutoff. Without such an ideal filter the 2.7 µm fluorescence has to be extracted from a large laser background at 2.7 µm. This is evident in Figure 7 where a 2.7 µm bandpass is used and a fluorescence excitation spectrum has been obtained. The 2.7 µm fluorescence is manifested as the small rotational structure on a large 2.7 µm laser scattered background (with water absorption lines). This spectrum can be compared to the one in Figure 8 where only Argon buffer gas is in the cell and all other conditions remain the same. Here the oscillations are not observed. This data demonstrates that it is difficult to observe the 2.7 µm fluorescence even without the losses associated with further spectral discrimination.

The intensity of the 4.3 µm data on the same experimental run is 112 mv vs 2 mv intensity of the 2.7 µm structure under the same conditions, 1 torr CO_2 and 50 torr Ar. The bandpass filters at 4.3 µm and 2.7 µm have the same throughput while the InSb detector is a factor of 1.5 times more sensitive at 4.3 µm than 2.7 µm.

3.3 Absorption

The absorption study was hampered by the dual mode radiation of the FCL. Since the FCL uses a near hemispheric resonator, a standing wave is set up in the cavity. This standing wave causes a second "hole-burning" mode to compete with the original mode. The spacing between these two modes is 10 GHz. When the absorption is measured using this dual mode of FCL operation, the mode tuned to the peak of a rotation line is absorbed significantly more than the mode not in resonance with a rotational line. The results become too convolved to perform the measurement properly. Therefore, an etalon was inserted into the FCL cavity to eliminate the "hole-burning" mode. This involved carefully controlling the length of the cavity, the distance between etalon surfaces and the grating position. A second etalon was used outside the cavity to measure the mode spacing and detect the presence of one or two modes. The nonorthogonal nature of this elaborate tuning scheme resulted in the ability to either obtain single mode tuning at a nonspecific wavelength or to obtain a specific wavelength with both modes. It was very difficult to obtain single frequency operation at a desired wavelength. Thus, this portion of the experiment was abandoned in favor of accepting the absorption cross sections published in DNA report #4238F by T.C. James.

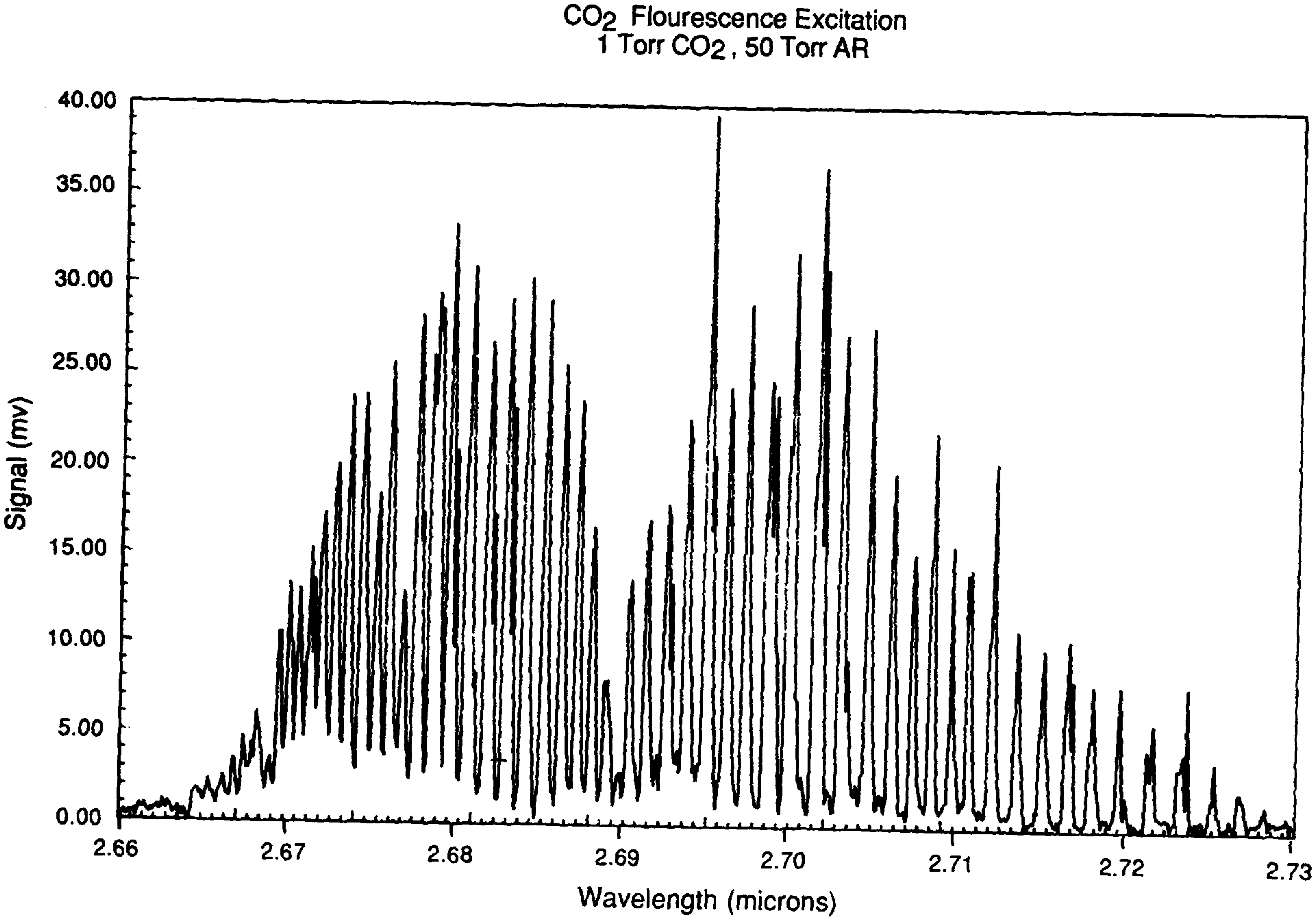

Figure 5. Fluorescence Excitation Spectrum - 1 Torr CO_2

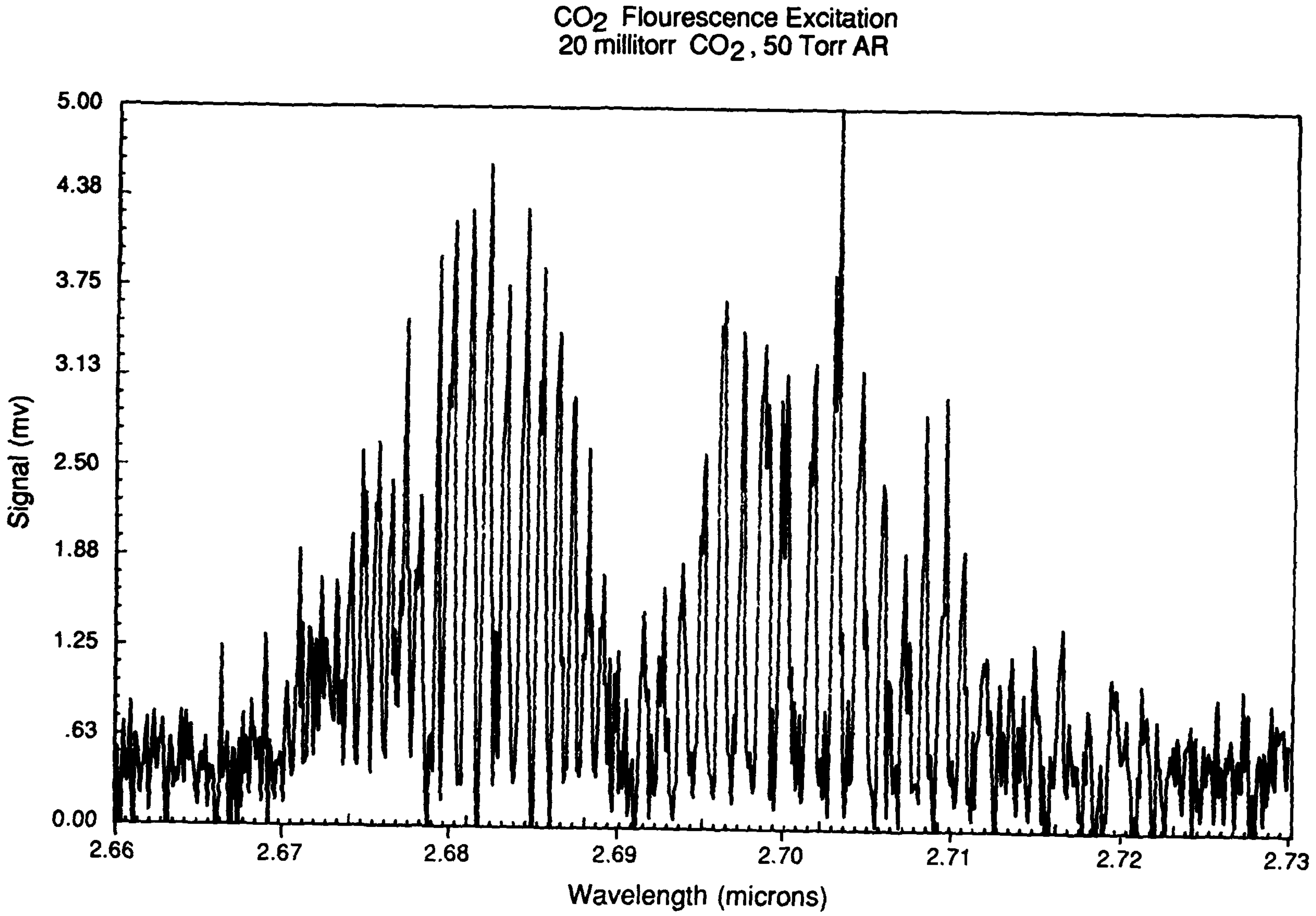

Figure 6. Fluorescence Excitation Spectrum - 20 Millitorr CO$_2$

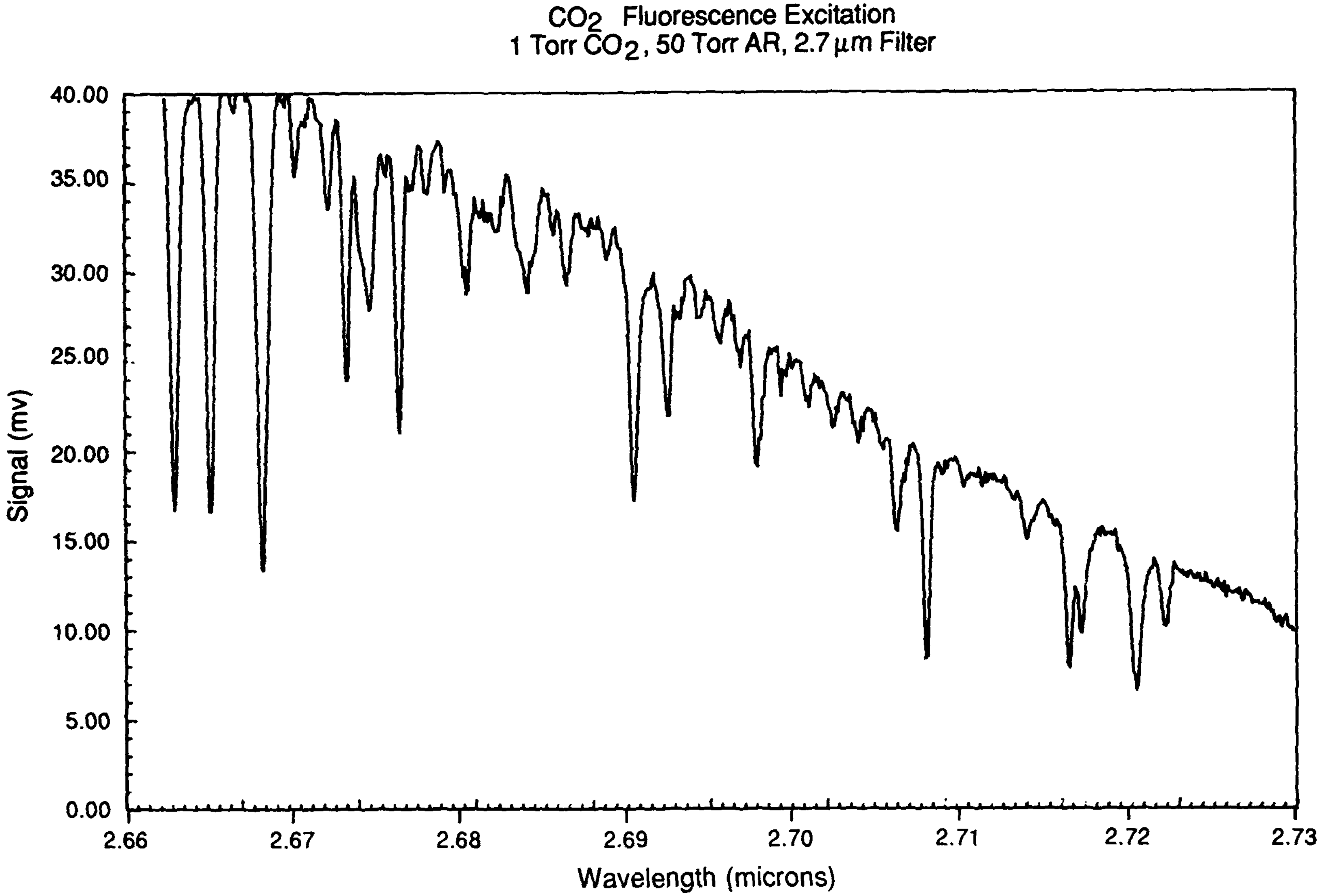

Figure 7. Fluorescence Excitation Spectrum - 2.7 µm Bandpass - CO_2

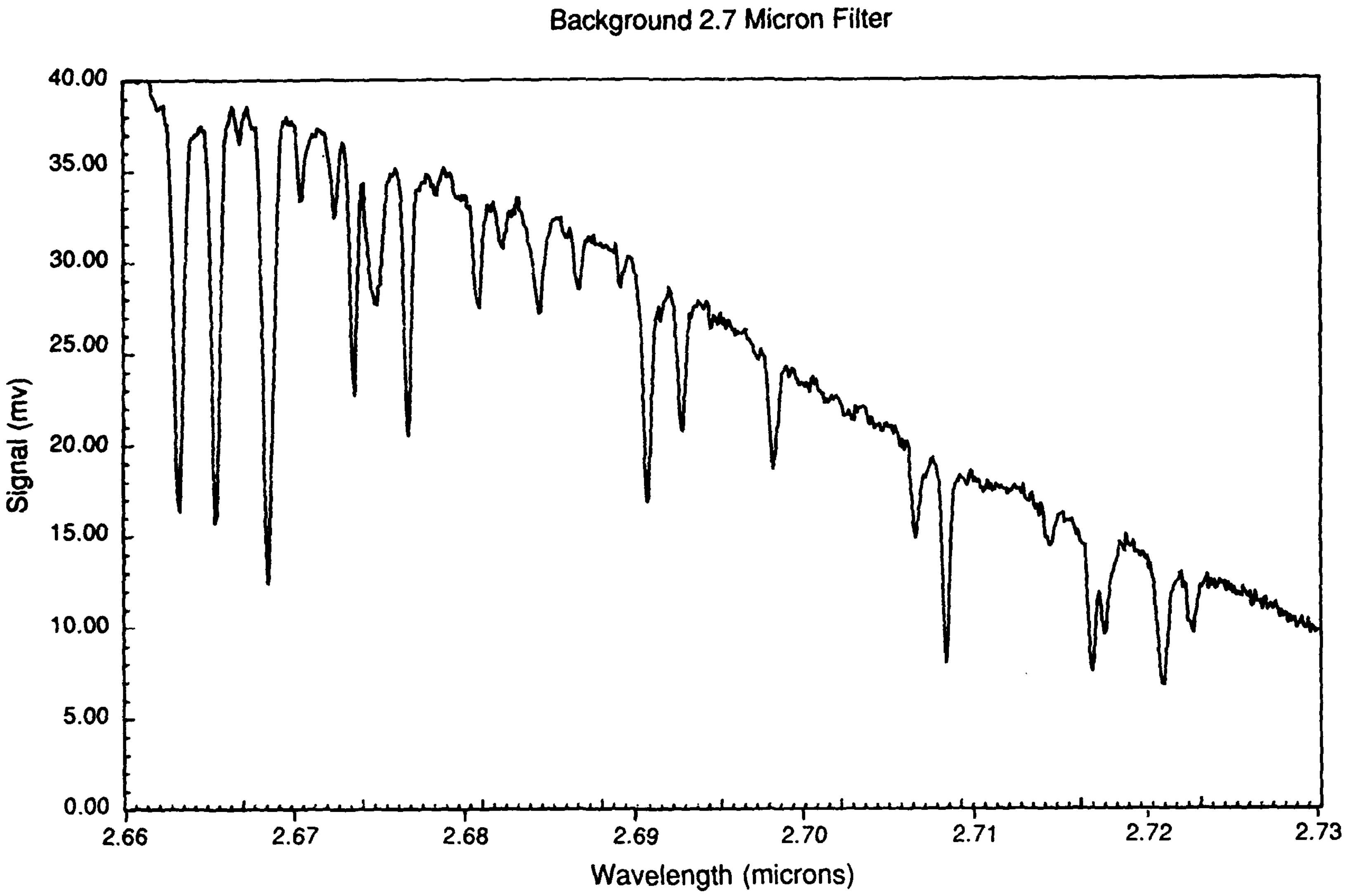

Figure 8. Fluorescence Excitation Spectrum - 2.7 µm Bandpass - No CO_2

3.4 Fluorescence Spectra

The final experimental step to determine the 4.3/2.7 μm branching ratio is resolving the CO_2 fluorescence into the following transitions; (021 → 020) at 4.3 μm, (021 → 000) at 2.7 μm, and (001 → 000) at 4.26 μm. This is accomplished using a calibrated Michelson interferometer as described in the experimental section. The results at 2.7 μm are shown in Figure 9. All features in this spectral region at all pressures investigated (20 mtorr to 10 torr) can be attributed to scattered laser light. This lack of any fluorescence at 2.7 μm [or at 2.77 μm - the Fermi resonant (101 → 000) transition] limits the results to predicting a lower limit of the 4.3/2.7 μm CO_2 branching ratio. The fluorescence results near 4.3 μm are shown in Figures 10 to 14. The 8 cm^{-1} instrument resolution provides the R and P branch envelopes without resolving the individual rotational lines. As can be seen most clearly in Figure 14, there are at least 2 overlapping vibrational bands observed. In order to determine which CO_2 bands contributed to these spectra a synthetic spectral modeling program was written, with a linear least squares fitting routine after Bevington[9] utilized. All data on vibrational transition probabilities, rotational line widths and positions were taken from the HITRAN[10] database at AFGL.

4. SPECTRAL MODELING

The basic flow of the program used for this modeling is as follows. Both experimental data and the rotational line positions, line strengths, and line widths of the CO_2 bands of interest from the HITRAN database are input to the program. The HITRAN line strength data is converted to Einstein A coefficients, the spectral line shape is determined using the linewidths, the sinc function response of the interferometer, and the appropriate line shape function for the pressure. These are a Doppler lineshape for pressures < 10 mtorr, a Lorentz lineshape for pressures > 10 torr and Voigt profile for pressures less than 10 torr and greater than 10 mtorr. The individual rotational lines are then combined with an appropriate resolution to form the respective vibrational band. If the vibrational band to be calculated is connected to the ground state, then an optical thickness parameter is calculated using equations derived in References 11 and 12. Each broadening mechanism (Doppler, Lorentzian, or Voigt) requires a unique calculation of the optical thickness. This optical thickness parameter ($0 < \gamma < 1$) becomes a multiplicative factor for the intensity of each wavelength point in the vibrational band. The fundamental band together with several hot and isotope bands form a basis set that can be fit to the experimental data. A linear least squares fitting routine calculates the relative amounts of each vibrational band in the basis set necessary to best fit the experimental data. An example of these fits is shown in Figure 15.

---

9. Bevington, P.R. (1969) *Data Reduction and Error Analysis for the Physical Sciences*, McGraw-Hill.
10. Rothman, L.S., and Young, L.D.G. (1981) Infrared Energy Levels and Intensities of Carbon Dioxide - II, *J. Quant. Spectrosc. Radiat. Trans.* **25**:505-524.
11. Caledonia, G.E., Green, B.D., and Murphy, R.E. (1982) On self-trapping of $CO_2(v_3)$ fluorescence, *J. Chem. Phys.* **77**:(10).
12. Green, B.D., Caledonia, G.E., Piper, L.G., Goela, J.S., Fairbairn, A., and Murphy, R.E. (1981) *LABCEDE Studies*, AFGL-TR-82-0060, ADA114389.

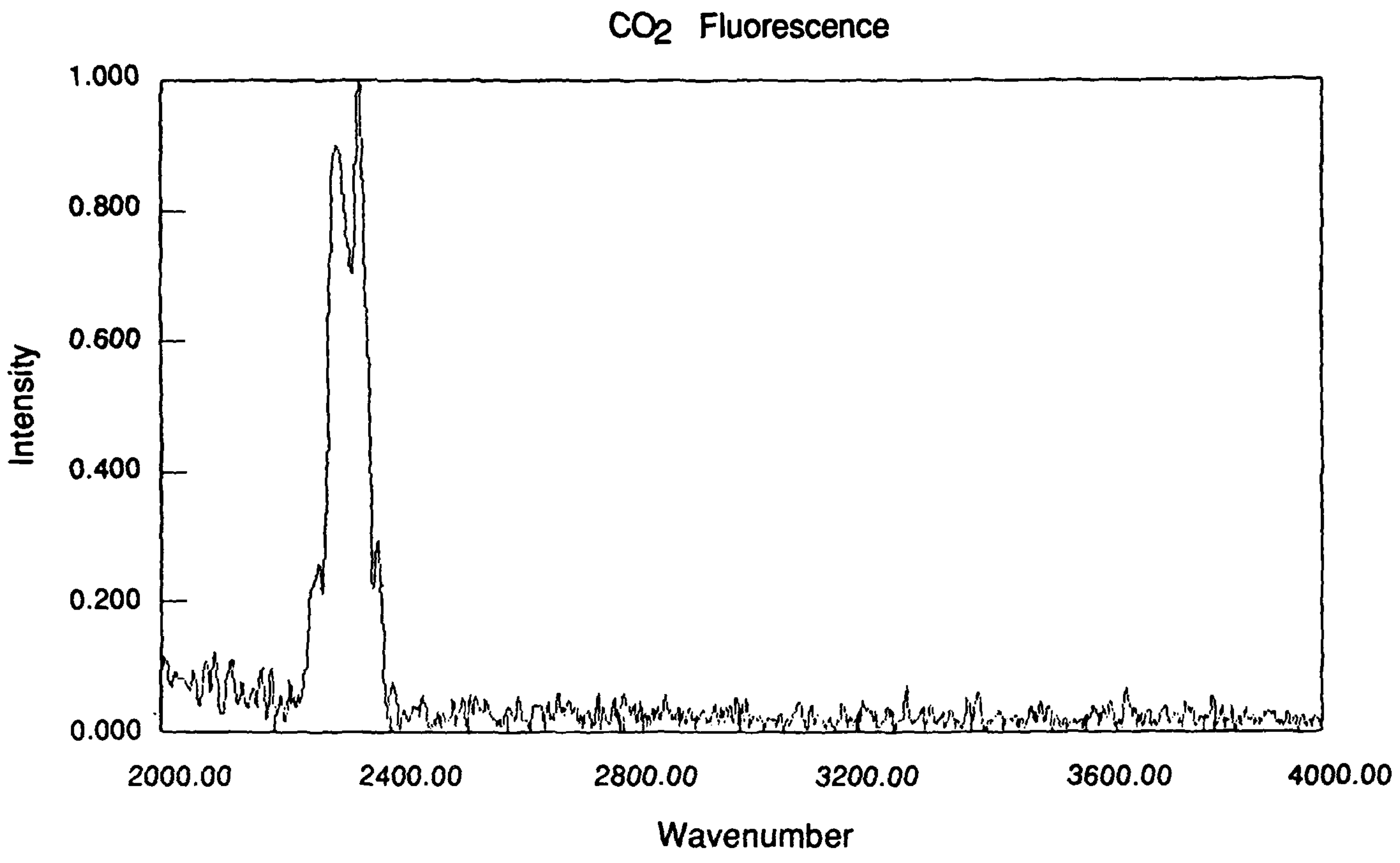

Figure 9. Fluorescence Spectrum - 2000 - 4000 cm^{-1} CO_2 50 Millitorr

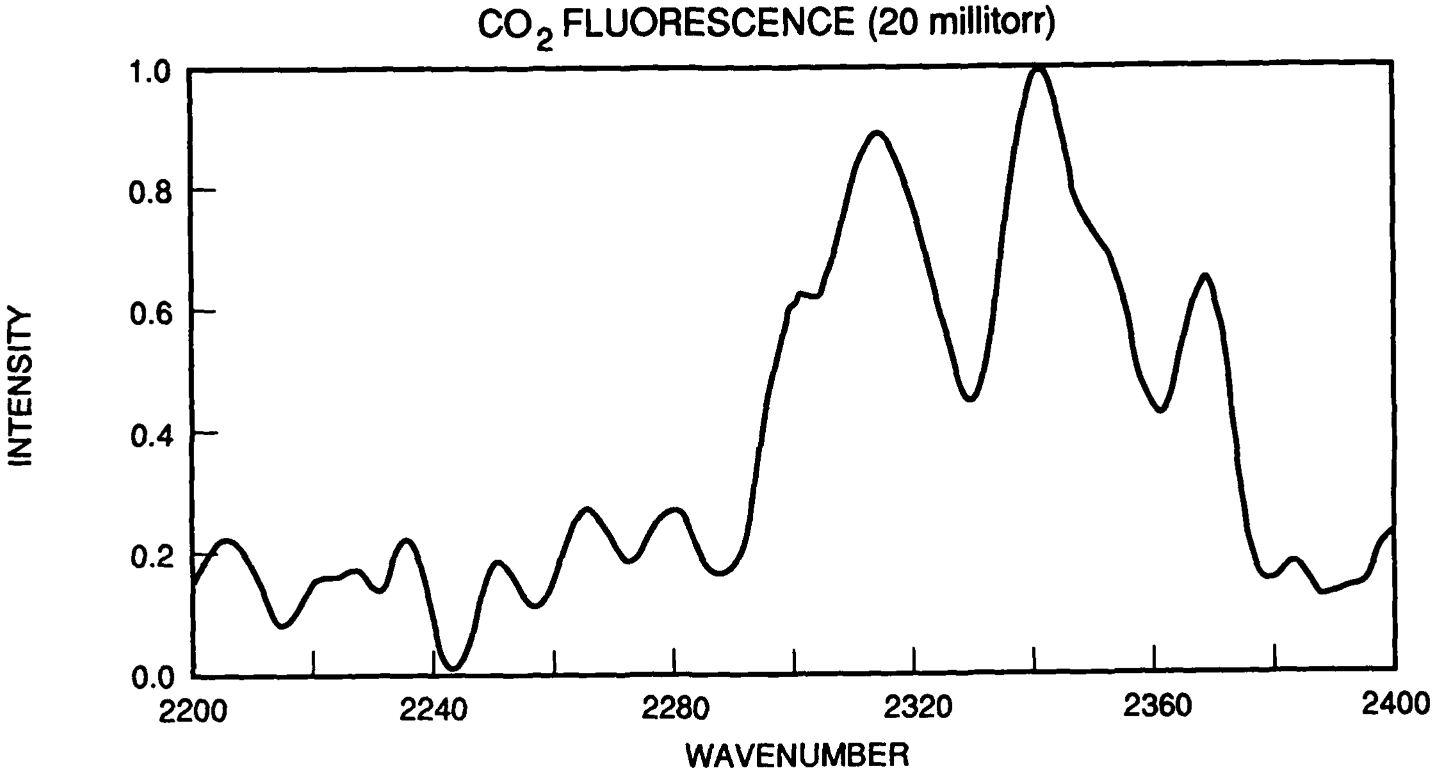

Figure 10. Fluorescence Spectrum - 2200 - 2400 cm^{-1} CO$_2$ 20 Millitorr to 1.1 Torr 4.3 μm Band

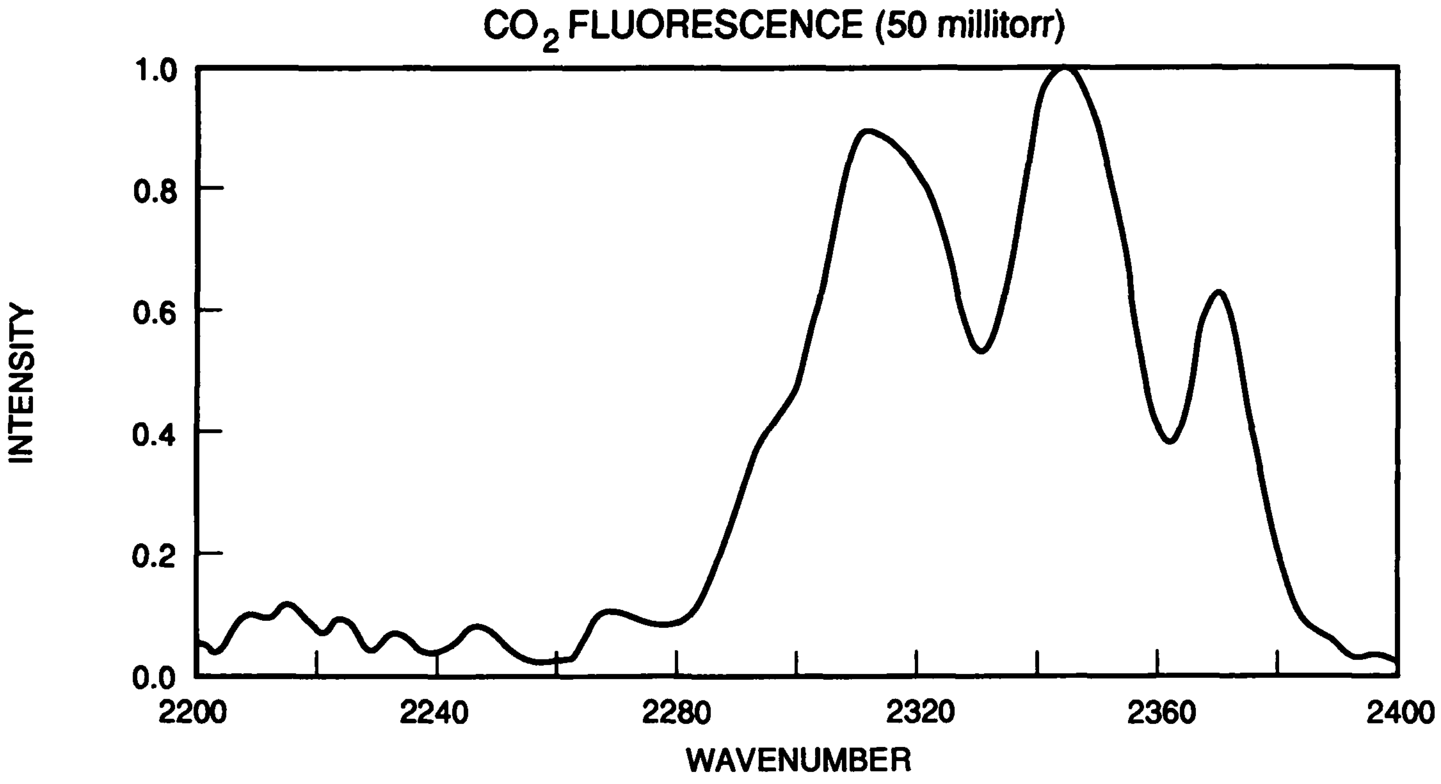

Figure 11. 50 mt

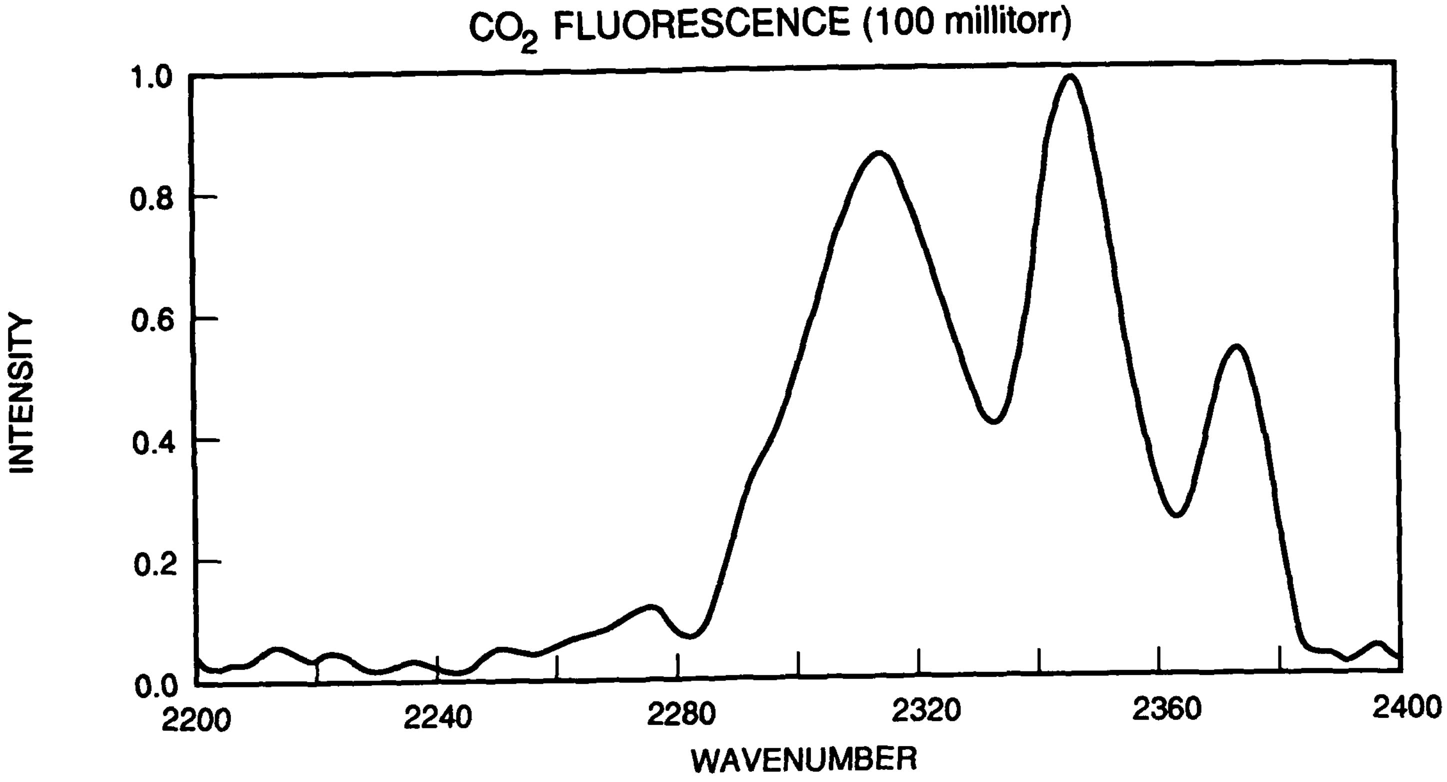

Figure 12. 0.1 t

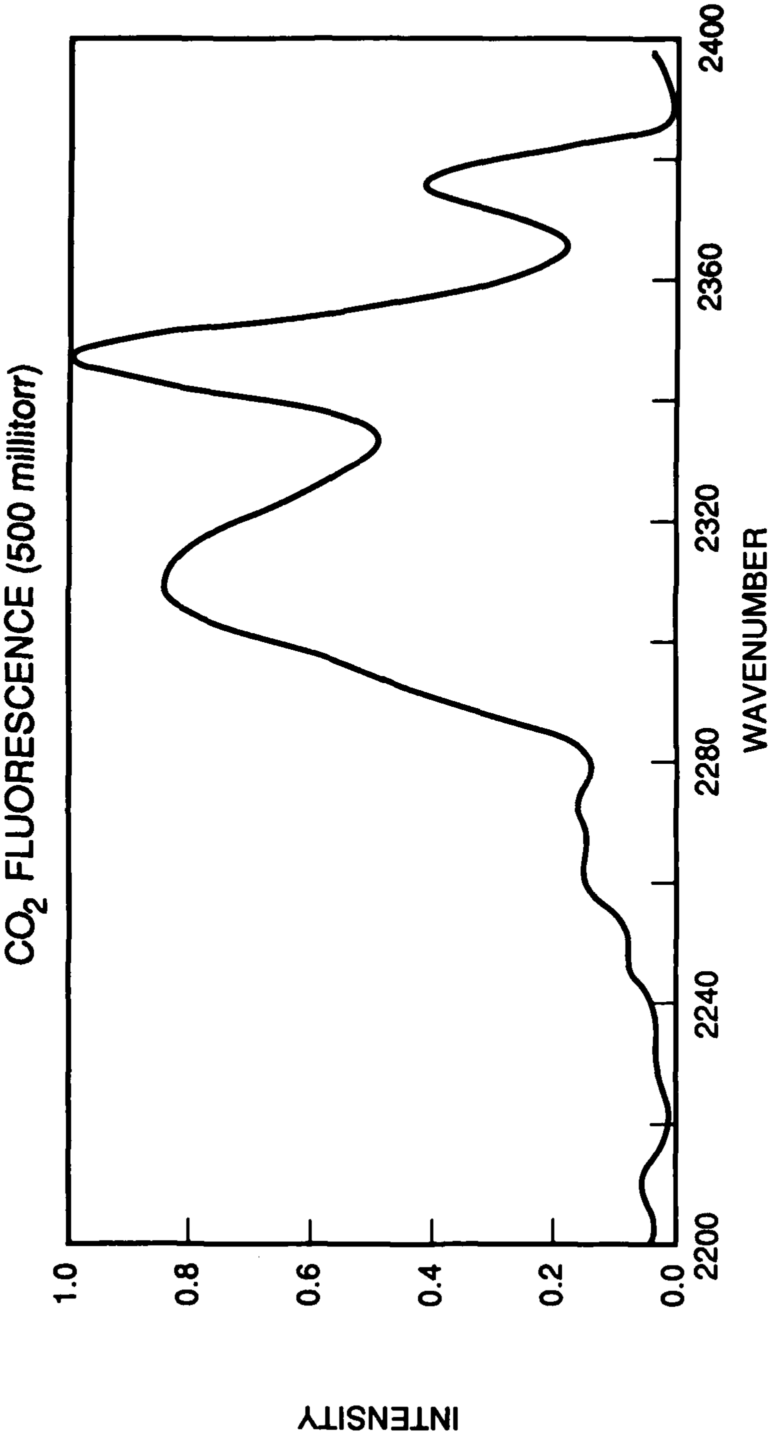

Figure 13. 0.5 t

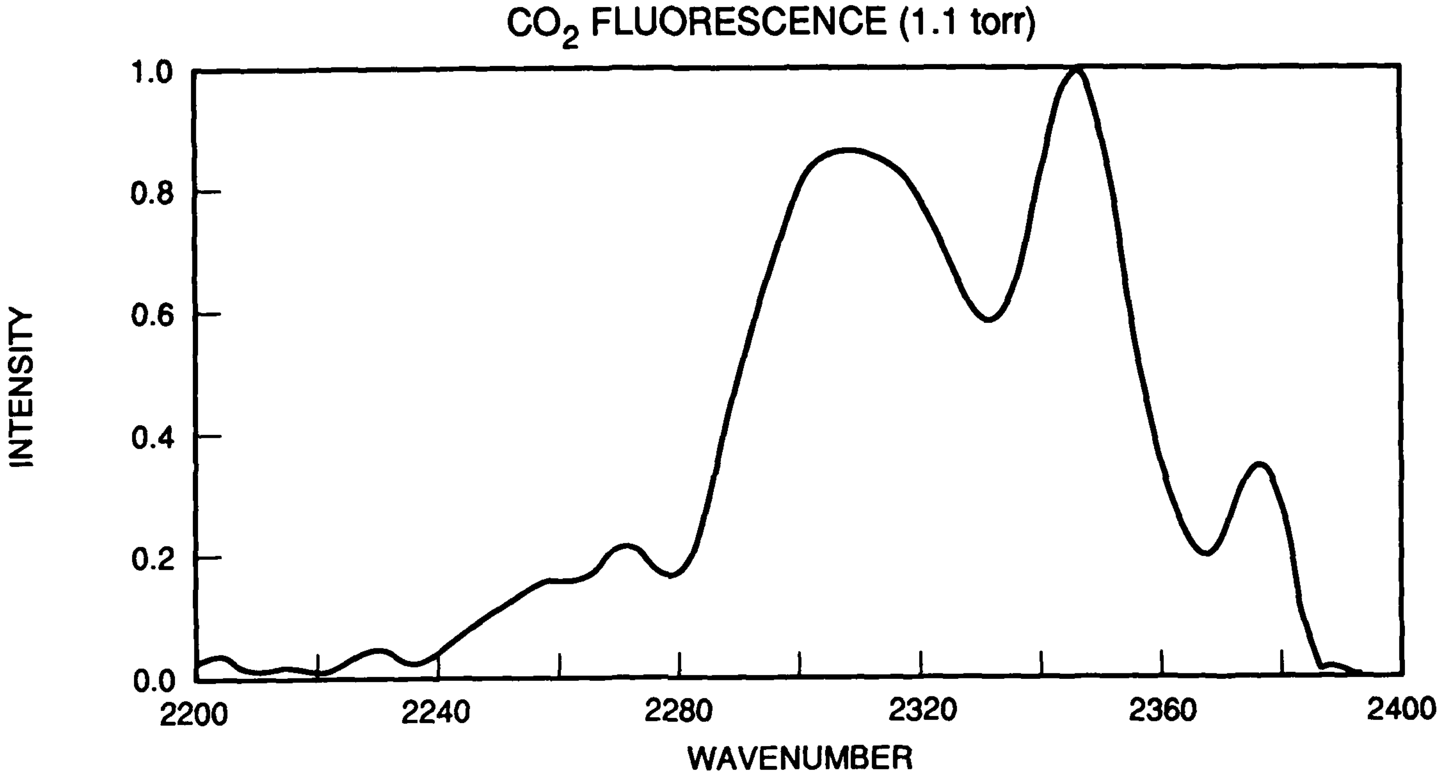

Figure 14. 1.1 t

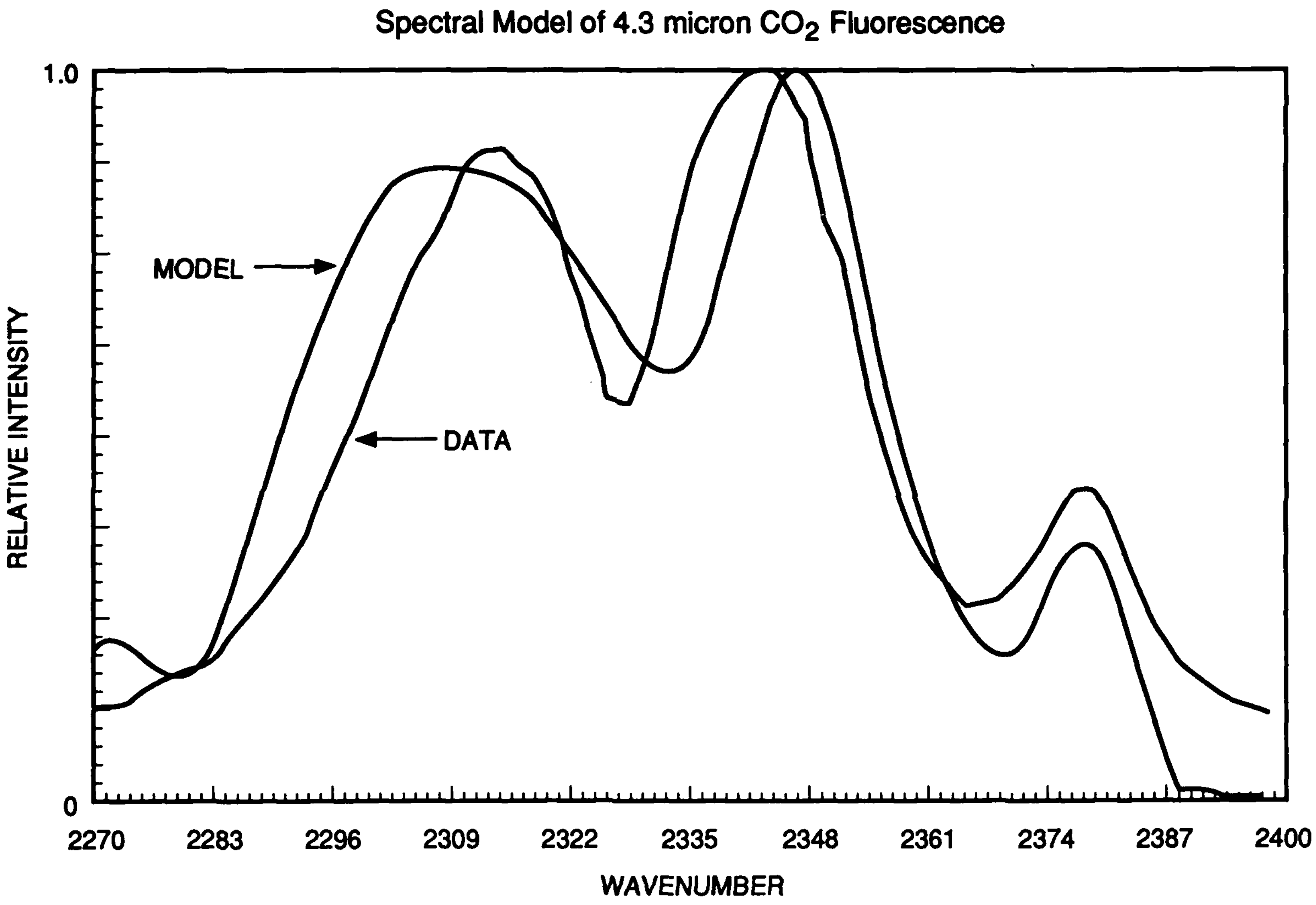

Figure 15. Spectral Fits

5. DISCUSSION

The main difficulty in what might be considered a rather straightforward molecular energy level branching ratio experiment remains a significant overlapping spectral contribution from radiating energy levels, populated solely by collisions (particularly the 001 → 000 transition). Although this can in principle be solved by operating at pressures low enough to preclude significant collisional contributions, there is not enough signal at these levels to obtain the signal to noise ratio required to measure a 40:1 branching ratio. The alternative approach of deconvolving the relative contributions of the purely radiative components from those involving collisions is taken here.

Utilizing the results of the fluorescence excitation spectra an upper limit on the branching ratio can be established.

$$I_{4.3}/I_{2.7} \bullet \text{Bandpass Transmission } (2.7)/\text{BP Transmission } (4.3) \bullet D^*_{2.7}/D^*_{4.3} = 0$$

$$40 \text{ millivolts}/1.4 \text{ millivolts} \bullet 0.55/0.65 \bullet 5 \times 10^{10}/7.5 \times 10^{10} = 16.1 \pm 5$$

where $I_{4.3}$ ($I_{2.7}$) = peak intensity of the radiation passing through the 4.3(2.7) micron filter and D^* is the figure of merit for the InSb detector at the appropriate wavelength. This can only be considered an upper limit since an unknown portion of the 4.3 micron intensity is emitted from the 001 vibrational level populated through collisional processes. An estimate of this contribution is provided in the discussion of the interferometric data.

Examining the interferometric data in Figure 10, we can see that the spectrum is composed of at least 2 convolved vibrational bands at 4.3 microns and no signal above the noise at 2.7 microns. The spectral modeling does a fair job of determining the relative contributions to the 4.3 micron band. The major contributor to this band is the 021 → 020 transition, the band needed for the branching ratio measurement, while as much as a third of the integrated intensity is due to the 001 → 000 band. The fit can be made more accurate by adding contributions from both hot and isotopic bands. Assuming that the collisional energy transfer rate from the 021 band to the 001 band is 3×10^{-10} molecules-cm^{-2}-sec^{-1} and the radiative rate of the 021 band is 420 sec^{-1}, at the 1 torr pressure of CO_2 in the cell the ratio of 021 radiation to 001 radiation should be 2.33×10^4. Some of this discrepancy can be accounted for by assuming that the nitrogen purge of the interferometer was ineffective at eliminating the CO_2 in the path of the fluorescence light. In this case, one must consider the optical thickness of all transitions connected to the ground state through a 50 cm path length of CO_2 with a partial pressure of 0.25 torr present in a standard atmosphere at sea level. Utilizing the appropriate line shape (Voigt profile), line strengths, and CO_2 pressures it was calculated that the integrated intensity of the 001 → 000 band radiation has been reduced by a factor of 1230 (see Table 1).

Table 1. Calculated Integrated Intensity of Vibrational Bands

	001 → 000 (4.3 μm)	021 → 000 (2.7 μm)
50 cm path to detector through interferometer	2.6	150
8 cm path to detector through filter	11.0	200
NO optical thickness	3200.00	230

This still leaves a discrepancy of approximately a factor of 20. Since the source of the nitrogen purge was liquid nitrogen boiloff it is unlikely that this could have enhanced the CO_2 concentration. The optical thickness calculations have been shown to work well in LABCEDE experiments and performing the calculations using Doppler or Lorentzian line shapes cannot account for this discrepancy. This evidence together with the results of Reference 11 imply that the collision quenching rate of the 021 energy level should be reexamined.

The absence of signal above the noise in the 2.7 μm band prevents a direct branching ratio measurement. A lower limit of the 021 → 020 to 021 → 000 branching ratio can be established by examining the signal to noise ratio at 4.3 microns together with the effect of optical thickness on the 021 → 000 transition (column 2 of Table 1). The signal to noise ratio of the best 1 torr spectrum of CO_2 is 50:1. This scaled by the ratio of the interferometer response, response (4.3)/response (2.7) = 2.5 would indicate a lower limit branching ratio of CO_2 (021 → 020)/CO_2 (021 → 000) ≥ 20. Taking into account the optical thickness of the 021 → 000 transition reduces this lower limit to CO_2 (021 → 020)/CO_2 (021 → 000) ≥ 13. Thus this result, together with the results of the filtered fluorescence excitation experiment, brackets the branching ratio: 13 < CO_2 (021 → 020)/CO_2 (021 → 000) < 16.1.

6. CONCLUSION

It can be concluded that the branching ratio of CO_2 (021 → 020)/CO_2 (021 → 000) must be greater than 13 and less than 16. This is slightly smaller than the ratios of the Einstein coefficients and line strengths alone, but is unlikely to affect the results of the upper atmospheric CO_2 models. Just as important is the determination that Finzi and Moore's reaction coefficient for CO_2 (021) + CO_2 (000) - → CO_2 (001) + CO_2 (020) of $k = 3 \times 10^{-10}$ molecules-cm^{-2}-sec^{-1} predicts a significantly different intensity[13] (×10) ratio of CO_2 (021) → CO_2 (020)/CO_2 (001) - → CO_2 (000). It would be worthwhile to update Finzi's and Moore's experiment to confirm this number.

---

13. Finzi, J. and Moore, C.B. (1975) Relaxation of CO_2(101), CO_2(021), and N_2O(101) vibrational levels by near-resonant V-V energy transfer, *J. Chem. Phys.* **63**:(6).

References

1. Stair, A.T., Jr., Ulwick, J.C., Baker, K.D., and Baker, D.J. (1975) Rocketborne observations of atmospheric infrared emissions in the auroral region, *Atmospheres of Earth and Planets*, ed. McCormac, B.M., Reidel, D., Dordrecht, Netherlands.
2. Kumer, J.B. (1974) *Analysis of 4.3 Micron ICE CAP Data*, Air Force Cambridge Res. Lab., Bedford, MA, AFCRL-TR-74-0334, ADA014847.
3. Sharma, R.D., Nadile, R., Stair, A.T., Jr., and Gallery, W. (1981)Earthlimb emission analysis of Spectral Infrared Rocket Experiment (SPIRE) data at 2.7 micrometers, Modern Utilization of Infrared Technology, *Proc. Soc. Photo Opt. Instrum. Eng.* **304**:139-142.
4. Stair, A.T., Jr., Sharma, R.D., Nadile, R.M., Baker, D.J., and Grieder, W.F. (1985) Observation of limb radiance with cryogenic Spectral Infrared Rocket Experiment (SPIRE), *J. Geophys. Res.* **90**:(A10).
5. Kumer, J.B. (1977) Theory of the CO_2 4.3 Aurora Related Phenomena, *J. Geophys. Res.* **82**:(16).
6. Sharma, R.D. (1985) CO_2 Component of Daytime Earth Limb Emission at 2.7 Micrometers, *J. Geophys. Res.* **90**:(A10).
7. James, T.C. (1976) *Laboratory Investigation of Infrared Fluorescence of* CO_2, HAES Report No. 60, Final Report to DNA 4238F, Cont. DNA 001-76-C-0017, ADA043524.
8. James, T.C. and Kumer, J.B. (1979) *Fluorescence Experimental and Auroral Data Evaluation to Improve Prediction of Nuclear Atmospheric Infrared Background*, DNA Report LMSC/D673384, ADA085724.
9. Bevington, P.R. (1969) *Data Reduction and Error Analysis for the Physical Sciences*, McGraw-Hill.
10. Rothman, L.S., and Young, L.D.G. (1981) Infrared Energy Levels and Intensities of Carbon Dioxide - II, *J. Quant. Spectrosc. Radiat. Trans.* **25**:505-524.
11. Caledonia, G.E., Green, B.D., and Murphy, R.E. (1982) On self-trapping of $CO_2(v_3)$ fluorescence, *J. Chem. Phys.* **77**:(10).
12. Green, B.D., Caledonia, G.E., Piper, L.G., Goela, J.S., Fairbairn, A., and Murphy, R.E. (1981) *LABCEDE Studies*, AFGL-TR-82-0060, ADA114389.
13. Finzi, J. and Moore, C.B. (1975) Relaxation of $CO_2(101)$, $CO_2(021)$, and $N_2O(101)$ vibrational levels by near-resonant V-V energy transfer, *J. Chem. Phys.* **63**:(6).

Contents

1. Introduction 161
2. Current Temperature Control System 161
    2.1 Description 161
    2.2 Shortcomings 163
3. New Temperature Control System 164
    3.1 Specifications 164
    3.2 Description 165
    3.3 Operation 165
    3.4 Software 168
4. Implementation of the CTCS 170
    4.1 Replacement Plan 170
    4.2 Replacement Progress 170
5. Enhancements 171

14. New Heater Control for COCHISE

by

D.R. Sinclair

1. INTRODUCTION

The COCHISE facility consists of a vacuum chamber containing a cryogenic reaction cell and monochromator held at about 20 K by a refrigerator using helium as the working fluid. A thermal shroud shields the interior components from the blackbody radiation given off by the walls of the vacuum vessel, which is at room temperature. The reactant gases enter the reaction cell by means of gas injectors held at 80 K to prevent clogging with frozen gas. In addition, there is a blackbody radiator inside the tank which operates between 220 K and 380 K. The operating temperatures are maintained under computer control.

2. CURRENT TEMPERATURE CONTROL SYSTEM

2.1 Description

A block diagram of the current temperature control system is shown in Figure 1. There are 24 channels of temperature sensing available, and the sensors are 500 ohm platinum resistance

COCHISE HEATER CONTROL
CURRENT SYSTEM
28 DEC 88

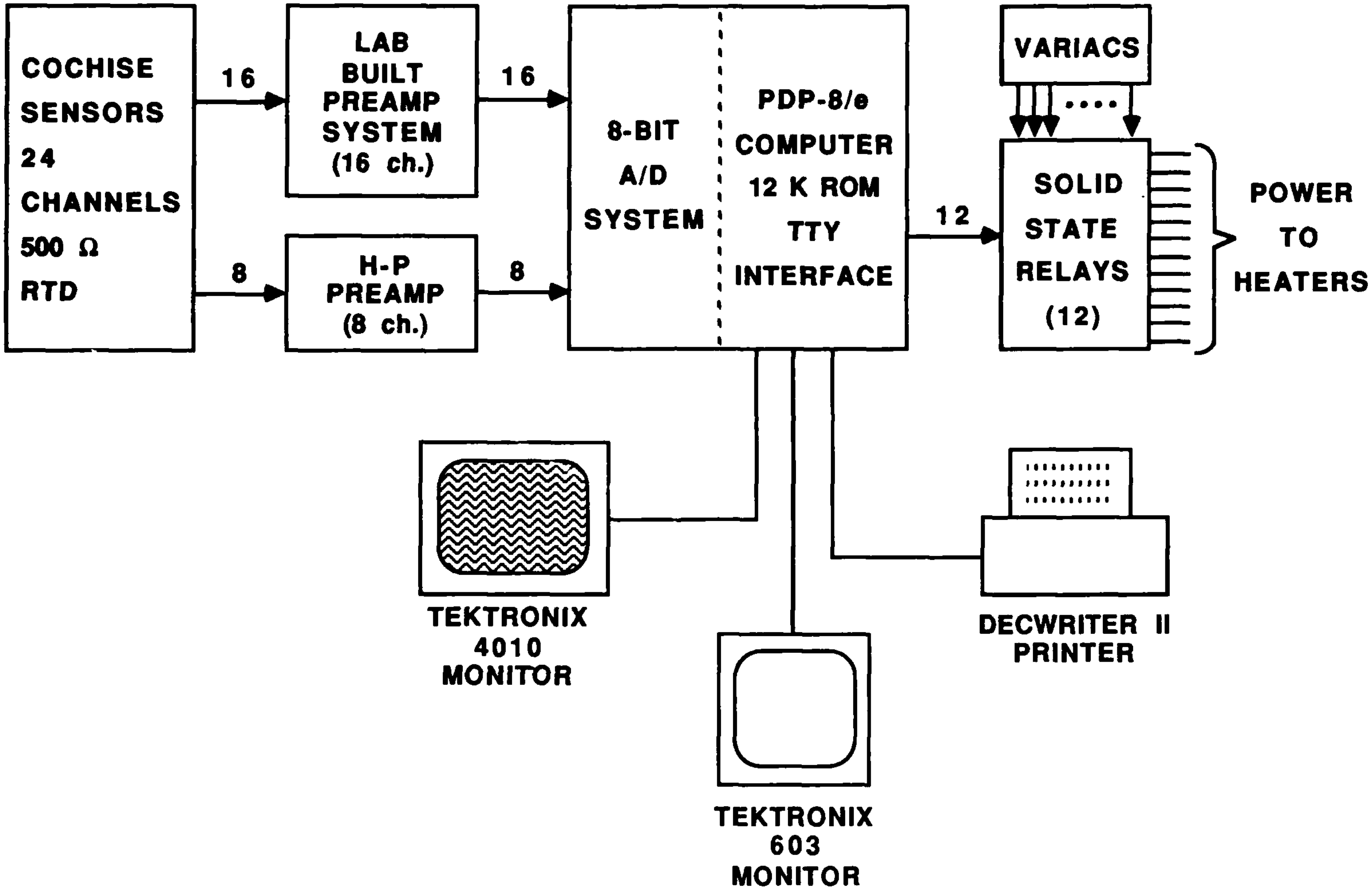

Figure 1

thermometers (RTDs) connected for two-wire resistance measurement. A lab-built circuit provides sensor biasing and signal preamplification. The preamp outputs are fed into am 8-bit A/D converter which is part of a DEC PDP-8 computer system. The computer converts the A/D value to degrees Kelvin and displays these values on Tektronix 4010 and 603 monitors. Eight channels are displayed, and are user selected by switches mounted in the COCHISE rack. The 603 monitor provides a digital readout of the temperatures while the 4010 monitor provides graphical output, allowing the user to follow warming and cooling trends as well as to check for stability once a setpoint has been reached. Every 5 minutes the temperature values of several channels are printed, providing a permanent record of system behavior. Once the temperatures have been displayed, the computer then calculates the heater response for the channels that are under computer control. Of the 24 sensor channels, 12 are part of a feedback loop. The computer varies the heater output power by varying the duty cycle of the waveform delivered to the heaters, from 0 to 100 percent in steps of 12.5 percent. The Variacs are used to set the coarse range of heater output, and are adjusted for minimum temperature ripple. Temperatures are monitored with resolution of 0.5 K and absolute accuracy of about ±3 K from 30 K to 370 K, and can be maintained to within ±1 K in the range from 60 K to 370 K.

2.2 Shortcomings

Although the temperature control system has performed adequately there are several arguments for its replacement. The strongest argument concerns the level of performance attained by the current system, specifically the measurement precision and the degree of control optimization. Much of the COCHISE refrigeration system operates at temperatures below 30 K, beyond the reliable temperature monitoring range. This makes it difficult to verify proper refrigerator operation and to identify and localize potential problems. In the case of the blackbody, temperature inaccuracy is reflected in decreased calibration accuracy, and temperature ripple at the 0.5 K range is clearly visible using newer detector systems such as the SSPM. The major sources of error are:

(1) RTD measurement error. RTD sensor response is proportional to temperature, and the resistance of the COCHISE sensors is less than 1 ohm at temperatures below 30 K. Since COCHISE uses a 2-wire resistance measurement circuit, lead resistance is added to sensor resistance. At low temperatures, lead resistance may be an order of magnitude large than sensor resistance, dominating the response, and the reading is meaningless. Nonlinearity in RTD response also detracts from accuracy.

(2) A/D resolution. The current system uses an 8-bit A/D converter and a linearization algorithm to convert signal voltage to temperature, so that the best attainable temperature resolution is about 0.5 K. The lack of resolution makes it difficult to follow slowly changing waveforms or to verify that a stable operating point has been reached.

(3) Heater output. The heater output can be varied in increments of 12.5 percent, which is insufficient to maintain both tight temperature control and rapid change of setpoint. In practice the operator turns us the variac when moving to a higher setpoint and turns it down when moving lower, thus centering the control range around the new setpoint. This procedure requires operator supervision and distracts the operator from the scientific tasks

at hand. Under most conditions changes in setpoint are not reached as quickly as they might be under optimal control, resulting in lost time.

Another series of system shortcomings concerns equipment reliability. The current hardware is over 15 years old and is long obsolete. There has been evidence of mechanical and electrical failure, and the cost of maintaining the system exceeds the purchase cost of a new system. After an initial "infant mortality" period, electronic equipment generally has a low failure rate until late in its useful life, when the failure rate increases dramatically. Operation of COCHISE is dependent on the temperature control system, and system failure results in aborted or prematurely terminated experiments and weeks of lost time.

These conditions argue for the decision to implement a new COCHISE temperature control system better able to meet the needs of future experiments by providing improved performance more reliably.

3. NEW TEMPERATURE CONTROL SYSTEM

3.1 Specifications

The new system was named the COCHISE Temperature Control System (CTCS), and after available technology had been surveyed, two sets of performance specifications were drawn up, called "best-case" and "live-with". These are:

Specification	Best-case	Live-with
No. of channels	Open-ended	32
Temperature range	4 K - 400 K	10 K - 380 K
Abs. accuracy	±0.1 K	±0.3K, 10 K - 30 K
	60 K - 400 K	±1.0 K, 30 K -380 K
Resolution	0.05 K	0.05 K, 10 K - 30 K
		0.2 K, 30 K - 380 K
Setpoint range	30 K - 400 K	50 K - 380 K
Deviation from setpoint	±0.1 K	±0.2 K

In addition to these numerical guidelines, the CTCS had to require minimal operator intervention ("set-and-forget") and minimal periodic calibration (no trimmers). It had to be able to run in parallel with the old system to avoid downtime until thoroughly proven. It had to be built using off the shelf components and programmed in high level languages wherever possible due to limited funds and manpower availability. The system as conceived meets all the requirements in the "live-with" list, and is capable of meeting the stricter standards with some effort. Rather than iterate on the design in order to meet the stricter standards, it was decide to implement the first pass immediately.

3.2 Description

A block diagram of the CTCS is shown in Figure 2. As can be seen from the diagram, the RTD sensors have been replaced by a new type of sensor known as a silicon miniature diode thermometer (SMDT). These sensors are widely used in cryogenic systems and are matched to a standard curve to ±0.1 K at 4.2 K and ±0.5 K at 77 K and 300 K. They are usable from 1 K to 435 K and have a reproducibility of 0.03 K. It is therefore possible to meet the "live-with" specifications on temperature measurement precision using these sensors, along with a suitable preamp and A/D system. The SMDTs have an equivalent series resistance of 5 0 kilohms or more, so that the effects of lead resistance are negligible. This allows accurate measurement using a 2-wire topology, which in turn reduces the number of feedthroughs necessary. The SMDTs require a simple current source for biasing, and they are inexpensive enough to allow redundant sensors for increased reliability.

The higher signal output of SMDTs makes preamplifier design easier as well, since bridge techniques are no longer necessary. The preamplifier under design uses only fixed resistors to set the gain, eliminating the need for trimmers and making periodic adjustments unnecessary. Variations in preamp gain are handled by system software.

The preamplifier outputs are routed to a computer system in the COCHISE rack which consists of a single board computer, 12-bit A/D converters, and a duty cycle modulator card. The single board computer, known as the BCC-52 and made by Micromint of Vernon, CT, was chosen for its low cost, BASIC language programmability, and available peripheral cards. The BCC-52 functions as an interface and communications controller for the console computer. One of the system peripherals is a 12-bit A/D card which allows better measurement resolution than the previous 8-bit system There are two such cards in the system, each providing 16 single-ended channels for a total of 32 channels. Also purchased from Micromint were two 8-channel solid state relay cards, providing a total of 16 relays capable of switching 3A at 140 Vac. These relays are driven by a lab-built card known as a duty cycle modulator card (DCM). As in the old system this card varies the heater power by varying the percentage on time, but whereas the old system allowed increments of 12.5 percent, the new design allows steps of 0.04 percent, resulting in smooth power changes and tighter temperature control capability. The solid state relays and the DCM use zero-voltage switching to eliminate switching transients that may cause induced noise in signal lines. A block diagram of the DCM is shown in Figure 3.

The console compute displays the temperatures read by the rack system and calculates the heater response. At regular intervals the console computer stores temperature readings on a hard disk for later analysis and prints them out on an Okidata printer. The system being used as a console computer is a Z-100 with hard disk, and was chosen because of its programmability in compiled BASIC and its ready availability. The programmability in BASIC allows later modification of the control algorithm and user interface, and makes a later transition to another computer easier.

3.3 Operation

Operation of the CTCS is straightforward. Every 5 seconds a bank of eight channels is read and sent by the BCC-52 to the Z-100. If the channels are to be displayed on the screen as one of 5 graphs or 8 digital displays, then this is done. Then the heater response is calculated and the results sent back to

COCHISE TEMPERATURE CONTROL SYSTEM
(CTCS)

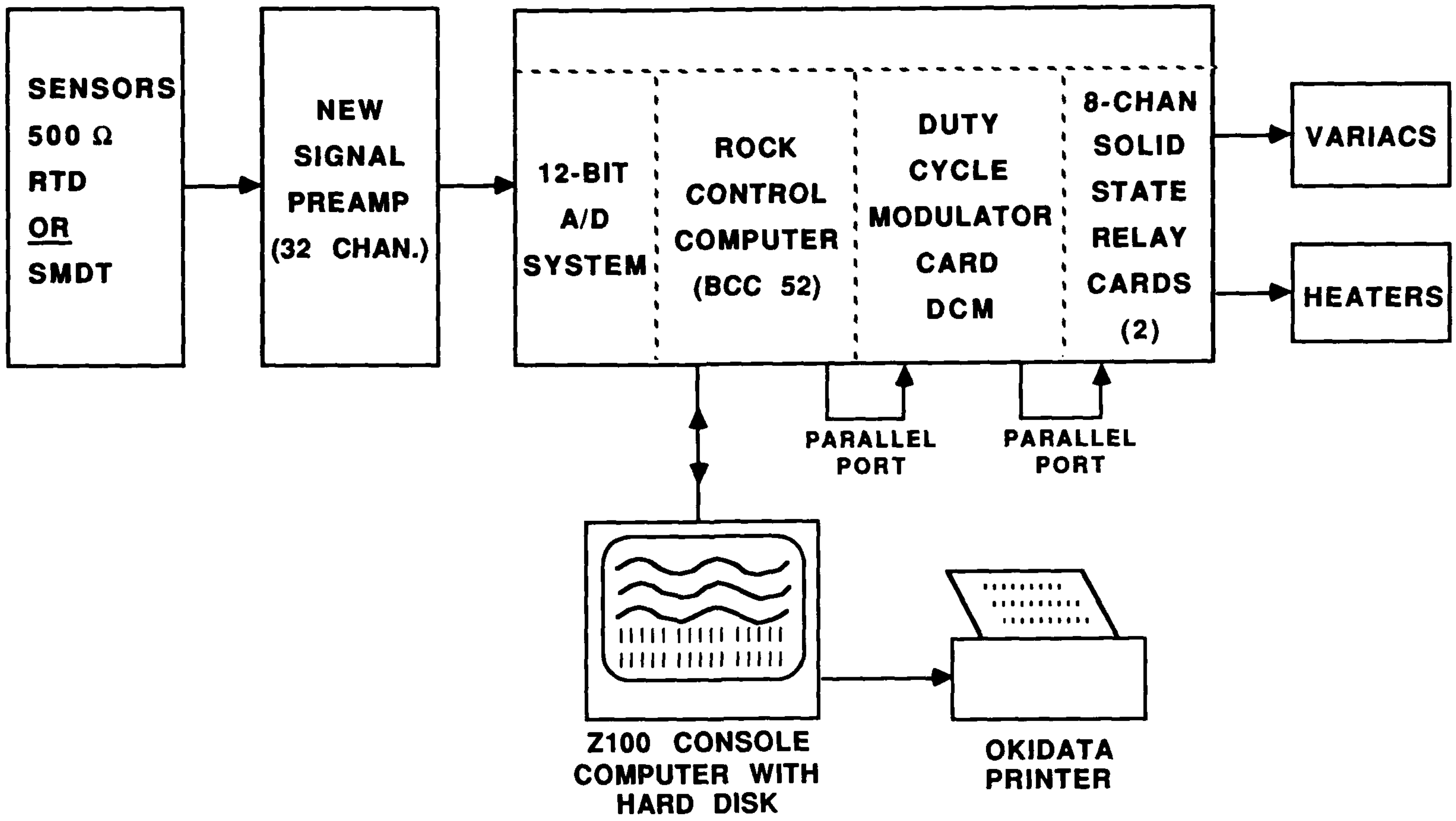

Figure 2

DUTY CYCLE MODULATOR
(DCM)
BLOCK DIAGRAM

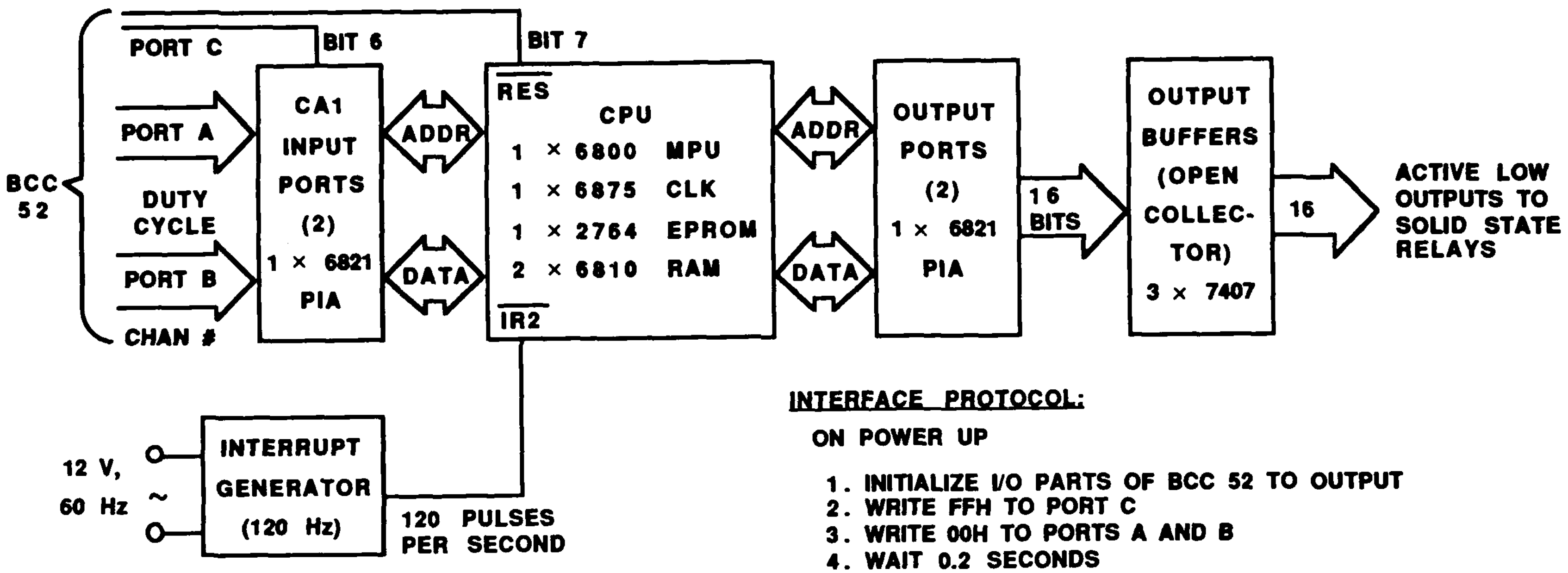

<u>INTERFACE PROTOCOL:</u>

ON POWER UP

1. INITIALIZE I/O PARTS OF BCC 52 TO OUTPUT
2. WRITE FFH TO PORT C
3. WRITE 00H TO PORTS A AND B
4. WAIT 0.2 SECONDS

TO UPDATE A DUTY CYCLE VALUE

1. WRITE NEW DUTY CYCLE VALUE TO PORT A
2. WRITE CHANNEL NUMBER TO PORT B
3. WRITE BFH TO PORT C
4. WRITE FFH TO PORT C
5. WAIT 0.05 SECONDS

Figure 3

the control rack. After 5 seconds have elapsed the next bank of channels is read and the process repeats. Since there are 4 banks of temperature data, a given channel is read and its response calculated every 20 seconds. As the thermal time constants are on the order of minutes, sampling is rapid enough to ensure accurate control. Every 5 minutes the temperatures of several critical channels are printed out and written to a data file for archival purposes.

3.4 Software

The CTCS software is made up of three different programs: the control console program COCHISE, the rack control program HEATERS and the DCM card ROM code.

The DCM program pseudocode is shown in Figure 4. The DCM divides a 2-second interval into 240 intervals, corresponding to 240 half-cycles of 60 Hz power. The number of half-cycles within this period for which the solid state relays is on is written to the DCM by the console computer via the BCC-52 rack controller. At each zero crossing of the ac waveform the DCM determines whether a given relay should be turned on for the duration of that half cycle and sets an output bit accordingly. This process repeats every half cycle of the 2-second interval. At the end of this interval the DCM repeats the process with the same duty cycle. Should the DCM be commanded to change the duty cycle, it begins a new 2-second interval immediately, not waiting for the previous interval to finish. With this configuration it is possible to control the duty cycle of 16 channels simultaneously.

Upon startup the BCC-52 waits for a signal from the console, and upon receipt sends the date and time maintained by its internal real-time clock. If the time and date are altered by the operator it receives the new values from the console and updates the clock. The HEATERS program then begins the control cycle. At 5-second intervals it sends voltage values read by the A/D to the console, receives the heater response curves, and writes these values to the DCM. The next bank of channels is then ready to be read. This process continues until the rack controller receives a termination message from the console computer.

The most complex program is the program COCHISE. The program allows the operator to make changes to control algorithm time constants and temperature setpoints while the control loop is active. It also allows the operator to change the channels displayed and whether a digital readout or a graphical display is to be used. The heater output of certain channels can be forced to a given value for diagnostic purposes, and commonly used sets of parameter values can be stored as a unit and recalled at will. The program uses a proportional-integral-derivative (PID) control algorithm, which is widely used in chemical process control.

Upon startup the program loads temperature lookup tables and default program settings from the hard disk. Then the program reads the time and date from the rack computer, asks the operator if he wants to change them, and sends the updated values back to the rack controller. The axes are plotted on the screen and the program waits for the first set of data to be sent. After receiving the temperature data the program then checks to see if any operator requests have been made. The program services these requests and then processes the channel temperature data. The program converts the A/D readings into temperatures by means of a lookup table, and both RTD and SMDT sensors are supported. After this step has been completed the program calculates the heater response using the PID algorithm. The latest iteration of the algorithm excludes the derivative term to reduce sensitivity to induced noise. The program writes the heater response to the rack controller, providing

Duty Cycle Modulator Card
Pseudocode Listing

```
Start
Initialize I/O prots and variables
Clear interrupt mask, infinite loop begins
When an Interrup occurs:
    Read input port status byte
    If a duty cycle is to be changed
        Read in new duty cycle (port A)
        Read in channel to be changed (port B)
        Put first byte of new data stream into RAM
    Assemble output bytes
        Take next bit in channel 0 stream,
        make this bit 0 of output port A
        If no more bits left in that byte then
            Load next stream byte into RAM
            If that was last byte in the stream then
                Change address of next byte to start of stream
            Else increment address to point to next byte
        Repeat this process for channels 1-7
        Output the assembled byte to port A
        Repeat the process for channels 8-15
        Output the assembled byte to port B
Keep this up until power is shut off
```

Figure 4. Duty Cycle Modulator Card

dummy values for channels that are not under temperature control. It is important to note that the control loop is interrupted while operator requests are being serviced. If this delay is longer than the time remaining in the 5 second sampling interval then the sample interval is extended so that no samples are skipped. This results in a small variation of the heater response from the theoretical optimum, but is without significant effect.

4. IMPLEMENTATION OF THE CTCS

4.1 Replacement Plan

To minimize the trauma associated with system changeover and to allow independent testing and verification of subsystems, it was decided to implement the new control system in at lest three phases.

Phase One of system implementation is the replacement of the PDP-8 system by the Z-100 and BCC-52 systems. This is to be accomplished by running the two systems in parallel and switching between them. This will allows the determination of control algorithm constant. Once all of the constants have been determined, the COCHISE apparatus will be run under control of the new system. Once the remaining bugs are eliminated the PDP-8 system will be retired. At this stage the old signal conditioners and Variacs will still be in use, and all of the temperature sensors will be RTDs.

Phase Two is the replacement of the signal conditioning system. New amplifier and biasing circuitry will be designed allowing the use of both types of sensors, and these boards will be bench-tested for correct operation before being installed. After a complete COCHISE session without failure the old signal conditioning system will be removed.

Phase Three involves replacement of the old sensors with SMDTs and alteration of the heater elements so that the Variacs can be removed. The sensors will be replaced as necessary, and the heaters replaced as the time permits. Replacement is expected to be performed on one channel at at time.

4.2 Replacement Progress

Phase One of the replacement process is close to completion. The COCHISE apparatus thermal time constants have been measured and the control system response constants approximated. Eleven of the twelve channels have been tested under the new system, the remaining channel having failed during the last session, preventing a test. In all cases tested, the new system functioned satisfactorily, exceeding the performance of the old system in all respects and already meeting many of the design specifications given above. The system is to undergo its first fill test in January 1989, and changeover is expected in February 1989, with disposal of the old computer set for March 1989.

Work on Phase Two has already begun, with a preliminary design for a signal conditioner awaiting prototyping. A deadline for completion cannot be given due to the early status of work on this phase of the project.

Several SMDTs have been purchased for implementation of Phase Three, but further work must wait for completion of Phase Two.

5. ENHANCEMENTS

Some possible enhancements to the CTCS are already evident. The most visible change would be to change the console computer from a Z-100 to a Z-248. Software portability is not a problem, and the availability of a color screen could be put to good use. Since this change does not involve large performance increases it can be put off until the Z-100 systems begin to show signs of deterioration and is not a high priority.

System reliability could be further enhanced by expanding the number of channels and using multiple sensors at each controlled point, and by integrating a watchdog computer into the system to detect power failure, pump shutdown, and other system failures so that appropriate steps to resolve the problem can be taken quickly.

Software performance could be enhanced by implementing a cyclic redundancy check on data transmitted between the rack controller and the console, allowing faster communication between subsystems and a faster sample rate. Although not necessary from a control point of view, more rapid updates give the operator a greater sense of security. Control performance could be enhanced by implementing a self-tuning controller, so that manual tuning could be avoided.

U.S. GOVERNMENT PRINTING OFFICE [illegible]